

The First Laboratory Searches for Low-Mass Axion Dark Matter

by

Chiara P. Salemi

B.S. Physics and Mathematics,
University of North Carolina at Chapel Hill (2017)

Submitted to the Department of Physics
in partial fulfillment of the requirements for the degree of
Doctor of Philosophy in Physics
at the
MASSACHUSETTS INSTITUTE OF TECHNOLOGY

September 2022

© Massachusetts Institute of Technology 2022. All rights reserved.

Author: _____

Chiara P. Salemi
Department of Physics
June 30, 2022

Certified by: _____

Lindley Winslow
Associate Professor of Physics
Thesis Supervisor

Accepted by: _____

Deepto Chakrabarty
Associate Department Head of Physics

The first laboratory searches for low-mass axion dark matter

Chiara P. Salemi

Submitted to the Department of Physics on June 30, 2022
in partial fulfillment of the requirements for the degree of
Doctor of Philosophy in Physics.

Abstract

Multiple astrophysical and cosmological observations have shown that the visible matter described by the Standard Model of particle physics is only a small fraction of the energy density of the universe. We believe that there is about five times as much matter that is ‘dark’. The dark matter is likely comprised of massive particles that interact very little or not at all with other matter. Despite this lack of interaction, the ubiquity of dark matter has allowed it to have profound effects on the history of our universe—including seeding the formation of structures such as the galaxy in which we live.

One of the most well-motivated dark matter candidates is the axion, a hypothetical particle that is predicted by the solution to another long-standing mystery in physics, the strong CP problem. The Standard Model predicts that CP symmetry should be violated by the strong force. However, precision measurements have shown that strong interactions conserve CP symmetry to better than one part in 10^{10} . At present, the most viable solution to this strong CP problem introduces a new particle, the axion. Within a wide range of parameters, the axion also satisfies all of the requirements to be dark matter.

This dissertation presents the first direct search for low-mass axion dark

matter, using an innovative lumped-element detection method. In a lumped-element detector, a strong magnetic field interacts with the field of dark matter axions around us, inducing an effective current. This effective current is read out via a superconducting LC circuit and measured with high-sensitivity quantum sensors. The entire device must be kept only barely above absolute zero in order to reduce backgrounds that could mask a signal.

The prototype experiment that is the primary focus of this thesis, ABRACADABRA-10 cm, set world-leading limits on axion dark matter. Over the course of two month-long physics runs from 2018 to 2020, it excluded axions with masses $0.31\text{--}8.8\,\text{neV}$ and couplings $g_{a\gamma\gamma} \gtrsim 3.2 \times 10^{-11}\,\text{GeV}^{-1}$. This thesis will cover the lifetime of the experiment from design to construction to analysis.

The success of ABRACADABRA-10 cm has now set the stage for the DM-Radio program, a series of larger detectors that will be capable of finding or definitively excluding axion-like particles and QCD axions over a wide range of masses below $1\,\mu\text{eV}$. I present initial sensitivity and design studies for the upcoming two generations of DMRadio, DMRadio-50 L and DMRadio-m³. I also discuss the path towards a future, large-scale experiment, DMRadio-GUT, which would probe of QCD axions at GUT-motivated masses.

The dark matter community is coalescing around the goal of probing the entire axion dark matter parameter space over the next couple of decades. The effort is driven by new ideas along with advances in cryogenic, magnet, and quantum sensing technology. The 1L, 1T ABRACADABRA-10 cm prototype experiment has formed the basis of a major component of the worldwide effort to find or exclude axions. The work in this dissertation represents the opening of new parameter space in the search for dark matter.

Thesis supervisor: Lindley Winslow
Title: Associate Professor of Physics

Contents

Contents	5
Acknowledgements	13
1 Introduction	16
2 Dark Matter	21
2.1 What is the universe made of?	22
2.1.1 The Standard Model	22
2.1.2 The dark side	25
2.2 Evidence for dark matter	26
2.2.1 Anomalous velocities	26
2.2.2 Gravitational lensing	27
2.2.3 The Cosmic Microwave Background	30
2.3 So what is the dark matter?	31
2.3.1 Did we write down gravity wrong?	32
2.3.2 Requirements on a new particle	32
2.3.3 Some particle dark matter candidates	34
Standard Model material	34
Novel particles	35
2.3.4 Wave-like dark matter	36

3 The Axion	37
3.1 The strong CP problem	37
3.1.1 The θ term	38
Features of the θ term	39
Contributions to the θ term	41
3.1.2 Limits on the neutron EDM	43
3.1.3 Naturalness	45
3.2 The PQ solution and axions	47
3.2.1 The PQ solution to strong CP	47
3.2.2 Axion particle	49
3.2.3 Axion models	51
PQWW	51
Invisible axions	52
Axion-like particles	52
3.3 Axion cosmology	53
3.3.1 Axions in an expanding universe	53
3.3.2 Post-inflationary PQ-breaking	57
3.3.3 Pre-inflationary PQ-breaking	60
4 Lumped-Element Detection	66
4.1 Axion detection	66
4.1.1 Non-photon interactions	66
4.1.2 Photon interactions	67
4.1.3 Mass regimes	70
4.2 The lumped-element method	72
4.2.1 Experimental sensitivity	72
Broadband SNR	74
Resonant SNR	77
Resonant scan rate	81
4.2.2 Detector components	83
Magnet	83
Pickup inductor	85
Readout circuit	86
Cryogenics	89
5 ABRACADABRA-10 cm	91
5.1 Experimental apparatus	92
5.1.1 Cryomechanical system	92

5.1.2	Magnet	95
5.1.3	Shielding	98
5.1.4	Cold readout	99
Run 1 pickup circuit	99	
Run 3 pickup circuit	101	
5.1.5	Warm electronics	102
Run 1	102	
Updates for run 3	103	
5.2	Data processing and physics runs	104
5.3	Data analysis	107
5.3.1	Calibration	107
Checking the detector response	108	
Converting our limits	113	
5.3.2	Noise and data cleaning	113
Low frequencies—vibrations	113	
High frequencies—electromagnetic interference . .	115	
Wide features	120	
Data cleaning pipeline	120	
5.3.3	Statistical analysis	121
Run 1 likelihood analysis for discovery and limit-setting	124	
Analysis updates for runs 2 and 3	126	
Signal injection tests	128	
5.3.4	Axion dark matter limits	131
5.4	Other similar experiments	133
6	DMRadio	137
6.1	Next-generation experiments	138
6.1.1	Science and technology goals	138
6.1.2	Preliminary designs	140
Magnet and pickup	140	
Readout circuit	147	
Cryomechanical	147	
6.2	DMRadio-GUT	148
6.2.1	Science and technology goals	148
6.2.2	R&D paths	150
Magnet and cryogenics	151	
Beyond-SQL amplifiers	154	

Resonator R&D	157
7 Conclusion	161
A Variables and Conventions	163
A.1 M_{ap}	163
A.2 \mathcal{G}	164
A.3 k	165
A.4 c_{PU}	166
B COMSOL Modeling	168
B.1 ABRACADABRA-10 cm	169
B.2 DMRadio-50 L	175
References	178

List of Figures

2.1	The energy content of the universe	22
2.2	The Standard Model of particle physics	24
2.3	Galactic rotation curve	27
2.4	Dark matter substructure in simulation	28
2.5	Gravitational lensing	29
2.6	The Bullet Cluster	30
2.7	The Cosmic Microwave Background	31
3.1	Higgs Yukawa interaction	43
3.2	CP violation with electric and magnetic dipole moments	44
3.3	Cartoon of the neutron EDM	44
3.4	Symmetry breaking	48
3.5	Misalignment mechanism of axion production	54
3.6	Evolution of the axion in its potential	56
3.7	Misalignment angle patches for post-inflation PQ breaking	58
3.8	Strings and domain walls	60
3.9	Available windows for f_a	62
3.10	Illustration of primordial fluctuations	62
3.11	Constraints on the anthropic argument	64
3.12	Axion parameter space under stochastic inflation	65
4.1	Axion-photon Feynman diagram	68
4.2	Axion detection regimes	70
4.3	Lumped-element method circuit diagram	73

4.4	Noise contributions	79
4.5	Toroid and solenoid magnet geometries	84
4.6	Pickup sheath geometries	86
4.7	Sensitivity bandwidth illustration	88
5.1	ABRACADABRA-10 cm detector in dilution fridge	94
5.2	Constructing the magnet	95
5.3	Magnet mounted in superconducting shielding can	97
5.4	ABRACADABRA-10 cm pickup structures	100
5.5	Run 1 calibration circuit	102
5.6	Run 3 calibration and readout circuit	104
5.7	Data processing flow for ABRACADABRA	105
5.8	Post-SQUID electronics chain calibration	109
5.9	2-stage SQUID diagram	110
5.10	Circuit diagram of calibration-pickup network	111
5.11	Calibrated flux-to-voltage conversion in runs 1 and 3	112
5.12	Run 1 averaged spectrum	114
5.13	SQUID correlation with accelerometer data	115
5.14	Magnet-correlated vibrational backgrounds	116
5.15	AM radio signal in the ABRACADABRA-10 cm data	117
5.16	Transient electromagnetic interference (EMI) in run 1	118
5.17	EMI combs in run 3	119
5.18	Bump reduction with warm electronics shielding	121
5.19	Data cuts pipeline for runs 1, 2, and 3	122
5.20	Effect of the run 3 nuisance parameter correction	129
5.21	Run 2 significant transient	130
5.22	Run 1 signal injection tests	130
5.23	Run 3 signal injection tests	131
5.24	Limits on $g_{\alpha\gamma\gamma}$ from run 1 and run 3	132
5.25	Zoom of run 3 limits	133
5.26	SHAFT experimental layout	134
5.27	Superconducting LC circuit Investigating Cold axions (ADMX SLIC) experimental layout	135
5.28	DMRadio Pathfinder experimental layout	136
6.1	DMRadio-50 L and DMRadio-m ³ sensitivity projections	139
6.2	DMRadio-50 L magnet and sheath design	141
6.3	Schematic of magnet gap region	142
6.4	Diagram of toroidal sheath gasket	143

6.5	DMRadio-m ³ magnet design	145
6.6	DMRadio-50 L shield suspension	147
6.7	Potential tunable capacitor design	148
6.8	DMRadio-GUT sensitivity projection	149
6.9	Noise domination regimes	157
6.10	Sensitivity bandwidth optimization, in and beyond the SQL	158
B.1	Meshing the ABRACADABRA-10 cm geometry	169
B.2	The axion effective current distribution	170
B.3	Axion-generated magnetic field	171
B.4	Magnetic field pattern with wire loop pickup	172
B.5	Magnetic field pattern with cylinder pickup	173
B.6	Magnetic fields in a twisted pair cross section	174
B.7	COMSOL geometry of DMRadio-50 L	175
B.8	Optimization of DMRadio-50 L sheath geometry	176
B.9	Optimization of DMRadio-50 L pickup geometry	177

List of Tables

5.1	Parameters from ABRACADABRA-10 cm’s physics runs	93
6.1	Target detector parameters for DMRadio-50 L and DMRadio-m ³ . .	139
6.2	R&D thrusts for achieving GUT sensitivities	150
6.3	DMRadio-GUT R&D scenarios	151

Acknowledgements

Over the course of my five years at MIT, I have been taught and supported by an amazing group of people. I could not hope to do justice to their contribution to my education and growth in the short pages of these Acknowledgements. Here I offer an abridged expression of gratitude to the people who made this work possible.

First, I would like to give a big thank you to my advisor, Lindley Winslow, who has taught me so much, not only about the science that we do on a daily basis, but about setting myself up for a career and navigating the social waters of our field. I have drawn much inspiration from her ability to juggle several world-leading experiments, service to the community, and life outside physics.

I would also like to thank the other members of my committee, Joe Formaggio and Anna Frebel. In addition to serving on my committee, Joe has been a source of well-thought-out guidance as my academic advisor (as well as a source of vacuum flanges as our across-the-hallway lab neighbor). In her role as GWIP advisor and as the instructor of the LEAPS course, Anna has taught me much about the soft skills that are needed to succeed in physics, in addition to her role in this last step of my Ph.D.

I would like to offer much thanks to Jon Ouellet, who has taught me almost everything I know about operating a dilution refrigerator, along with a multitude of other useful skills and information. Under his guidance, I went from being a lost first-year graduate student who had barely touched a soldering iron to a knowledgeable member of the experimental team. It's an

honor to say that along the way we have become good friends. Jon was also instrumental in shaping this dissertation with a plethora of useful comments and suggestions.

I would never have gotten to MIT in the first place without Reyco Henning. He saw potential in me my first semester in college and opened my eyes to the world of physics research in his group at UNC. I have been so fortunate in grad school to get to continue to work with him and learn from him about how to think about building and operating an experiment. I am so happy that we will be able to continue our collaboration on DMRadio after I graduate.

These acknowledgements would not be complete without the inclusion of my office-mate and work-wife Kaliroë Pappas. She has been there to laugh about our mistakes, bemoan our frustrations, and celebrate our successes. I thank her for being a guinea pig as I learn how to mentor and for making the long hours of noise hunting in the lab fun.

Many thanks go out to the members of the ABRACADABRA and DMRadio collaborations, who have created a welcoming and curiously-supporting environment for young scientists like myself. On ABRACADABRA-10 cm, I would particularly like to thank Yoni Kahn and Ben Safdi, who helped me develop my theoretical intuition. Ben also provided comments on the axion theory section of this thesis.

There are many people at MIT that have made it feel like home. I would particularly like to thank Field Rogers, who is my kindred spirit dark matter lady and thesis writing partner extraordinaire. Alex Leder, who so generously allowed me to adopt Olaf from him, is one of the kindest individuals I have ever met. He made me feel welcome when I arrived feeling intimidated. Julieta Gruszko arrived at MIT around the same time I did, and quickly became both a role model and close friend. She is always a source of inspiration and encouragement.

The community of graduate students and post-docs in LNS was an integral component of my experience at MIT. Too many people to name helped me as I prepared for my oral exam, including my study group in my cohort as well as the older graduate students who had already overcome the challenge and were eager to help others going through it. The same community of people creates a welcoming atmosphere and fosters curiosity with the student seminar and journal club. I would especially like to thank the other members of the Winslow group with whom I have shared many lunches.

The research described in this thesis would not be possible without the

support of the incredible staff at LNS and in the MIT physics department. I would particularly like to thank Jack McGlashing, who has helped me with everything from running helium lines through the ceiling, to moving my desk to a different office, to making sure that I received my mail. He is always a friendly face in the hallway, and hearing him whistling as he goes about his day never fails to cheer me up. Elsye Luc, Nicole Laraia, Lauren Saragosa, Alisa Cabral, Lily Xu, Joe Cucinotta, Cathy Modica, and Sydney Miller, just to name a few, have seamlessly taken care of all of the administrative, travel, and financial needs that have come up during my years in LNS and MIT. Finally, there are many people who invisibly support the research we all do: custodians, facilities and computing staff, and more. Thank you for making my work possible.

Outside of MIT, I have been supported by an incredible collection of people. Friends near and far kept me sane throughout my years at MIT, including through the dark, isolating days of the pandemic. I would like to give special thanks for my family, especially my parents and siblings, for always supporting me in whatever ventures I have chosen to take on. And finally I would like to thank my partner, David, an unexpected and amazing outcome of my years here, who encouraged and advised me through thick and thin, and who is joining me for the next adventures.

1

Introduction

We study physics to better understand the world around us. Through the scientific method, we can decode the physical principles dictating the lifecycles of stars, the movement of electrons in exotic materials, and the interactions of the tiny particles that comprise all the matter in the universe. The foundation of everything we know is a set of fundamental particles and the interactions between them, known as the Standard Model (SM) of particle physics. It can explain the underpinnings of almost everything we have observed of the universe. The ‘almost’ in that sentence is an important one, however; there are several places where the SM falls short. Although far from a complete list, most physicists would agree that the following are some of the most urgent questions that the SM is either wrong about or does not even try to answer:

1. What is the extra, undetected mass in the universe? This is what we term ‘dark matter’.
2. Why is there something rather than nothing? The universe is almost entirely made of matter, with very little antimatter to annihilate the matter away.
3. Why do neutrinos have mass, and what are their masses? The SM assumes that the neutrinos are massless, but experiments have shown

that they have a non-zero, although very small, mass.

4. What is causing the universe to rapidly expand? For lack of a better understanding, we call this ‘dark energy’.
5. How does gravity work at the smallest scales? Although early scientists understood more about gravity than about the three other fundamental forces, today it is the least understood of them, and the SM says nothing about how gravity works.

As you can see, these are large holes in a model that claims to explain the foundations of everything.

The SM was not always ‘standard.’ It came about from collecting experimental evidence and trying to understand why matter behaves as it does. Over time, these pieces of evidence and disparate models grew together into a unified picture, like sections of a jigsaw that start to fit together. At some point the puzzle was complete enough to make out a picture in the jigsaw, and so the physics community stamped it as ‘standard’ and continued the work to fill in the gaps. At this point, there are some large empty chunks as well as a few spots with only a piece or two missing. But the problem is that we don’t know if we even have all of the pieces to work with. Are we only working on a small section of the puzzle, and it actually fits into a larger picture? The only way we can find out is to try to piece together the pieces we have, and see if and how they fit together.

My Ph.D. work has been on one of the larger holes in our puzzle, the first point in the list above, dark matter (DM). We have had an inkling of the existence of DM since the 1930’s. In 1937, astronomer Franz Zwicky published a paper that laid out two different methods of ‘weighing’ clusters of galaxies [1]. In it, he found that the different methods gave wildly different results for how much matter the cluster contained. The first method was to measure the amount of light coming from the stars and other luminous material as a proxy for the cluster’s mass. The second method was to observe the motion of individual galaxies in the cluster; by understanding how they were pulling on each other gravitationally, Zwicky could figure out how massive they were. The latter method indicated that the galaxy cluster held much more mass than revealed by the luminosity measurements. Although Zwicky assumed that this missing matter, which he termed ‘dark matter,’ was just gas, cold stars, or other normal material, later research showed that the DM had to be something more exotic

Despite our not knowing its identity, we can glean a fair amount of information about DM from its gravitational interactions and its lack of other interactions. Its first characterizations come from Vera Rubin’s work in the 1970’s and 1980’s. She and her collaborators found that Zwicky’s finding of extra dark mass in galaxies was correct, and they were able to map out its distribution [2]. These maps revealed that in many galaxies, dark matter outweighs regular matter and is distributed out to huge distances from the centers of galaxies, beyond where most of the stars live.

Since the discovery of this anomaly, further research has produced considerable independent evidence that there is matter in the universe that does not significantly interact with the SM particles or with itself. In Chapter 2, I discuss the body of evidence for dark matter along with potential solutions for what it can be. My research focuses on a hypothetical particle called the axion, which is one possible solution to this problem, or a candidate to be the dark matter.

If it exists, the axion is unique among the fundamental particles. It would not have been created in the same way as the particles of the SM. According to the theory of inflation, all the SM particles came from the decay of one field in the early universe, the inflaton. Right after the Big Bang, the soup of inflaton decay products lived in a hot, dense environment. The particles quickly came into thermal equilibrium, constantly bumping into each other, interacting, and forming new particles. The dark matter axion, on the other hand, has a different origin story. It did not come from the decay of the inflaton and was never in thermal equilibrium with the other particles. The axions that waft through the universe today are the same solitary axions that were born in the earliest moments of the universe, never interacting other than to slowly clump together under the influence of gravity. In Chapter 3, I go into more detail into this origin story and why axions are so important to life today, despite their lonely existence.

The extremely small mass of the axion is also unique. The axions that I describe in this dissertation are about a million billion times lighter than an electron, which is in turn two thousand times lighter than the proton. (Neutrinos—the lightest known massive particles—are still about a million times heavier than the axion.) Because they have such a low mass, it makes more sense to think of axions as waves instead of as particles. This approach is the same as how we treat photons; photons are massless particles that make up visible light and the other parts of the electromagnetic spectrum. Instead of talking about light particles, we talk about light waves which can

diffract in a prism or pass through polarized sunglasses. We can treat axions the same way, and build detectors to look for axion waves.

The question is then, if axions exist, why haven't they been discovered yet? Their tiny mass and interaction strength makes detection require extremely sensitive detectors. Most previous DM experiments searched for a hypothetical particle called a WIMP, which would weigh several orders of magnitude more than a proton. Even though it would interact only rarely, if a WIMP hit a detector, the nucleus it hit would recoil, leaving a relatively big signal. Axions do not interact often *and* when they do interact, they are so small that they do not leave much of signal for us to detect. Imagine a ping pong ball bouncing against a bowling ball—the bowling ball barely moves! Even if an axion deposited all of its energy in such a detector, the signal would be some billion billion times smaller than we are capable of detecting.

Instead of hanging our heads and saying that axions are undetectable, we can think outside the box. In particular, we can make use of their huge numbers, wave-like nature, and the fact that they ever-so-slightly interact with photons. By making precise observations of photons—of electromagnetism, we can see if electric and magnetic fields work the way we would expect based on the SM, or if they are slightly modified because of axion interactions. The experiments that I work on, ABRACADABRA-10 cm and DM-Radio, make extremely precise measurements of electromagnetism, looking for small electric currents that will appear in a magnetic field if axions are present. I describe this technique in Chapter 4.

Technology with the capability to detect this small current is relatively new. We need detectors that can sense tiny amounts of energy and we need the environment around our experiment not to overpower the axion signal. Advances in sensors and cryogenics over the last couple of decades have begun to address these needs, and ongoing work especially in quantum sensing is preparing us for definitive experiments to search for axions. The ABRACADABRA-10 cm experiment is the first time that we have been able to search for low-mass axion dark matter in the lab, and it makes use of these technologies, combining quantum sensors called SQUIDs with a donut-shaped magnet inside a refrigerator that keeps the entire experiment below 1 K (equivalently, -272 °C or -458 °F). Chapter 5 describes the construction, operation, analysis, and results of this experiment.

ABRACADABRA-10 cm was small but mighty, and its success in demonstrating this new method to search for axions lays the groundwork to build

larger experiments that will be able to detect axions that interact even more feebly with the SM. As I cover in Chapter 6, we have begun the design and construction of a suite of future experiments, DMRadio-50 L, DMRadio-m³, and DMRadio-GUT, that will be orders of magnitude more sensitive than the ABRACADABRA-10 cm prototype. In particular, DMRadio-m³ and DMRadio-GUT will be able to test for axions that are the most ‘preferred’ by theory calculations, called QCD axions, which can solve the strong CP problem.

2

Dark Matter

Over the past few centuries, scientists have successfully identified the slew of particles that make up all the matter we can see: electrons, quarks, gluons, etc. It turns out, however, that this zoo of particles only makes up a tiny fraction of the contents of our universe.

In this chapter I will lay out our current understanding, and lack thereof, of the composition of everything. This will start with a brief overview of the universe's three major components, visible matter, dark matter, and dark energy in Section 2.1. In that section I will provide a little bit of detail about the Standard Model (SM) and dark energy, of which we know a lot and almost nothing, respectively. In the remaining sections I will discuss the primary focus of this chapter, dark matter (DM), which we believe is five times more plentiful than the ‘regular matter’ of the SM and whose identity we have some ideas about but have not directly detected (yet). Section 2.2 describes the plethora of evidence we have for DM from astrophysics and cosmology. Section 2.3 lays out potential solutions to the DM problem and the status of evidence for or against them.

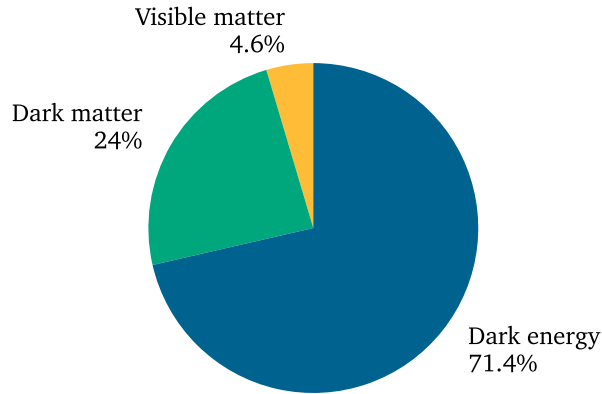


Figure 2.1: The energy content of the universe has three components: dark energy, dark matter, and visible matter. In the present day, dark energy dominates.

2.1 What is the universe made of?

The universe as we know it has three components, visible matter, dark matter, and dark energy. As shown in Figure 2.1, today, dark energy is by far the most ubiquitous, making up $\sim 70\%$ of the energy content. Everything we interact with on a daily basis falls into the small, yellow slice of visible matter—the SM particles.

2.1.1 The Standard Model

The SM describes the particles and interactions of all of the visible matter. It has been highly successful, withstanding decades of high-precision testing. Figure 2.2 summarizes the model. Similar to how the periodic table of elements organizes the chemical building blocks of nature based on their atomic number and material properties, the SM organizes the fundamental particles in terms of various quantum numbers that determine their interactions.

The first quantum number that is relevant for organizing the particles is spin. Fermions have half-integer spin and bosons have whole integer spin, with the Higgs being spin-0 and the gauge bosons spin-1. Particles with half-integer spin are subject to the Pauli exclusion principle, meaning that two fermions cannot occupy the same state. Bosons are not subject to the same restriction, and can have an unlimited number of particles occupying

the same quantum state. This fundamental behavior leads to interesting macroscopic effects that we can see in our daily life. For example, the colors that we see when light reflects off of surfaces are a result of atomic electrons changing between different states. Without the Pauli exclusion principle, all of the electrons could sit in the lowest energy state, and so the transitions and colors we see would be very different. On the other hand, the bright, concentrated light from lasers is possible only because the photons that make up that light beam are bosons that can pack together in the same state, making a coherent beam.

Spin is a particularly important number for dark matter models, as we will discuss later in this chapter. In a nutshell, the fermionic or bosonic nature of the dark matter will determine how closely you can pack the dark matter particles, and hence how dense the dark matter can be.

After dividing the particles by spin, we are left with a variety of other properties with which to organize everything. This includes electric charge, color charge, weak charge, and mass.

Electric charge, associated with electromagnetism, is carried by all of the fermions except for the neutrinos. The charged leptons, electron, muon, and tau, all carry charge -1 and their corresponding antiparticles carry charge +1. The quarks either have $+1/3$ or $-2/3$ charge (or correspondingly $-1/3$ or $+2/3$ for the antiquarks). Quarks are typically grouped in twos or threes, and so the only bare charges we see are integers. Photons, the electromagnetic force carrier, only interact with charged particles, but are themselves neutral.

Only quarks and gluons carry color charge, namely red, green, and blue. Color charge is the charge associated with the strong force, for which gluons are the force carrier. From a distance, everything is ‘colorless’ meaning that every composite particle must either have all three colors or contain a color and its anticolor. At first glance, this might seem similar to how bare electric charges try to pair with their opposite charge, but in fact the statement is much stronger for color. As two color charges separate from each other, the strength of the force between them does not decrease as it does in electromagnetism, and so the color-charged gluons can create new pairs of particles, preventing bare charges from escaping on their own. This is known as confinement.

All of the above fermions¹ are charged under the weak force, interacting with the W and Z bosons. This is the only way that neutrinos interact, and

¹In particular, all of the left-handed fermions; the right-handed fermions are not weakly charged.

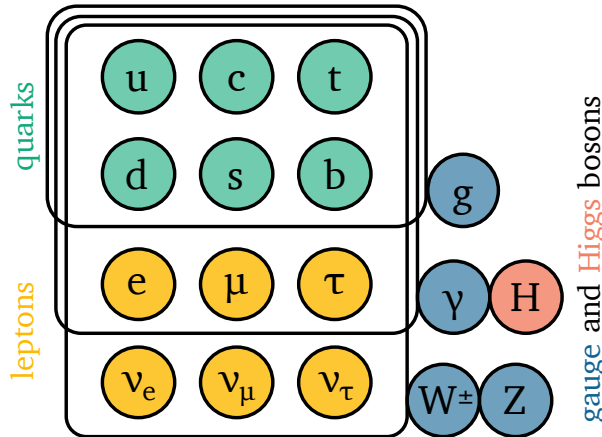


Figure 2.2: The SM is composed of fermions (quarks, *green*, and leptons, *yellow*), force-carrying gauge bosons, *blue*, and the Higgs boson, *pink*, which is responsible for particles masses. The fermions come in three generations, shown here from lightest on the left to heaviest on the right. The boxes around the fermions show which bosons they interact with, and hence which of the four fundamental forces they are subject to. Only the quarks interact with gluons, the strong force carrier. Both the quarks and the charged leptons (electron, muon, and tau) interact electromagnetically, or via the photon. Finally, all of the fermions can undergo weak interactions via the W and Z bosons. The SM does not attribute any mass to the neutrinos in bottom row of the fermions, and so does not predict any neutrino-Higgs interactions. This is a shortcoming of the SM—we know that the neutrinos have mass—and experiments are still working to discover how neutrinos gain their mass and if they interact with the Higgs boson.

as a result they don't interact very much with the rest of the SM and are difficult to measure experimentally. For this reason, scientists thought that neutrinos might actually make up the DM, but as will be discussed later in this chapter, their properties prevent them from satisfying the requirements to match observations.

The final particle to complete the picture, and the most recently discovered SM particle, is the Higgs boson. The Higgs interacts with all of the massive particles in the SM, so everything except the photon and gluon. The SM does not predict Higgs-neutrino interactions, but experiments have shown that the neutrinos do actually have a mass [3–6]. There is still work to be done to figure out how the Higgs and neutrinos may interact.

The SM says nothing about gravitational interactions. Our current under-

standing of gravity works at large distance but breaks down at small scales, and so is not included in the picture of Figure 2.2 [7].

Despite neglecting gravity and neutrino masses, the SM does a remarkably good job at making precise predictions about the interactions of the 5% of our universe that is visible matter.

2.1.2 The dark side

The remaining 95% of the universe is dark. The dark side doesn't interact very much with visible matter, and thus has proved difficult to study. The way that we have circumvented this problem is by making measurements on huge scales, so that we can detect the collective effect of lots of dark matter or dark energy, rather than trying to tease out minute interactions from individual particles.

Measurements of the motion of distant galaxies show that the universe is rapidly expanding, indicating that there is dark energy pervading the universe, expanding space itself [8]. This dark energy actually makes up the majority of the energy content of the present-day universe. Because we have only seen its effects on large scales rather than in controlled laboratory experiments, we are not yet able to identify what dark energy actually is, although there are many theories [9].

About a quarter of the content of the universe is dark matter, which acts similarly to visible matter in that has attractive gravitational interactions (and does not cause the expansion of space like dark energy). Dark matter is ‘dark’ because it doesn't interact (at least not much) with the SM or even with itself. Our knowledge of dark matter is similar to that of dark energy, coming from observations of large bodies in the universe rather than from the laboratory. Dark matter's effects are also relevant on smaller scales such as within galaxies, so we can make more precise astronomical observations and get a better understanding of the requirements on its identity. The following section will go into detail about the evidence we have for dark matter and how that informs our theories.

2.2 Evidence for dark matter

2.2.1 Anomalous velocities

The first experimental evidence² that the universe contains more than it seems was revealed in 1933 with Franz Zwicky's observations of the Coma Cluster [11]. Zwicky 'weighed' the cluster in two ways. First, he measured the amount of light coming from the stars in the cluster and used that to approximate the sum of the mass of those stars. Second, he measured the motion of the individual galaxies orbiting in the cluster. Using the virial theorem, he could calculate how mass should be distributed in the cluster based on the measured velocities:

$$\frac{GM}{r} \sim v^2 \quad (2.1)$$

Here G is the gravitational constant, M is the mass inside a particular galaxy's orbit, and v is the velocity of that galaxy relative to the center of mass of the cluster. What he found was striking. The amount of mass required to support the observed motion of the galaxies was far higher than could be accounted for by the luminous matter.

In the 1980's, Vera Rubin led a team to better quantify the missing mass [2]. They observed 21 diverse galaxies and mapped out the velocities of the stars inside them as a function of radius. With this data, they were able to show that not only was there more mass in the galaxies than expected, but the mass was distributed out much farther from the galactic center than the majority of the stars. This effect is shown in Figure 2.3 for the galaxy NGC 3198.

In the decades since this pioneering work, observations of many galaxies and galaxy clusters have confirmed this effect. Most recently, surveys of the stars in our own galaxy such as Gaia have been able to provide more detailed models of the distribution of dark matter [13–15]. These high-statistics datasets indicate that in addition to the virialized halo, there may be a complex substructure such as clumps and streams of dark matter, see Figure 2.4. These features may modify the signals that we can see in direct dark matter searches. This idea will be discussed further in Chapter 4 in the context of axion searches.

²Although Zwicky's paper was the first published evidence of dark matter, the idea that there might be additional matter in space that did not shed light was well-established [10].

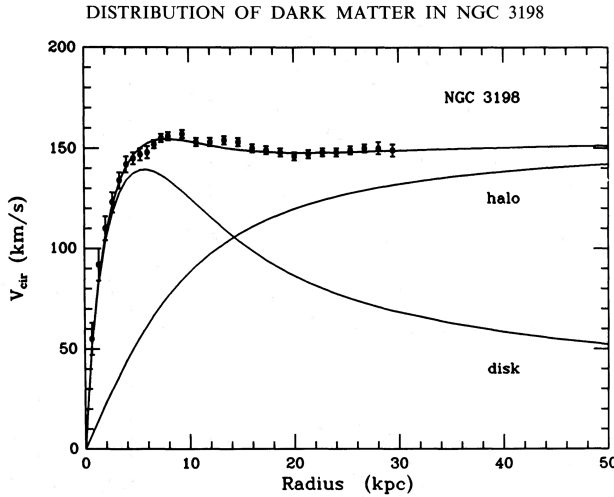


Figure 2.3: The rotation curve of barred spiral galaxy NGC 3198 [12]. The data points are measurements of the velocity of galactic hydrogen gas. The bottom curve shows a model for the luminous matter in the galactic disk. The matter is concentrated in the center of the galaxy, so distant objects would move more slowly as the gravitational pull drops off. The curve labeled ‘halo’ gives a fit for the additional matter that must be there to recreate the observed rotation curve. The dark matter is distributed more homogeneously to the outer reaches of the galaxy, and so causes the outer stars and gases to orbit more rapidly.

2.2.2 Gravitational lensing

The above observations indicate that there is more mass in galaxies and galaxy clusters than we expected. Another way to think about this is that the gravitational wells are deeper than we thought, so the motion of matter through them is modified from our expectation. This is a direct result of Einstein’s general relativity—the geometry of space is modified by the massive objects occupying it, and in turn the motion of objects will follow the consequent bent trajectories. A modified gravitational well not only affects bodies such as the stars and gas clouds measured in rotation curves, but also changes the trajectory of light as it passes through.

This bending effect on light is known as gravitational lensing, and is shown in Figure 2.5. If we observe a massive object, it is possible for light from a source behind that object to be bent around it, giving us a modified image of the background object. The distortion is affected by the amount and distribution of the mass in the intermediate ‘lens,’ and so observations

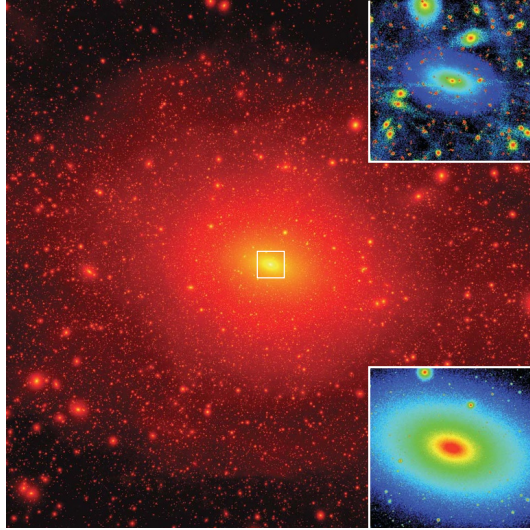


Figure 2.4: Simulations showing dark matter substructure in a galaxy similar to ours, from [16]. The *upper right inset* shows the phase space distribution of streams and infalling clumps in the galaxy’s central region.

of gravitational lensing provide another probe of mass that does not rely on the matter being visible.

Figure 2.5 shows an image of strong lensing, where the background image shows obvious distortion. Striking images like these are only a small fraction of the lensing we see. Smaller effects are more common and often more useful for determining the dark matter distribution. In weak lensing, instead of measuring the distortion of a single background object, one measures the statistical distribution of the preferred stretching direction of many background galaxies. Not only does this open up more objects to observation, but it also can give an approximate map for the distribution of mass in the foreground object. Additionally, microlensing is when shape distortions are not visible at all, but there is a time-dependent effect on the image brightness as the lens and background object move relative to each other in our field of view.

There have been many observations of lensing on a wide variety of scales that point to a large dark matter component in the structures in our universe [17]. This dark matter component appears to be clumped at large scales, but have a much more smooth distribution over smaller scales. The clumping at large scales is a result of a long history of gravitational attraction; gravity

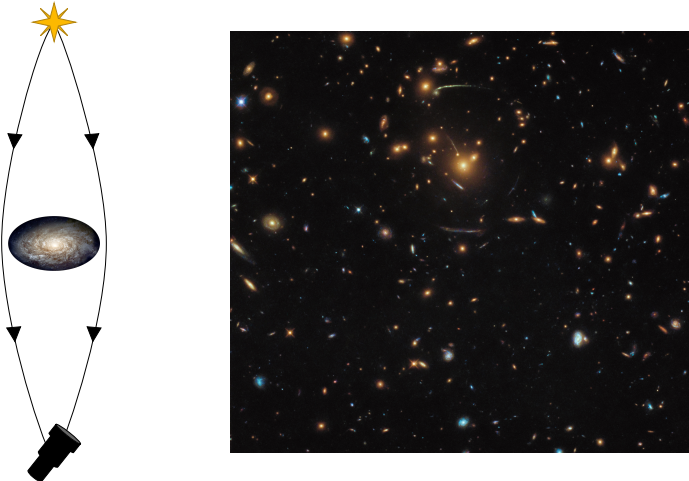


Figure 2.5: Gravitational lensing occurs when the light from a distant object curves as it moves through a gravitational well, *left* [18]. This effect distorts the images of those distant light sources when they reach our telescopes, as can be seen in this dramatic photo of strong lensing from the Hubble telescope, *right* [19]. The background source shows up as arcs surrounding the galaxy cluster that caused the lensing.

is a feeble force, but over billions of years has caused matter to cluster into strands and nodes of higher density. The small scale homogeneity results from dark matter's lack of other, stronger interactions that can bind particles into structures such as stars or dust clouds.

One particularly strong piece of evidence for dark matter comes from observations of gravitational lensing in the Bullet Cluster [20]. The Bullet Cluster is actually two galaxy clusters that are in the process of merging. The two clusters collided some time ago. Compact objects such as stars and galaxies, being relatively sparse and far apart, largely passed by each other without collision, but the gas and plasma which dominate the visible matter component of the clusters, are distributed more widely and so were stopped during the collision by their interactions. The plasmas emit X-rays, which are observable by telescopes such as Chandra. The X-rays provide a map of the majority of the visible mass in the cluster, as shown by the heat map in Figure 2.6.

In addition to observing the plasma's X-rays, astronomers took measurements of the weak lensing of background galaxies through the cluster. These measurements mapped a very different distribution of mass, shown in the

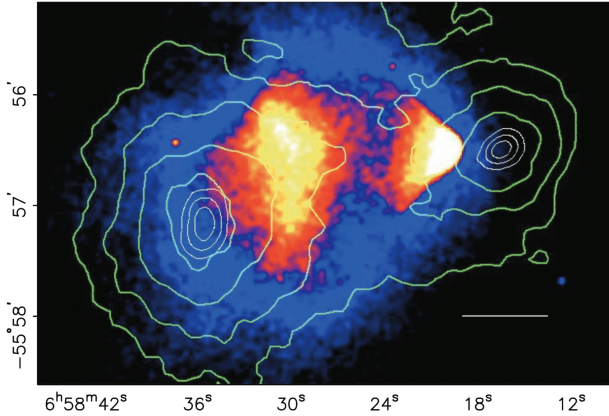


Figure 2.6: Map of the Bullet Cluster, two colliding galaxy clusters, shown with a scale bar of 200 kpc [20]. The heat map shows the distribution of X-rays from plasma, the dominant visible-matter component of the clusters. The green and white contours denote the mass distribution as determined by weak lensing constraints. The separation between these distributions demonstrates that there is missing, non-interacting matter.

contours in Figure 2.6, which trace the distribution of the non-interacting galaxies. The galaxies themselves cannot account for the gravitational potential, meaning that there must be another, non-interacting component of the clusters, namely dark matter.

2.2.3 The Cosmic Microwave Background

The evidence we have discussed so far is all collected from the (relatively) modern universe. Observations of anomalous velocities and gravitational lensing provide insights on dark matter after structure has formed. However, our current understanding of dark matter is that it has been around since long before structure formation, perhaps even since the fractions of a second after the Big Bang.

This belief is grounded in observations of the cosmic microwave background (CMB), which is the earliest probe we have of our nascent universe. Approximately 300,000 years after the Big Bang, the plasma of electrons and light nuclei cooled sufficiently for neutral atoms to form. At this point, photons that previously were constantly interacting with the bare charges were able to stream freely through the now-neutral universe. The CMB is the ph-

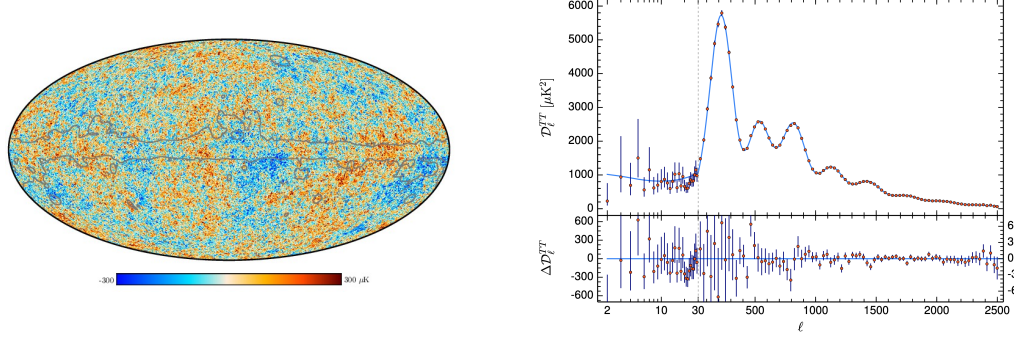


Figure 2.7: Measurements of the CMB from the Planck space observatory [Planck2020]. *Left* is a map of the temperature fluctuations of the CMB. Red is hotter, indicating an overdensity, and blue is vice versa. The scale of these density perturbations is driven by the relative amounts of visible matter, dark matter, and dark energy in the early universe. On the *right* is a power spectrum of the size of the fluctuations, measured in terms of l , the multipole moments. Changes to cosmological parameters would change the relative heights of the peaks in the power spectrum.

tons from this moment, known as the surface of last scattering, that have been traveling through the universe since that early time. By detecting these photons, we have a direct handle on the distribution and energy of matter at that moment.

The CMB is largely uniform across the sky, with small perturbations in the photons' temperature at smaller scales. Figure 2.7 shows a map of the CMB photons and a power spectrum of their temperature fluctuations. A variety of cosmological parameters determines the exact shape of this power spectrum, including the content of visible and dark matter and dark energy. The amazing precision of recent measurements allows us to pin down a precise value for the dark matter content of the universe and differentiate between many cosmological models.

2.3 So what is the dark matter?

The preceding section gives a broad overview of the overwhelming evidence for an additional component of matter that does not interact very much with the known particles of the SM. This evidence is one of the strongest indications we have of beyond the Standard Model (BSM) physics. For that rea-

son, DM has been the object of a huge body of scientific work. Despite this widespread interest, DM has proved elusive; over the almost-century since the first evidence for it, there have been no confirmed detections via non-gravitational interactions from indirect astronomical observations or from any interactions in direct measurements in the laboratory.

2.3.1 Did we write down gravity wrong?

Before we propose an exotic new theory to explain the anomalies we see, it is responsible to first ask if there is a more mundane explanation. Because we have only seen the gravitational effects of DM, a reasonable explanation is that our theory of gravity is wrong. We do know that outside of the anomalies listed in Section 2.2, the predictions of general relativity match observations to a high degree of precision. So, any modified theory needs to maintain those predictions while also accounting for the outlier data.

Although many versions of modified gravity³ have been proposed, none are able to consistently explain all of the different effects we see [21]. In particular, the discovery of gravitational waves in 2017, which were predicted by traditional general relativity, invalidated many theories [22].

Even the theories that get close to recreating observations are far from the simple Occam’s razor solution to our problem that we would like—they basically act as an emulator for particle dark matter. It appears that the simplest solution to the anomalies we see is that our SM is missing at least one particle.

2.3.2 Requirements on a new particle

From our observations, we can figure out some restrictions on the properties of particle DM. Here I will describe some of the most widely accepted requirements on a DM model.

Mass ■ Fundamentally, the range of potential dark matter particle masses extends many orders of magnitude: $\sim 10^{-22} \text{ eV} - 5 M_\odot$ [8]. At the top end of the mass range, the mass is limited by the smallest known galaxies—a single dark matter particle cannot weigh more than the entire galaxy it resides inside. At the bottom end we are limited by the diameter of the smallest

³Modified gravity is often generically called modified Newtonian dynamics (MOND), but MOND is technically one of many theories.

known galaxies, because the wavelength of the dark matter particle, $\lambda_{\text{DM}} = \hbar c / m_{\text{DM}}$, must fit inside its galaxy in order to be spatially resolved there. In practice, this range is further limited by rotation curves and gravitational lensing measurements, which provide a rough map of the varying density inside the dark matter clump.

Fermion or boson ■ Star surveys that map the velocities of objects in the Milky Way can give us a more precise density map in our region. These surveys indicate that the local DM energy density is⁴ $\rho_{\text{DM}} \approx 0.3\text{--}0.5 \text{ GeV/cm}^3$ [8, 23]. Knowing a figure for the energy density gives us a relationship between the DM particle mass and the number density; lower mass DM particles must have a higher number density. At masses less than $\sim 100 \text{ eV}$, fermionic dark matter is limited by the Pauli Exclusion Principle and can no longer pack together tightly enough to maintain the required energy density. Thus, DM models lighter than that must be bosonic [24–27].

Temperature ■ From structure formation, we know that the dark matter has to be relatively slow-moving in the early universe. Instead of clumping into gravitational potentials, relativistic or ‘hot’ DM can stream away, never forming the clumps that seed large- and small-scale structure [28]. For a time, people thought that neutrinos, with their minimal interactions, could be DM, but they are relativistic and so can not recreate the CMB and baryon acoustic oscillations (BAO) spectra. So, DM must be cold, which means that if it was ever in thermal equilibrium with the SM, it must be heavy. Alternatively, as with axions, the DM can be light but must not have been in thermal equilibrium with the SM.

Self-interactions ■ Because we haven’t been able to detect it, we know that DM does not interact very much with the SM, but it could in principle have self-interactions. However, the Bullet Cluster puts stringent limits on those self-interactions. The DM must interact little enough to pass through during the collision, giving a distribution that traces the galaxies, not the gas.

⁴There is some controversy over the correct value to use for DM searches. Most axion experiments use $\rho_{\text{DM}} = 0.45 \text{ GeV/cm}^3$, which is the value we use in the sensitivity projections for DM Radio. The ABRACADABRA-10 cm limits use a more conservative $\rho_{\text{DM}} = 0.4 \text{ GeV/cm}^3$.

2.3.3 Some particle dark matter candidates

There are far more theories on what the DM is than I can discuss in these limited pages—many reviews have been written on the subject, for example [8, 29, 30]. Below I describe a few notable categories of candidates.

Standard Model material

Once again, it is important that we first ask ourselves if it is possible to explain our observations with something we know exists, namely the SM, and in fact we do believe that there is SM material in galaxies that does not emit much or any light.

An example of non-emitting objects we know about is brown dwarfs, which are substellar objects—they would be a star except that they do not have enough mass to support fusion in their cores. Because they do not have fusing cores, they cannot emit light in the same way that our sun does, and so they would escape the detection of our telescopes. Brown dwarfs and other non-emitting, composite objects are collectively known as massive compact halo objects (MACHOs). The fact that they are compact means that they would naturally sit at wide distances from each other and other objects; just like the galaxies in the Bullet Cluster, their distance would prevent them from interacting. Unfortunately, this attractive, simple explanation for the extra mass does not hold up to testing [31]. MACHOs, being highly massive and localized, would create many lensing effects as they travel across our sky in front of bright objects. Observations have not found nearly enough lensing events for MACHOs to make up the DM. Additionally, the evidence from the CMB requires DM to exist before structure formation, and hence before the formation of these compact objects.

Another potential SM dark matter candidate is the neutrinos, which do not directly interact with photons and came into existence alongside the other SM particles in the early universe. For these reasons, neutrinos actually do contribute to the DM abundance. However, SM neutrinos are both light and were formed in thermal equilibrium with the other particles, and as such are either relativistic or became non-relativistic far too late in our cosmological history. So, although they are part of the missing mass, we still need to find another explanation for the many cold dark matter phenomena we observe [32].

Novel particles

It turns out that there are not any SM explanations which can properly account for the full dark matter abundance, and so we are left looking for new particles to fill in the gap. As I alluded to before, there are many, many ideas as to what those new particles are. Instead of cataloging them here, I note a few categories of theories.

Broadly, most DM models predict a single DM species, but it is possible that there is an entire ‘dark sector’ of particles with their own interactions that are decoupled from the SM. This decoupling could be entire, or there could be a portal between the dark and visible sectors. The most common example of such a portal is a dark photon that mixes with the regular photon [33]; dark matter particles could emit a dark photon which would mix into a visible photon that could be detected. One thing to note about dark sector models is that limits on self-interactions from the Bullet Cluster can actually restrict the kinds of interactions available within the dark sector, even though we do not have a direct particle physics probe of them [34].

Within single-species theories, candidates can be divided by their mass and abundance, or equivalently, how we can detect them. At higher masses, for the particle to make up the full DM energy abundance, there is a lower number density than for low-mass particles, which need to have a high density in order to contribute enough energy. Thus at high masses, the interactions we search for are of individual DM particles interacting with a detector. There are not a lot of them around and the coupling is small, so the interactions are rare, but when they do interact, there can be a significant energy/momentum transfer.

The prototypical example of such a massive DM candidate is the weakly interacting massive particle (WIMP), with mass $\mathcal{O}(\text{GeV} - \text{TeV})$ [35]. WIMPs’ elastic collisions can be described very well by simple kinematics, and are analogous to pool balls in billiards. If the WIMP is the cue ball, it may hit one of the numbered balls (one of the nuclei in the detector material), causing the ball to recoil. The cue ball is redirected, and the now-rolling numbered ball may proceed to interact with other balls on the table.

At the lower end of the mass spectrum, where the occupation number is high, DM candidates behave less like individual particles, and more like a classical wave. The following section will describe what this means for their detection.

2.3.4 Wave-like dark matter

In the billiards analogy of the particle-like interactions of heavy DM, wave-like DM could be thought of as an individual air molecule. The molecule may collide with one of the numbered balls, but the interaction does not have enough energy to have any detectable effect. So, instead of designing an experiment to interact with individual air molecules, one should design an experiment to look for wind—the coherent effect of the field of individual air particles—which might look something like a windmill. Many molecules make up the air stream that turns the blades of the windmill. In a wave-like DM experiment, the same collective behavior is used; in field-theoretic language, we interact with a classical field, rather than with an individual excitation of a quantum field. Although there may be some observable astronomical effects of a wave-like DM candidate versus a particle-like one [36], as of now there is no prior reason to prefer one over the other.

In order to be light enough to be wave-like, the DM must be a boson, and so candidates can be scalar, pseudoscalar, vector, or axial-vector. Each of these possibilities carry different sets of interactions and thus different detection signatures. The most prominent candidates among these categories are pseudoscalar axions (motived by the strong CP problem) and axion-like particles and vector hidden or dark photons (which arise in hidden sector models).

3

The Axion

The previous chapter discussed one of the most blatant downfalls of the SM: the missing dark matter in the universe. This chapter will describe another mystery of our current understanding of particle physics: why isn't there more charge parity (CP) violation in the strong force? It turns out that the answer to this question may also provide a solution to the dark matter problem, because the resolution predicts a new particle, the axion, which satisfies all of our requirements in Section 2.3.2 to explain the DM abundance.

In this chapter, we will first describe the origin of the strong CP problem in Section 3.1. In Section 3.2, we discuss the Peccei-Quinn solution to the strong CP problem and the resulting axion particle. Those sections will give a brief overview of the theoretical underpinnings of the axion with a focus on the parts of the theories that are necessary for motivating the axion as a DM candidate. Finally the chapter concludes with the cosmological consequences of the new particle in Section 3.3.

3.1 The strong CP problem

The strong CP problem is usually described as the problem that quantum chromodynamics (QCD) should violate CP symmetry, but experimentally,

does not. This is true, but the ‘should’ hides a lot of interesting physics. Instead of approaching the problem from that perspective, I will instead ask the question, what terms can we write down in the SM¹? After all, in the words of Murray Gell-Mann, “any process which is not forbidden by a conservation law actually does take place with appreciable probability” [39].

3.1.1 The θ term

Chromodynamics can be written in terms of the Lagrangian [40],

$$\mathcal{L} = -\frac{1}{4}F^{a\mu\nu}F_{\mu\nu}^a + \sum_{\alpha} \bar{\psi}_{j,\alpha}(i\cancel{D}_{jk} - m_{\alpha}\delta_{jk})\psi_{k,\alpha} \quad (3.1)$$

where the sum is over the flavors $\alpha = u, d, s, \dots$ and repeated color indices $j, k = 1, 2, 3$ are summed over. The $\psi_{j,\alpha}$ fields are the color charge-carrying quarks. The gauge field strength tensor

$$F_a^{\mu\nu} = \partial^{\mu}A_a^{\nu} - \partial^{\nu}A_a^{\mu} - g f_{abc} A_b^{\mu} A_c^{\nu} \quad (3.2)$$

contains the fields A_{μ}^a , representing the eight gluons, which also carry color charge. g is the gauge coupling and f_{abc} are the structure constants. Note that the f_{abc} 's, and hence the final term in Equation (3.2), vanish for Abelian gauge groups (as in quantum electrodynamics (QED)) but not for non-Abelian ones (such as QCD).

In addition to the terms in Equation (3.1), there is another possible term that we could include in our QCD Lagrangian:

$$\mathcal{L}_{\theta} \sim g^2 \theta F_a^{\mu\nu} \tilde{F}_{a\mu\nu} \quad (3.3)$$

where $\tilde{F}_{a\mu\nu}$ is the dual of the field strength tensor,

$$\tilde{F}_{a\mu\nu} = \frac{1}{2}\epsilon_{\mu\nu\rho\sigma}F_a^{\rho\sigma}, \quad (3.4)$$

¹I have attempted to design this and the following section to be mostly self-contained and limited to the most important information to motivate the axion particle as a DM candidate. This necessarily prevented me from including the historical context of these impressive theoretical advances. Much of the content of this section is drawn from the lecture notes of Tracy Slatyer’s Particle Physics of the Early Universe class, Ben Brubaker’s thesis on HAYSTAC [37], and Roberto Peccei’s contribution to the 1996 KOSEF-JSPS Winter School [38].

θ is some dimensionless coefficient, and $\epsilon_{\mu\nu\rho\sigma}$ is the antisymmetric Levi-Civita symbol.

In Section 3.1.3, we will ask if we can eliminate this ‘ θ term’ using a conserved symmetry of the SM, but for now we will assume that the term is allowed and thus must be a part of our theory. First, we will discuss some interesting features of this term and their measurable consequences. Then, we will attempt to determine θ .

Features of the θ term

The first thing to note is that \mathcal{L}_θ is actually a total derivative. If we define

$$K^\mu = \epsilon^{\mu\nu\rho\sigma} \left(A_\nu^a F_{\rho\sigma}^a - \frac{g}{3} f^{abc} A_\nu^a A_\rho^b A_\sigma^c \right) \quad (3.5)$$

then we have

$$\mathcal{L}_\theta \sim g^2 \theta \partial_\mu K^\mu \quad (3.6)$$

If $\partial_\mu K^\mu = 0$, then this term disappears and our Lagrangian’s symmetries will match those of the classical case of Equation (3.1). In fact, we can identify K^μ as the $SU(3)$ singlet axial current, carrying ‘handedness’ or ‘parity’. Following Noether’s theorem, the fact that K^μ is divergenceless–parity is conserved–means that the classical theorem has a symmetry², in this case a $U(1)$ axial symmetry:

$$\psi \rightarrow \psi' = e^{-i\theta\gamma_5} \psi. \quad (3.7)$$

If this conservation law and symmetry are indeed broken, then we are seeing what is known as an ‘anomaly.’ Anomalies are defined as classical conservation laws that are broken by the equivalent quantum theory, and things can get funky when they appear. Before we jump to this conclusion, however, we need to remember that dynamics and thus physical observables do not come directly from the Lagrangian but rather from the action,

$$S = \int d^4x \mathcal{L}(x), \quad (3.8)$$

²A more familiar example of Noether’s theorem is the conservation of electric charge, in which the electric current is divergenceless. The corresponding symmetry is the gauge invariance of the electromagnetic field, which is symmetric under the combination of $\phi \rightarrow \phi' = \phi - \partial\chi/\partial t$ and $\mathbf{A} \rightarrow \mathbf{A}' = \mathbf{A} + \nabla\chi$.

and if \mathcal{L} is a total derivative (as it is in this case) then the action depends only on the surface terms, i.e. the field values at spatial and temporal infinity³. In our case, we can see that the effect this new θ term has on the Lagrangian is

$$\delta S \sim g^2 \theta \int d^4x \partial_\mu K^\mu \quad (3.9)$$

$$\sim g^2 \theta \oint_{\Omega} K^\mu d\Omega_\mu \quad (3.10)$$

where Ω is the surface at infinity. In an Abelian gauge theory like QED, this term vanishes⁴, but in a non-Abelian theory, the surface term does not necessarily limit to zero.

I will not provide a rigorous derivation for why this is the case, but I can provide some intuition. In QED,

$$\mathcal{L}_{\text{QED}} = \bar{\psi} (i\gamma^\mu D_\mu - m) \psi - \frac{1}{4} F_{\mu\nu} F^{\mu\nu}, \quad (3.11)$$

we know that the action

$$S \supset -\frac{1}{4} \int d^4x F_{\mu\nu} F^{\mu\nu} \quad (3.12)$$

is finite, so we can see that the electromagnetic field tensor, $F_{\mu\nu} = \partial_\mu A_\nu - \partial_\nu A_\mu$ ⁵, must fall off faster than $1/r^2$, and thus the strength of the gauge fields, A_μ , fall off faster than $1/r$.

Now applying the QED gauge field scaling to \mathcal{L}_θ , we see that K^μ falls off faster than $1/r^3$, which is fast enough to make Equation (3.10) disappear; the area of the boundary surface in 4D spacetime over which we are integrating, Ω , is $\propto r^3$ with $r \rightarrow \infty$.

In contrast, we know that in QCD, the gauge fields do *not* fall off quickly with distance; recall from Section 2.1.1 that the strong force exhibits confinement! In non-Abelian gauge theories, there do exist gauge field configurations, A_μ , that do not fall off fast enough to make Equation (3.10) limit to zero at infinity. In particular, one set of non-perturbative solutions to the equations of motion has gauge field configurations of $A \propto 1/r$, producing

³This comes directly from integrating by parts.

⁴The term does generically vanish, but in certain Abelian theories with magnetic monopoles, the θ term can still be important. This is called the Witten effect [41].

⁵Recall that the f_{abc} 's (Equation (3.2)) are zero for Abelian theories.

finite, non-zero surface terms. These are called ‘instantons.’ It should be noted that the instanton solution is only relevant at temperatures $T < \Lambda_{\text{QCD}}$. Although I will not go into detail about why this is true, this scale makes intuitive sense, being the scale of confinement.

To simplify the later discussion I drop the generic $F_a^{\mu\nu}$ and rewrite the θ term here in terms of only the contributing (gluon) field tensors, $G_a^{\mu\nu}$:

$$\mathcal{L}_\theta = \frac{\alpha_s}{8\pi} \theta G_a^{\mu\nu} \tilde{G}_{a\mu\nu} \quad (3.13)$$

I have also substituted $g^2 \rightarrow \alpha_s$, the strong coupling constant, and added in the traditional normalization factor of 8π .

So, what we have learned here is that the θ term that we wrote down cannot be neglected; it will have physical effects that we can measure experimentally. We can now ask ourselves what the term’s interesting features are to measure, and it turns out that there are, in fact, some very interesting things indeed.

The first interesting feature is that the term is odd under the flip of all spatial coordinates, so it is P-odd (making the whole theory P-violating). This ties directly into what we have just discovered, that QCD has a chiral anomaly—it does not conserve parity despite the predictions of the classical theory. I will not discuss the physical effects of this in the SM in detail, but it will come up again in the context of axions.

The term is also odd under the flip of the time coordinate, making the theory T-violating. Because the SM is CPT-conserving, the time violation also implies CP violation. This broken symmetry should be measurable, with strength dictated by the coefficient θ . The most precise way people have been able to probe this term is by searching for the neutron’s electric dipole moment (EDM), which, as we will see in Section 3.1.2, has yielded surprising results.

Before I move on, take note that both of these features only exist in the low-temperature limit, i.e. $T_{\text{univ}} < \Lambda_{\text{QCD}}$, because instanton solutions do not exist for higher temperatures.

Contributions to the θ term

The strength of any observable is tied to the term’s coefficient, θ . To predict the size of this dimensionless parameter, we ask what are the sources of terms with the $G\tilde{G}$ form. There are two such sources in the SM.

QCD vacuum ■ We have already seen the first source in the previous discussion of gauge fields in QCD. The QCD vacuum is a superposition of many different gauge field configurations⁶, including instanton solutions [42]. Instantons actually represent tunneling between different discrete ‘false vacuum’ states, each of which is labeled with a winding number, n , as $|n\rangle$. The true vacuum should not be able to be tunneled out of—that would not be a universe compatible with life! Fortunately, there are superpositions of the different winding number states that are stable, which can be written as

$$|\theta\rangle = \sum_n e^{-in\theta} |n\rangle . \quad (3.14)$$

One of these superpositions is the vacuum we live in, which we label as $|\theta_{\text{QCD}}\rangle$. Remember, $|\theta_{\text{QCD}}\rangle$ must include many different gauge field configurations, including the instantons, which guarantee a contribution to \mathcal{L}_θ . The strength of the contribution the vacuum makes to \mathcal{L}_θ is usually defined as θ_{QCD} .

Quark mass ■ The second source for θ comes from an entirely different part of the SM, namely the quarks’ Yukawa coupling with the Higgs. As with all of the known particles (with the possible exception of the neutrinos), the quarks get their mass from interacting with the Higgs field. The way this occurs is shown in Figure 3.1. A left-handed quark comes in, interacts with the Higgs, and becomes a right-handed quark (or the reverse direction). This process thus not only gives the quarks mass, but also mixes the previously-separate chiralities,

$$\mathcal{L}_{\text{quark mass}} \sim \bar{q}_L \hat{M}_q q_R + h.c. \quad (3.15)$$

Here q_R and q_L are the right- and left-handed quark states and \hat{M}_q is the (complex-valued) mass matrix. In order to get real quark masses, one needs \hat{M}_q to be diagonal with real-valued eigenvalues. This can be achieved by applying a chiral transform on the quark fields, which generates a new term of the form $G\tilde{G}$! The coefficient of the new term is $\arg(\det(\hat{M}_q))$.

Putting it together ■ Combining our two sources of $G\tilde{G}$ -type terms, we now have

$$\mathcal{L}_\theta = \frac{\alpha_s}{8\pi} \bar{\theta} G_a^{\mu\nu} \tilde{G}_{a\mu\nu} . \quad (3.16)$$

⁶Vacuum gauge field configurations must satisfy the equations of motion for free gauge fields under $\mathcal{L}_{\text{free}} = -\frac{1}{4} F_a^{\mu\nu} F_{a\mu\nu}$.

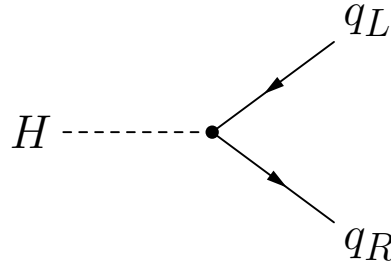


Figure 3.1: Feynman diagram of the Higgs-quark Yukawa interaction. This is the mechanism by which the quarks get their mass, and it also results in a chiral rotation of the quark fields.

with coefficient

$$\bar{\theta} = \theta_{\text{QCD}} + \arg(\det(\hat{M}_q)) \quad (3.17)$$

Note that θ_{QCD} and $\arg(\det(\hat{M}_q))$ are unrelated angles that are not fixed by the theory, so their sum is also an arbitrary angle, $\bar{\theta} \in [0, 2\pi]$, that must be determined experimentally.

3.1.2 Limits on the neutron EDM

The best experimental tests of $\bar{\theta}$ are measurements of the neutron's electric dipole moment. Before we discuss the experiments or their results, I first offer an intuitive picture of why this is a good test of the CP-violating θ term.

The existence of an EDM for the neutron is inherently CP-violating, as can be seen from Figure 3.2. In the diagram, the green and blue arrows represent the magnetic and electric dipole moments, respectively. In our intuitive⁷ picture, the EDM is caused by an offset between the positive and negative charges in the neutron, and the magnetic dipole moment (MDM) is caused by the ‘spinning’ of those charges. In a CP-symmetric theory, a flip of both charge and parity would have no effect. Clearly, if the neutron has both an EDM and a MDM, then we have CP violation (and we know that the neutron’s MDM is nonzero: $\mu_n/\mu_N \approx -1.91304273 \pm 0.00000045$ according to experiment⁸ [43]).

⁷...but unphysical—the structure of the neutron is much more complicated than the point charge and three valence quark picture of Figures (3.2) and (3.3) would suggest. A complete description with the quark and gluon sea is beyond the scope of this thesis.

⁸This value is given as a ratio of the MDM, μ_n , to the nuclear magneton, $\mu_N = e\hbar/2m_p$.

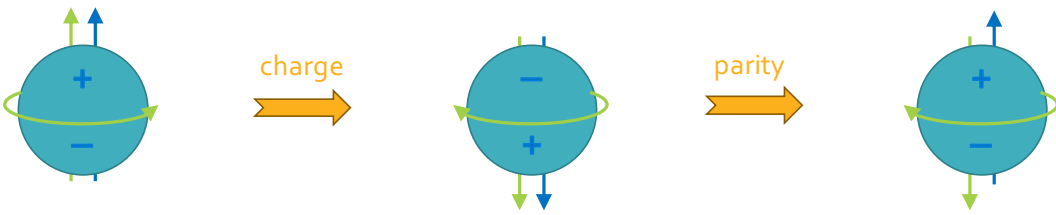


Figure 3.2: Illustration of how a neutron with both an EDM (blue) and an MDM (green) would violate CP symmetry.

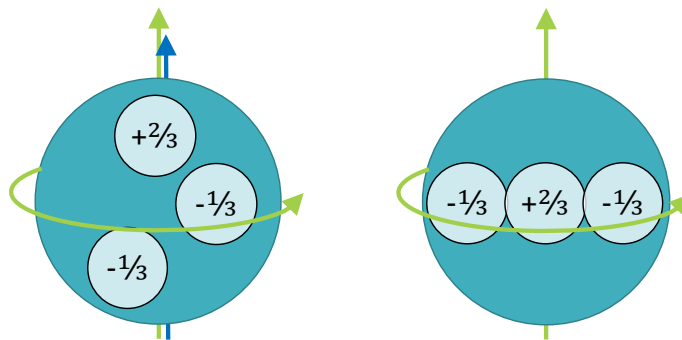


Figure 3.3: Cartoon of the neutron EDM. *Left*, randomly distributed valence quarks create a non-zero EDM. *Right*, when the valence quarks are tuned to ‘align,’ the result is a vanishing EDM.

Because we know the neutron’s MDM, a measurement of the EDM would give us a measurement of the CP violation in the system. I show another intuitive, but unphysical, picture of the EDM in Figure 3.3. For randomly distributed constituent quarks, there should be a random-valued, non-zero EDM from the charge being asymmetrically distributed. The only way to get a vanishing EDM in this picture is to tune the positioning of the quarks to align, cancelling out any dipole moment in the charge distribution. From this simplified picture, we can see how QCD interactions tied to the CP-violating θ term could cause a CP-violating quark distribution inside the nucleon⁹. The parametrization of the neutron’s EDM in terms of $\bar{\theta}$ depends on the nuclear

⁹I emphasize again that this is an intuitive but incorrect picture of the dynamics inside the neutron.

model [44], but is approximately

$$\begin{aligned} d_N &\sim \bar{\theta} \frac{em_q}{m_N^2} \\ &\sim 10^{-16} \bar{\theta} \text{ e-cm} \end{aligned} \quad (3.18)$$

where e is the electron charge, m_N is the neutron mass, and m_q is an effective quark mass [45–47] often written as

$$m_q \sim \frac{m_u m_d}{m_u + m_d}. \quad (3.19)$$

As the title of this subsection suggests, current experimental measurements of the neutron EDM are not actually a measurement of a non-zero value, but rather a very strong upper limit [48],

$$d_N < 1.8 \times 10^{-26} \text{ e-cm} \quad (3.20)$$

leading to a limit on $\bar{\theta}$,

$$\bar{\theta} \lesssim 10^{-10}. \quad (3.21)$$

3.1.3 Naturalness

$\bar{\theta}$ is clearly not $\mathcal{O}(1)$ as we would expect for a randomly picked angle. Much of theoretical physics is guided by principles of elegance and naturalness, and at first glance, $\bar{\theta}$ does not fit those principles. This kind of situation is called a fine-tuning problem; $\bar{\theta}$ has a value pegged very close to zero, despite there not appearing to be any physical laws to guide it there; this implies an accidental symmetry of nature! This particular fine-tuning problem is called the ‘strong CP problem.’ We consider here a few potential solutions to the problem, which we will see are not sufficient to explain the fine-tuning.

The first thing to note is that the θ term adds energy to the Lagrangian, so having the coefficient be zero is actually the preferred, lowest energy state [49]. However, because θ_{QCD} and $\arg(\det(\hat{M}_q))$ are static parameters, there is no way for them to relax from whatever their initial values are to being zero. This fact is extremely relevant to the PQ solution in Section 3.2.

A potential resolution is to ask if there is a way that θ_{QCD} and $\arg(\det(\hat{M}_q))$ can naturally cancel each other. However, there is no connection between the two terms that would cause them to be related in the first place, so there is no reason for the terms to cancel for physical reasons. But

maybe there is a solution that is related to how we formulated the theory; after all, the quark mass matrix term comes from many chiral rotations to diagonalize the masses. Is it possible to perform a transformation that essentially absorbs θ_{QCD} into the quark fields? This absorption works, but only if there is at least one massless quark. Experimental evidence and first-principles theoretical work rules this solution out [8, 50]¹⁰.

Another possible work-around for the strong CP problem is to ask if there is actually a fundamental symmetry that is protecting the neutron from gaining an EDM. If CP or P symmetry are ‘good’ symmetries, then despite \mathcal{L}_θ being a term that we can write down, it may not be physically allowed. However, both CP and P violation are found in other parts of the SM. The weak force is maximally parity violating, as first demonstrated in the famous Wu experiment [51]. The first evidence for CP violation was found in the decays of neutral kaons in the 1960s by James Cronin, Val Fitch, and collaborators [52]. Since then, further CP violation has been found in the quark sector, and there is also recent evidence of CP violation with neutrinos [53, 54]. Evidently there is not an explicit symmetry preventing this term from existing.

Although *explicit* symmetry breaking is not the answer, there is a way to have *spontaneous* symmetry breaking solve the problem. By having CP be a spontaneously broken symmetry rather than one that is explicitly broken in the theory, people have found ways to make CP violation exist in some places in the SM and not in others. Current experimental evidence supports explicitly broken CP symmetry to a high degree of precision, but convoluted models of spontaneous CP-breaking can give only very high-energy signatures and hence are not ruled out. These models unfortunately also introduce quite a lot of new physics and new fine-tunings. For more on these models, see [44] which has since been ruled out and [55–57].

When there is no clear fundamental reason for a term having a particular value, it is worth investigating anthropic arguments. The idea is that by existing to make the measurement, humans have inherently changed the prior—we will never measure a parameter’s value that is inconsistent with the universe supporting life. Unfortunately, this argument does not hold here, as there is no obvious reason why a neutron EDM would prevent large-

¹⁰The latter citation addresses the interesting point that the masses of the quarks have multiple contributions, including a topological effective mass that would not contribute to $\bar{\theta}$. Their lattice calculations show, however, that the topological contribution to the up quark mass is too small to explain the discrepancy in the neutron EDM.

scale structure formation or any other features of our universe that are necessary for us to be here.

It is possible that the universe is just not as elegant as we thought. Maybe $\bar{\theta} \approx 0$ by accident. But, that certainly seems weird, and in 1977 Roberto Peccei and Helen Quinn came up with an alternative explanation, as we will see in the following section.

3.2 The PQ solution and axions

The Peccei-Quinn solution to the strong CP problem makes the CP invariance of QCD a natural consequence of field dynamics. Here I will first lay out the backbone of the solution, and then in Sections 3.2.2 and 3.2.3 we will discuss a few different implementations and their physical consequences.

3.2.1 The PQ solution to strong CP

Somehow we need the coefficient of \mathcal{L}_θ to be extremely close to zero. This is difficult in the SM, because $\bar{\theta} = \theta_{\text{QCD}} + \arg(\det(\hat{M}_q))$ is a static coefficient that has no reason to be defined to be zero. The PQ solution to the strong CP problem, devised in the seminal works [58, 59], ‘promotes’ $\bar{\theta}$ from being a static number to being a dynamic field.

For the PQ solution to work, we need two things. The first is a global axial¹¹ symmetry, $U(1)_{\text{PQ}}$, that spontaneously breaks at a large energy scale, f_a (see Figure 3.4). The second is at least one quark that gains mass by interacting with a complex scalar field via a Yukawa interaction. The quark and scalar fields would transform under $U(1)_{\text{PQ}}$ in the following way:

$$\begin{aligned} q_L &\rightarrow e^{ia} q_L \\ q_R &\rightarrow e^{-ia} q_R \\ \Phi &\rightarrow e^{2ia} \Phi \end{aligned} \tag{3.22}$$

and the Yukawa interaction between them is

$$\mathcal{L}_{\Phi\bar{q}q} \sim \Phi \bar{q}_L q_R + h.c.. \tag{3.23}$$

By applying the transformations of Equation (3.22) to Equation (3.23) we can see that the interaction is invariant under $U(1)_{\text{PQ}}$.

¹¹Acting oppositely on left- and right-handed fields.

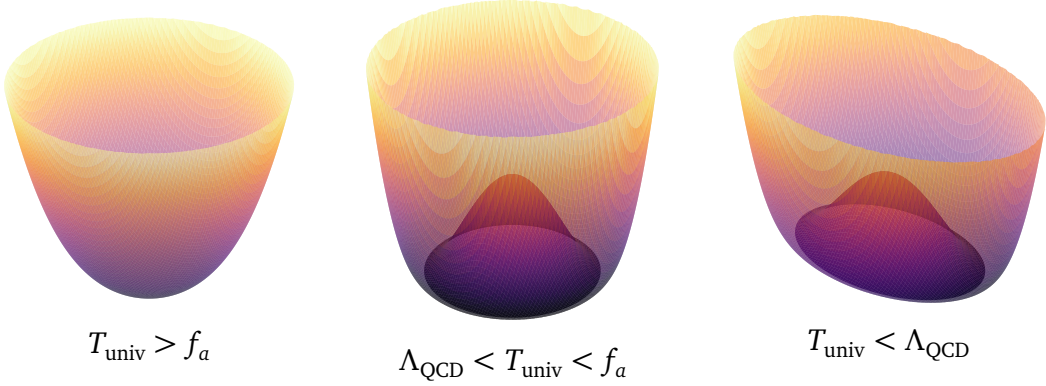


Figure 3.4: The stages of symmetry breaking with temperature for a complex scalar field. *Left*, in the early, hot universe, the symmetry is unbroken and the minimum of the potential is at zero. *Middle*, when the universe cools sufficiently such that $T_{\text{univ}} < f_a$, the potential's shape changes such that there is now an energy degeneracy among the continuum of states with different azimuthal angles. The symmetry is spontaneously broken as the field ‘chooses’ a $\theta = \theta_i$ and gains a vacuum expectation value, $\langle \Phi \rangle = |\Phi|$. *Right*, finally, the universe cools to $T_{\text{univ}} < \Lambda_{\text{QCD}}$. Here, interactions between the field representing the angular degree of freedom, a , and the gluons cause the entire potential to tip, creating a preferred value of $\theta = \bar{\theta}$ that is unrelated to the initial field configuration, $\bar{\theta} \neq \theta_i$.

As the temperature cools, $T_{\text{univ}} < f_a$, Φ ’s potential changes according to Figure 3.4, spontaneously breaking $U(1)_{\text{PQ}}$ because the field must choose an angular direction, θ_i , to remain in a minimum energy state at the bottom of the wine bottle. By moving away from the origin, the radial component of Φ also gains a non-zero expectation value, which causes the above interaction to be mass-generating for the quarks, $m_q \sim \langle \Phi \rangle$.

For $T_{\text{univ}} < \Lambda_{\text{QCD}}$, something interesting happens. The chiral anomaly guarantees that whenever we do a chiral transformation as we did in Equation (3.22), there is an additional $G\tilde{G}$ -type term generated from instanton effects. In the Lagrangian, we must also add a term¹²

$$\mathcal{L}_{agg} = \xi \frac{\alpha_s}{8\pi f_a} \frac{a}{f_a} G_a^{\mu\nu} \tilde{G}_{a\mu\nu} \quad (3.24)$$

where ξ is a model-dependent parameter and a is the azimuthal degree of freedom of the Φ field. We can intuitively think of this as an interaction be-

¹²The axion field has dimensions of energy, so it always carries around a normalization of f_a , where the combination is dimensionless.

tween the field a , commonly called the axion field, and two gluon fields, G . In our picture of the Φ potential in Figure 3.4, the interactions lead to the potential tipping, because the $G\tilde{G}$ term explicitly breaks $U(1)_{\text{PQ}}$ symmetry in this low temperature limit. The potential minimum is no longer degenerate in the azimuthal angle¹³, but instead has a single minimum that I will call θ_{\min} . There is no reason for the axion field's initial value to be at the minimum (i.e. $\theta_i \neq \theta_{\min}$), but being dynamical, the field will 'roll' down to the bottom of its potential to minimize its energy¹⁴.

Equation (3.24) is a third contribution to \mathcal{L}_θ , so the new term is

$$\mathcal{L}_\theta = \frac{\alpha_s}{8\pi} \left(\bar{\theta} + \frac{a}{f_a} \right) G_a^{\mu\nu} \tilde{G}_{a\mu\nu}. \quad (3.25)$$

Now recall from Section 3.1.3 that the total energy is minimized if the coefficient of this term is zero. The tipping of the potential, being a dynamical process involving the interaction between the axion and gluon fields, will thus *naturally* occur in a direction that minimizes the energy, and consequently

$$\langle a \rangle = \theta_{\min} = -f_a \bar{\theta}. \quad (3.26)$$

Thus, $\mathcal{L}_\theta \rightarrow 0$, and the strong CP problem is solved.

3.2.2 Axion particle

Not long after the publication of the original Peccei and Quinn papers, Frank Wilczek and Steven Weinberg independently realized that the spontaneous breaking of PQ symmetry combined with its explicit breaking from the chiral anomaly would give rise to a massive pseudo-Goldstone boson [60, 61]. Generally, when a symmetry breaks spontaneously, there is a massless Goldstone boson associated with the angular degree of freedom, but the chiral anomaly provides an additional explicit breaking, giving the particle a mass¹⁵.

¹³Assuming $\Lambda_{\text{QCD}} < f_a$, the rotation by a in Equation (3.22) will now cause a change in energy in the full Lagrangian.

¹⁴This energy minimization process can occur in a variety of ways, with the process and initial conditions producing wildly different phenomena. We will discuss some of the cosmological options in Section 3.3.

¹⁵Something similar happens with electroweak symmetry breaking and with the chiral symmetry breaking of $SU(3)$ in QCD.

One can see how this happens by expanding around the minimum of the tipped potential. The precise definition for the axion potential in the low-temperature limit ($T \ll \Lambda_{\text{QCD}}$) is [62]

$$V(a) = -m_\pi^2 f_\pi^2 \sqrt{1 - \frac{m_u m_d}{(m_u + m_d)^2} \sin^2\left(\frac{a}{2f_a}\right)} \quad (3.27)$$

Expanding this potential to quadratic order¹⁶ in a provides a mass term $V(a) \approx \frac{1}{2} m_a^2 a^2$, with [62]

$$m_a^2 \approx \frac{m_u m_d}{(m_u + m_d)^2} \frac{m_\pi f_\pi}{f_a^2} \quad (3.28)$$

$$= 5.70(7) \mu\text{eV} \left(\frac{10^{12} \text{ GeV}}{f_a} \right). \quad (3.29)$$

It might seem strange at first that the axion's mass is dependent on the pion mass, m_π , and decay constant, f_π . However, the quantum numbers for these two particles are identical, both being pseudoscalar pseudo-Goldstone bosons¹⁷. Because of their shared quantum numbers, they can mix. Although I will not discuss their mixing or its effects in detail, it causes their properties to depend on each other [47].

The realization that a massive particle would accompany the breaking of $U(1)_{\text{PQ}}$ was very important, because it enables us to look for a present-day, low-energy effect of an otherwise high-energy, un-probe-able theory. The form of those low-energy effects depends on the specifics of the model, such as the identity of the complex scalar and quark fields and which particles are charged under $U(1)_{\text{PQ}}$. In the following section we will examine a few models to see what physical observables they predict.

¹⁶Expanding to fourth order provides the axions' self-interaction strength, $\lambda_a = -\frac{m_u^2 - m_u m_d + m_d^2}{(m_u + m_d)^2} \frac{m_a^2}{f_a^2}$ [62]. This is very small! Note that this expansion is around the minimum of the potential. If the axion sits near the top of the potential, one would actually expect increasing amounts of self-interactions, which could lead to interesting clumping phenomenology.

¹⁷Goldstone bosons are spin-0 and characterized by the quantum numbers of generators of the broken symmetry. In the axion case, $U(1)_{\text{PQ}}$ is an axial symmetry, rotating left- and right-handed particles in opposite directions. The axion is therefore a pseudoscalar, changing sign under parity transformation. Similarly, the pions come from the breaking of $SU(2)_A$.

3.2.3 Axion models

PQWW

The original work by Peccei, Quinn, Wilczek, and Weinberg made minimal additions to the SM and became known as the PQWW model [58–61]. They assumed that the quarks that participate in the Yukawa interaction of Equation (3.23) were SM quarks and that all of the SM fermions were PQ-charged. The simplest situation would be to have the scalar field Φ be the SM Higgs doublet, but that does not work out for symmetry reasons. Essentially, independent rotations of the up and down quark fields would not respect $U(1)_{\text{PQ}}$. This problem is easily remedied with an additional Higgs doublet, so we have now Φ_1 and Φ_2 which separately couple to up- and down-type particles respectively¹⁸:

$$\mathcal{L}_{\text{Yukawa}} = - \sum_{i=1}^3 \sum_{j=1}^3 \left(y_{ij}^u \bar{Q}_{Li} \Phi_1 u_R + y_{ij}^d \bar{Q}_{Li} \Phi_2 d_R \right) \quad (3.30)$$

where the i and j indices denote the three generations of quarks, the left-handed quark doublets are

$$Q_L = \begin{pmatrix} u_L \\ d_L \end{pmatrix} \quad (3.31)$$

and after electroweak symmetry breaking the Higgs doublets are

$$\Phi_1 = \frac{\nu_1}{\sqrt{2}} \begin{pmatrix} 1 \\ 0 \end{pmatrix} e^{i a \nu_2 / f_a \nu_1}; \quad \Phi_2 = \frac{\nu_2}{\sqrt{2}} \begin{pmatrix} 0 \\ 1 \end{pmatrix} e^{i a \nu_1 / f_a \nu_2} \quad (3.32)$$

with ν_1 and ν_2 their vacuum expectation values (VEVs) and $f_a = \sqrt{\nu_1^2 + \nu_2^2} = \nu_{\text{EW}} \approx 250 \text{ GeV}$: $U(1)_{\text{PQ}}$ symmetry breaking at the electroweak scale. The axion now corresponds to the common phase between Φ_1 and Φ_2 .

In addition to minimally changing the SM, another advantage of the PQWW model is that it was immediately experimentally testable. A relatively low f_a results in axion couplings strong enough to leave evidence in the decays of heavy mesons, reactor emissions, neutrino beam dump experiments, etc. [61]. Unfortunately, no axion signatures were found in any experiments [63] or in astrophysical probes such as stellar cooling rates [64, 65], which led to theories of ‘invisible’ axions.

¹⁸Up- and down-type quarks and leptons of all generations.

Invisible axions

To make axions invisible to experiments, theories need to provide a reason for $f_a \gg v_{\text{EW}}$. Being $\propto 1/f_a$, the axion-SM couplings and m_a can thus be small. One can come up with a variety of ways to do this, but two models have come to stand out as benchmarks for experimental searches, Kim-Shifman-Vainshtein-Zakharov (KSVZ) and Dine-Fischler-Srednicki-Zhitnitsky (DFSZ) [66–69].

In the KSVZ model, the quark and scalar fields are not SM fields. Instead we have a new, heavy quark, $M_Q \sim f_a$, and a new complex scalar, Φ , whose angular degree of freedom is the axion. In this model, only the new quark and scalar field carry PQ charge, and because they are not SM fields, there is no reason for $U(1)_{\text{PQ}}$ -breaking to align with electroweak symmetry breaking— f_a can be much higher.

The axion does not interact with the PQ-uncharged leptons at all, and only interacts with the light SM quarks via the strong and electromagnetic anomalies,

$$\mathcal{L}_{\text{KSVZ, int}} = \frac{a}{f_a} \left(\frac{\alpha_s}{8\pi} G_a^{\mu\nu} \tilde{G}_{a\mu\nu} + 3e_Q \frac{\alpha}{4\pi} F^{\mu\nu} \tilde{F}_{\mu\nu} \right). \quad (3.33)$$

Here e_Q is the electromagnetic charge of the heavy quark and α is the fine structure constant.

The DFSZ model is more similar to PQWW. It retains the two Higgs doublets and PQ-charged SM fermions but adds another singlet complex scalar with $\langle \Phi \rangle = f_a \gg v_{\text{EW}}$. Because the new Φ is not the same Higgs that are responsible for the fermion masses, there is no issue with the f_a scale being completely decoupled from the electroweak scale.

These two models are not an exhaustive list. There are major and minor variations of the two models as well as entirely different approaches [70]. Generally, however, the axion couplings vary by $\mathcal{O}(1)$ factors from each other in the different theories. The parameter space covered by these models is usually termed the ‘QCD axion band,’ because it is the possible space of axions that solve the strong CP problem in QCD.

Axion-like particles

Similar particles that do not lie in the QCD band—and do not solve the strong CP problem—are called axion-like particles (ALPs). Everything that we have discussed about the strong CP problem and PQ-symmetry breaking does not apply (namely, they do not have a $G_a^{\mu\nu} \tilde{G}_{a\mu\nu}$ term), but I mention them here

because many experiments that aim to search for QCD axions naturally also are sensitive to ALPs.

These particles are more than just a small bonus for axion searches, however. Many high-energy theories predict light pseudoscalars, especially at the lower end of the axion mass range. Axions are ubiquitous in string theories [71–77] and come out of many grand unified theory (GUT) field theories [78–84], some, but not all of which are concomitant with a PQ solution to strong CP.

Throughout this thesis, I will generically refer to QCD axions and ALPs as ‘axions’ unless I need to make a distinction. For the rest of this chapter, I will discuss the universe’s history in the context of QCD axions, but much of the phenomenology can be the same for ALPs.

3.3 Axion cosmology

Because the energy scale of PQ symmetry breaking is high, axions’ history stretches back into the very early universe. Knowledge of early-time cosmology can provide insight into present-day axion phenomena, and, if axions are discovered, they may provide a window into the moments after the Big Bang that cannot otherwise be probed. This section will discuss the production and behavior of axions in a few different cosmological scenarios and the accompanying effects we could measure today. We will see that axions are an excellent candidate to be the dark matter, as they can be produced in the correct abundance and are cold and stable.

3.3.1 Axions in an expanding universe

In Section 3.2.1, we discussed the origin of the axion particle. The QCD interactions of a complex scalar, Φ , tip its potential. The field, a , associated with Φ ’s angular degree of freedom thus obtains a non-constant potential, $V(a/f_a)$, with a minimum at $\bar{\theta}$. Equation (3.27) is the form of that potential after it has tipped¹⁹.

At the moment when the potential gains a minimum, the field already has some value, $a/f_a = \theta_i$, from when $U(1)_{\text{PQ}}$ spontaneously broke. The fact that

¹⁹The potential and axion mass both have a temperature dependence, see [62], particularly for temperatures near Λ_{QCD} . We will ignore that dependence, but it can effect the timing and scale of the effects we discuss here.

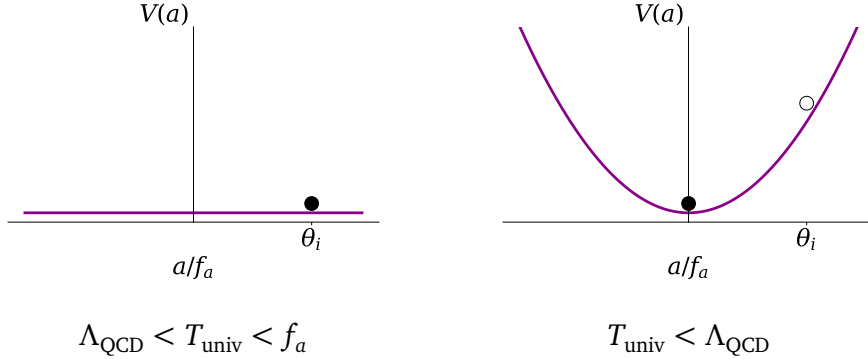


Figure 3.5: The axion field in its potential before and after PQ symmetry breaking. The axion field is initially misaligned with the potential minimum, and so must relax to the bottom. The misalignment angle corresponds to the potential energy in the axion field and influences the eventual abundance of cold axions.

$\theta_i \neq \bar{\theta}$ actually leads to the production of a population of cold axions; this is called the ‘misalignment mechanism.’ It is this population of axions that can be the cold dark matter of the universe. To see how this occurs, consider that the initial field value is (possibly) far from its energy-minimizing value, as shown in Figure 3.5. The picture is the same as a ball on the side of a valley; by rolling downhill the ball will reduce its potential energy, converting it into kinetic energy. In the field picture, the field rolling to the bottom of the potential will convert the potential energy into field excitations, namely axion particles. The axions will be at rest, as there is no source of momentum or preferred direction of travel.

To make our intuitive picture precise, we can write down an equation of motion for the system:

$$\ddot{a} + 3H\dot{a} + \frac{\partial V}{\partial a} = 0 \quad (3.34)$$

This is the familiar equation for a damped harmonic oscillator in a potential. H is the Hubble parameter, which varies with time

$$H(t) = \frac{\dot{R}}{R}, \quad (3.35)$$

where R is a dimensionless scale factor of the expanding universe. If we take a quadratic approximation near the bottom of the potential²⁰, $V(a) \approx \frac{1}{2}m_a^2a^2$,

²⁰It is of course not strictly correct to take a quadratic approximation because we have

then it simplifies to

$$\ddot{a} + 3H\dot{a} + m_a^2 a = 0 \quad (3.36)$$

and we can identify each term with the following correspondence: friction or damping, $c \leftrightarrow 3H$, and oscillation frequency, $\omega_0^2 \leftrightarrow m_a^2$.

There are a few different regimes of behavior depending on the relative values of H and m_a . If $m_a \ll 3H$, then the system is extremely over-damped; we can set the final term to zero and see that $\dot{a} = 0$ is a solution—the field value is frozen to its initial value. For the less extreme case of $m_a \lesssim 3H$, then the system is still over-damped, experiencing too much friction to exhibit oscillations. The ball (or field) will only sluggishly move through its potential, in what is known as ‘slow roll’ behavior.

In the opposite case, $m_a \gtrsim 3H$, we have the fast roll regime, in which the oscillator is under-damped. The ball will roll up and down the sides of the valley with amplitude degradations from the friction term. In the limit where $m_a \gg 3H$, there is essentially no amplitude damping at all; we can set the H term to zero, producing the limit case of a perfect, undamped harmonic oscillator.

In Equation (3.36), the friction term is parametrized by H , the Hubble parameter, which is dependent on temperature and evolves as the universe cools (see Section 2.1). The axion will therefore experience each type of behavior as the universe expands. The changing behavior is illustrated in Figure 3.6. In the green line of the top figure, the axion, after being frozen at θ_i , initially slowly rolls down the potential and eventually oscillates around the minimum with gradually decreasing damping. The final form of the axion field is a stable oscillation, with the following solution to Equation (3.36):

$$a(t) = C \sin(m_a t) \quad (3.37)$$

where C is some constant describing the amplitude of the oscillation²¹. For the axions in the present day to be all of the local dark matter density, $C \approx \sqrt{2\rho_{DM}}/m_a$.

The precise timing of this process and the final amplitude of the oscillations are highly dependent on the cosmological model of our expanding

no reason to assume $|\theta_i - \bar{\theta}|$ is small. However, the behavior we will see under this approximation is qualitatively correct.

²¹Notice that the oscillatory behavior of the field means that although the *time-averaged* magnitude of the θ term is zero, it does have a time-dependent oscillation. This means that the neutron EDM oscillates between non-zero values, but averages to zero over the period.

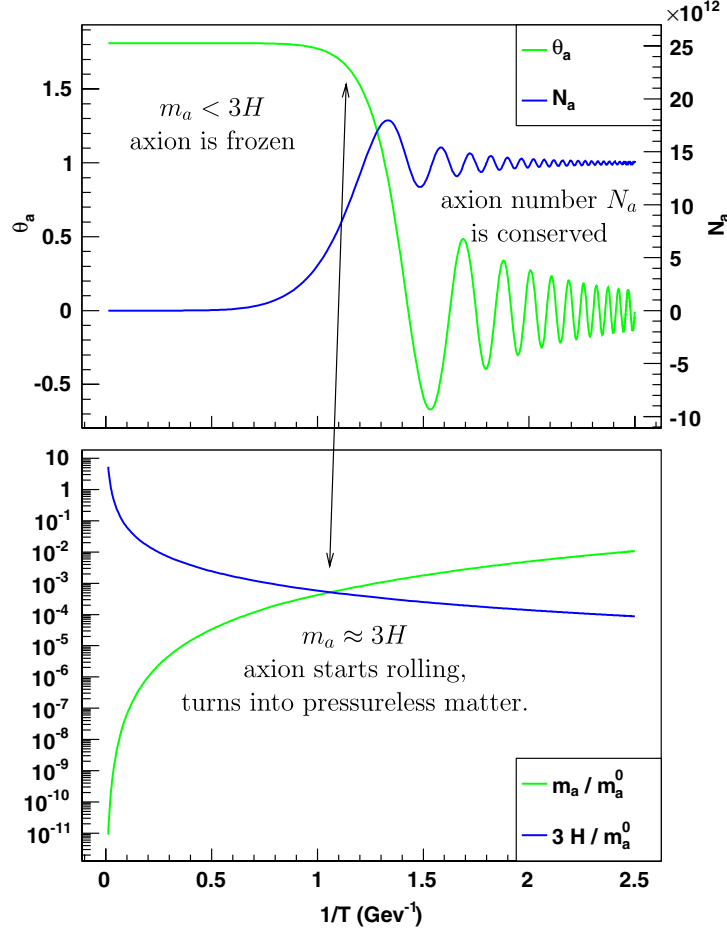


Figure 3.6: Evolution of the axion, figure from [85]. The *top* figure shows the qualitatively different regimes where the axion is first frozen at its misalignment angle, then begins to slowly roll down its potential, and eventually oscillates around the minimum, acting as a field of cold matter. The N_a shown in the figure is the total number of axion particles per comoving volume. The *bottom* figure shows how the transition from frozen to moving occurs when $m_a \approx 3H$. In the text I made the simplifying assumption that only H was changing with time, but in fact, as is included in this plot, both H and m_a are dependent on temperature and are thus dependent on the cosmological model.

universe, but there are some universal qualitative features we should note. The first is that despite having a non-uniform potential immediately after PQ-breaking, the axion continues to act as a *massless* particle until $m_a \approx 3H$. It is only when oscillations begin that it begins to act as a pressureless field of massive particles. At that time, the total energy density of the axion field is now the sum of the potential and kinetic energies,

$$\rho_a = \frac{1}{2}m_a^2a^2 + \frac{1}{2}\dot{a}^2, \quad (3.38)$$

just as we expect for normal matter. After that moment, the axion matter will dilute in the expanding universe just like the visible matter. Critically, because the timing of this transition is driven by the relative sizes of H and m_a , a lower mass axion unintuitively leads to a *larger* axion energy density in the present universe; the transition is later, so there is less time for dilution.

The relic energy density—the energy density of axions in our present universe—thus depends on the axion mass (or equivalently f_a) and the misalignment angle, $\theta_0 = \theta_i - \bar{\theta}$, of the initial field value from the potential minimum. The latter sets the energy density at time ‘zero,’ $T_{\text{univ}} \approx \Lambda_{\text{QCD}}$, and the former determines how diluted that energy density gets. However, there is no reason for every point in space to pick the same θ_i at the moment of PQ symmetry breaking, $T_{\text{univ}} \approx f_a$. Doing so would actually violate causality. Instead, every non-causally connected patch of space will end up with an independent angle. The consequences of this distribution of angles are qualitatively very different depending on the relative timing of the breaking of $U(1)_{\text{PQ}}$ and inflation. In the next couple of sections, we will explore those effects in more depth.

3.3.2 Post-inflationary PQ-breaking

To start, we will explore the phenomenology of axions for PQ-breaking after inflation²². In this case, we can ignore inflation entirely and just consider what happens when we have many patches of different θ_0 , as shown in Figure 3.7.

Although each individual θ_i will initially control its local energy abundance, since the time of PQ symmetry breaking, those patches have come into causal contact. The relic density will thus depend on the misalignment

²²PQ symmetry may be broken before the end of inflation in this scenario, as long as the symmetry is restored during reheating so that it can be broken again after inflation.

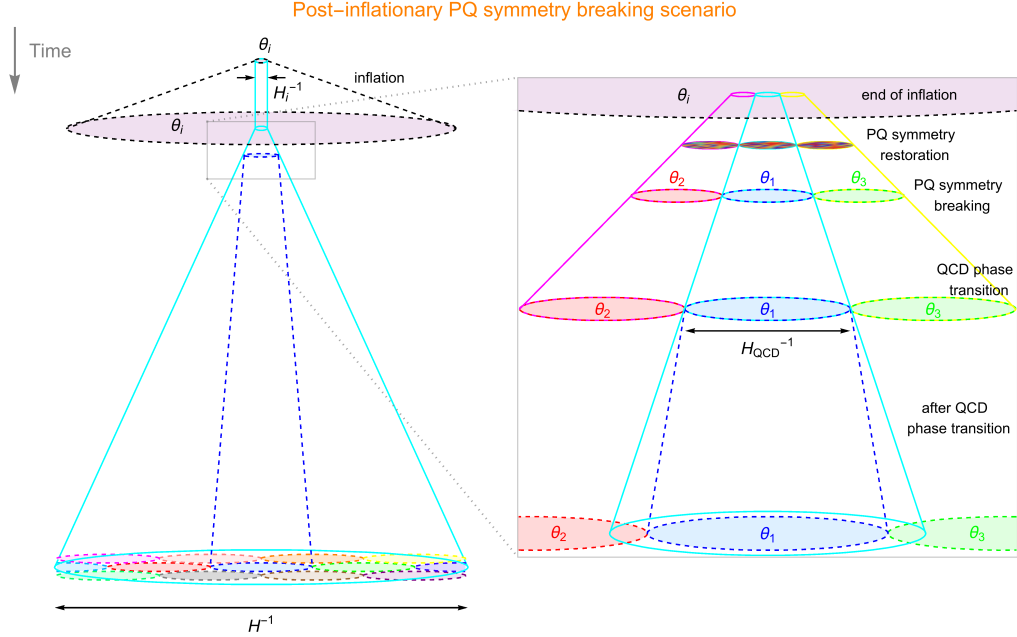


Figure 3.7: Schematic of post-inflationary PQ symmetry breaking causing many patches of different θ_0 , from [86]. In this scenario, the temperature of the universe after inflation (during reheating) is higher than f_a . After some time, the symmetry is broken, and each patch of space picks a different misalignment angle. Each patch, with angle θ_n , expands with the universe.

angle averaged over the many patches that have been able to interact. Under standard cosmological evolution the resulting relic energy density is [47, 87]

$$\Omega_a \sim 0.1 \langle \theta_0^2 \rangle \left(\frac{f_a}{10^{12} \text{ GeV}} \right)^{7/6}. \quad (3.39)$$

Assuming a uniform distribution of θ_0 , the variance of the angle is $\langle \theta_0^2 \rangle = \pi^2/3$. So, to get $\Omega_a = \Omega_{\text{DM}} \approx 0.24$, the symmetry-breaking scale must be $f_a \sim 10^{12} \text{ GeV}$. Converting to axion mass using Equation (3.29) gives $m_a \sim 10^{-6} - 10^{-5} \text{ eV}$. This prediction is very tidy, presenting a narrow window within which to search experimentally. For this reason, the most long-running axion experiment, ADMX, looks for axions in this range.

Having patches with different initial angles, however, presents some interesting topological phenomena that are not quite as tidy. There are two types of artifacts: strings, from the breaking of $U(1)_{\text{PQ}}$, and domain walls,

from the chiral anomaly. Here I give an introductory discussion of these phenomena (drawn from [88]) and their effects.

When PQ symmetry spontaneously breaks at $T_{\text{univ}} \sim f_a$, the scalar field becomes $\Phi = \langle \Phi \rangle e^{-\theta}$ with $\langle \Phi \rangle \neq 0$. The causally connected patches will have smoothly varying $\theta \in [-\pi, \pi]$, while the more distant, causally disconnected patches have unrelated angles. Following any path in space back to the original point, the integrated change in angle must be $\Delta\theta = 2\pi n$, because the θ is uniquely defined at that point (see Figure 3.8). If we now imagine shrinking that loop by moving our path over smoothly varying regions in space, any $n \neq 0$ cannot be reduced to zero—there is a discontinuity e.g. between $n = 0$ and $n = 1$. For a $n = 1$ loop, there must be somewhere inside where the phase is undefined, meaning $\langle \Phi \rangle = 0$. This zero expectation value is a false vacuum, forced away from the minimum energy state by the topology of θ states. The false vacuum cannot be only a 0-dimensional point, or else the loop could be closed above or below it. To prevent the loop from closing, it must instead be a 1-dimensional string that is either infinite or forms a closed loop²³. We expect a network of such strings would form throughout the universe as regions of space that were causally disconnected at PQ symmetry breaking come into causal contact²⁴.

These strings, having a lot of energy and tension, will vibrate, releasing energy in the form of massless axions [90]. This condition persists until, after the potential tips, the field can relax to the potential minimum at $m_a \approx 3H$ [85]. Modeling suggests that the axions released through the strings' oscillations are likely to be the dominant mechanism of axion production, more than the misalignment mechanism over a wide range of parameters. Calculating the precise contribution is difficult, however, because the extremely large aspect ratio of the string poses difficulties for simulations that need to take into account effects spanning orders of magnitude in scale [91].

The breaking of the azimuthal symmetry after the axion gets mass can create another topological defect, domain walls²⁵. For N PQ-charged quarks, there are N distinct vacua with $\theta_{\min} = \bar{\theta} + 2\pi n$. When the field values relax to the potential minimum, a string with $n = 1$ will border one domain wall,

²³The string is not truly 1-dimensional; it actually has a finite diameter, $d_A \sim 1/f_a$.

²⁴String formation is expected from the spontaneous breaking of any continuous symmetry.

The process is called the Kibble mechanism, and is one of the reasons why inflation is such an attractive theory—any strings from high-scale symmetry breakings are diluted away, in line with our non-observation of cosmic strings [89].

²⁵Domain walls are a generic feature of a spontaneously broken discrete symmetry. Here, $U(1)_{\text{PQ}}$ has the discrete subgroup $Z(N)$.

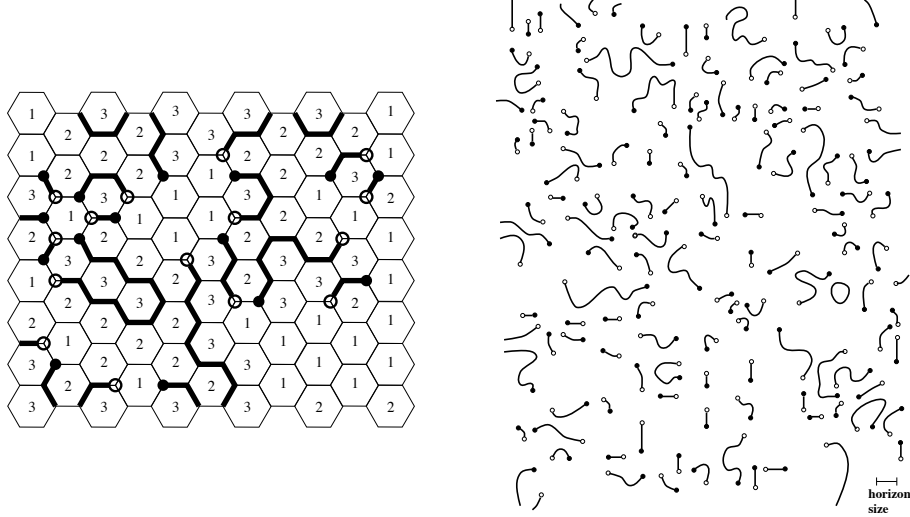


Figure 3.8: Strings and domain walls, from [92]. *Left* shows a toy model with three discrete possible axion angles. Wherever the phase circles back around ($1 \rightarrow 2 \rightarrow 3 \rightarrow 1$ or vice versa) there will be a string, shown as the filled or open circles for a string going into or out of the page, respectively. Domain walls form edged by strings. *Right* shows a zoomed out view with a reference bar for the horizon size under the simulations run in [92], showing that under their model, the expected number of domain walls in a horizon volume is $\sim 2/3$.

which separates the θ vacuum from a separate region of space which relaxed into the $\theta + 2\pi$ vacuum. Domain walls are 2-dimensional structures with a huge surface energy, enough to dominate the energy density of the universe and destroy the observed isotropy [44]. For this reason, $N > 1$ models are excluded unless additional physics is added to explicitly break the $Z(N)$ symmetry.

3.3.3 Pre-inflationary PQ-breaking

The case where PQ symmetry breaks before the end of inflation is in some ways much simpler. Note that the symmetry could be broken at any point before or during inflation; the only requirement is that the reheating temperature is not large enough to restore $U(1)_{\text{PQ}}$, in which case we return to the post-inflationary PQ-breaking scenario discussed in the previous section. In this scenario, each patch of θ_i is rapidly expanded past the horizon such that even in the present day, the different patches are not in causal contact.

The entire visible universe started from a single patch with a single value of θ_i . There are not any topological defects to consider because the boundaries were all ‘blown away’—diluted such that $\langle N \rangle < 1$ [92].

The difficulty of this scenario is that the relic axion energy density may be harder to achieve naturally. If we assume that the energy scale of inflation was high (which is generally easier to achieve), then $f_a > E_I$ means that f_a must be quite large, with a correspondingly tiny m_a . If we replace the averaged initial angle in Equation (3.39) with the single θ_0 of the patch that grew into our observable universe,

$$\Omega_a \sim 0.1 \theta_0^2 \left(\frac{f_a}{10^{12} \text{ GeV}} \right)^{7/6}, \quad (3.40)$$

we see that for axions to be the DM abundance, $\theta_0 \ll 1$. So, we are back to a fine-tuning problem, albeit not one that is quite of the magnitude of 1 in 10^{10} . If we consider a reasonable $f_a \sim 10^{15} \text{ GeV}$, we need $\theta_0 \sim 10^{-2}$.

The degree of tuning gets worse when you consider how the existence of axions would constrain inflation. Pre-inflationary axions generate something called ‘isocurvature fluctuations.’ The non-observation of isocurvature sets stringent limits on the available parameter space of axion and inflationary properties (shown in Figure 3.9). To understand these bounds, I begin with a brief story from the beginning of time: inflation.

The standard story of inflation is that before the rapid expansion, there was a scalar field called an ‘inflaton.’ Like any good quantum field, the inflaton had vacuum fluctuations, the creation and annihilation of field excitations. As inflation progressed, those fluctuations rapidly expanded to create over- and under-abundances of energy in the nascent universe. Sometime after inflation, in the phase called ‘reheating,’ the inflaton decayed into the SM particles. Because all of the SM particles were sourced from the same field, they all have the same source density distribution on the sky (illustrated in Figure 3.10). These correlated density profiles are called ‘adiabatic fluctuations.’

In contrast, the axion field was not sourced by the decay of the inflaton. Instead, in the pre-inflationary scenario, the axion field experienced its own vacuum fluctuations that were expanded by inflation alongside the inflaton. There is no reason for the axion’s fluctuations to have coincided with those of the inflaton, and so the distributions would be different, shown schematically by the red line in Figure 3.10. This component of the primordial density distribution that varies differently from the others is isocurvature.

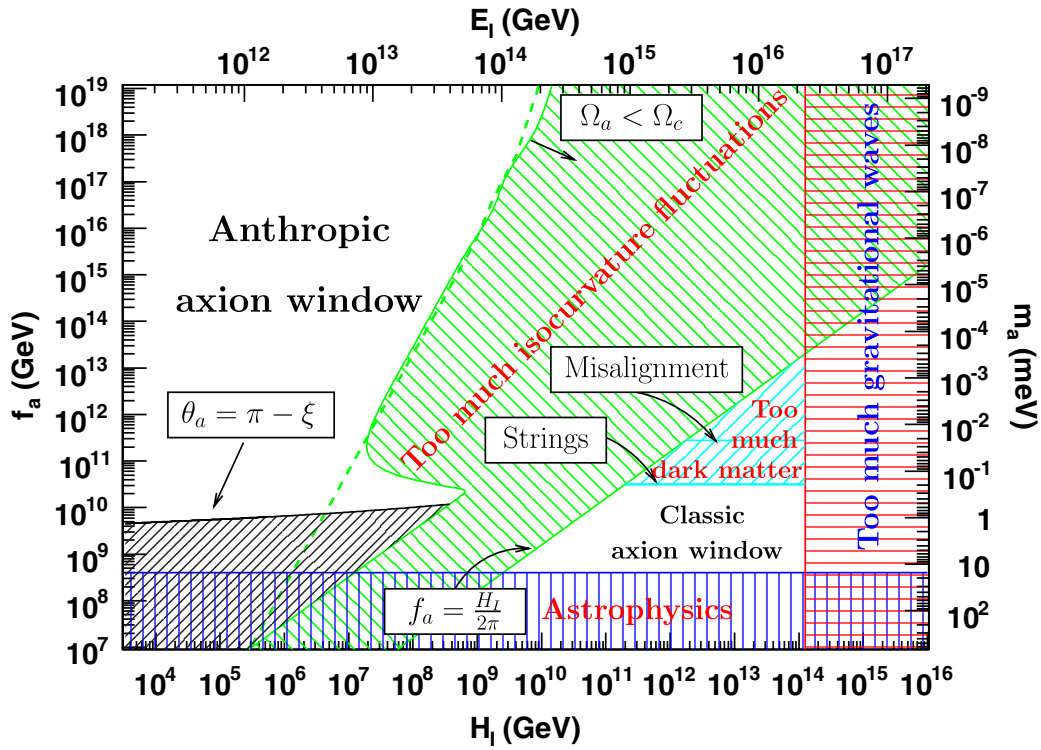


Figure 3.9: Available windows for combinations of f_a and E_l under standard cosmology, from [85].

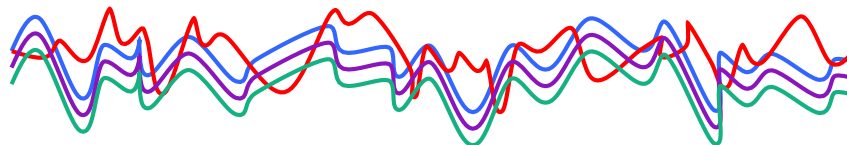


Figure 3.10: Illustration of primordial fluctuations. The blue, purple, and green lines each represent SM fields. Their over- and under-abundances match spatially, because they were all sourced from the same inflaton field. The red line represents a density profile such as the axion that does not match the other fields, because it was not generated from inflaton decay.

The amount of isocurvature that axions would provide depends on the relative timing of inflation and PQ symmetry breaking (E_I and f_a in terms of energy) and the energy density in the axion field, set by θ_0 . To date, no evidence of isocurvature has been found, with the best current limits set by the Planck telescope's measurements of the CMB [93]. The corresponding limits on the space of f_a versus E_I are shown as the green, hatched area in Figure 3.9. In that region, the energy density in the axion field would create observable isocurvature, in conflict with Planck. Below the hatched green region, PQ symmetry breaks after inflation ends, which would create no isocurvature. Thus we can see that these isocurvature limits force axion models farther to the top and left of Figure 3.9 where more fine-tuning of θ_0 is necessary to create the correct axion abundance. Is pre-inflationary axions thus too fine-tuned to provide a natural solution to the strong CP problem?

The simplest answer would be to say that the fine-tuning is relatively small, especially compared to that of strong CP, so perhaps the issue is a non-issue. We do not have to tune θ_0 by many orders of magnitude, and we could happen to live in a universe with a low scale of inflation. This is certainly an option, but given that the origins of the argument for axions were naturalness, we should consider other ideas.

The classical way to approach the fine-tuning problem is with an anthropic argument. Unlike the CP-symmetry of QCD, which is not necessary for the existence of living observers, a larger Ω_{DM} could be catastrophic for the universe's habitability. In particular, as we saw in Section 2.1, the relative quantities of DM, dark energy, and visible matter are perfectly balanced for a flat universe. Too much DM would lead to gravitational collapse (known as ‘overclosure’), where galaxies and stars would never have the chance to form. Although anthropics are a nice explanation in principle, in practice, the amount of tuning necessary to prevent overclosing the universe may be far less than we need to explain the smallness of θ_0 , as shown in Figure 3.11 [94].

The remaining explanations for our seemingly unnaturally small θ_0 usually make modifications to the ‘standard’ cosmological model used to generate Equation (3.40) or to the axion model. People have devised many ways to explain the abundance: new models of inflation, entropy dumps, exotic particles, etc. [95–106]. Here I will describe only one particularly compelling explanation, stochastic inflation, which does not require any new physics [107].

The stochastic inflation scenario supposes that there is a long period of

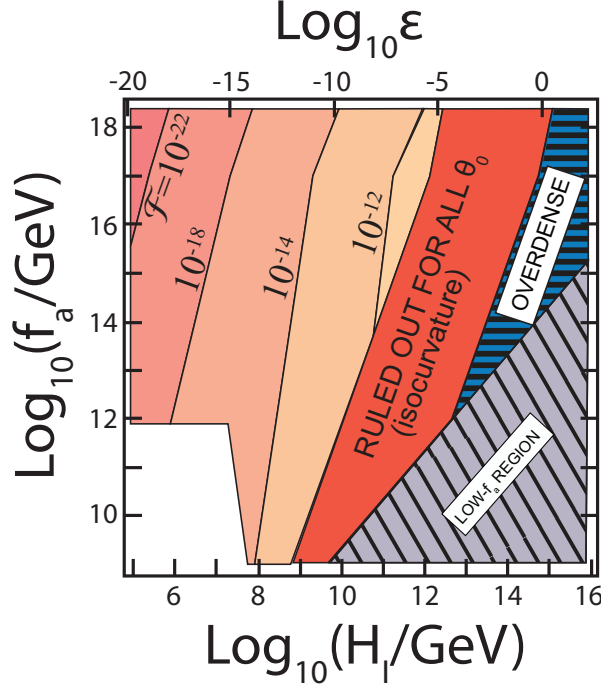


Figure 3.11: The anthropic necessity of fine-tuning with pre-inflationary axions, from [94]. $\mathcal{F} = \epsilon \times \theta_0$ with ϵ a measure of the flatness of the universe. $\mathcal{F} \lesssim 10^{-11}$ is a rough constraint on the maximum overdensity that would still support structure formation and life. The blue, horizontally hatched region is thus eliminated by anthropic arguments for all possible values of θ_0 . The pink contours show the degree of fine-tuning on top of the flatness requirements. The grey, diagonally hatched region corresponds to post-inflationary axions.

inflation at a relatively low scale. During inflation with a low Hubble scale, $H_I < m_a$, the axion field value rolls down towards the minimum of its potential, slowed only by the Hubble friction (the middle time period in Figure 3.6). If the inflationary period is sufficiently long, the axion would classically fall all the way to the bottom of the potential. However, quantum fluctuations prevent the field from staying at the bottom, instead making a distribution of field values around the minimum with expectation value $\langle \theta \rangle \approx H_I^2/m_a f_a \approx H_I^2/\Lambda_{\text{QCD}}$ in the present day. This distribution naturally provides the correct energy density of axions for a wide swath of f_a, E_I parameter space, as shown by the green likelihood contours in Figure 3.12.

Stochastic inflation is only one of many cosmological scenarios that can

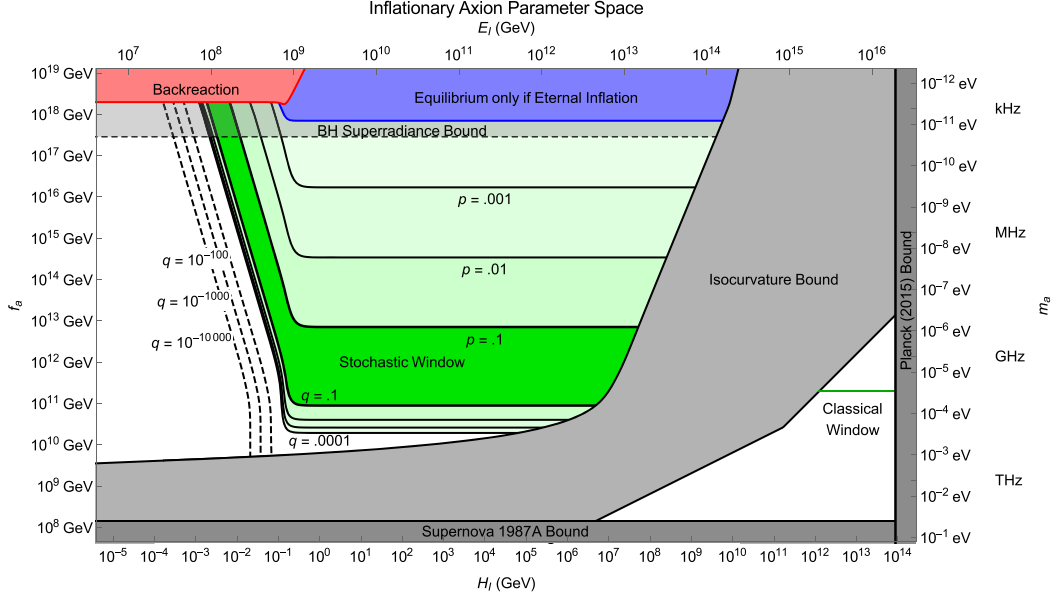


Figure 3.12: The parameter space of pre-inflationary axions under a stochastic inflation scenario, from [107]. The green shaded contours are marked with the probability that the axion field ‘jumped’ into the misalignment angle value that corresponds to $\Omega_a = \Omega_{\text{DM}}$. In particular, p is the probability $|\theta| \leq \theta_{\text{DM}}$ and $q = 1 - p$ is the probability $|\theta| > \theta_{\text{DM}}$ where θ_{DM} is the required misalignment angle to produce Ω_{DM} .

explain away the fine-tuning problem of pre-inflationary axions. We see that low-mass axions with $f_a > E_I$ can make up the entire dark matter abundance, are cold, and do not suffer from the topological defects that are concomitant with low-scale PQ-breaking. From the perspective of high-energy theories, a large f_a is actually more natural than the lower one that is necessary to generate the classical, $m_a \sim 10^{-6} - 10^{-5}$ eV axion. GUT and string theories generically predict new physics at high scales such as $f_a \sim 10^{16}$ and would in fact need to be fine-tuned to explain why $U(1)_{\text{PQ}}$ would break at such a low energy.

4

Lumped-Element Detection

So far, we have learned that dark matter is an important missing piece in our model of the universe and that axions are a highly motivated candidate to be that missing piece. As discussed in the previous chapter, we expect axions to interact with the SM a little bit, and so we can build detectors to look for them. Because axions are so light and so prevalent—being wave-like—detecting them requires very different techniques than traditional detectors that search for individual particle interactions. In Section 4.1 we will discuss how to detect axions: how they interact and how experiments can be designed to look for them. Section 4.2 will describe lumped-element detection, a new method to search for low-mass axions.

4.1 Axion detection

4.1.1 Non-photon interactions

QCD axions must interact with the gluon fields in order to solve the strong CP problem (Equation (3.24)), so observing the interaction is a relatively model-independent independent test of the PQ solution to the strong CP problem. Experiments such as CASPEr hope to probe this interaction directly with measurements of time-dependent nuclear EDMs [108–110]. Through

its gluon interaction, the ambient axion field gives nuclei a small, oscillating EDM. Recall that the Peccei-Quinn resolution to the strong CP problem zeros out the neutron EDM *on average*—the axion field oscillates about its minimum. Using nuclear magnetic resonance (NMR), CASPER hopes to measure an AC component to the EDM, even if the average value is zero.

Although only the interaction with gluons would definitively identify the QCD axion, as discussed in Section 3.2.3, axion models predict other interactions as well that we can exploit to detect these illusive particles.

4.1.2 Photon interactions

The most common coupling investigated by axion searches is the axion-photon interaction,

$$\mathcal{L}_{a\gamma\gamma} = \frac{g_{a\gamma\gamma}}{4} a F_{\mu\nu} \tilde{F}^{\mu\nu} \quad (4.1)$$

Although this is not a leading-order process (as shown in Figure 4.1), it is a popular signal to look for because QED provides very clean signals and there is a lot of existing technology that can measure photon interactions with high precision. The photon interaction is also a universal feature of the axion, although the interaction strength does depend on the specific model.

Practically, this diagram proceeds with one of the photons provided by a strong electromagnetic field, either from a magnet in a laboratory or from the high fields in stars. In the presence of the field, there is conversion between axions and photons. Without the high intensity field, interaction probabilities are extremely low. A difficulty with searching for axion-photon conversion in this way is the inherent mismatch between the massless photon and massive axion. In order to conserve both energy and momentum, the dispersion relations need to be matched [111]. This can be achieved in a variety of ways, in particular by breaking translational invariance; a few of these methods are discussed below. First we will reformulate Equation (4.1) using electric and magnetic fields in place of the electromagnetic field tensors,

$$\mathcal{L}_{a\gamma\gamma} = g_{a\gamma\gamma} a \mathbf{E} \cdot \mathbf{B} \quad (4.2)$$

As we discussed in the previous section, because of their low mass and large occupancy, we can treat axions as a classical field. Treating the entire

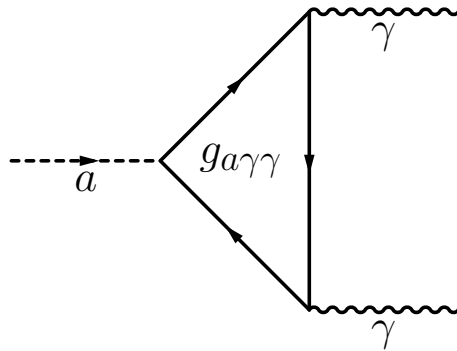


Figure 4.1: Because they are electrically neutral, axions' interactions with photons happen via a loop, with effective interaction strength $g_{a\gamma\gamma}$. To expedite the process of axion-photon conversion, experiments use a strong magnetic field as the source of one of the photons. This interaction of a pseudoscalar with photons in strong electromagnetic field is called the (inverse) Primakoff effect, and it also takes place inside stars and nuclei¹.

problem classically, the new Lagrangian modifies Maxwell's equations:

$$\nabla \cdot \mathbf{E} = \rho - g_{a\gamma\gamma} \mathbf{B} \cdot \nabla a \quad (4.3a)$$

$$\nabla \cdot \mathbf{B} = 0 \quad (4.3b)$$

$$\nabla \times \mathbf{E} = -\frac{\partial \mathbf{B}}{\partial t} \quad (4.3c)$$

$$\nabla \times \mathbf{B} = \frac{\partial \mathbf{E}}{\partial t} + \mathbf{J} - g_{a\gamma\gamma} \left(\mathbf{E} \times \nabla a - \frac{\partial a}{\partial t} \mathbf{B} \right) \quad (4.3d)$$

Because the gradient of the axion field is naturally small², the final term in Ampère's law (Equation (4.3d)) is the strongest signal to search for.

The sources for classical Ampère's law are the current, \mathbf{J} , and displacement current, $\partial \mathbf{E} / \partial t$, so the axion contribution will also take the form of an

¹The effect is named after Henry Primakoff, who observed the process with π^0 mesons [112]

²The gradient arises from velocity dispersion. However, axions, having been created at rest, will have only a small momentum dispersion derived primarily from a history of gravitational interactions.

effective current³. Using the expression for the axion field from the misalignment mechanism in Equation (3.37), we write

$$\mathbf{J}_{\text{eff}} = g_{a\gamma\gamma} \sqrt{2\rho_{DM}} \cos(m_a t) \mathbf{B} \quad (4.4)$$

Note that we have not made any assumptions here as to the axion mass or the mechanism of its photon coupling; the frequency and strength of the oscillating effective current depend on the mass and coupling respectively, but the existence of the effect is independent of the axion model. At high frequencies, it can be more intuitive to think in terms of electric and magnetic fields, rather than currents and voltages, but the formalism is still correct.

The signal in an actual detector is not quite as clean as the simple sine function of Equation (4.4). Because we live in the Milky Way galaxy with a virialized DM halo, the individual DM particles will have a velocity dispersion that blurs out the sinusoidal current [119],

$$a_i(v, t) = \frac{\sqrt{2\rho_{DM}/N_a}}{m_a} \sin\left(m_a \left(1 + \frac{v_i^2}{2}\right) t + \phi_i\right) \quad (4.5)$$

where i indexes the individual axion particles, N_a is the number of axions that make up the local density, v_i is the velocity of the i^{th} axion, and ϕ_i is a random additional phase⁴. In a detector, the velocity component can be thought of like a Doppler shifting of the signal to higher frequencies⁵. Note that this smearing will be present in any interaction, because we have modified $a(v, t)$ directly.

The shape of the signal, an important input to axion searches, depends thus on the velocity distribution of the local DM. In the analyses here, we assume that the DM is fully virialized and follows the Standard Halo Model (SHM) distribution,

$$f_{\text{SHM}}(v|v_0, v_{obs}) = \frac{v}{\sqrt{\pi} v_0 v_{obs}} e^{-(v+v_{obs})^2/v_0^2} \left(e^{4vv_{obs}/v_0^2} - 1\right) \quad (4.6)$$

where $v_0 \approx 220 \text{ km/s}$ is the speed of the local galactic rotation curve and $v_{obs} \approx 232 \text{ km/s}$ is the speed of the Sun relative to the DM halo rest frame.

³It should be noted that there has been controversy on whether this term is best measured as a current or as an oscillating electric field that can be directly measured [113, 114]. See [115–118] for detailed explanations of why the effective current interpretation leads to a higher sensitivity.

⁴It must be chosen under the assumption that the axions are coherent within a given length scale (their coherence length).

⁵As the velocity is squared, there will be no additional signal for $f < m_a$.

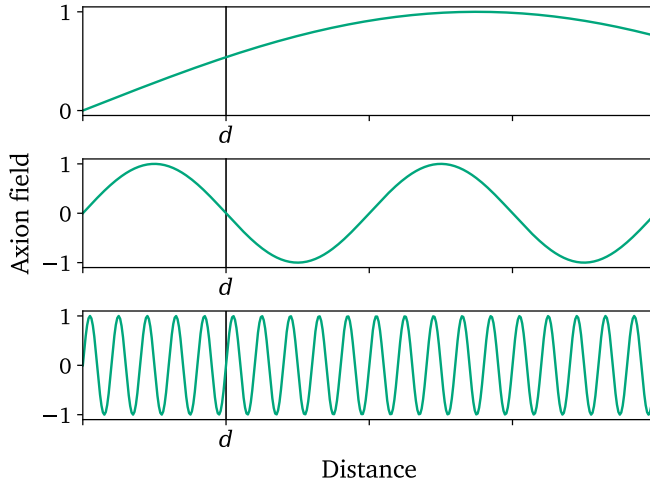


Figure 4.2: Axion detection can be broken up into three regimes based on the relationship between the axion wavelength and detector characteristic size, d . *Top* is the lumped-element regime, in which the axion wavelength is much longer than d . Traditional cavity haloscopes can operate in the intermediate regime, *middle*, by exploiting boundary conditions on the axion wave. At higher masses, *bottom*, multiple wavelengths fit inside the detector, and so other methods must be used.

Future analysis of the ABRACADABRA and DMRadio data will take into account other dark matter halo models, including the possible local Sagittarius stream or other substructure (see Section 2.2).

4.1.3 Mass regimes

Although the effective current is universal, the detectable signature can vary significantly at different axion masses. This is illustrated in Figure 4.2. We can divide up the detection regimes by comparing the axion wavelength to the size of a reasonable table-top experiment. When the Compton axion wavelength is significantly larger than the experiment, the effective current is in phase across the entire detector. At intermediate masses, the wavelength is comparable to the detector, and thus the current is no longer in phase across the device. Instead, we see the same phenomenon as in RF electronics where the axion wave can ring up different modes depending on the device's geometry. Finally, at the highest masses, the axion wavelength is so small

that many periods fit inside the detector, giving signatures that approach that of particles rather than classical waves.

An important point to note is that these mass regimes are determined by the Compton wavelength, not the de Broglie wavelength. The Compton wavelength,

$$\lambda_C = \frac{h}{mc} \quad (4.7)$$

is determined by the intrinsic properties of the axion, namely its mass, and it determines the phase of the axion wave over the detector. Unless specified otherwise, here wavelength means the Compton wavelength. The de Broglie wavelength,

$$\lambda_B = \frac{h}{mv} \quad (4.8)$$

contains information about the speed of the individual axions, with the distribution of v determined by the dark matter halo. The distribution of those velocities gives a length scale over which the axion field is coherent. Because $\Delta v \sim 10^{-3}c$ [119, 120], we expect the signal to be coherent over the detector as long as there are less than ~ 1000 wavelengths that fit inside. This is another way of stating that we are looking for wave-like, rather than particle-like, DM. The velocity spread can also be translated into a coherence time for the axions,

$$\tau \sim 10^6 \times (2\pi/m_a). \quad (4.9)$$

For several decades, axion searches looked solely in the intermediate and high mass regimes. At high masses, existing particle detectors could make limits [63], probing the PQWW model. It quickly became clear that the axion was much lower in mass than existing experiments could look for. In 1983, Pierre Sikivie proposed a detector called a cavity haloscope, which could be used to search at intermediate masses [121]. As shown in the middle plot of Figure 4.2, in this regime, a reasonably-sized detector can be built that matches the axion wavelength, spurring a resonant conversion of axions to photons. Several cavity haloscopes have since been built, including notably ADMX, the most long-running experiment using the technique, which recently reached DFSZ sensitivities, and HAYSTAC, which recently incorporated beyond-standard quantum limited amplification [122–126].

At higher masses, cavities must shrink to continue to match the decreased wavelength. This is problematic for maintaining experimental reach because the sensitivity scales directly with the cavity volume. Several methods have

been proposed to get around this, including multiplexed cavities and entirely new geometries such as dielectric stacks and plasma haloscopes [127–129].

4.2 The lumped-element method

For axions with masses below $\mathcal{O}(1 \mu\text{eV})$ or equivalently with wavelengths above $\mathcal{O}(1 \text{ m})$, a new approach is needed. Because the signal is in phase across the entire device, there is negligible time delay of signals. This is equivalent to saying that displacement currents are negligible or that we are within the magnetoquasistatic (MQS) approximation.

The MQS regime is that of classical circuits. In standard circuit diagrams, components such as inductors, capacitors, etc. can be drawn as separate lumped elements because signals are in phase across each element. This is the same situation we find ourselves in with the effective axion current, and so we can draw a circuit to read out that current using a simple inductive coupling, as shown in Figure 4.3⁶.

In the diagram, we see that the axion effective current acts as a current source. The effective current is connected via a transformer to a superconducting circuit, which develops an induced, real current in response to the axion signal. The real current is very small, because $g_{a\gamma\gamma}$ and thus J_{eff} are very small, but with highly sensitive electronics, it may be detectable. The current can be directly detected with a quantum sensor, agnostic of its frequency (known as a broadband search), or it can first be used to ring up an LC resonator. The LC resonator can enhance the signal strength before detection with the quantum sensor if the signal and resonance frequency match. This ‘resonant’ readout must be tunable to search over the wide range of unknown axion mass.

In the following sections we explore the sensitivity of such a device and then discuss in more depth each component of the circuit in the context of designing a detector.

4.2.1 Experimental sensitivity

Because the axion mass is unknown, our experimental sensitivity cannot be defined simply by how small of a $g_{a\gamma\gamma}$ it can reach. Instead, the correct

⁶The lumped-element technique can actually be used in a limited range of frequencies in the MQS breakdown regime also, albeit with a modified sensitivity. See Section 6.1.

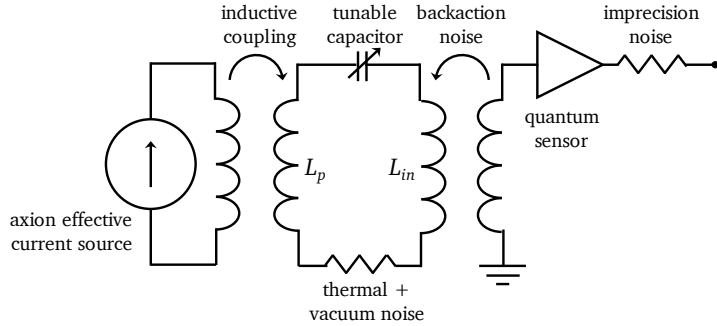


Figure 4.3: Circuit diagram for a lumped-element axion search. On the left, the axion interactions in a strong magnetic field create an effective current source that can be inductively coupled to a superconducting circuit. The circuit can be read out in broadband with the omission of the capacitor. Adding in a capacitor turns the central loop into an LC resonator, which can enhance signals that match the resonance frequency by the resonator's quality factor, Q . To scan over a range of axion masses, the capacitor can be tuned. Finally, the signal is read out using high-precision quantum sensors and analyzed offline. Noise enters the system in the resonator as thermal and vacuum noise and on the readout as amplifier-added noise.

figure of merit (FOM) is an integrated sensitivity that takes into account the search's bandwidth,

$$\text{FOM} \sim \text{SNR}^2 \times \text{BW} \quad (4.10)$$

where SNR is the signal-to-noise ratio and BW is the range of masses probed. Note that SNR is squared because we are measuring power⁷.

In a broadband search, the bandwidth is set by experimental practicalities rather than fundamental limitations; in the absence of noise or amplifier bandwidth limitations, one could theoretically read out all frequencies at once. Of course, this is not realistic—see Section 5.1 for an explanation of the achieved bandwidth in ABRACADABRA-10 cm. However, for this reason, the sensitivity of broadband experiments is often described by the signal-to-noise ratio (SNR) alone, and in this chapter, for broadband searches, we will discuss the SNR optimization only.

For a resonant search, the bandwidth of a single configuration is very small, but by changing the configuration one can scan the narrow window over a wide range of frequencies. The achievable SNR for a given set of

⁷On average, the axion signal amplitude is zero. We measure the average power deposited in the detector.

parameters may also vary with frequency. To reflect this complexity, we use a frequency-dependent scan rate as our FOM⁸. This allows us to fix a goal SNR, e.g. to attain $\text{SNR} = 3$ over the entire frequency range, and ask how long it takes to scan to achieve a given sensitivity to $g_{\alpha\gamma\gamma}$.

For both types of searches the SNR is defined at the amplifier output. However, it is common in electrical engineering to recast the signal and noise in terms of the equivalent quantities on the amplifier input. We will follow this practice here, as it allows us to be agnostic as to the specifics of the amplifier.

Here I will first lay out a derivation of the SNR for the simplest case—a broadband readout. Then I will generalize the SNR to a resonant readout and conclude with a derivation of the resonant scan rate equation that will ultimately define the reach of experiments like DMRadio. In each section I will use the conventions used for the corresponding experiment—ABRACADABRA for broadband and DMRadio for resonant—but I will note how to convert between those conventions in this chapter and in Appendix A.

Broadband SNR

We can begin our derivation of the SNR from the Dicke radiometer equation,

$$\text{SNR} = \frac{P_{\text{sig}}}{P_n} \sqrt{t \Delta \nu_{\text{sig}}}, \quad (4.11)$$

where P_{sig} and P_n are the measured, input-referred signal and noise powers, respectively, t is the integration time, and $\Delta \nu_{\text{sig}}$ is the signal bandwidth. If we were to take an instantaneous measurement, the SNR would simply be the ratio P_{sig}/P_n ; by integrating for time t , we can improve on this. For N discrete, independent measurements of a signal, the SNR increases by \sqrt{N} . Similarly, over a continuous integration period of an incoherent signal⁹, the SNR improves¹⁰ by $\sqrt{t \Delta \nu_{\text{sig}}}$.

For a low-frequency lumped-element receiver read out by a flux-to-voltage amplifier (e.g. a SQUID), such as ABRACADABRA-10 cm, we can recast the amplifier’s power output as a flux on its input inductor. For

⁸We will see in the later discussion that a scan rate FOM is fully compatible with our suggestion of the FOM structure in Equation (4.10).

⁹The signal in the axion experiments is generally coherent over a time shorter than the integration time.

¹⁰See the appendix of [108] for nice, detailed explanation of the time scaling.

the signal power, this is basically equivalent to dividing by the gain of the amplifier. For the noise power, which is sourced both on the amplifier input and within the amplifier itself, this conversion provides a way of abstracting this complication. The radiometer equation can be recast as

$$\text{SNR} = \frac{|\Phi_{\text{in}}^{\text{sig}}|^2}{|\Phi_{\text{in}}^n|^2} \sqrt{t \Delta \nu_{\text{sig}}} . \quad (4.12)$$

where $\Phi_{\text{in}}^{\text{sig}}$ is the signal flux on the amplifier input and Φ_{in}^n is the noise's equivalent input flux, usually generically written in terms of the power spectral density (PSD), $S_{\Phi\Phi}^n$, times a bandwidth, $\Delta \nu_{\text{sig}}$. In a broadband experiment, either amplifier noise (flux noise for a superconducting quantum interference device (SQUID)) or environmental noise sources dominate. I will not specify the noise type for this broadband discussion, but will go into more detail in the following discussion of resonant readout.

The signal bandwidth is determined by the axion's coherence time, τ_a ,

$$\Delta \nu_{\text{sig}} = \frac{1}{\tau_a} = \frac{\nu_a}{Q_a} . \quad (4.13)$$

Notice that the signal bandwidth can be recast as an effective quality factor for the axion, Q_a .

The signal current (measured on the central loop of Figure 4.3) can be determined by observing that the \mathcal{EMF} ¹¹ around the loop must be zero because it is superconducting,

$$\mathcal{E} = \frac{d\Phi_T}{dt} = \frac{d}{dt} (I_p L_T + \Phi_a) = 0 \quad (4.14)$$

I_p is the current on the pickup and Φ_a is the magnetic flux through the pickup inductor generated by the axion effective current. L_T is the total inductance of the loop, including the pickup inductor, amplifier input inductor, and any parasitic inductance. The signal is oscillating, so we can assume the argument of the time derivative is also zero. We have assumed that any capacitance and resistance in the circuit is negligible for this simplified broadband scenario; we will generalize for arbitrary Z when discussing the resonant case. Rearranging the above equation to extract I_p gives

$$I_p = \frac{\Phi_a}{L_T} \quad (4.15)$$

¹¹For an illuminating discussion of when to use \mathcal{EMF} versus voltage drop versus potential difference, see [130].

The flux on the amplifier input is then

$$\Phi_{\text{in}}^{\text{sig}} = I_p M_{\text{in}} = \frac{M_{\text{in}}}{L_T} \Phi_a \quad (4.16)$$

In order to use this to optimize detector design, we would like to deconstruct Φ_a to separate the axion physics from detector quantities¹². One way to write the axion flux in the pickup is

$$\Phi_a = g_{a\gamma\gamma} \sqrt{2\rho_{DM}} \cos(m_a t) B_0 V \mathcal{G}, \quad (4.17)$$

where

$$\mathcal{G} \equiv \frac{1}{B_0 V} \int_{\text{pickup}} dA \int_{\text{all space}} dV' \hat{\mathbf{n}} \cdot \frac{\mathbf{B}(\mathbf{r}') \times (\mathbf{r}' - \mathbf{r})}{|\mathbf{r}' - \mathbf{r}|^3}. \quad (4.18)$$

B_0 is a characteristic field strength, usually pegged to the nominal maximum, and V is a characteristic volume, fixed either to the magnetic field volume (as is done in ABRACADABRA-10 cm) or to the pickup volume (as is done in DMRadio). The above equations are derived from applying the Biot-Savart law with the axion effective current density from Equation (4.4) as the source current. An advantage of \mathcal{G} as a way of characterizing the detector geometry is that it is scale invariant, allowing us to compare design efficacies between detectors of different sizes and field strengths.

Using Equation (4.16) to convert to amplifier input flux and taking the root-mean-square (RMS) time average gives us

$$|\Phi_{\text{in}}^{\text{sig}}| = g_{a\gamma\gamma} \sqrt{\rho_{DM}} \cdot B V \mathcal{G} \cdot \frac{M_{\text{in}}}{L_T}. \quad (4.19)$$

Plugging this into the radiometer equation, (4.12), along with the noise we have

$$\text{SNR} = g_{a\gamma\gamma}^2 \rho_{DM} \cdot (B_0 V \mathcal{G})^2 \cdot \left(\frac{M_{\text{in}}}{L_T} \right)^2 \cdot \frac{(\tau t)^{1/2}}{S_{\Phi\Phi}^n}. \quad (4.20)$$

Note that sometimes the above is reported as the square of the SNR, rather than the SNR itself (see, e.g., [131]), depending on if one is referring to power SNR or $g_{a\gamma\gamma}$ SNR. Either way, the goal is to maximize its value in order to increase the sensitivity to a given coupling, $g_{a\gamma\gamma}$. We can see here that the reachable $g_{a\gamma\gamma}$ is proportional to the quarter-root of time for a given fixed SNR, indicating that simply running the experiment for a longer period of time has diminishing returns.

¹²See Appendix A for a discussion of the different ways we can compare detector geometries and their relative merits.

Resonant SNR

We can similarly derive the a resonant experiment's SNR, but with a generalized readout circuit impedance, Z , that does not assume the response is purely inductive. In the MQS limit, the induced current from the axion drive is

$$|I_p|^2 = \frac{\left| \frac{\partial \Phi_a}{\partial t} \right|^2}{|Z(\omega)|^2} \quad (4.21)$$

where the flux from an axion signal on the pickup inductor, Φ_a , is the same as given in Equation (4.17). The total circuit impedance can be deconstructed into effective lumped elements as

$$Z(\omega) = R + i \left(\omega L - \frac{1}{\omega C} \right). \quad (4.22)$$

Using the resonant frequency, $\omega_r = 1/\sqrt{LC}$, and the quality factor, $Q^2 = L/R^2C$, we find (with some algebra)

$$\frac{1}{|Z(\omega)|^2} = \frac{Q^2}{\omega_r^2 L^2 \left[1 + Q^2 \frac{\omega_r^2}{\omega^2} \left(\frac{\omega^2}{\omega_r^2} - 1 \right)^2 \right]} \quad (4.23)$$

$$\approx \frac{Q^2}{\omega_r^2 L^2 \left[1 + 4Q^2 \delta_\omega^2 \right]} \quad (4.24)$$

for $\delta_\omega \equiv (\omega^2 - \omega_r^2)/\omega_r^2$, the fractional detuning from the resonance frequency. The approximation works for small detunings, i.e. $\delta_\omega \ll 1$ or $\omega \approx \omega_r$.

Substituting the impedance and axion flux into Equation (4.21), we find that the pickup current is

$$|I_p|^2 = \frac{m_a^2 g_{a\gamma\gamma}^2 \rho_{DM} B_0^2 V^2 \mathcal{G}^2 Q}{\omega_r^2 L^2} \left[\frac{Q}{1 + 4Q^2 \delta_\omega^2} \right]. \quad (4.25)$$

The term in brackets contains the Lorentzian frequency response from the resonator. Although it is fine to leave the current in terms of \mathcal{G} , in DMRadio, we typically use a different measure of the experiment-axion coupling, c_{PU} , related to \mathcal{G} by

$$c_{PU}^2 = \frac{V^{1/3}}{2L_p} \mathcal{G}^2 \quad (4.26)$$

instead. This new variable has the advantage that it combines the geometry of the magnet and pickup structure with the response of the pickup inductor. This is preferable because the inductance is directly tied to the pickup geometry¹³. To make this substitution I will assume that the pickup inductance is the dominant inductance in the system ($L \approx L_p$):

$$|I_p|^2 = \frac{m_a^2 g_{a\gamma\gamma}^2 \rho_{DM} B_0^2 V^{5/3} c_{PU}^2 Q}{\omega_r^2 L_p} \left[\frac{Q}{1 + 4Q^2 \delta_\omega^2} \right]. \quad (4.27)$$

We can convert into a pickup flux on the amplifier input using Equation (4.16),

$$|\Phi_{in}^{sig}|^2 = M_{in} \frac{m_a^2 g_{a\gamma\gamma}^2 \rho_{DM} B_0^2 V^{5/3} c_{PU}^2 Q}{\omega_r^2 L_p} \left[\frac{Q}{1 + 4Q^2 \delta_\omega^2} \right]. \quad (4.28)$$

The SNR for a resonant experiment is thus

$$\text{SNR} = M_{in} g_{a\gamma\gamma}^2 \rho_{DM} \left(\frac{m_a^2}{\omega_r^2} \right) \left(\frac{B_0^2 V^{5/3} c_{PU}^2 Q}{L_p} \right) \left(\frac{(\tau t)^{1/2}}{S_{\Phi\Phi}^n} \right) \left[\frac{Q}{1 + 4Q^2 \delta_\omega^2} \right]. \quad (4.29)$$

For the broadband SNR, we left the noise as a general PSD, $S_{\Phi\Phi}^n$; neglecting environmental sources, the leading noise contribution is the flat amplifier noise, which is approximately constant throughout the frequency range of interest for the SQUIDS used in ABRACADABRA. For the resonant SNR, we need to examine the frequency dependence of the noise contributions more thoroughly.

The noise in a lumped element experiment consists of thermal, vacuum, amplifier, and environmental contributions, which can have different frequency-dependent behavior. Converting from flux noise density to current noise density, we have,

$$S_{II}^n = \frac{S_{\Phi\Phi}^n}{M_{in}} = 4\hbar\omega \left(n_T + \frac{1}{2} \right) \frac{\Re[Z(\omega)]}{|Z(\omega)|^2} + S_{II}^{\text{imp}} + \frac{S_{VV}^{\text{BA}}}{|Z(\omega)|^2} + S_{II}^{\text{env}}. \quad (4.30)$$

We will again assume the environmental contributions are negligible. The amplifier noise on its output (known as imprecision noise, S^{imp}), as in the

¹³ c_{PU} is also useful at the upper end of the lumped-element frequency range where the MQS approximation begins to break down; above the MQS limit, the pickup structure has a complex impedance rather than being fully capacitive, and a more rigorous definition of c_{PU} in terms of the coupled energy allows us to remove L_p from the sensitivity equation.

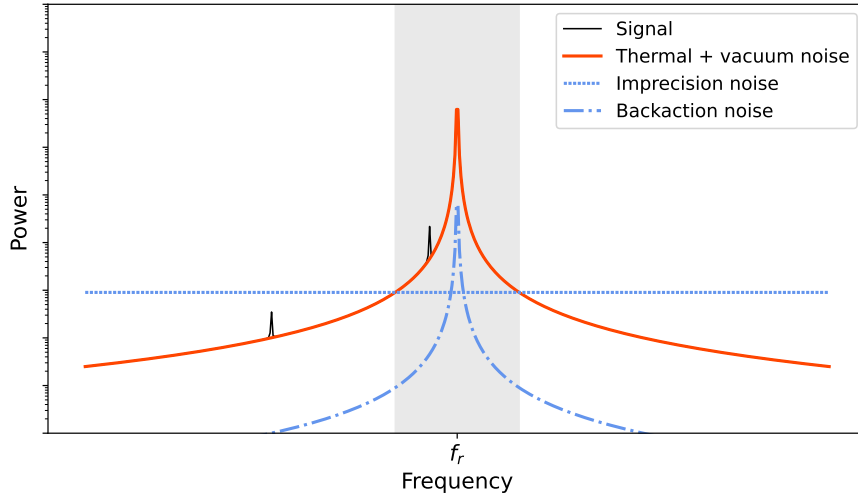


Figure 4.4: The frequency dependence of the various noise contributions to a resonant readout. The sensitivity bandwidth is illustrated by the grey band.

broadband case, is approximately frequency independent—it is added to the signal on the amplifier output, so does not interact with the resonator. Any noise sources upstream of the amplifier, however, are shaped in frequency space by the resonator. These upstream sources include the thermal and vacuum contributions in addition to noise from the amplifier that ‘back-acts’ on its input. The frequency dependence of the various noise sources are illustrated in Figure 4.4.

In a resonant readout at low frequencies with a critically coupled amplifier, the noise is thermally dominated within the experiment’s resonator bandwidth¹⁴. Intuitively, the resonator rings up the pre-amplifier noise by its Q-value, so even if amplifier imprecision noise beats out thermal noise in the broadband case, the thermal noise is dominant for resonant readouts as long as it is not a factor of Q lower than imprecision noise—a situation we can avoid by selecting near-quantum-limited amplifiers.

We will now temporarily take the approximation that the noise is solely thermal to see the effect on the SNR in the resonator band. The number of

¹⁴Indeed, more precisely, thermal noise dominates in the sensitivity bandwidth, defined in the below discussion of scan rate.

thermal noise photons in-bandwidth at temperature T is

$$n_T(\omega, T) = \frac{1}{\exp(\hbar\omega/k_B T) - 1} \quad (4.31)$$

$$\approx \frac{k_B T}{\hbar\omega} \quad (4.32)$$

for $\hbar\omega/k_B T \ll 1$, giving a noise contribution

$$S_{II}^{\text{therm}} = 4k_B T \frac{\Re[Z(\omega)]}{|Z(\omega)|^2}. \quad (4.33)$$

The magnitude of the contribution is driven by the system temperature, T , and the shape is the resonator's Lorentzian (determined by the $Z(\omega)$ of the circuit). Substituting in the circuit's impedance (from Equations (4.22) and (4.23)) and converting to units of flux results in

$$S_{\Phi\Phi}^{\text{therm}} = 4k_B T M_{\text{in}} \frac{RQ}{\omega_r^2 L^2} \left[\frac{Q}{1 + 4Q^2 \delta_\omega^2} \right] \quad (4.34)$$

$$= \frac{4k_B T M_{\text{in}}}{\omega_r L} \left[\frac{Q}{1 + 4Q^2 \delta_\omega^2} \right], \quad (4.35)$$

where the second step comes from substituting $Q = \omega_r L / R$.

Now substituting this noise equation into Equation (4.29)'s SNR and making the approximation that $m_a \approx \omega_r$, we have

$$\text{SNR} = g_{a\gamma\gamma}^2 \rho_{DM} m_a \left(\frac{c_{\text{PU}}^2 B_0^2 V^{5/3} Q (\tau t)^{1/2}}{4k_B T} \right). \quad (4.36)$$

Recall that this equation only applies for small detunings from the resonance frequency and if thermal noise dominates. If we were to plug in some reasonable numbers for these values, we would see that the Q value enhancement over the broadband SNR means that we can reach DFSZ sensitivities in only a few minutes of integration. So if we knew the axion mass, detection would only take a few minutes. This fact means that once the axion is discovered, confirmation is relatively very easy. It also means that if we find axions, undergraduate students could potentially one day detect axions in their senior lab classes.

Resonant scan rate

In a resonant experiment, the SNR is not a complete picture of the sensitivity of the experiment. Imagine the situation in which you are able to achieve an incredibly high SNR, but at an infinitesimally small range of frequencies; it would take far too long to scan the available axion mass range for such an experiment to be useful. Instead, we need to use a combination of the SNR and bandwidth as a benchmark, such as that shown in Equation (4.10). A more intuitive and directly applicable FOM is the scan rate, which defines how fast we can scan the resonant frequency, ν_r , to achieve a given SNR. The scan rate is approximated as a continuous function, but in practice is a set of discrete resonator tunings,

$$\frac{d \nu_r}{dt} = \frac{\Delta \nu_{\text{sens}}}{t}. \quad (4.37)$$

Here $\Delta \nu_{\text{sens}}$ is the sensitivity bandwidth (also written in the literature as visibility bandwidth [126, 132]), the range of frequencies over which the detector can maintain an approximately constant SNR for a given signal strength, and will be the frequency step size between tunings. t is the integration time at each frequency step.

By rearranging the Dicke radiometer equation of (4.12), we find

$$\frac{d \nu_r}{dt} = \frac{\Delta \nu_{\text{sens}} \Delta \nu_{\text{sig}}}{\text{SNR}^2} \frac{|I_{\text{sig}}|^4}{|I_n|^4}. \quad (4.38)$$

Notice that I have converted from amplifier input flux to current through the resonator for consistency with the notation used in DMRadio papers. The input inductance on the amplifier is identical for both signal and noise, so M_{in} cancels in the numerator and denominator.

The sensitivity bandwidth, $\Delta \nu_{\text{sens}}$, is set by the relative amounts of frequency-independent and frequency-dependent noise (see the grey band in Figure 4.4). The signal is shaped by the same Lorentzian as the frequency-dependent noise, so when flat noise begins to dominate (farther away from the central resonance frequency), the experiment rapidly loses sensitivity to signals. This is illustrated by the off-resonance signal peak in Figure 4.4 that is entirely buried under the imprecision noise, despite staying well above the thermal and backaction noise levels.

The frequency-dependent noise current and sensitivity bandwidth must thus be co-optimized to maximize the scan rate. In practice, this can be

done by tuning the strength of the amplifier input coupling. For a given amount of amplifier noise, adjusting the input coupling can redistribute the noise between imprecision and backaction, i.e. between flat and shaped noise contributions. By increasing the amplifier coupling from the naive matched coupling shown in Figure 4.4, the imprecision noise level can be decreased (increasing the sensitivity bandwidth) at the cost of increasing the backaction noise. This tradeoff can be seen by defining the imprecision and backaction noise in terms of the total number of amplifier noise photons, η_A , as

$$\mathcal{S}_{II}^{\text{imp}} = \frac{\eta_A}{\kappa^2}, \quad (4.39)$$

$$\mathcal{S}_{VV}^{\text{BA}} = \eta_A \kappa^2, \quad (4.40)$$

where κ characterizes the amplifier input coupling strength.

As long as the backaction noise stays below the thermal noise, the SNR on-resonance is maintained. This optimization process will be discussed further in Chapter 6 and is derived in great detail in [133]. In the limit that the thermal noise contribution is much larger than amplifier noise temperature¹⁵, $n_T \gg \eta_A/2, 1$, the optimized sensitivity bandwidth scales with the ratio of the thermal to amplifier noise,

$$\Delta \nu_{\text{sens}} \propto \frac{n_T}{\eta_A} \Delta \nu_r. \quad (4.41)$$

Note that experiments such as DMRadio-m³ will actually leave the limit of large thermal occupation at the upper end of the frequency range, but I will ignore the subtleties of that regime here. In short, the optimal coupling and sensitivity bandwidth are slightly different.

The signal bandwidth, $\Delta \nu_{\text{sig}}$, is determined by axion physics and is given in Equation (4.13) in the situation where the axion bandwidth is narrower than the sensitivity bandwidth. If the axion signal is wider, then the experiment only samples part of the signal at a time, and the effective signal bandwidth is just the entire sensitivity bandwidth:

$$\Delta \nu_{\text{sig}} \sim \min\left(\Delta \nu_{\text{sens}}, \frac{\nu_a}{Q_a}\right), \quad (4.42)$$

¹⁵Noise temperature is just the noise converted into units of temperature as if its source were thermal.

The signal current is the same as before, given by Equation (4.27). The noise current we will again assume is thermally dominated in the sensitivity bandwidth (as is true after the amplifier optimization has taken place), and so is given by Equation (4.34) divided by M_{in} .

Putting these pieces together gives us the scan rate,

$$\frac{d\nu_r}{dt} \approx \frac{6.4 \times 10^5 \pi}{\text{SNR}^2} \left(g_{a\gamma\gamma}^4 \rho_{DM}^2 \nu_r \right) \left(\frac{c_{\text{PU}}^4 B_0^4 V^{10/3} Q}{6\sqrt{3}k_B T \eta_A} \right). \quad (4.43)$$

Here I have substituted Q_a for a more precise integration of the axion halo model and used the full expression for the optimized sensitivity bandwidth (in the thermal limit) from [133]. This scan rate equation is the FOM that we will use to characterize the reach of lumped element experiments. It can be directly compared to the scan rate used for higher-mass axion searches such as cavity haloscopes, but note that the included factors of frequency (including those hidden in $g_{a\gamma\gamma}$ for KSVZ or DFSZ scans) make the rate highly frequency dependent.

4.2.2 Detector components

The above sensitivity equations, (4.20) and (4.43), are our guide as we design the experiments. In this section, we discuss the major components of a detector, the primary decisions that must be made in the design of those components, and how those decisions affect the overall sensitivity of the experiment.

Magnet

The first, critical component of any axion-photon search is the magnet that stimulates the interaction. Improvements in magnet strength and volume drive the fastest improvements in sensitivity for resonant searches, as shown by the scaling in Equation (4.43). The construction of a high-powered magnet can also be the driver of cost, with price typically scaling with the stored energy,

$$U_B \sim B^2 V \quad (4.44)$$

With larger stored energy, designs must increasingly account for mechanical forces, quench protection, material critical temperatures and fields, and cryogenic requirements. For high sensitivity experiments, larger fields can also create backgrounds, as we discuss in Section 5.3.2.

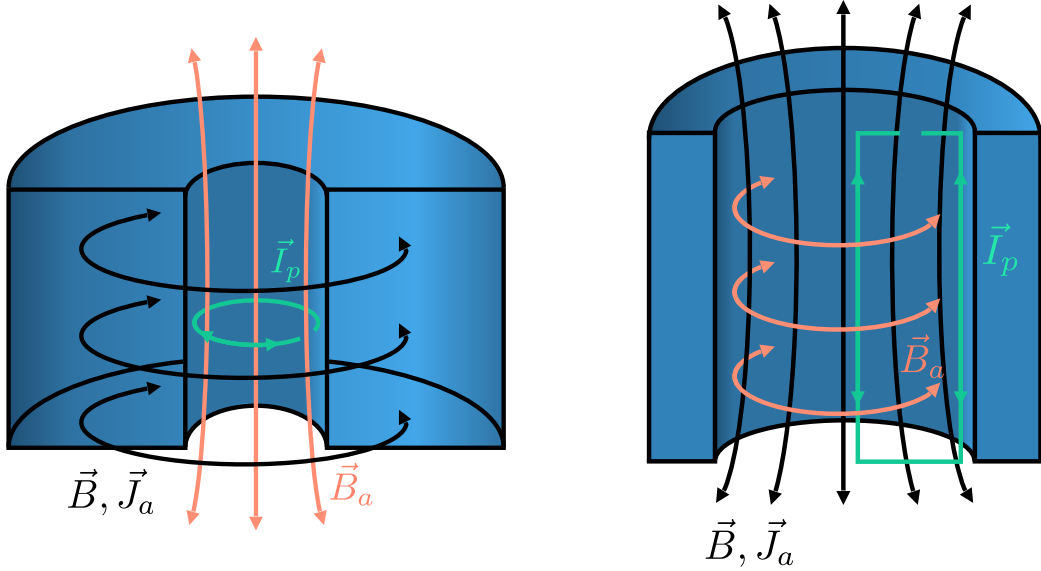


Figure 4.5: Magnet geometries. In a toroid, *left*, the primary magnetic field, \vec{B} , and corresponding axion effective current, \vec{J}_a , run azimuthally, contained within the magnet bore. The real magnetic field induced by the axions, \vec{B}_a , causes a change in flux through a pickup structure in the toroid’s center, inducing a real current in the superconductor, \vec{I}_p . The fields in a solenoid, *right*, are oriented along the axis of the cylinder inside the bore. At the endcaps the fields fringe before wrapping around the outside. The resulting vertical \vec{J}_a creates an azimuthal \vec{B}_a which can be picked up by an inductor in the orientation shown. In both geometries, the pickup structure has a gap to force the current to return through a connected readout circuit¹⁶

There are two primary magnet geometries that have been used for lumped-element experiments, solenoid and toroid, shown in Figure 4.5. The toroid geometry, used in ABRACADABRA-10 cm, contains its fields entirely within the bore of the magnet. This is a distinct advantage from both a safety and sensitivity perspective. On the safety side, contained fields mean that in the event of a quench, the resulting rapid and large mechanical forces are confined to inside the magnet bore and do not affect other components of the experiment such as the dilution fridge, support structures, or readout electronics. In terms of sensitivity, the pickup inductor and superconducting

¹⁶Alternatively, the readout can be inductively coupled. The gap is still necessary to cause the current to return along the outside of the pickup structure where it can be ‘seen’ by the readout input inductor.

amplifiers can sit in a nominally field-free region, respectively reducing first-order backgrounds and not interfering with operation. The downside of toroids is that they are more difficult to build and are not as commonly constructed as solenoids.

Superconducting solenoidal magnets are ubiquitous, used in fundamental physics applications such as accelerators as well as for medical applications such as MRI machines. Solenoids thus tend to be cheaper to construct for a given stored energy. However, with this comes the trade-off of a high-field pickup region and large fringe fields. A less-obvious advantage of the solenoid geometry is that the corresponding readout has higher-frequency parasitic resonances, allowing sensitivity to higher mass axions. This particular consequence is explored in more detail in Sections 4.2.2 and 6.1.

Pickup inductor

The geometry of the pickup inductor is dependent on the magnet geometry and must be co-optimized with the rest of the readout circuit. The most simple pickup structure designs are shown in Figure 4.5, where the pickup is simply a loop of wire that surrounds a region of axion magnetic flux. This simple design can be improved to increase the axion-pickup coupling, decrease the pickup inductance, and, for a resonant readout, increase the quality factor. One way of achieving this is to replace the wire with a sheath, shown for both toroid and solenoid geometries in Figure 4.6.

The coupling is improved because the sheaths are essentially better able to catch more of the flux lines, increasing \mathcal{G} in Equation (4.20) or c_{PU} in Equation (4.43).

The sheath's impact on Q factor is more nuanced. In the toroid design, the sheath also shields the readout circuit from the materials in the magnet. Any dielectric or normally conductive materials that the fields in the readout circuit can reach will degrade the Q of the resonator. Lossy materials are necessary to construct a high powered magnet and cool it down to single-Kelvin temperatures, but if they are enclosed by the superconducting sheath, they will not affect the resonator. Because there must be a gap in the sheath to get the signal out, there will be some loss from these materials, but with careful design, their impact can be mitigated.

The solenoid design does not get the same shielding benefit as the toroid, because the sheath cannot surround the magnet while still optimally coupling to the axion-generated magnetic field. Instead, the benefit comes from

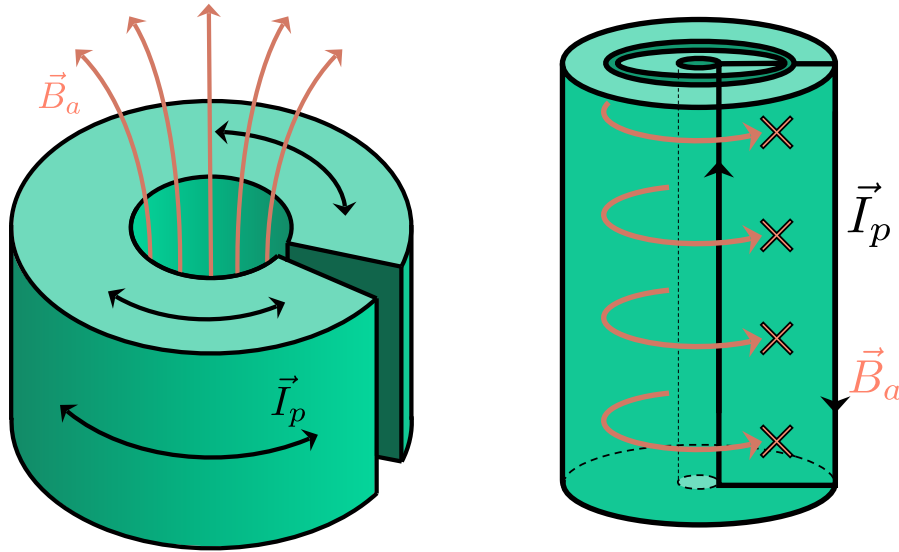


Figure 4.6: Pickup sheath geometries. *Left*, the sheath surrounds the toroidal mag- net, protecting the circuit from its lossy materials. *Right*, the pickup sits inside the bore of the solenoidal magnet.

the fact that generally Q improves for larger structures with lower surface area-to-volume ratios.

An important consideration in the construction of the pickup structure is its materials. Superconductors are the best choice, because Johnson noise from resistive materials can dominate a signal and drastically reduce the Q of a resonator (see the following section for more on this). However, for the solenoid geometry, the pickup is located in the high-field region. Low- T_c superconductors such as NbTi do not function well in magnetic fields, and so in the solenoid case, for large geometries with low surface areas, ultra-pure normal conductors such as high-purity copper may provide better performance. Studies of low-frequency resonators constructed with high- T_c materials that perform better in strong fields have not yet been done, but work is ongoing to study them for other high- Q applications such as microwave cavity surface treatments [134].

Readout circuit

The readout circuit is responsible for taking the current induced on the pickup structure out from the sensitive region and amplifying it to levels

that can be recorded by a digitizer. Because the current is so tiny, the readout must attenuate the signal as little as possible and protect it from being swamped by noise before it reaches the amplifier. The amplifier must be highly responsive to small signals and contribute ultra-low levels of noise. In practice, this is achieved with quantum sensors such as SQUIDS.

As discussed in the caption of Figure 4.3, there are two configurations for the readout; a broadband response is achieved with a purely inductive circuit, while the addition of a tunable capacitor converts it into a resonant readout. Although the broadband circuit is easier to construct and operate, the highest sensitivities can be achieved by exploiting resonant signal enhancement [135].

To see why this is the case, we can consider the time it takes to achieve a certain sensitivity. For a broadband readout reaching coupling strength $g_{\alpha\gamma} = g_0$, take the total integration time be T to cover bandwidth Δf . A resonant circuit can improve the sensitivity by its quality factor, Q , but only within the resonator bandwidth, $1/Q$. Thus a resonant experiment can integrate at each frequency step for time only T/Q , but it must take Q steps to cover Δf . Initially it would seem that both approaches need the same time, T , to achieve the same sensitivity over the same bandwidth. However, in the resonant case, there is actually additional sensitivity outside of the resonator bandwidth¹⁷, as illustrated in Figure 4.7. Because we get additional sensitivity from the tails of the resonator shape, we do not have to integrate as long at each step. Depending on how much sensitivity there is in the tails, the reduction in total integration time can be a significant improvement over the broadband case.

There is considerable optimization that must go into the design of the readout, including co-optimizations with the rest of the experiment components. I will leave in-depth discussions of readout design to Chapters 5 and 6 in the context of specific experiments, but for now will summarize the basic principles that we can draw from the sensitivity equations (4.20) and (4.43).

Broadband ■ In the broadband case, it is immediately clear that reducing the total inductance of the readout circuit, L_T , can improve the SNR. One must be careful, however, because

$$M_{\text{in}} = k_{\text{in}} \sqrt{L_{\text{in}} L_{\text{amp}}} \quad (4.45)$$

¹⁷This is maximized by tuning the coupling of the amplifier to the rest of the readout circuit. See Section 6.1 for more on this.

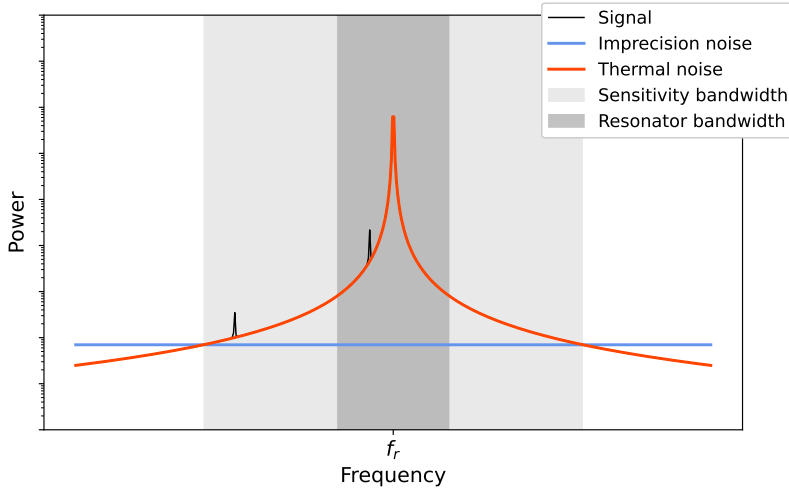


Figure 4.7: Illustration of sensitivity bandwidth versus resonator bandwidth. The sensitivity bandwidth can be much wider than the resonator bandwidth, and signals will have approximately the same SNR throughout.

and

$$\mathcal{G} \sim L_p \quad (4.46)$$

both include inductances that are included in

$$L_T = L_p + L_{\text{in}} + L_Q \quad (4.47)$$

where L_{in} is the input inductance to the amplifier, L_p is the pickup inductance, L_Q is parasitic inductance, and L_{amp} is the amplifier inductance. $k_{\text{in}} \leq 1$ parametrizes how well coupled the amplifier is to the pickup circuit.

So, although it is indeed useful to reduce L_T , the best way to do so is to reduce parasitic inductance, L_Q . Reducing L_{in} can also be useful, but only if that can be achieved while still maximizing the amplifier coupling. Reducing L_p does not help at all!

The fundamental noise in this simple circuit is dominated by the amplifier-added noise. By being at sub-K temperatures and using a fully superconductive circuit, thermal and Johnson noise are reduced.

Resonant ■ The ideal L and C values for the resonant case are hidden in the scan rate of Equation (4.43). Increasing the pickup inductance, but keeping all other inductances small, maximizes the sensitivity. Similarly, mini-

mizing all parasitic resistance is critical for maximizing the transfer function from pickup to amplifier. The ideal circuit would have the $L = L_p$ and C chosen to fix the resonant frequency. Of course, for a SQUID-based readout, there will have to be some additional inductance on the amplifier's input. As we see in Section 6.2, moving beyond SQUIDs will be a part of the long-term plan for sensitivity improvements with this method. No matter which amplifier is used, its coupling needs to be optimized to maximize the sensitivity bandwidth.

Another consideration for a resonant readout is tunability. Generally, one can manufacture capacitors that can be tuned up or down by an $\mathcal{O}(1)$ factor, but the desired range for a lumped-element axion search is several orders of magnitude wide. This means that the capacitor needs to be swapped out a few times over the scan.

Cryogenics

Independent of the configuration of the readout, it must be superconducting and therefore kept at cryogenic temperatures. To get a sufficiently strong magnetic field, the magnet must generally also be superconducting. This places an upper limit on the cryostat temperature of a few Kelvin, assuming the use of traditional, low- T_c superconductors.

For a broadband search, which is not limited by thermal backgrounds, this is sufficient to operate. However, in a resonant search, reducing the temperature as much as possible directly improves the experimental sensitivity by cutting the dominant, thermal noise background. The lowest temperatures that can be maintained over a long period of time with a large cold mass are $\mathcal{O}(\text{mK})$, achievable with a dilution refrigerator. Low temperatures are perhaps even more important for low-mass axion searches than they are for high-mass searches (such as ADMX or HAYSTAC), because the thermal occupation number at low frequencies is higher.

In addition to just getting the experiment cold, successful cryogenic systems need to provide long-term temperature stability. Long term operation is necessary to achieve a long integration time for improved sensitivity or temporal analyses. Single-digit Kelvin operation is possible with a variety of helium-based fridges, but multi-month cold times are best achieved with a dry, mechanically-cooled system [136]. In particular, the price of helium makes any fridge that cannot recycle its cryogens prohibitively expensive for longer runs. A downside of mechanically-cooled fridges is the inherent

presence of vibrational backgrounds. Wet systems such as dip probes avoid this, but lack the longevity of mechanical systems¹⁸. Fortunately, dilution refrigerators have become much more commonly accessible recently with the proliferation of quantum computing and quantum sensing applications.

¹⁸The SHAFT experiment used a liquid-helium-bath cryostat, but only ran for a few days [137]. SHAFT is discussed in Section 5.4.

5

ABRACADABRA-10 cm

ABRACADABRA-10 cm was the first experiment to set limits on axions using the lumped-element method. Using a grapefruit-sized, 1 T magnet and a broadband readout, it provided a world-leading exclusion on axion dark matter over more than a decade of masses around 1 neV. In this chapter we discuss the details of this experiment, the limits that it set, and lessons learned that lay the stage for the next generations of lumped-element detectors. Section 5.1 describes the hardware configurations for the two physics runs. Section 5.2 lays out the experiment’s runs and data management strategy. In Section 5.3 we discuss how we convert the raw data into physical limits, including the calibration, noise studies, and statistical analysis. It also presents the results from both the 2018 and 2020 physics runs (runs 1 and 3, respectively). Finally, in Section 5.4 I mention a few other similar experiments that, together with ABRACADABRA-10 cm, provide the foundation for the next generations of lumped-element experiments discussed in Chapter 6.

The work presented in this chapter corresponds to three publications: ABRACADABRA-10 cm’s results from run 1, [138], the design and implementation, [131], and the results of run 3, [139].

5.1 Experimental apparatus

The ABRACADABRA (A Broadband/Resonant Approach to Cosmic Axion Detection with an Amplifying B-field Ring Apparatus) 10 cm prototype detector was the first experiment to publish limits on low-mass axion dark matter using a lumped-element detection method. Being the first of its kind, it was built with the goal to provide a proof-of-concept within a limited budget. We built and operated the experiment at MIT, on the ground floor of building 24, in a dilution refrigerator initially allocated for R&D for the CUORE neutrinoless double-beta decay experiment [140]. ABRACADABRA-10 cm used a broadband, SQUID-based readout combined with a small toroidal magnet to search for axions from the Milky Way’s dark matter halo. This section describes the details of detector construction and the hardware upgrades for subsequent runs. This discussion includes the challenges we encountered that now inform the design of future generations of lumped-element dark matter detectors. A summary of the detector and run parameters for the two physics runs, run 1 and run 3, is shown in Table 5.1.

5.1.1 Cryomechanical system

ABRACADABRA-10 cm was located in Olaf, an Oxford Instruments Triton 400 dilution refrigerator [141], shown open in Figure 5.1. Olaf’s base temperature is ~ 10 mK, but for ABRACADABRA’s operation, the mixing chamber reached only $\mathcal{O}(100)$ mK and the magnet shield sat at ~ 1 K because of meager thermalization of the magnet wiring (described further in Section 5.1.2). However, being limited by amplifier, not thermal noise, these temperatures were sufficient for operation.

The magnet and pickup structure are held in a shield that hangs at the bottom of the fridge. As described in more detail in Section 5.1.2, we thermalized the structure to the lowest, mixing chamber plate. For structural support, we strung a Kevlar thread through a bolt that was screwed into the top of the shield, attaching the other end to a spring mounted inside a pipe at the very top of the fridge. The pipe is connected to a vacuum-sealed actuator that allowed us to raise and lower the magnet while cold. Using this system we could make sure that the weight of the magnet was on the Kevlar, not the magnet or readout wires, as the materials experienced differential thermal contraction during the cooldown. By pulling the top of the can flush against the underside of the mixing chamber plate, we were also able to im-

	Parameter	Run 1	Run 3
<i>Magnet</i>	B_0	1 T	
	V_B	890 mL	
	\mathcal{G}	~ 0.027	~ 0.031
<i>Pickup circuit</i>	L_p	95 nH	20 nH
	L_Q	—*	288 nH
	L_{in}	150 nH	
	L_T	$\sim 1.6 \mu\text{H}$	800 nH
<i>SQUIDs</i>	M_{in}	2.52 nH	
	T	870 mK	450 mK
<i>Run</i>	t	~680 hrs	~430 hrs
	m_a	0.31 – 8.3 neV	0.41 – 8.27 neV

*This value was not simulated in run 1 and could only be deduced from L_T .

Table 5.1: Parameters from ABRACADABRA-10 cm runs 1 and 3. B_0 and V_B are the magnet's measured peak field and total magnetic field design volume, respectively. \mathcal{G} is the geometric factor describing the axion-detector coupling (as simulated with COMSOL, see Appendix B), and $L_T \approx L_p + L_Q + L_{in}$ is the pickup circuit's total self inductance, described in more detail in Section 4.2.1. L_p is derived from simulations, as is L_Q in run 3, and L_{in} is the SQUID spec. L_T was extracted from calibration data; the difference in this number from the sum of the other inductances comes from unsimulated parasitic impedance in the system. M_{in} (also from spec) describes the input coupling to the SQUID amplifiers, kept at temperature T , measured on the fridge plate. Each run took data for a total time, τ , over a range of axion masses, m_a .



Figure 5.1: ABRACADABRA-10 cm detector in the run 1 configuration hanging in Olaf, an Oxford dilution refrigerator. The plates, from bottom to top, are: mixing chamber plate, cold plate, still plate, 4 K plate, 70 K plate. The ABRACADABRA magnet is hung from a room temperature support at the top of the fridge and thermalized to the mixing chamber plate. The thermalization via two thick copper braids shown in this image was used for testing only. In the physics runs we used shorter, thin copper tapes that provided less mechanical connection between the magnet can and mixing chamber plate.

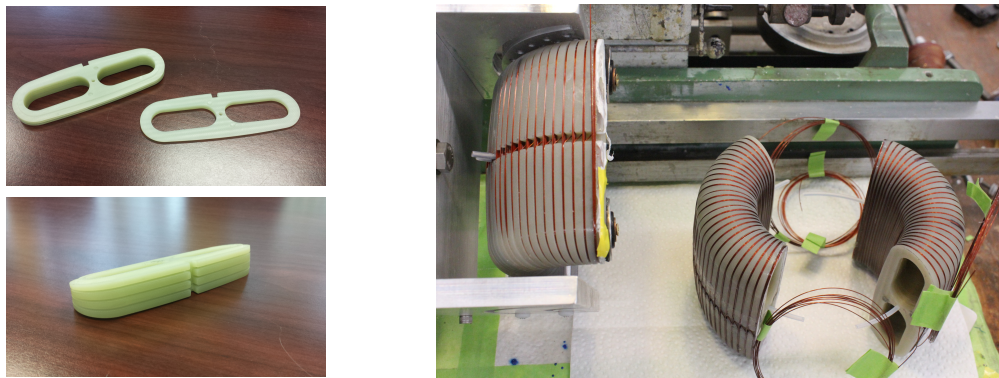


Figure 5.2: *Left*, G-10 wedges in the process of being glued together to form the mandrel. *Right*, three pieces of the magnet after being wound and before being attached. On the left side of the image the final piece to be wound is still mounted in the winding stand.

prove heat transfer out of the magnet during the cooldown, and then lower it during running to decouple it vibrationally.

5.1.2 Magnet

The ABRACADABRA-10 cm magnet was constructed by Superconducting Systems, Inc. (SSI) [142], a company based in Billerica, MA that primarily builds specialty MRI magnets. The design was unusual for them: it is a toroid, is much smaller than their typical projects, and is operated at $\sim 1\text{ K}$ in a dilution refrigerator, rather than at 4 K with a simple pulse tube system.

The magnet is composed of NbTi(CuNi)¹ wires wound onto a mandrel made of G-10 laminate. The mandrel is made of 80 individual pieces that are epoxied together, first into three sections for winding, and then together into the full toroid after the wires are in place. The resulting toroid is 12 cm tall with a 12 cm diameter and 3 cm inner radius. There are 16 windings per mandrel slice, for a total of 1280 wraps, laid in grooves in the G-10 and potted in epoxy. It is fully counter-wound in order to eliminate any net current in the azimuthal direction, which could mimic an axion signal. Photos of the magnet under construction are shown in Figure 5.2.

¹Multifilament NbTi in a CuNi matrix

The wires in the three sections are connected with superconducting ‘praying hands’ joints². The joints are then fixed to the outside of the toroid.

In the center of the G-10 structure (at radius 4.5 cm) there is a hole with a 0.5 mm diameter NbTi wire running through it, parallel to the field lines, which is used for calibration (see Section 5.3.1). Additionally, there was a Hall probe inserted into the mandrel region, which was used to measured the magnetic field strength. We characterized the field strength to be 1 T (with precision $\sim 1\%$) at the toroid’s inner radius when charged to 121 A. Uncertainty on the field strength is due to uncertainty on the probe’s position in the field. We observed no decay in field strength after one week of running in persistent mode up to $\lesssim 0.1\%$. After field testing, we removed the Hall probe to prevent it from introducing backgrounds into the field region.

The magnet is supported by an external, non-conductive frame (made of G-10 composite) and is wrapped with braided copper straps to improve thermalization.

The entire structure is mounted inside a superconducting shielding can. The can is made in two halves of ~ 1 mm-thick copper, which are spin-coated with tin ($T_c \sim 3.7$ K [143]) in a $25 - 75 \mu\text{m}$ -thick layer. In run 1, the two halves were soldered together. In runs 2 and 3, in order to have access to the magnet and pickup structure, we switched to gluing the halves together using a silicon-based putty (silithane 803). In order to improve the electrical connection between the halves, we inserted a piece of unmelted PbSn solder ($T_c \sim 7 - 8$ K [144]) into the puttied joint along the entire circumference. In both setups, we left a small hole in the halves’ seal for wires to pass through. Figure 5.3 shows the magnet mounted in the shielding can.

A 12 mm-thick aluminum puck was glued to the top of the can, from which we thermalized and mounted the can and magnet. Several flexible copper pieces were bolted between the puck and the underside of the mixing chamber plate for thermalization. In run 1, we used braided copper straps, which we replaced for runs 2 and 3 with thinner copper tapes to reduce transferred vibrations.

After passing outside the can, the magnet’s wire leads traveled as a twisted pair up to the 4 K plate where they terminated in a superconducting switch (the squat cylinder in the upper right of Figure 5.1). Along the way, the wires were thermalized with copper tape to the plates and, in runs 2 and 3, to a vertically-mounted copper rod. Above the switch, the NbTi wires

²As opposed to ‘shaking hands’ joints—in the latter, the wires’ ends are pointed in opposite directions, while with ‘praying hands’ joints the ends point in the same direction.



Figure 5.3: *Left*, the magnet mounted in the superconducting shielding can. My hand for scale. *Right*, the closed shielding can in the run 1 configuration. The wires on the right side of the image are passing through the gap in the two shielding halves. The cable taped to the can is the calibration circuit.

transition to high- T_c , YBCO superconducting tapes, wrapped in a spiral to increase their length, then to copper wires at the 70 K stage³. The magnet was charged through a vacuum feedthrough mounted on top of the fridge. We covered the leads on the top of the fridge in plastic then aluminum foil to prevent them from acting as antennae, taking electromagnetic interference (EMI) signals from the room to the magnet. We know that the leads are a sensitive source of backgrounds because touching them rails the SQUID response. This is discussed further in Section 5.3.2.

There are several lessons that we learned in operating this magnet that will guide different design choices for future experiments. First, thermalization could be greatly improved in order to put less load on the refrigerator. Most of the wiring material is CuNi, which, being highly thermally conductive, could transfer heat between the fridge temperature stages. The magnet lead wiring was shorter than ideal in a dilution fridge setting, putting a high heat load on the mixing chamber, which has only microwatts of cooling power. SSI is accustomed to working with 4 K systems, for which the wire lengths would have been long enough to fully thermalize the system. Although the temperatures of ~ 1 K on the magnet (approximately on par with

³The 70 K name for the plate is historical; it actually sits closer to 40 K during operation.

the still temperature) and ~ 800 mK on the mixing chamber plate were sufficient for our needs⁴, future searches with larger cold masses and thermally-limited noise will require stricter tolerances.

As we will discuss in Section 5.3.2, magnet fringe fields vibrating through the pickup region were our dominant source of noise at low frequencies. Future magnets will need to be constructed with this in mind, by, for example, reducing fringe fields from wire joints. This can be accomplished by using a single wire strand or by joining wire sections with ‘shaking hands’ joints that are carefully located away from regions of interest. Shielding or deliberate placement of the twisted pair magnet leads once they leave the shielded area may also help reduce fringe field-sourced backgrounds.

5.1.3 Shielding

In addition to the superconducting Cu/Sn can around the magnet and pickup structure, we used several other layers of shielding to protect from environmental backgrounds. The dilution refrigerator itself has two layers of aluminum thermal shields hanging from the 4 K and 70 K plates. On the room temperature stage, it also has a thick aluminum shield that contains the vacuum. These layers each act as Faraday cages, shielding against high-frequency electromagnetic noise. However, there are many holes in the shielding on the plates and at the top of the fridge for wires and helium to pass through, which reduce their efficacy.

To supplement the fridge’s cans and add additional protection from ambient magnetic fields, we added mu-metal shielding on the room temperature vacuum can. We used several 200 μm -thick, $\sim 0.25 \text{ m}^2$ mu-metal sheets leftover from accelerator R&D at Bates Research and Engineering Center [145], attached with tape and nylon straps to the can’s vertical walls (two layers, inside and outside) and bottom (a single layer inside). Using a large Helmholtz coil, we measured the DC magnetic field attenuation of the mu-metal-covered can *ex situ* to be a factor of $\sim 5 - 10$. The magnetic shielding is something that could be improved in the future with dedicated mu-metal and a better design.

⁴Despite the experiment being happy to sit at a higher temperature, the high load on the dilution fridge significantly advanced its maintenance schedule.

5.1.4 Cold readout

The cold part of the readout circuit consisted of a pickup structure in the central bore of the magnet, twisted pair wiring from pickup to amplifier, a two-stage SQUID current sensor/amplifier, and cabling to bring the signals to the room-temperature electronics. The SQUIDs and cabling to room temperature remained the same between the two physics runs, but everything upstream of the SQUIDs was replaced after run 1 to improve the detector's sensitivity.

For both runs, we used commercial SQUIDs from Magnicon [146] in a two-stage configuration controlled with their XXF-1 electronics in flux-locked loop (FLL) feedback mode [147]. This setup had a linear response over dynamic range $\pm 11\text{ V}$ ($\sim \pm 8.5\Phi_0$) and was spec'd to achieve a typical noise floor of $\sim 0.8\mu\Phi_0^2/\text{Hz}$ at 4.2 K^5 . Both stages resided in a single superconducting can to protect the sensitive electronics from ambient magnetic fields.

In run 1, we mounted the SQUIDs to the still plate, achieving an operating temperature of 870 mK . We operated with the SQUIDs with a flux-to-voltage conversion of $\partial V / \partial \Phi_S = 1.29\text{ V}/\Phi_0$, chosen to maximize signal gain while preventing environmental noise from railing the SQUID electronics. In run 3, we moved the SQUIDs to the mixing chamber plate, reducing the total wiring length and reducing the SQUID operating temperature to 450 mK , which lowered the noise floor. We were also able to increase the flux-to-voltage gain to $4.3\text{ V}/\Phi_0$.

Run 1 pickup circuit

The first iteration of ABRACADABRA-10 cm's pickup inductor was a wire loop, as shown in Figure 5.4, centered inside the magnet toroid. The wire was a continuous piece of solid NbTi with wire diameter 1.0 mm wrapped around a PTFE (polytetrafluoroethylene, i.e. Teflon) cylinder of diameter 4 cm . Outside of the loop, the wire was twisted together, passed beneath the magnet, and then outside of the superconducting shield. Inside the shield, the wire was threaded through a plastic tube to electrically isolate it from nearby conductors. Outside the shield, we enclosed it in a stainless steel mesh sleeve.

⁵Magnicon designed our SQUID package to have better performance at $< 1\text{ K}$ temperatures, but never formally characterized them below 4 K . Because we ran the SQUIDs at sub- 4 K temperatures, the expected noise floor was thus lower than spec.

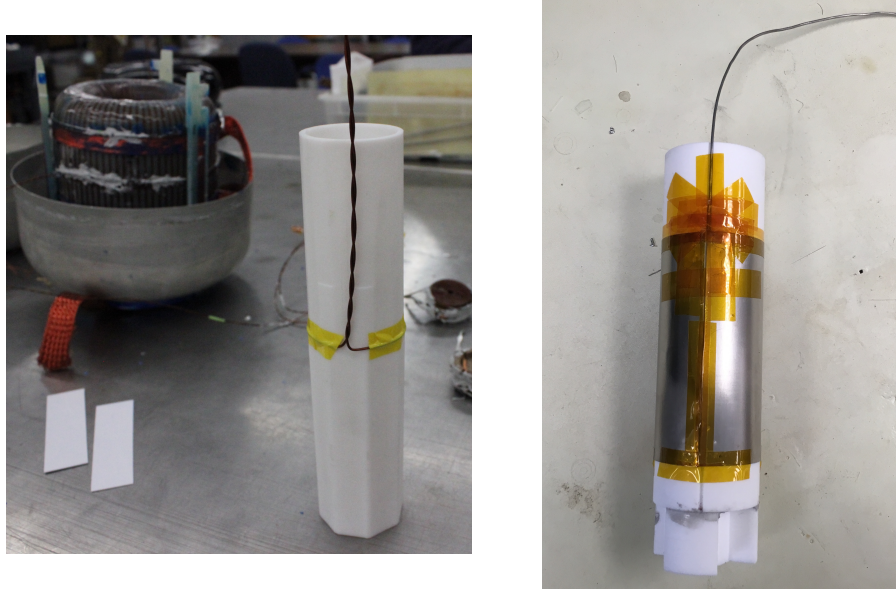


Figure 5.4: The pickup structures for the first, *left*, and second and third, *right*, physics runs. The run 1 structure is a 1 mm-diameter solid NbTi wire wound around a Teflon cylinder. After passing outside the superconducting shielding, the twisted wires are soldered and crimped to a smaller, 75 μm -diameter twisted pair of solid NbTi. The runs 2 and 3 pickup was constructed from a 150 μm -thick Nb sheet wrapped into a cylinder shape around a Teflon tube. The same NbTi twisted pair wiring was spot-welded to the upper corners of the Nb sheet, three welds per wire for redundancy. The connection was mechanically supported with Teflon tape applied over the welds.

Approximately 15 cm above the shield gap, we joined the wires to a twisted pair with a smaller gauge, 75 μm -diameter perfluoroalkoxy (PFA)-insulated solid NbTi. To assure that the entire circuit remained superconducting (to reduce signal loss and Johnson noise), we made the connection by crimping the wires together inside hollow, superconducting (PbSn) solder capillary [148]. We crimped the joint to break through the oxide layer. The thin NbTi wires above the joint ran through longer hollow superconducting solder capillaries for approximately 1 m before entering the first stage SQUID can.

The inductances of each element of this circuit are compiled in Table 5.1. The pickup structure inductance, $L_p \approx 95 \text{ nH}$, and SQUID input inductance, $L_{in} \approx 150 \text{ nH}$, were chosen to be close to each other to facilitate

an impedance match (in order to maximize the transferred signal power [149]). We later realized that our optimization was not ideal, as it did not fully take into account the rest of the readout circuit. A particular issue is that we neglected to include the parasitic inductance of the wiring, L_Q , in our optimization. Although we did not simulate or measure this parasitic inductance on its own, by calibrating the system and extracting a total gain, we determined that the total pickup circuit inductance, L_T , was approximately $1.6 \mu\text{H}$, far higher than the sum of L_p and L_{in} . As can be seen from Equation (4.20), this increase led to a reduction in SNR by a factor of ~ 6 .

The geometric factor for run 1 was $\mathcal{G} \approx 0.027$, which characterizes the overlap of the magnetic field strength with the magnet volume as well as how well-coupled the pickup structure is to the axion current (see Section 4.2.1 and Appendix A for more details on the meaning of \mathcal{G}). The magnetic volume is the same for all runs, but the strength of the transformer inductive coupling from the axions to the pickup changes with the pickup geometry. This was the main improvement between runs 1 and 3. \mathcal{G} was calculated based on simulations of the geometry run in COMSOL (see Appendix B).

Run 3 pickup circuit

To improve the experiment's sensitivity in run 3, we replaced the pickup inductor and wiring based on the optimization of simulated designs (Appendix B). As shown on the right side of Figure 5.4, the new pickup structure was constructed from a $150 \mu\text{m}$ -thick niobium sheet wrapped around a polytetrafluoroethylene (PTFE) cylinder. The cylinder's height and diameter were 10 cm and 5.1 cm respectively. The new geometry decreased the pickup's self inductance ($L_p \approx 20 \text{ nH}$) while improving its coupling to the axion current, J_{eff} . The improved coupling is reflected in the increased $\mathcal{G} \approx 0.031$.

We removed the lower section of thick NbTi wiring and used a much shorter section of the upper, solder-shielded thin NbTi twisted pair. Thus we had a shorter length and lower per-unit-length inductance, reducing L_Q . Simulations of the wire estimated $L_Q \approx 288 \text{ nH}$ for the $\sim 57.5 \text{ cm}$ of readout wiring. Calibration data indicated that the true parasitic inductance was higher by a factor of ~ 1.8 ; this may be due to imprecision in constructing the twisted pair or to additional parasitic impedance in the joints. As discussed above, shortening the wires required us to move the SQUID amplifier to a

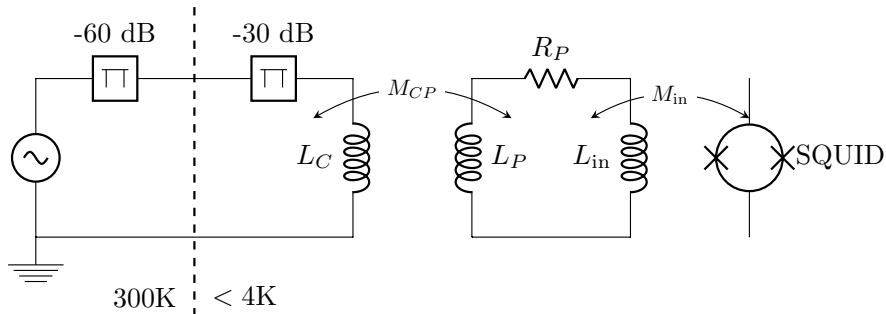


Figure 5.5: Run 1 calibration circuit, readout not shown.

lower plate in the fridge, resulting in a lower SQUID noise floor as well. Together, these improvements resulted in a gain in sensitivity to $g_{a\gamma\gamma}$ of ~ 3 over most of our frequency range.

5.1.5 Warm electronics

Run 1

The warm electronics for ABRACADABRA-10 cm's run 1 had two distinct parts: the readout and calibration systems. The calibration and cold part of the readout is shown in the circuit diagram of Figure 5.5

Readout ■ In run 1, the output of the SQUID amplifier ran through the Magnicon controller electronics boxes and a series of filters to an AlazarTech 9870 8-bit digitizer [150] clocked to a Stanford Research Systems FS725 rubidium frequency standard [151]. We operated the digitizer at the minimum voltage range, ± 40 mV, achieving a baseline digitizer noise floor of 3.5×10^{-9} mV 2 /Hz at our sampling rate of 10 MS/s across most of our frequency range. The filters consisted of a 10 kHz high-pass filter (HPF) and 2.5 MHz low-pass filter (LPF); the former prevented the high levels of noise below ~ 20 kHz (see Section 5.3.2) from entering and railing the digitizer and the latter prevented signal aliasing.

Calibration ■ The ABRACADABRA-10 cm detector response was measured using a full end-to-end calibration (see Section 5.3.1). A Stanford Research

Systems SG380 signal generator (clocked to the same rubidium frequency standard) delivered sinusoidal signals to mimic the axion's signature [151]. The signal generator was connected to a BNC feedthrough at the top of the fridge and then to a RG196 coax cable in the cold region, which connects to the calibration loop threaded through the magnetic field region. Note that we used 60 dB of room temperature attenuation and 30 dB of cold attenuation on the 4 K stage to reduce the calibration signals to levels that would not rail the SQUIDS or warm up the fridge. During running, we $50\ \Omega$ -terminated the vacuum feedthrough.

Updates for run 3

The improved $g_{a\gamma\gamma}$ sensitivity of the run 3 readout also increased the experiment's sensitivity to environmental noise. These elevated noise levels were too high to be able to run the warm electronics in the same configuration as run 1—the SQUIDS themselves were saturated. In particular, as we discuss in more detail in Section 5.3.2, vibrations at low frequencies delivered orders of magnitude more power than backgrounds in our frequency range of interest (ROI). The result was a dynamic range problem; tuning the SQUIDS to large voltage swings from vibrations would make any tiny axion signal invisible. In run 1, we could add a HPF after the SQUID electronic to prevent the digitizer from railing, but that would not affect the noise on the SQUID. Any sort of filtering to the signal before the SQUIDS would add unmanageable amounts of noise and reduce our signal sensitivity. We did not try adding filtering between the SQUIDS and their electronics box; adding elements in between would be challenging from the perspective of impedance matching and noise.

To combat this problem, we implemented a warm feedback system that took the SQUID output, transformed it, and fed signals back onto the pickup cylinder via the calibration loop. This system was possible because the majority of the noise was much lower in frequency than the signal region; we used a Stanford Research Systems SIM960 analog PID controller [151] in combination with a 1 kHz LPF on its output to guarantee that it did not interfere with the ROI. A circuit diagram is shown in Figure 5.6. In order to keep the calibration and running circuits identical enough to have the calibrations be accurate, we connected these systems with power combiners and splitters (shown in orange). Again, during running we removed the signal generator from the circuit, instead terminating its input to the power com-

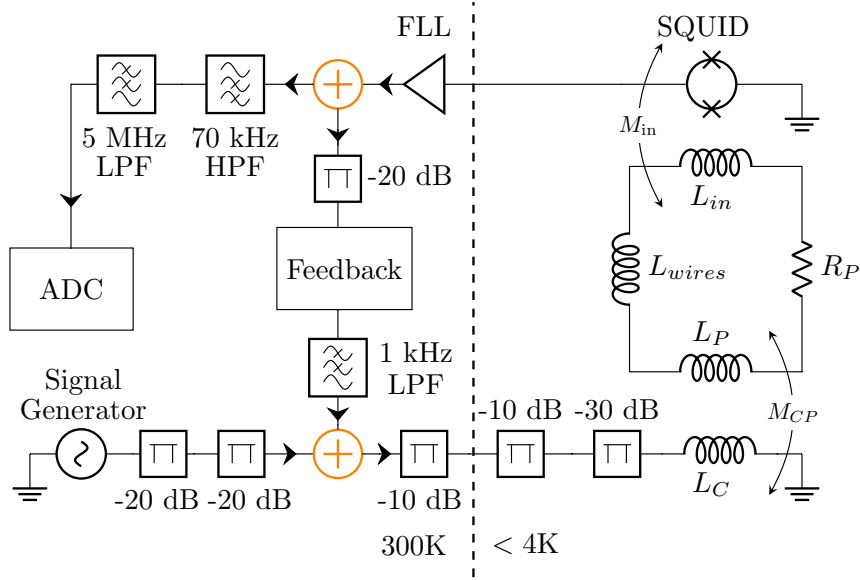


Figure 5.6: Diagram of the run 3 calibration and readout circuit. The box marked ‘Feedback’ is the PID controller. The PID’s output ran through a 1 kHz LPF before being added back into the calibration system, preventing any possible interference of the PID in the frequency range of interest. The configuration shown is used for calibration; the run configuration is identical up to replacing the signal generator and attenuators on the input to the (orange) power combiner with a $50\ \Omega$ terminator.

biner with a $50\ \Omega$ terminator.

With this system, we were again able to operate the digitizer with a $\pm 40\text{ mV}$ input range and operate the SQUIDs with an increased flux gain of $4.3\text{ V}/\Phi_0$.

5.2 Data processing and physics runs

During the run, the lab remained closed and unoccupied, with the exception of every ~ 2 weeks when we entered to refill the nitrogen dewar holding the cold trap. We left all electronic devices outside the lab and left as soon as the fill was complete.

The ABRACADABRA-10 cm data is collected as a time series of voltages, sampled at 10 MHz (e.g. 10 MS/s) with 8-bit precision. The signal, however, is a peak in frequency space at the axion mass, so what we would like to do is

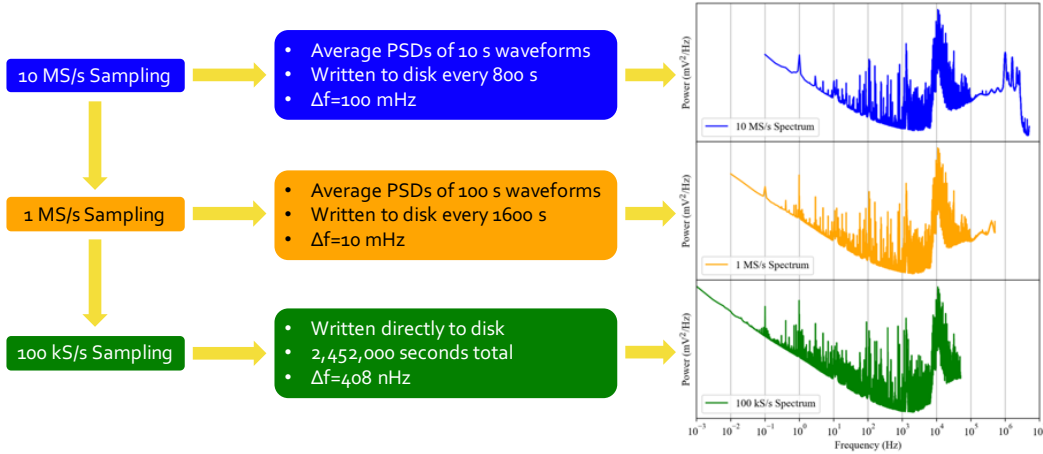


Figure 5.7: Data processing flow chart for the ABRACADABRA-10 cm data acquisition (DAQ). Image credit: J. Ouellet.

take a Fourier transform and run the search in frequency space. One way to do this would be to save all the data as a time series and then perform a huge discrete Fourier transform (DFT) offline after the run was complete. Unfortunately, for a \sim month-long run, this would lead to saving and operating on hundreds of TB of data, something which was out of reach for us computationally. Instead, we implemented a novel, on-the-fly method to transform and save our data.

The method is based on multiple stages of downsampling and transforming, shown in Figure 5.7. The original, 10 MS/s time series data follows two paths:

1. 10 s buffers (of 10^8 samples each) are DFT'd into a PSD via FFTW [152] and then saved in memory. Each subsequent 10 s buffer is transformed and then averaged with the previous PSD (s) for 800 s. The resulting average is saved to disk as a single spectrum we call $\bar{\mathcal{F}}_{10\text{M}}$. $\bar{\mathcal{F}}_{10\text{M}}$ has Nyquist frequency $f_N = 0.5 \times 10 \text{ MHz} = 5 \text{ MHz}$ and frequency resolution $\Delta f = 1/10 \text{ s} = 100 \text{ mHz}$. With this frequency resolution, we can resolve axion signals (with $\Delta f_a/f_a \approx 10^{-6}$) down to $f_a = \Delta f/10^{-6} = 100 \text{ kHz}$ with at least one bin. In practice, we use this data stream to search the range 500 kHz–5 MHz.
2. In parallel, the 10 MS/s data stream is downsampled by a factor of 10 to a 1 MS/s time series saved in memory in 100 s buffers (still 10^8 sam-

ples per buffer). This data then undergoes the same DFT and averaging process, this time being saved to disk after 16 averages (or equivalently 1600 s). This PSD, $\bar{\mathcal{F}}_{1M}$, has $f_N = 500$ kHz and $\Delta f = 10$ mHz, reaching $f_a \in [10, 500]$ kHz with minimum one bin resolution. We use the $\bar{\mathcal{F}}_{1M}$ data to search below 500 kHz.

In the first run of ABRACADABRA-10 cm, we further downsampled the 1 MS/s data to create a time series with sampling rate 100 kS/s, which was written directly to disk as a 2.45×10^{11} S stream. After the run, we could have applied a DFT to the long time series to create $\bar{\mathcal{F}}_{100k}$ with $\Delta f \approx 408$ nHz. Theoretically, this data could search for axions down to $f_a = 1$ Hz. However, the data ended up not being used because of excess low-frequency noise, for which reason we decided not to save this stream in run 3.

Our downsampling method consisted of averaging ten sequential time bins and saving the average as a single bin. Then the following ten time bins are averaged and saved, and so forth. The full data acquisition process used a write rate of 12.4 Mbps (clocked with the run 1 procedure including the final $\bar{\mathcal{F}}_{100k}$ step), which was manageable with our desktop PC, olaf1.

In run 1, we collected data with the magnet on continuously from July 16, 2018 to August 14, 2018, giving us a total integration time of $t = 2.45 \times 10^6$ s. After physics data taking was complete, we did a two week-long run in the same configuration except with the magnet off, used for vetoing backgrounds (see Section 5.3). The combined runs resulted in 3.8 TB of stored data.

In run 3, we collected magnet-on data non-continuously from June 5 to June 29, 2020 with $t \approx 430$ h. A series of DAQ crashes prevented continuous running, but this did not hinder our analysis. Once again, after the run was complete, we took data with the magnet off. In between these two physics runs, we took uncalibrated ‘run 2’ data partway through detector upgrades. Although not used for setting limits, 10% of the run 2 data was used to tune our analysis procedure in order to run a blind analysis for run 3.

After processing, the data was stored on the olaf1 DAQ computer as well as on multiple backups. Every 24 hours during running, an automatic script transferred the data files to long-term storage on an off-site cluster. In run 1, we used the University of Michigan’s Great Lakes cluster and for run 3, we used UC Berkeley’s Lawrencium cluster, each of which were also used for analysis post-run. After each run, the data was also backed up on external hard drives in the lab.

5.3 Data analysis

There are three critical components to converting the raw PSDs to limits on $g_{a\gamma\gamma}$ (or to the discovery of an axion in the data): calibrating the detector response, removing noise contamination, and running a statistical analysis of the clean data. This section covers these topics and then presents the results from the analysis of runs 1 and 3.

5.3.1 Calibration

The primary purpose of the calibration is to convert the saved PSD in units of mV²/Hz to an equivalent axion-photon coupling, $g_{a\gamma\gamma}$, in units of GeV⁻¹. Secondly, we would like to check that our understanding of the detector response matches the real system, confirming that everything is working as expected. The ideal way to achieve these goals would be to inject an axion of known coupling strength and observe the strength of the digitized signal, i.e. measure $\partial V_{\text{ADC}} / \partial I_a$. Unfortunately, we have no way to use an actual axion to do this, so we must make do with a fake axion: a sinusoidal current on a wire in the magnetic field region. Because the signal is artificial, we have to account for how the signal differs from a real axion, namely its geometric distribution and the electronics that provide the signal. The full calibration circuits are shown in Figures (5.5) and (5.6) for runs 1 and 3 respectively.

We can break down the detector response to an axion signal as

$$\frac{\partial V_{\text{ADC}}}{\partial I_a} = \frac{\partial V_{\text{ADC}}}{\partial V_{\text{SQUID}}} \cdot \frac{\partial V_{\text{SQUID}}}{\partial \Phi_p} \cdot \frac{\partial \Phi_p}{\partial I_a}, \quad (5.1)$$

where the left-hand side (LHS) is the change in voltage on the digitizer, V_{ADC} , per unit change in axion current, I_a (the effective current density integrated over the magnetic field region). Each term on the right-hand side (RHS) represents a portion of the detector. The first term is the gain of the post-amplifier electronics (with V_{SQUID} the SQUID output voltage). The second term is the flux-to-voltage conversion of the readout circuit, with Φ_p being flux through the pickup structure. The final term is the amount of flux we expect on the pickup from a given axion current (which is identical to M_{ap} as defined in Appendix A).

Similarly, the response to a calibration signal is

$$\frac{\partial V_{\text{ADC}}}{\partial V_{\text{SG}}} = \frac{\partial V_{\text{ADC}}}{\partial V_{\text{SQUID}}} \cdot \frac{\partial V_{\text{SQUID}}}{\partial \Phi_p} \cdot \frac{\partial \Phi_p}{\partial I_C} \cdot \frac{\partial I_C}{\partial V_{\text{SG}}}. \quad (5.2)$$

The LHS is now the change in digitizer voltage per unit change in signal generator output voltage, V_{SG} . The first and second terms on the RHS are identical to those of Equation (5.1), because the detector response to any source of flux on the pickup structure is the same. The third term is the ratio of flux on the pickup to source calibration current, I_C . The term would be identical to the third term of Equation (5.1), except that the fake axion is confined to a wire in the sensitive region whereas the real axion is distributed according to the magnetic field strength. The final term converts the measurable output voltage of the signal generator and converts it into the resulting calibration current.

Checking the detector response requires confirming that the LHS and RHS of Equation (5.2) match, and converting our limits requires determining the LHS of Equation (5.1). I will first discuss the former, which will give us the tools to calculate the latter.

Checking the detector response

The LHS of Equation (5.2)—the total gain of the system from signal generator to digitizer—is directly measurable. Following the schematic of Figure 5.5 (run 1) or Figure 5.6 (run 3), we attached the output of a signal generator to the fridge and applied a series of sinusoidal signals with varying amplitude and frequency. We collected this data using similar digitizer software as for the run, as described in Section 5.2. By measuring the peak height in the resulting PSD, we can calculate $\partial V_{ADC} / \partial V_{SG}$. We used the nominal peak-to-peak output voltage of the signal generator for V_{SG} , which we checked was accurate in independent tests.

The first term on the RHS of Equation (5.2), $\partial V_{ADC} / \partial V_{SQUID}$ —the gain of the ‘post-SQUID’ circuit from the output of the SQUID electronics to the DAQ input—was determined with a direct calibration of the warm electronics and sanity checked with an analytic circuit calculation. The plotted gains of the post-SQUID electronics chains for runs 1 and 3 are shown in Figure 5.8.

The second term, $\partial V_{SQUID} / \partial \Phi_p$, contains two distinct parts of the circuit: the SQUID response to a given input current and the readout circuit’s response to an incident magnetic flux,

$$\frac{\partial V_{SQUID}}{\partial \Phi_p} = \frac{\partial V_{SQUID}}{\partial I_p} \cdot \frac{\partial I_p}{\partial \Phi_p} \quad (5.3)$$

In Equation (5.2), we combined these two parts into a single term, because it is the combination that sets the SNR of the system.



Figure 5.8: Gain curves from post-SQUID electronics chain calibrations ($\partial V_{\text{ADC}} / \partial V_{\text{SQUID}}$), run 1 (top) and run 3 (bottom). The strange shape of the run 1 gain curve at low frequencies comes from using a 50Ω input impedance to the 10 kHz filter, which was designed to have a high output impedance. Because most of this behavior is outside our frequency range and we can calibrate the response, this is unimportant. In run 3, we swapped the HPF to one with a 70 kHz roll-off that was spec'd for a 50Ω input and output impedance.

The first, SQUID response part of Equation (5.3) we can calculate using the SQUID specification parameters measured and reported by Magnicon,

$$\frac{\partial V_{\text{SQUID}}}{\partial I_p} = \frac{R_f}{M_f} M_{\text{in}} \quad (5.4)$$

R_f and M_f are the FLL feedback resistance and mutual inductance, and M_{in} is the SQUID input mutual inductance. A simplified diagram of the SQUID circuit is shown in Figure 5.9, showing how the feedback circuit backreacts onto the input. For more details about how FLL operation works, see [147, 153].

The second part of Equation (5.3) (the flux-to-pickup current conversion)

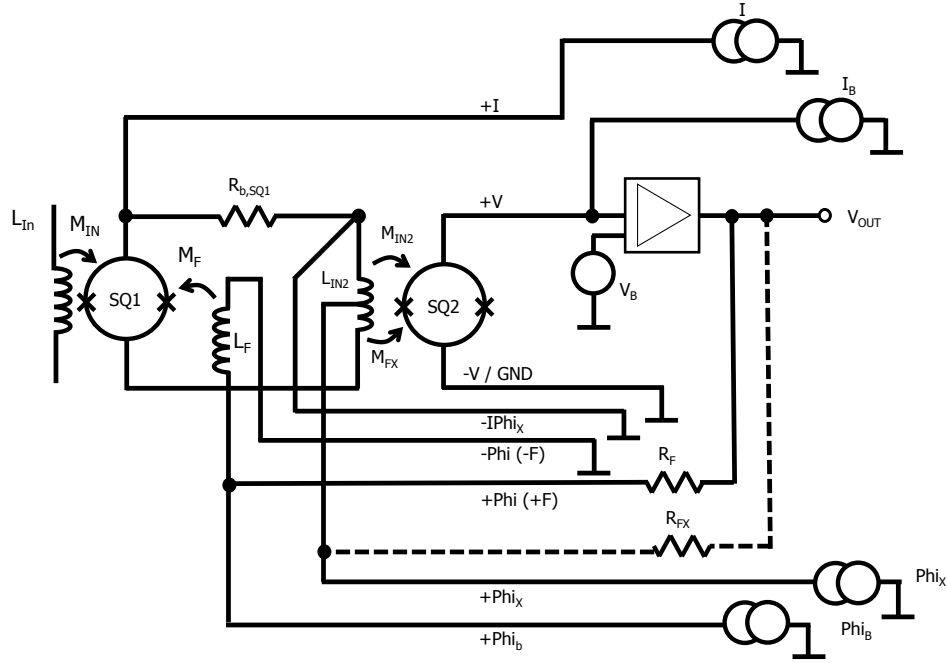


Figure 5.9: Diagram of the 2-stage SQUID used for ABRACADABRA-10 cm data collection, from Magnicon [146]. The feedback loop that controls the SQUID gain in FLL mode is marked with R_f , the tunable feedback resistance, and M_f and L_f , the feedback's mutual and self-inductance. The feedback is applied directly to the first stage SQUID.

is challenging to calculate purely analytically, because the readout circuit was hand-made, rather than having parts of known impedance. The pickup circuit can also only operate while cold, preventing a direct measurement with our setup. In run 1, we used an analytic approximation of the circuit with the SQUID specification value for L_{in} and an analytically calculated value for the inductance of the pickup loop. This method resulted in a misestimation of the system gain by a factor of 6.5, as we discuss further below. In run 3, we improved the calculation by including parasitic inductance in the wiring, estimated using electromagnetic field simulations of the twisted pair with COMSOL. The simulations are described in further detail in Appendix B.

Returning to the overall gain in Equation (5.2), the third term, $\partial\Phi_p/\partial I_C$,

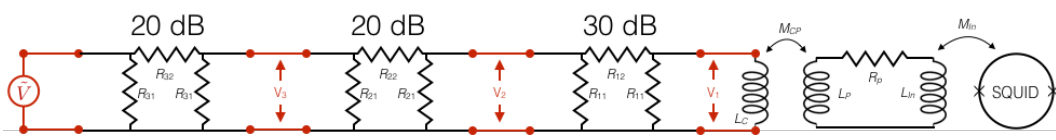


Figure 5.10: Calibration-pickup circuit diagram used to calculate the calibration current response to a signal generator voltage input, credit J. Ouellet. The attenuator values shown are not accurate to both runs; see Figures (5.5) and (5.6) for correct values.

describes the magnetic flux through the pickup structure from a calibration current. This response cannot be measured directly, so instead we calculated the term using COMSOL (Appendix B).

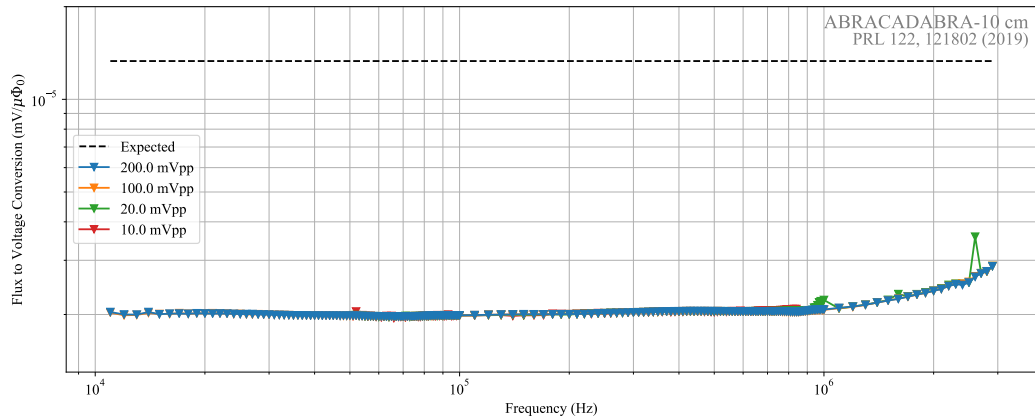
Equation (5.2)'s fourth term, $\partial I_C / \partial V_{SG}$, which is a simple passive circuit, could be fully analytically calculated based on the diagram of Figure 5.10. We also independently measured the transfer function of the warm components to check that they met specifications across our frequency range.

In practice, rather than comparing the LHS of Equation (5.2) to its RHS, we compare the second term of the RHS—the pickup flux-to-voltage conversion—to the LHS divided by the remaining terms:

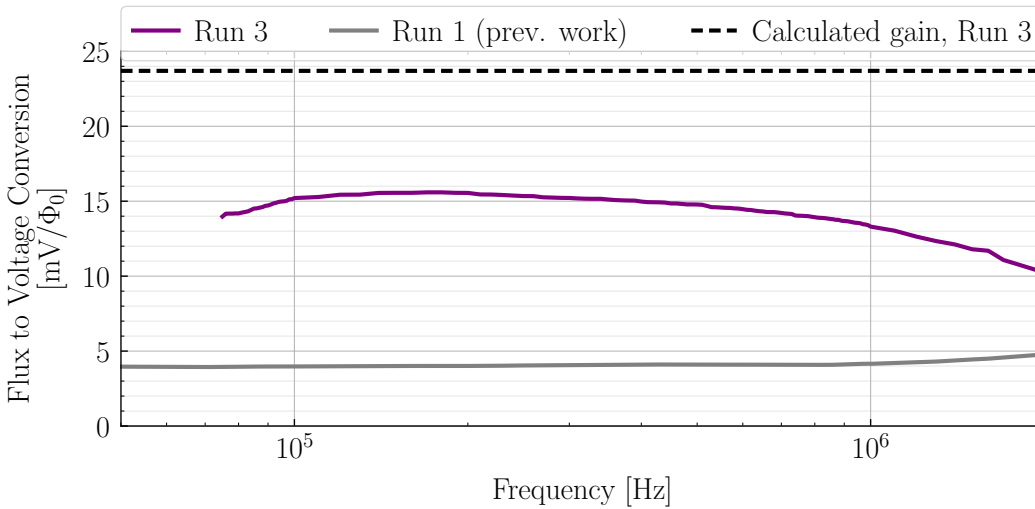
$$\frac{\partial V_{SQUID}}{\partial \Phi_p} ? = \frac{\frac{\partial V_{ADC}}{\partial V_{SG}}}{\frac{\partial V_{ADC}}{\partial V_{SQUID}} \cdot \frac{\partial \Phi_p}{\partial I_C} \cdot \frac{\partial I_C}{\partial V_{SG}}} . \quad (5.5)$$

The reason for using this term as our metric is two-fold. First, the second term is the one that determines the SNR of the experiment—the most important indicator of the experiment's sensitivity—and thus is the most useful point of comparison between different run configurations or different experiments. Secondly, we cannot directly measure $\partial V_{SQUID} / \partial \Phi_p$; instead, we compare its calculated expectation value to its ‘measurement’ via the other, measurable terms.

This comparison is shown for runs 1 and 3 in Figure 5.11. In run 1, our calculation of the expected flux-to-voltage gain was higher than measured by a factor of ~ 6.5 . The difference was a result of failing to account for parasitic impedance in the wiring between the pickup loop and the SQUID input. Including this effect in our calculations for run 3 improved the match, with a difference factor of ~ 1.8 . The difference can be attributed to additional, uncharacterized impedance in, e.g. the wire connections to the cylinder.



(a) Flux-to-voltage conversion in run 1, from [131]. The calibrations are linear over most of the frequency range and consistent between different input amplitudes.



(b) Flux-to-voltage conversion in run 3, from [139]. The run 1 conversion is also plotted, showing the improved sensitivity after the upgrades.

Figure 5.11: Flux-to-voltage gain in runs 1 and 3, comparing the calculated and measured values. The gain is reported as conversion from pickup flux to SQUID output voltage.

In addition to showing the improved prediction, the run 3 conversion plot shows the sensitivity improvement achieved with the readout upgrades.

Converting our limits

In order to convert our limits from units of digitizer voltage to units of axion effective current, we need to have a measurement of Equation (5.1). The first two terms on the RHS, the post-SQUID circuit response and the flux-to-voltage conversion, are identical with an axion or calibration source signal, so we can use the measurements from the previous section. Note that, as discussed above, the flux-to-voltage conversion is not measured directly, but extracted from system measurements with Equation (5.2). The final term is determined using the same type of COMSOL simulation as used for the current-to-flux response of the third term of Equation (5.2). Once the data is converted into an equivalent I_a , we can use the distribution of the magnetic field, axion physics (Equation (4.4)), and knowledge of the galactic dark matter velocity distribution to get $g_{\alpha\gamma\gamma}$.

5.3.2 Noise and data cleaning

The limiting source of noise in a broadband lumped-element experiment is amplifier noise. ABRACADABRA-10 cm’s SQUID amplifiers could achieve a flux noise floor of $\lesssim 1 \mu\Phi_0/\sqrt{\text{Hz}}$. In run 1, the detector reached its fundamental noise floor over a wide range of frequencies, shown in Figure 5.12. In run 3, the increased sensitivity of the readout circuit magnified other backgrounds above the SQUID noise floor. In both runs, there were significant backgrounds that needed to be cleaned from the data before running the analysis. Although the run 1 procedure was not blind, we had a fully blind data cleaning and analysis pipeline for run 3 that we tuned on a subset of uncalibrated run 2 data. After the completion of run 3, we did a systematic study of the noise backgrounds with the goal of cataloguing relevant sources in preparation for DMRadio. In this section we discuss the backgrounds observed during the runs and the cleaning procedures we used to handle them, as well as backgrounds measured during the post-run 3 noise investigation.

Low frequencies—vibrations

In both runs, the low-frequency end of the ABRACADABRA spectrum was dominated by vibrational backgrounds, appearing as a stochastic

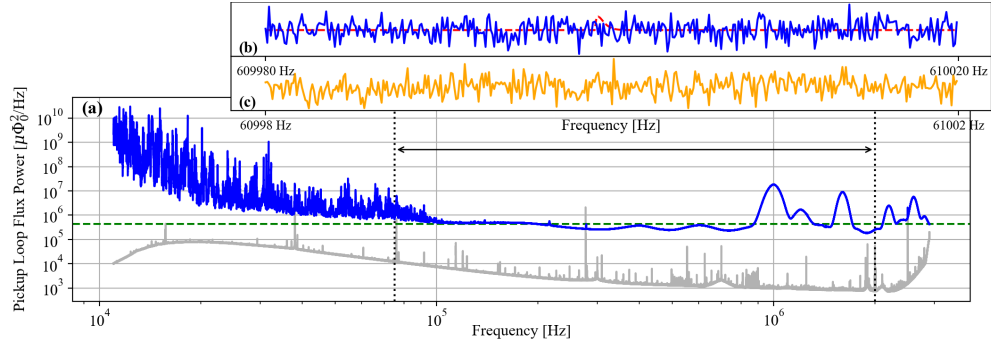


Figure 5.12: Averaged spectrum, in blue, of the run 1 data in units of pickup flux, from [138]. The green dashed line is the approximate noise floor of the SQUIDS and the grey spectrum is the digitizer noise floor. The inset shows a zoomed view of the 10 MS/s data (top, blue) and 1 MS/s data (bottom, orange) over a small range. The red dashed line shows a reference signal at the 95% upper limit.

background rising with falling frequency. We determined that much of this low-frequency noise was mechanical in origin by measuring their correlation with accelerometer data. We affixed an accelerometer to the top plate of the fridge (in atmosphere), oriented either horizontally or vertically. By concurrently taking data from the SQUIDS and the accelerometer in one of the two configurations, we could determine correlations in the pickup spectrum with x - y - and z -vibrations, shown in Figure 5.13 for run 1. There was a significant degree of correlation up to frequencies measurable by our accelerometer, and we believe that the vibrational noise continued up to higher frequencies until it becomes subdominant to the SQUID flux noise at ~ 100 kHz.

Any ambient magnetic fields that vibrate through the pickup structure generate current signals at their oscillation frequency. The ambient fields can be environmental—Earth’s field or anthropogenic—or can stem from the toroidal magnet. To first order, the toroidal field is contained inside the doughnut of the doughnut, but fringing naturally happens in the gaps between the wire windings and from the wire connections between the three sections of the toroid. The pickup cylinder for run 3 had a larger diameter than the run 1 pickup loop, and so we expected that more pickup of vibrating fringe fields was likely. To counteract some of this effect, we attempted to stabilize the pickup and magnet relative to each other, reducing relative motion, by clamping the pickup’s mounting cylinder firmly to the shielding can holding

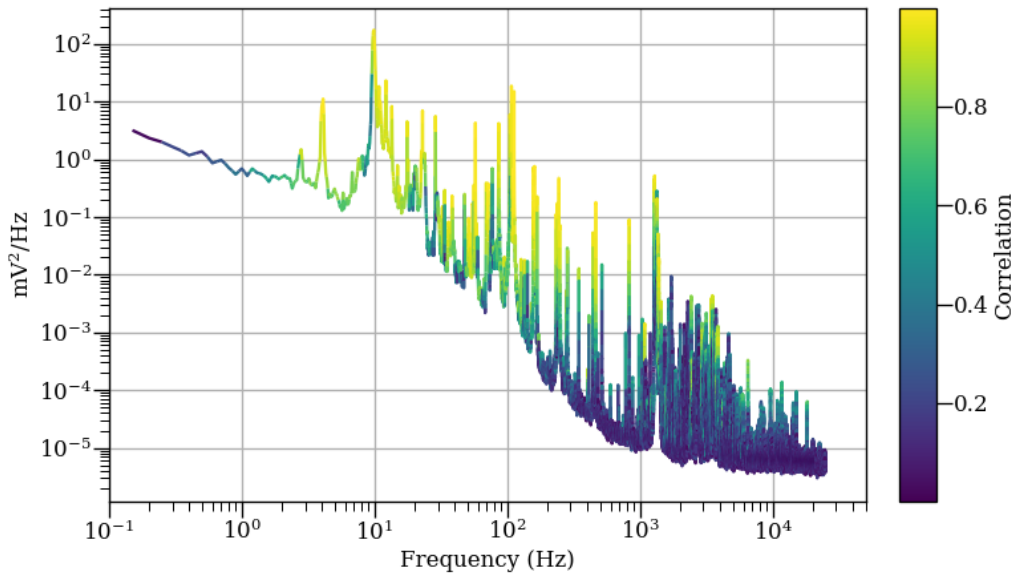


Figure 5.13: Data from the SQUID output with the detector in the run 1 configuration with color marking correlation with data taken from an accelerometer measuring motion in the z (vertical) direction. The accelerometer loses accuracy above ~ 450 Hz, but below that shows a significant degree of correlation. We believe the vibrational spectrum continues with decreasing magnitude to higher frequencies, falling beneath the SQUID noise floor.

the magnet. Even with this modification, we saw significant backgrounds that correlated with the magnetic field strength, shown in Figure 5.14.

The rising vibrational backgrounds at low frequencies were too spiky to be able to successfully apply a bump-hunting procedure for the axion signal, so we excluded the low end of our frequency range from the analysis in both runs, cutting at 75 kHz (100 kHz) in run 1 (3).

High frequencies—electromagnetic interference

Throughout the spectrum, but particularly at higher frequencies, we saw considerable EMI with a variety of signatures. We were able to identify the sources of some, but not all of the EMI backgrounds. Generally, they are characterized by sharp peaks, and many have clear features such as a temporal dependence or a regular spacing that provide a way to discriminate from an axion signal.

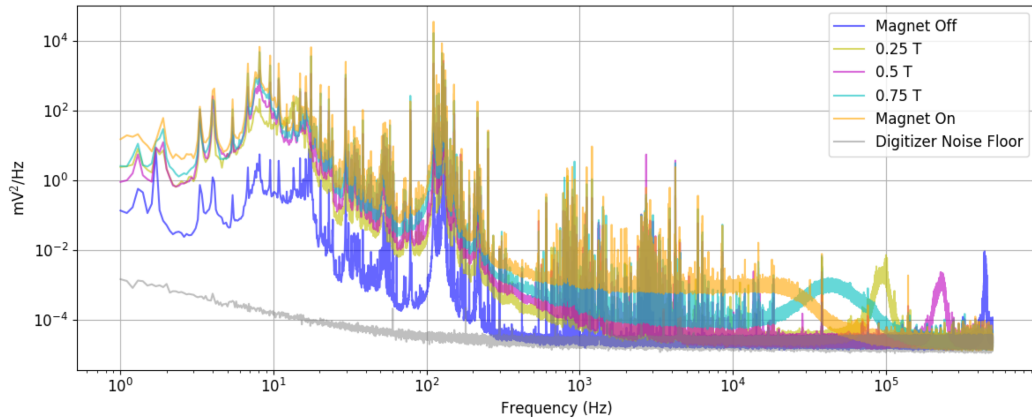


Figure 5.14: The low-frequency vibrational backgrounds tracked with the strength of the toroidal magnetic field, credit: K. Pappas.

One identifiable feature was a collection of peaks corresponding to AM radio stations. An example is plotted in Figure 5.15. By demodulating the data stream offline, we could listen to the radio broadcasts. The radio lines are at known frequencies and can be individually vetoed from the data. We did this by applying a 15 Hz-wide mask centered on the radio signal peak.

There were also many unidentified transient EMI features in the run 1 and run 3 data. During run 1, there were 2-3 distinct data-taking periods with a lot of EMI peaks. There was an initial noisy period of approximately one week, followed by a few days of noisy data that coincided with us reentering the lab to refill the liquid nitrogen dewar. Shown in the top of Figure 5.16, the noise had a distinct, regularly-spaced comb structure of narrow peaks. These peaks were difficult to differentiate from a coherent axion signal in our analysis, and so we discarded the data from the noisy periods. Although distinguishing the periods was possible by eye, to prevent ourselves from biasing the sample, we set a threshold on the number of 3σ excesses. Any spectrum with ≥ 30 significant excesses was removed. Although there were less-noisy frequency ranges in the discarded spectra, this method of removal prevented us from biasing any frequency points. Any exotic models with ≥ 30 axions would no longer be probe-able after this cut, but the baseline model of one (or even a few) axions is unaffected. We retained 70% of our original exposure after discarding the noisy spectra.

The transient combs were also present in runs 2 and 3, a few examples of which are shown in Figure 5.17. These combs often had regular, base-ten

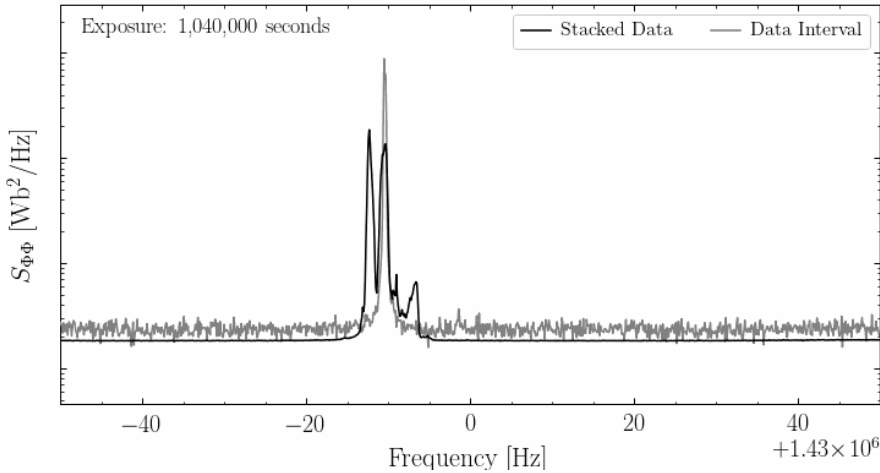
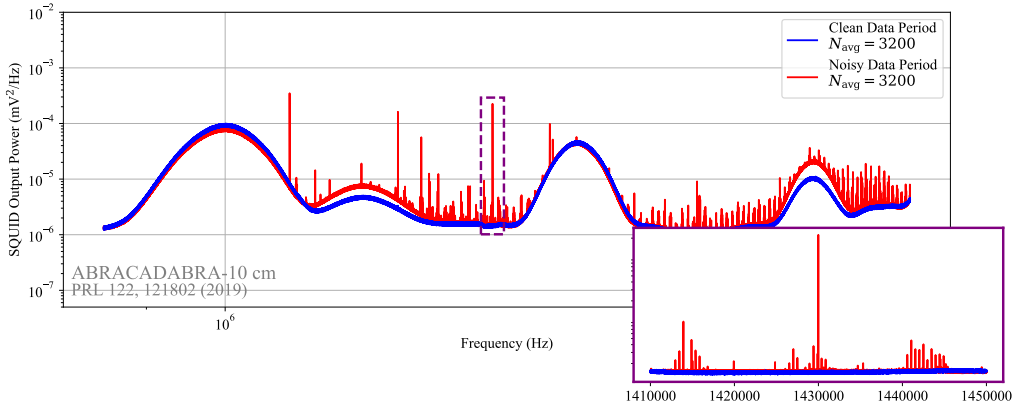


Figure 5.15: An AM radio signal in the ABRACADABRA-10 cm data, specifically WKOX “Buenas Nuevas,” a local Boston Spanish-language Christian station transmitted at 1430 kHz, credit: J. Foster. The black line is the averaged spectrum over 1.04 Ms, and the grey line is an 800 s exposure.

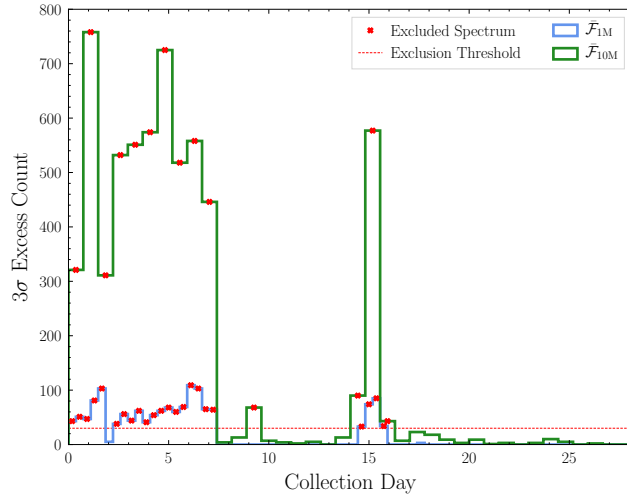
spacings like 50 Hz or 100 Hz, and many of the peaks drifted in frequency over the course of the run. Unlike in the run 1, however, there were not distinct noisy and clean time periods. Instead of simply cutting out time periods as we did in run 1, we developed a method to exclude the combs from the analysis. The peaks in the combs were almost all exactly one bin wide, much narrower than we expect for a virialized axion signal. Therefore, we were able to use a single-bin peak width as a selection cut.

The way we made this cut was with a two step procedure, first on the unstacked spectra and second on the stacked spectra used in the full analysis. With both types of data, we determined the significance of the data in each frequency bin by comparing it to the mean and standard deviation of the 10 bins on either side. We flagged any bins with $\delta\chi^2 > 100$ in the unstacked datasets and $\delta\chi^2 > 35$ in the stacked datasets. We masked the 21 frequency bins centered on each flagged bin. The reason for using this procedure on both stacked and unstacked data and for using a wide mask was to account for peaks with frequency drift and for low-power peaks that only became significant after stacking.

After the single-bin peak removal, we applied another cut to remove high-power, transient peaks. To do this, we divided the run 3 data into 22 subin-



(a) 3200 averaged spectra during a clean data-taking period (blue) and noisy data-taking period (red) credit: J. Ouellet. The noisy period spectra featured regularly-spaced combs of sharp spikes, shown in the zoomed inset.



(b) 3 σ excesses over the length of run 1 in the 10 MS/s data (green) and 1 MS/s data (blue), from [131]. There are 2-3 distinct time periods when the transient EMI created many significant excesses in the data. To avoid data contamination, we discarded all spectra with an excess count over the threshold (red dashed line).

Figure 5.16: Transient EMI in run 1.

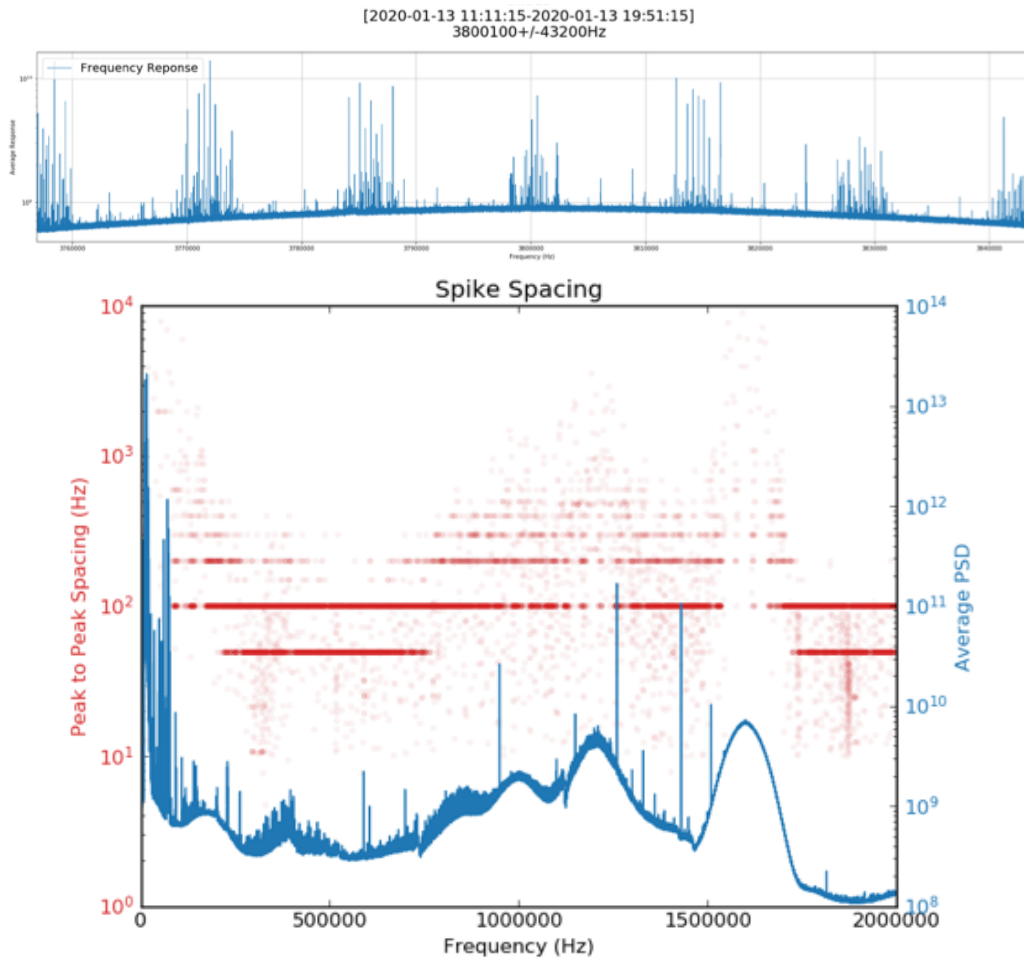


Figure 5.17: EMI combs in run 3. *Top*, a small frequency range exhibiting envelopes of spikes. *Bottom*, the full PSD plotted in blue, with the most common peak-to-peak spacing over the range shown in red. Clear patterns of 50 Hz, 100 Hz, etc. spacings are visible.

tervals in time and run the analysis, described in Section 5.3.3, to each subinterval independently. At every test axion mass, the 50% of subintervals with the lowest test statistic (TS) and all remaining subintervals with $TS < 9$ are kept and stacked to be used in the full analysis. Note that this procedure thus is guaranteed to remove no more than 50% of spectra. The single-bin and transient cuts removed a combined 3.8% of the mass points from our search.

A final way to discriminate between peaks from axion signals and peaks from environmental backgrounds is to recognize that the strength of an axion signal disappears with vanishing magnetic field, while EMI should be agnostic. We run the analysis procedure on both magnet on and magnet off data. Any look-elsewhere effect (LEE)-corrected 5σ candidate masses that are present in both datasets are removed as discoveries. The mass points are kept in the analysis for setting 95% upper limits, although they give a much-reduced limit-setting power compared to other places in the spectrum. In run 1, there were only a few such points—83 masses in the $\bar{\mathcal{F}}_{10M}$ data, 500 kHz to 2 MHz, and none in the $\bar{\mathcal{F}}_{1M}$ data, 75 to 500 kHz. There were more masses caught by this cut in run 3, $\sim 0.07\%$ of the ~ 11.1 million total mass points. The increase is in line with the increase in other noise in run 3.

Wide features

At mid to high frequencies, there were several wide bumps in frequency space that moved around with time, shown in Figure 5.18. These appear to be the result of backgrounds entering our warm electronics chain, either via the SQUIDs or the DAQ. They were wide enough features that we could simply apply our analysis procedure on top of them, albeit with a reduced sensitivity to g_{ayr} . During our noise investigation campaign after run 3, we moved all of the electronics into a server rack and applied more layers of shielding to the magnet leads, which seemed to have improved the performance. These changes included a more centralized grounding layout, which is an important consideration for DMRadio. The Olaf laboratory is next door to a server room, which likely contributed to both the wide features and the transient spikes discussed in the previous section.

Another relatively wide peak appeared in our data at 70 kHz after the upgrades for runs 2 and 3. The peak had some motion in frequency and change in amplitude over the course of the two runs and the later noise testing period. Although investigations are ongoing, it could be due to a mechanical resonance in the cylindrical pickup structure. For run 3, we cut off our search at 100 kHz due to the forest of vibrational lines, so the 70 kHz peak was not an issue.

Data cleaning pipeline

The data cleaning pipeline for runs 1, 2, and 3 is shown in Figure 5.19. In runs 2 and 3, we did an identical series of cuts. The line labeled ‘Data Clean-

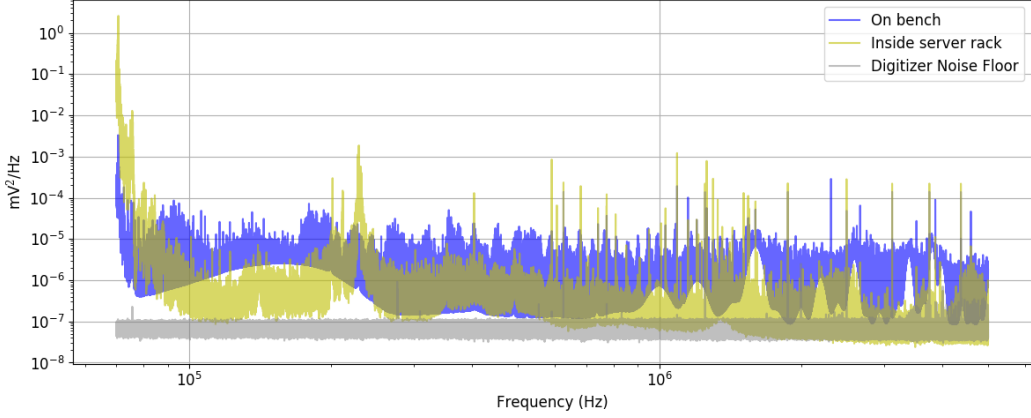


Figure 5.18: Wide frequency bumps in the ABRACADABRA-10 cm data, credit: K. Pappas. Moving the warm electronics from the lab bench to a closed server rack considerably reduced their amplitude.

ing' includes removing AM radio stations and single bin excesses with the methods described above. The cut on magnet-off peaks is shown separately. The final, nuisance tuned line will be described in the following section.

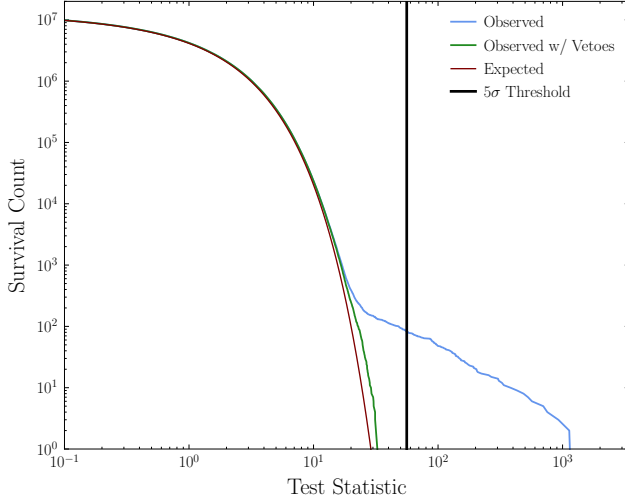
5.3.3 Statistical analysis

As discussed in Section 4.1.2, an axion signal appears in a lumped-element experiment as an oscillating current with frequency pegged to the axion's mass and distribution determined by their velocity distribution. In our baseline analysis, which follows the method outlined in [119], we assume the axions follow the SHM distribution with $\Delta f/f \sim 10^{-6}$. As described in Section 5.2, we collect a series of N_{tot} PSDs, each covering a fraction of the run length, $\Delta T = \tau_{\text{tot}}/N_{\text{tot}}$. As discussed in Section 5.2, the data was saved as two collections of averaged PSDs of different resolution, $\bar{\mathcal{F}}_{10\text{M}}$ and $\bar{\mathcal{F}}_{1\text{M}}$, each covering a time period of $\Delta T \approx 800$ s and $\Delta T \approx 1600$ s, respectively.

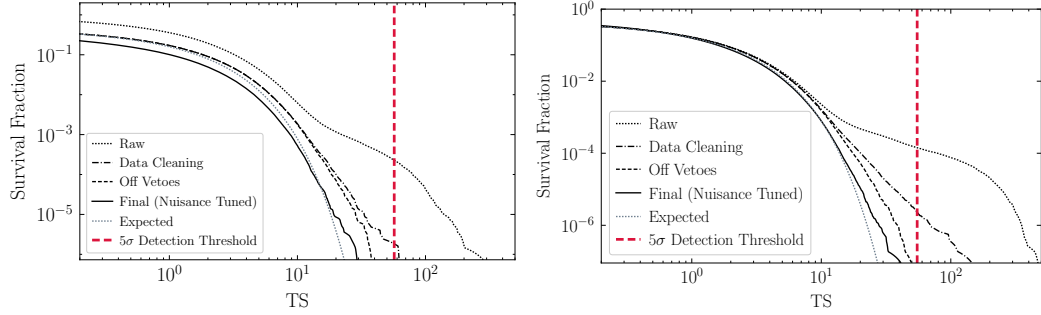
The analysis is performed on a series of \mathcal{N} stacked PSDs, made by further averaging the independent $\bar{\mathcal{F}}_{10\text{M}}$'s and $\bar{\mathcal{F}}_{1\text{M}}$'s,

$$\bar{\mathcal{F}}_k^n = \frac{1}{N_{\text{avg}}} \sum_{i=1}^{N_{\text{avg}}} \bar{\mathcal{F}}_{k,i} \quad (5.6)$$

where $\bar{\mathcal{F}}_{k,i}$ represents a single 800 s $\bar{\mathcal{F}}_{10\text{M}}$ or 1600 s $\bar{\mathcal{F}}_{1\text{M}}$ averaged spectrum, k indexes the frequency bins, $n \in [1, \mathcal{N}]$. The result is \mathcal{N} PSDs, $\bar{\mathcal{F}}_k^n$, each



(a) Data cuts and TS distribution for run 1, from [131]. The blue line is the full magnet on dataset after the noisy transient periods were removed. Green is after the magnet on peaks are vetoed. The red expectation line matches well to our data, showing that our Gaussian noise model was very accurate. No axion candidates survived the vetoes.



(b) Data cuts and TS distributions for the unblinded 10% of run 2 data, *left*, on which the procedure was tuned and for run 3, *right*, from [139]. The line marked ‘Data Cleaning’ removes AM radio stations and single bin excesses. The ‘Off’ line additionally removes peaks vetoed by the magnet off data. The nuisance parameter cut, designed to improve our fit to the expected distribution without biasing our results, is described in Section 5.3.3.

Figure 5.19: TS distributions throughout the data cleaning pipeline for runs 1, 2, and 3.

composed of N_{avg} averaged PSDs⁶. N_{avg} may float from spectrum to spectrum due to different total averaging times—the PSDs at the end of the run did not cover as long a time period as the others. In run 1, we ran the analysis on $\mathcal{N} = 53$ (24) subintervals for the $\bar{\mathcal{F}}_{10M}$ ($\bar{\mathcal{F}}_{1M}$) data. In run 2, we divided both datastreams into 20 subintervals, and in run 3, we divided them both into 22 subintervals. The division was decided by balancing computational load with the ability to let our background model vary with time.

For binned data, the expected signal power in the k^{th} bin (with frequency f_k) is $A s_k$ with

$$s_k(m_a) = \begin{cases} \frac{\pi f(v)}{m_a v} |_{v=\sqrt{4\pi f_k/m_a - 2}} & f_k > m_a/2\pi \\ 0 & f_k \leq m_a/2\pi \end{cases} \quad (5.7)$$

$f(v)$ is the SHM velocity distribution given in Equation (4.6) and $f_{\text{rest}} = m_a/2\pi$ is the frequency of an axion with zero relative velocity to us.

$$A(g_{a\gamma\gamma}) \equiv g_{a\gamma\gamma}^2 \rho_{DM} B_0^2 V^2 \mathcal{G}^2 = \langle \Phi_a \rangle^2 \quad (5.8)$$

is the parameter that controls the signal strength, and is equivalent to the time-averaged pickup flux from an axion signal with coupling $g_{a\gamma\gamma}$. Because of the statistics of the axion field (see [119]), s_k in a single PSD is exponentially distributed; for the stacked PSD, $\bar{\mathcal{F}}_k$, this becomes an Erlang distribution,

$$P(\bar{\mathcal{F}}_k; N_{\text{avg}}, \mu_k) = \frac{N_{\text{avg}}^{N_{\text{avg}}}}{\mu_k^{N_{\text{avg}}} (N_{\text{avg}} - 1)!} \bar{\mathcal{F}}_k^{N_{\text{avg}}-1} e^{-\bar{\mathcal{F}}_k N_{\text{avg}}/\mu_k}, \quad (5.9)$$

with mean μ_k and shape parameter $N_{\text{avg}} \gg 1$. Note that this expression does not take advantage of the large- N_{avg} limit via the central limit theorem, because we sample the distribution an enormous number of times (k runs to very large numbers—there are many independent m_a in our frequency range); we see the full tail shape of the Erlang.

We expect the backgrounds to be incoherent and Gaussian distributed in the time domain. Although the expected background distribution will not be constant across the entire frequency range, it varies slowly over each axion search window. In run 1, the variation was slow enough to approximate the

⁶To clarify, N_{avg} is the number of non-averaged PSDs that are averaged together in a single $\bar{\mathcal{F}}_{10M}$ or $\bar{\mathcal{F}}_{1M}$ ‘averaged PSD’ while \mathcal{N} is the number of $\bar{\mathcal{F}}_{10M}$ or $\bar{\mathcal{F}}_{1M}$ PSDs that are averaged together to make a ‘stacked PSD’ that is used as one of the final subintervals for the analysis.

background as having a constant mean over the window, $b_k = b$. In runs 2/3, the background had more variation, so we chose to characterize it with a first-order polynomial defined by the two-component vector, \mathbf{b} , which has the mean and slope of the fit as its first and second components, respectively. Accordingly, the model is $b_k = \mathbf{b}_0 + \mathbf{b}_1(f_k - m_a)$. We can cast the run 1 background model into an equivalent form by specifying $\mathbf{b} = (b, 0)$. Thus, for all runs, the combined signal plus background distribution in each bin is also Erlang distributed, with mean $\mu_k = As_k + b_k(\mathbf{b})$ and shape parameter N_{avg} .

Thus the background-related nuisance parameters for our analysis are the mean for run 1 and, for runs 2 and 3, the mean, slope, and an additional parameter, σ describing the variation of the background, which I describe below. We verified that the results of the analysis were not dependent on the size of the search window. We also allow the background to vary over the course of the run in the \mathcal{N} independent time windows: $\mathcal{B}_k = (b_k^1, b_k^2, \dots, b_k^{\mathcal{N}})$.

Run 1 likelihood analysis for discovery and limit-setting

We use a frequentist likelihood procedure to search for signals. The likelihood we use for run 1 is based on the Erlang distribution of Equation (5.9) (both the signal and background are expected to follow the Erlang distribution),

$$\mathcal{L}_{R1}(d|m_a, A; \mathcal{B}) = \prod_{n=1}^{\mathcal{N}} \prod_{k=k_i(m_a)}^{k_f(m_a)} P(\bar{\mathcal{F}}_k^n; N_{\text{avg},n}, \mu_k). \quad (5.10)$$

The likelihood is a function of three parameters: the signal position and strength, m_a and A , and the background mean, \mathbf{b} . Because the background is fixed to follow an Erlang distribution, its variation is simply a function of its mean.

To differentiate between the null, background-only hypothesis and the signal+background hypothesis, we define a test statistic (TS) from the model's log-likelihood ratio,

$$t(m_a, A) = 2 \ln \left[\frac{\mathcal{L}(d|m_a, A; \hat{\mathbf{b}})}{\mathcal{L}(d|m_a, A = 0; \hat{\mathbf{b}})} \right]. \quad (5.11)$$

Here we have profiled over the nuisance parameter \mathbf{b} to maximize the likelihood. The double hat value is the one that provide an overall optimization with nothing fixed. The single hat value in the denominator maximizes the

likelihood under the null hypothesis—for $A = 0$. Note that for the overall best fit with A not fixed to zero, generically $\hat{\mathbf{b}} \neq \hat{\mathbf{b}}$.

The discovery TS for a given m_a is the maximum value that can be attained by varying A ,

$$\text{TS}(m_a) = \max_A t(m_a, A). \quad (5.12)$$

In order to treat the TS as a χ^2 -distributed variable under Wilks' theorem, we allow A to vary to both positive and negative values. A negative best-fit for A can be interpreted as a statistical underfluctuation; there is no physical interpretation for a negative-strength axion signal. For our discovery search, we therefore fix $\text{TS} = 0$ when the likelihood is maximized for $A < 0$, giving a discovery TS following the distribution

$$p(\text{TS}) = \frac{1}{2} (\delta(\text{TS}) + \chi_{k=1}^2(\text{TS})). \quad (5.13)$$

We expect an equally likely split between under- and over-fluctuations of A , so we give equal weight to the Dirac δ function of $\text{TS} = 0$ results and the results of positive A fluctuations that follow a χ^2 distribution with one degree of freedom. By inverting the distribution of Equation (5.13), we can determine the local significance of any excess.

We apply this procedure to over 10 million mass points, and therefore must account for the look-elsewhere effect (LEE). The LEE takes into account that even if a given event has a very small probability, with enough trials, there is a large probability for it to happen. As an example, in a dataset with 10^7 independent tests, an excess that is locally significant with $p = 0.001$ is expected to occur 10,000 times even under a background-only scenario! In our frequency range, nearby windows are not independent, however, and so we must take into account their correlation. Fully accounting for the LEE and these correlations, the threshold TS for an $N\sigma$ detection is

$$\text{TS}_{\text{thresh}}(N) = \left[\Phi^{-1} \left(1 - \frac{4\nu_0^2 \Phi(N)}{3 \ln(f_{\text{max}}/f_{\text{min}})} \right) \right]^2 \quad (5.14)$$

with Φ the cumulative density function (CDF) of the normal distribution with mean zero and unit standard deviation and Φ^{-1} its inverse distribution. f_{max} and f_{min} delineate the frequency range of the search. In run 1, $f \in [75 \text{ kHz}, 2 \text{ MHz}]$, and in run 3, $f \in [100 \text{ kHz}, 2 \text{ MHz}]$. A 5σ detection thus has $\text{TS}_{\text{thresh}} \approx 56$ for run 1. Note that this equation is semi-empirical based on the SHM [119].

We define an alternative TS for setting upper limits,

$$t_{\lim}(m_a, A) = \begin{cases} 2 \ln \left[\frac{\mathcal{L}(d|m_a, \hat{A}; \hat{\mathbf{b}})}{\mathcal{L}(d|m_a, A; \hat{\mathbf{b}})} \right] & A \geq \hat{A} \\ 0 & A < \hat{A} \end{cases} \quad (5.15)$$

where again the hatted values maximize their likelihoods, and the background nuisance parameters are profiled after fixing A or \hat{A} . The $A_{95\%}$ corresponding to the 95% confidence level (C.L.) limit is determined by setting $t_{\lim}(m_a, A_{95\%}) = 2.71$. Recall that \hat{A} can be negative. We therefore apply one-sided power-constrained limits to prevent setting limits more than 1σ stronger than our expected sensitivity [154]. The results of this limit-setting procedure are shown in Section 5.3.4.

Analysis updates for runs 2 and 3

In run 1, the expected background distribution had a variation that was fixed as a function of the mean to follow the Erlang distribution. We found that the background in runs 2 and 3 deviated from that earlier model. We used the central limit theorem to model our background as Gaussian-distributed, but floated σ to accomodate additional variance in the data. Including σ as a floating nuisance parameter meant that it was now appropriate to model the signal+background as a Gaussian distribution,

$$\mathcal{L}_{R2,3}(d|m_a, A; \mathbf{b}, \sigma) = \prod_{k=k_i(m_a)}^{k_f(m_a)} \frac{1}{\sqrt{2\pi}\sigma} \exp \left[-\frac{(d_k - As_k - b_k(\mathbf{b}))^2}{2\sigma^2} \right] \quad (5.16)$$

where d_k is the average stacked data and σ we treat as a nuisance parameter, estimating it from data. We see that the likelihood is now a function of five parameters for runs 2/3: the signal position and strength, m_a and A , and background mean, slope, and fluctuation, \mathbf{b} and σ .

We use a similar TS as in run 1, now including the σ nuisance parameter,

$$t(m_a, A) = 2 \ln \left[\frac{\mathcal{L}(d|m_a, A; \hat{\mathbf{b}}, \hat{\sigma})}{\mathcal{L}(d|m_a, A=0; \hat{\mathbf{b}}, \hat{\sigma})} \right]. \quad (5.17)$$

The discovery TS is again the maximum value of the TS that can be achieved by varying A . We use the same LEE-correction procedure to define

an $N\sigma$ detection (Equation (5.14)) to search over the frequency range $f \in [100 \text{ kHz}, 2 \text{ MHz}]$. A 5σ detection thus has $\text{TS}_{\text{thresh}} \approx 55$.

The limit-setting TS was also updated for runs 2 and 3 to include the background variation nuisance parameter,

$$t_{\text{lim}}(m_a, A) = \begin{cases} 2 \ln \left[\frac{\mathcal{L}(d|m_a, \hat{A}; \hat{\mathbf{b}}, \hat{\sigma})}{\mathcal{L}(d|m_a, A; \hat{\mathbf{b}}, \hat{\sigma})} \right] & A \geq \hat{A} \\ 0 & A < \hat{A} \end{cases} \quad (5.18)$$

While tuning this procedure on the unblinded 10% of run 2 data, we realized that the distribution of the clean data TSs did not match with our expectation of an asymptotic, one-sided χ^2 distribution, as in Equation (5.13). The difference can be seen between the dashed ‘Off Veto’ curve and gray dotted ‘Expected’ curve in the left of Figure 5.19b. Unlike in run 1, Figure 5.19a, the distributions are significantly different even down to low TS.

To combat the discrepancy in the TS distribution, we modified our likelihood and TS with an additional nuisance parameter correction:

$$\begin{aligned} \mathcal{L}'(d|m_a, A; \mathbf{b}, \sigma, A_m, \sigma_{A_m}) &= \mathcal{N}(A_m|0, \sigma_{A_m}) \times \\ &\prod_k \frac{1}{\sqrt{2\pi}\sigma} \exp \left[-\frac{(d_k - (A + A_m)s_k - b_k(\mathbf{b}))^2}{2\sigma^2} \right] \end{aligned} \quad (5.19)$$

$$\text{TS}'(m_a, A|\sigma_{A_m}) = 2 \ln \left[\frac{\max_A \mathcal{L}(d|m_a, A; \hat{\mathbf{b}}, \hat{\sigma}, \hat{A}_m, \sigma_{A_m})}{\mathcal{L}(d|m_a, A = 0; \hat{\mathbf{b}}, \hat{\sigma}, \hat{A}_m, \sigma_{A_m})} \right]. \quad (5.20)$$

A_m and σ_{A_m} are new nuisance parameters that depend on the signal window (axion mass). The nuisance parameters are by design degenerate with the signal up to a penalty factor. The penalty factor, $\mathcal{N}(A_m|0, \sigma_{A_m})$, is a Gaussian of mean zero and width σ_{A_m} evaluated at A_m .

The σ_{A_m} hyperparameter controls the magnitude of the penalty, allowing us to tune the TS distribution to match the asymptotic expectation from Equation (5.13). Because the nuisance parameters are specific to the mass window, we can tune the observed distribution, $\text{TS}(m_a, A|\sigma_{A_m})$, to the expected distribution in the vicinity of the frequency of interest. Specifically, we take the nearest 94,723 mass points, excluding the 11 mass points centered on the mass point of interest and any points vetoed during data cleaning (including magnet off vetoes). We then tune σ_{A_m} such that there are only three points with $\text{TS}' > 16$ in the ensemble of mass points, as we would expect for a distribution following Equation (5.13). σ_{A_m} can be translated in an

effective nuisance parameter $g_{a\gamma\gamma}^{\text{nuis}}$, which intuitively means that this process effectively sets a floor to our limit-setting power on $g_{a\gamma\gamma}$ (see Figure 5.20).

After unblinding the remaining 90% of run 2 data, even after this nuisance parameter correction, there were a small number of excesses that remained with TS in excess of the 5σ threshold. All of the excesses occurred in a narrow range of nearby frequencies, and after manual examination, we realized they were associated with a single transient, time varying signal, shown in Figure 5.21. The peak was not present in run 3 and has a broad spectral signature, which, along with its transient nature, allowed us to manually exclude the peak as a candidate. We chose not to change our analysis procedures and proceed with unblinding the run 3 data in order to maintain our fully blind analysis. No similar significant features were found in the analysis of the run 3 production data.

Signal injection tests

As a part of tuning the analysis for both runs, we tested to make sure that synthetically injected signals were correctly identified as axion candidates. This step is critical to ensuring that a real signal will not be rejected by our analysis and can be recovered at the correct signal strength, $g_{a\gamma\gamma}$.

In run 1, we generated Monte Carlo (MC) data under the null model with background \hat{b} and N_{avg} averaged PSDs identical to the real data. We then add an artificial SHM axion signal with varying parameters. We run the full analysis procedure on the spectra, including doing quality cuts and evaluating both the best-fit detection parameters and the 95% $g_{a\gamma\gamma}$ limit. Figure 5.22 shows the results of this procedure at four mass points. The upper row shows the reconstructed coupling strength while the bottom row shows the recovered TS. Both show excellent consistency between the true (expected) and recovered values, demonstrating the efficacy of our analysis procedure for both setting limits and correctly characterizing a signal.

In run 3, we did a similar procedure with MC data and additionally did signal injections on real data. These each provide self-contained tests of the analysis procedure. We picked five representative mass points and again added synthetic signals of varying coupling strength to each of the real data and the MC null model data. We did the full analysis procedure from cuts through limit setting and signal fitting, using the nuisance parameter from the real data in the vicinity of the mass point for both the real data and MC pipelines. The results of the real data injections are shown in Figure 5.23,

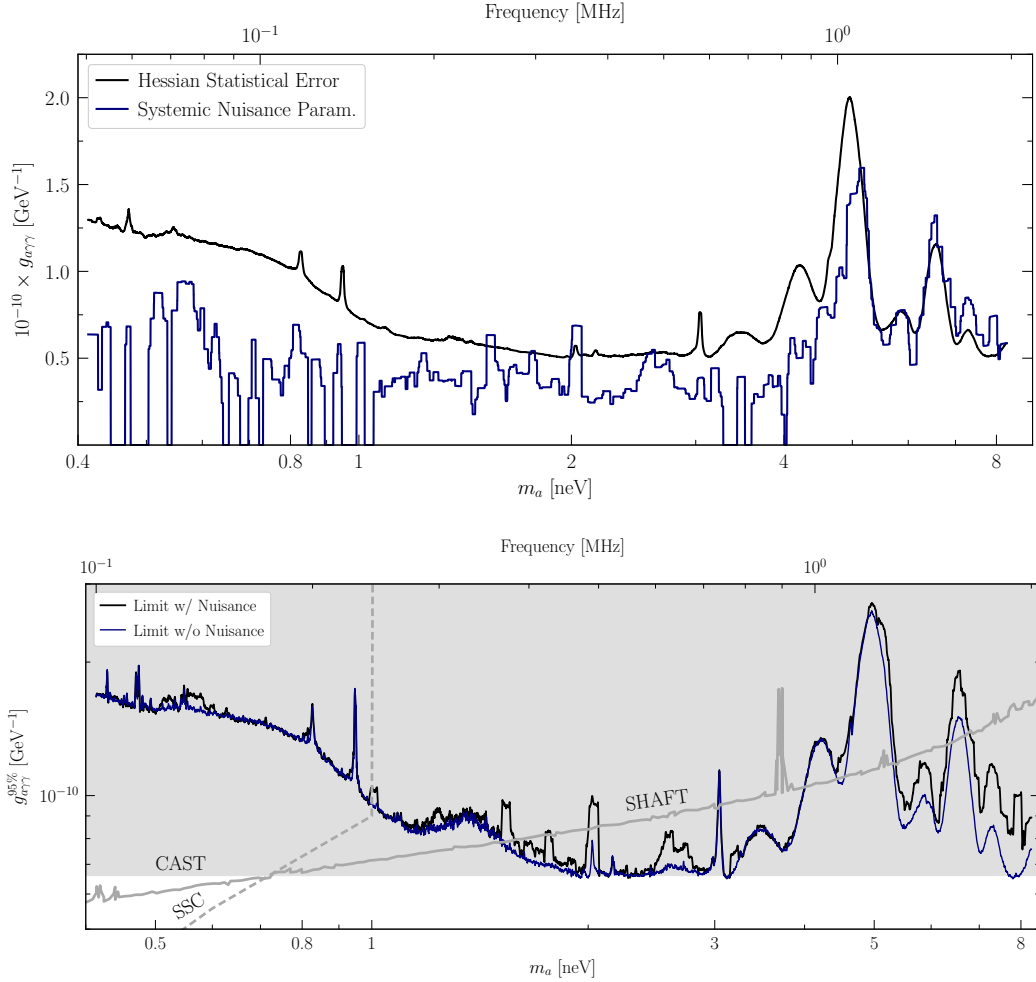


Figure 5.20: *Top*, the hyperparameter, σ_A , converted to the units of $g_{a\gamma\gamma}$, ($g_{a\gamma\gamma}^{\text{nuis}}$) as a function of axion mass (labeled Systematic Nuisance Param.). The comparison is to the statistical uncertainties (labeled Hessian Statistical Error), which are computed from the Hessian for the log-likelihood without systematic uncertainties about the best-fit axion coupling. *Bottom*, a comparison of our limits with and without the nuisance parameter correction. The features and limit-setting power are broadly similar, but generally the nuisance parameter-corrected limit is slightly weaker.

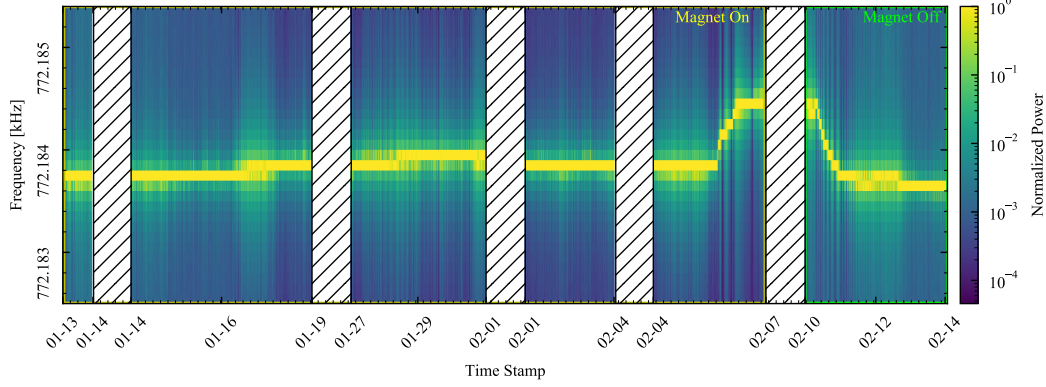


Figure 5.21: The spectral evolution of a time-varying feature in run 2 data that resulted in an un-caught 5σ candidate, from [139]. This peak was not present in run 3 data. No other similar features remained significant during analysis tuning on the initial unblinded 10% of run 2 data or in run 3. This feature is qualitatively different from an axion in its time varying frequency, transient existence, and broad spectral signature.

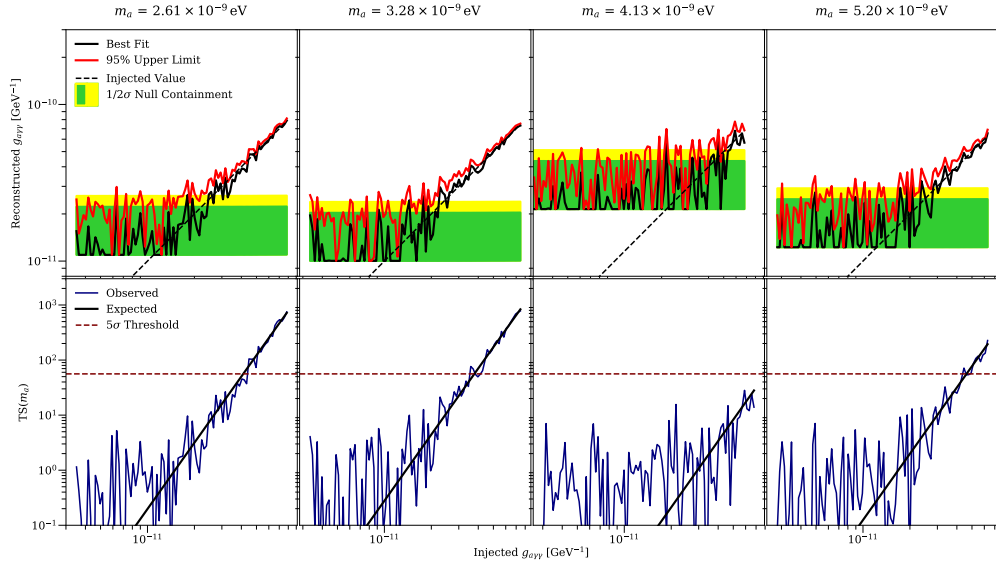


Figure 5.22: Run 1 signal injection tests, from [131].

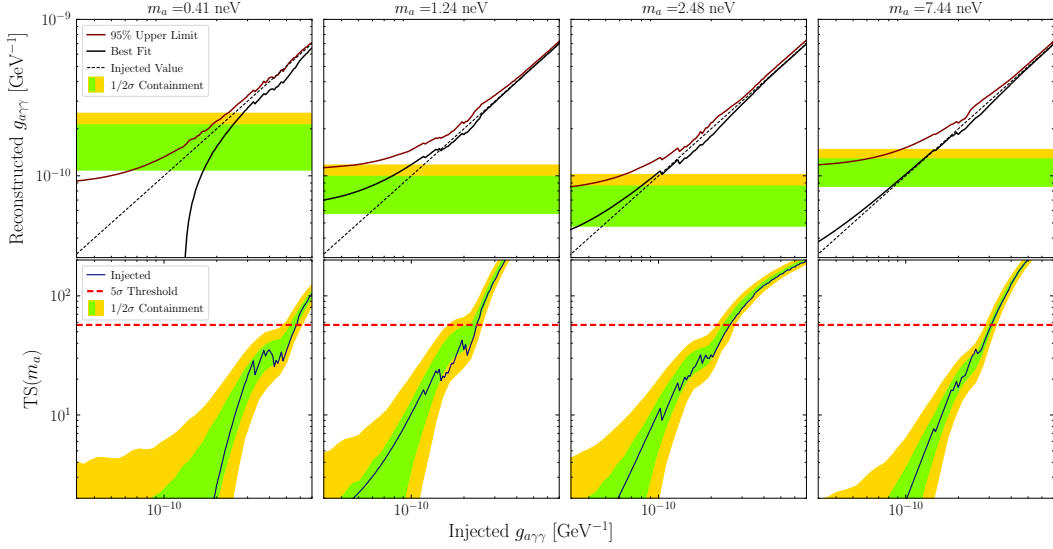


Figure 5.23: Run 3 signal injection tests, from [139].

again indicating an accurate evaluation of the fake signals. Note that the filtering in our analysis procedure, which removes at most 50% of the spectra (see Section 5.3.2), weakens the calculated limit and detection significance from the expectation based on a complete dataset. The bias is removed in our limits with a $\leq 8\%$ TS-dependent correction.

5.3.4 Axion dark matter limits

No axions were discovered in either of ABRACADABRA-10 cm's runs. Instead, we set 95% C.L. limits, shown in Figure 5.24. For both runs, we use the $\bar{\mathcal{F}}_{1\text{M}}$ data to search for frequencies $f < 500 \text{ kHz}$ and the $\bar{\mathcal{F}}_{10\text{M}}$ data to search $f > 500 \text{ kHz}$. The two limits are then combined to span the entire frequency range, 75 kHz–2 MHz (0.31 – 8.27 neV) in run 1 and 100 kHz–2 MHz (0.41 – 8.27 neV) in run 3.

Because we have several million mass points, the limits shown in the bottom of Figure 5.24 are downsampled for clarity. Although not shown, one third of the exclusion limit lies on the bottom of the green 1σ containment band. The run 1 limits were less downsampled, and so the extent of the limits is more visible. A zoom of a small portion of the run 3 frequency range is shown in Figure 5.25 to show the limit variation. Notice that the limits never extend below the 1σ containment as a consequence of setting

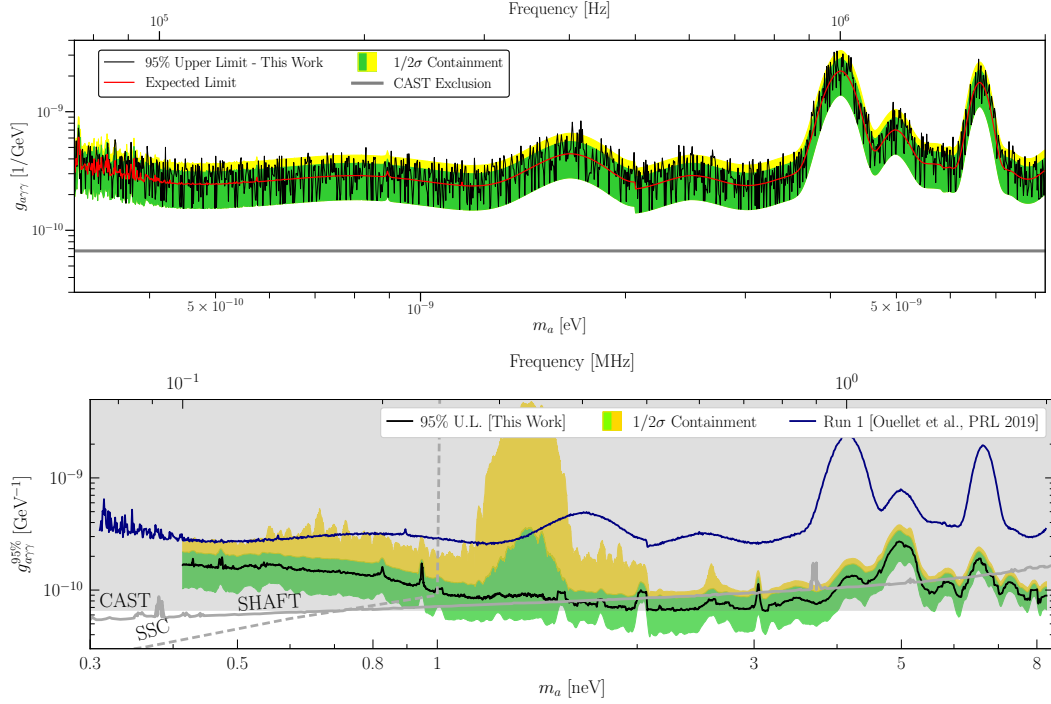


Figure 5.24: Limits on $g_{a\gamma\gamma}$ from run 1 (top, [138]) and run 3 (bottom, [139]).

one-sided power constrained limits.

Run 1 set the first limits on axion dark matter in this frequency range. Previously, the only limits on axion DM were at higher masses, $m_a \gtrsim \mu\text{eV}$. As shown in Figure 5.24, there were previous limits on solar axions from the CAST experiment [155] over a wide range of masses. In run 3, we improved our sensitivity, setting limits below the CAST band and becoming the most sensitive search for axions in this mass range.

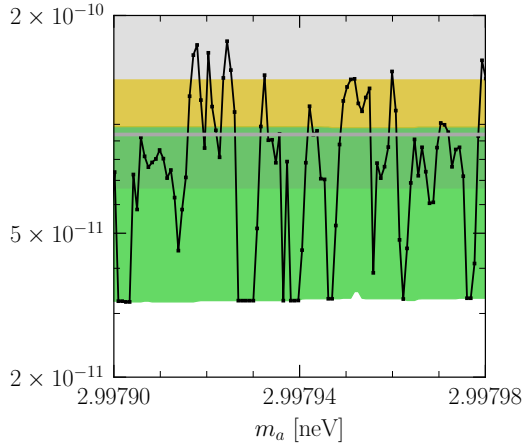


Figure 5.25: Zoom of run 3 limits showing variation hidden by the downsampling in Figure 5.24, from [139].

5.4 Other similar experiments

After the publication of the run 1 ABRACADABRA-10 cm results, two other experiments came online and released limits on axion DM with the lumped-element detection method. Search for Halo Axions with Ferromagnetic Toroids (SHAFT) used a similar design to ABRACADABRA, with toroidal magnets and a broadband readout. Superconducting LC circuit Investigating Cold axions (ADMX SLIC) used a solenoidal geometry with a resonant readout. Another experiment, DMRadio Pathfinder, used a similar lumped-element method to look for dark photons, with a resonant readout but no magnet. I will briefly discuss the design of these three experiments here as they are useful inputs to the design of the DMRadio experiments in the following chapter.

SHAFT ■ SHAFT used four small toroidal magnets, with two oriented with opposite field direction, shown in Figure 5.26 [137]. For an experiment built with air-core magnets, this design would not be very sensitive—the toroids have a small volume and would be limited to $B_0 = 0.062$ T with their design current of 6 A. The innovation they used was that the magnets have a high permeability, ferromagnetic core, increasing the peak field 24× to $B_0 = 1.51$ T. By having multiple toroids with different orientations, they were also able to systematically reject environmental backgrounds. This

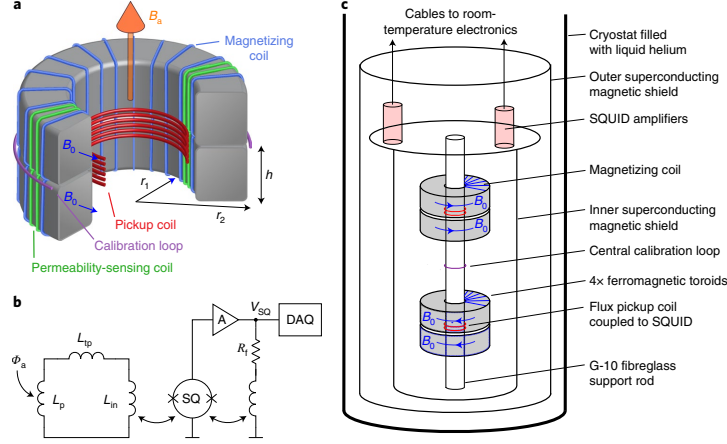


Figure 5.26: SHAFT experimental layout, from [137].

design allowed them to set limits on the axion-photon coupling down to $g_{a\gamma\gamma} \gtrsim 4.0 \times 10^{-11} \text{ GeV}^{-1}$.

Although the ferromagnetic cores are a fantastic way to increase the sensitivity in a small experiment, they are less practical for large-volume detectors. The large mass of an at-scale core would be both difficult to cool and a safety hazard in the event of a magnet quench. The multi-channel rejection of systematics is more practical, although expensive. Generally, the cost of axion searches is driven by magnet construction, so building two or more DMRadio-50 L- to DMRadio-GUT-scale toroids would likely be cost-prohibitive.

Another major difference between ABRACADABRA-10 cm and SHAFT is that SHAFT used a wet Helium fridge, which provides a much more vibrationally quiet environment. This difference allowed them to set limits at lower masses than ABRACADABRA-10 cm, which was limited at low frequencies by vibrational noise. Unfortunately, wet fridges are less practical for long-term operation, as we plan for the DMRadio experiments.

ADMX SLIC ■ The ADMX SLIC design is different from ABRACADABRA-10 cm and SHAFT, but is more similar to the planned design for DMRadio-m³ described in Section 6.1 [156]. They use a solenoidal magnet with a loop of superconducting wire in the high field region as their pickup, see Figure 5.27. Solenoid magnets are generally cheaper to construct and easier to purchase, and this fact is reflected in the higher fields ADMX SLIC reaches,

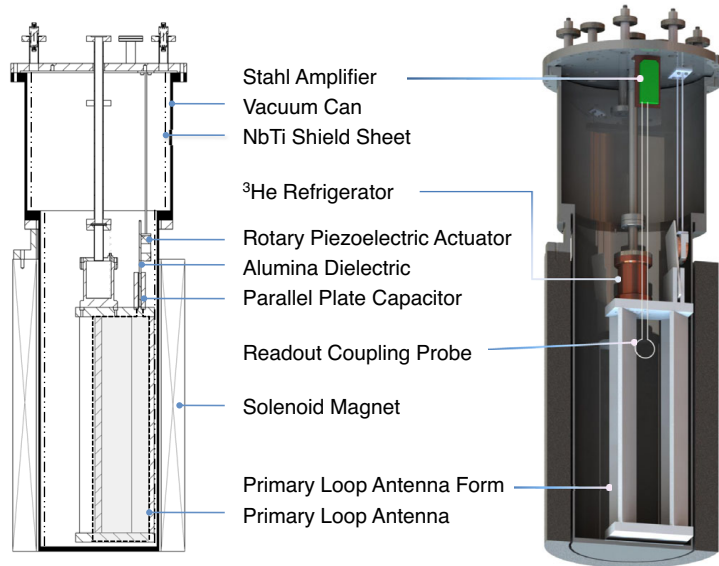


Figure 5.27: ADMX SLIC experimental layout, from [156].

with $B_{\text{avg}} = 7.5 \text{ T}$. The other major difference in the experiment's design is their readout circuit, which includes a tunable parallel plate capacitor to provide a scannable resonant enhancement. With this layout, they set limits of $g_{a\gamma\gamma} \lesssim 10^{-12} \text{ GeV}^{-1}$ over a narrow range of masses.

The ADMX SLIC design is much more scalable than SHAFT, as is reflected by the similarity to the DMRadio-m³ conceptual design. A primary difference between the two is the geometry and materials of the pickup structure. ADMX SLIC suffered from considerable Q value degradation that scaled with the magnetic field strength, as is expected for traditional superconductors [157, 158]. To combat this problem, as discussed in Section 6.1, DMRadio-m³ will use ultra-pure normal conductors with a large volume coaxial shape that also aids in vibration reduction.

DMRadio Pathfinder ■ DM Radio Pathfinder uses a resonant lumped-element approach to search for dark photons rather than axions [159, 160]. With a slightly different geometry (Figure 5.28) and no magnet, they can use the same readout circuit and search for a similar signal. The dark photon is expected to mix with the SM photon, producing a signal with orientation determined by the dark photon polarization. Experience building the readout circuit will be applied to the future generations of

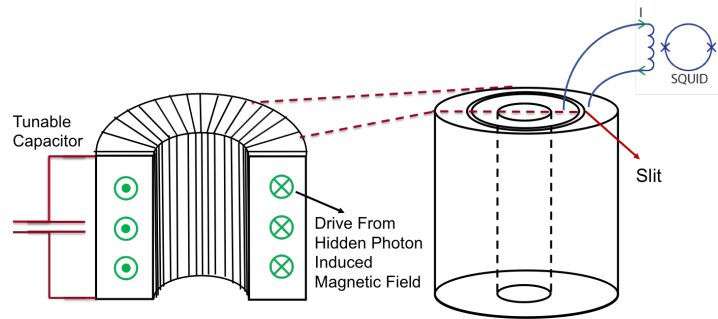


Figure 5.28: DM Radio Pathfinder experimental layout, from [160]. The green lines are the induced magnetic field from an oscillating dark photon-driven electric field oriented in the z -direction. Real currents are induced up through the central hole and around following the black lines shown on the *left*. An azimuthal slit in the sheath, shown at *right*, allows the signal current to be redirected towards a current sensor.

DMRadio axion experiments.

6

DMRadio

ABRACADABRA-10 cm, SHAFT, ADMX SLIC, and DMRadio Pathfinder have paved the way for future generations of lumped element detectors. Building on the successes and challenges encountered by these experiments, we are now designing larger detectors with the DMRadio program. The axion community and indeed the wider dark matter community as a whole would like to search over the widest possible range of models [161] because we do not know *a priori* what the dark matter looks like. The DMRadio program will provide the means to search a wide swath of parameter space at the lower end of the axion mass range, in complement to the many experiments aiming to probe higher masses. In this chapter we discuss the goals and designs of the next-generation experiments DMRadio-50 L and DMRadio-m³ (Section 6.1) as well as, in Section 6.2, the ultimate lumped-element axion detector, DMRadio-GUT, which aims to find or exclude QCD axions at GUT-scale masses.

The papers [162] and [163] lay out some of the work discussed here for the DMRadio-m³ and DMRadio-GUT experiments, respectively.

6.1 Next-generation experiments

There are two next-generation experiments planned in the DMRadio program, DMRadio-50 L and DMRadio-m³. DMRadio-50 L is currently in design with plans to start construction this year (2022). DMRadio-m³, funded for a design study through the DOE Dark Matter New Initiatives program, is also in the design phase. These experiments aim to cover new axion dark matter parameter space by integrating the advances made by predecessor experiments into scaled-up designs.

6.1.1 Science and technology goals

The predicted sensitivity for DMRadio-50 L and DMRadio-m³ is shown in Figure 6.1. DMRadio-50 L will cover a wide range of frequencies, 5 kHz–5 MHz ($m_a \sim 20\text{ peV}–20\text{ neV}$), with couplings $g_{a\gamma\gamma} \gtrsim 5 \times 10^{-15}\text{ GeV}^{-1}$. This improved reach compared to existing experiments comes primarily from scaling up the design—its magnet will be $\sim 50\text{ L}$ in volume, compared to ABRACADABRA-10 cm’s 0.89 L. Similar to ADMX SLIC, DMRadio-50 L will integrate an axion-sourcing magnetic field with a highly sensitive resonant readout, but this time with a toroidal design and a wider range of frequency tuning. This first of the ‘next-generation’ experiments will not attempt to reach into the preferred QCD band, however, and instead will focus on searching for ALPs in addition to serving as a ‘test-bench’ for future improvements to the lumped-element method.

In contrast, DMRadio-m³ aims to definitively probe a portion of the QCD band, reaching DFSZ couplings for $m_a \in [120, 800]\text{ neV}$ ($\sim 30 – 200\text{ MHz}$) and at least KSVZ couplings for $m_a \in [40, 120]\text{ neV}$ ($\sim 10 – 30\text{ MHz}$). The m³ magnet will be much larger ($\sim 1000\text{ L}$) and stronger ($\sim 4 – 5\text{ T}$) than that of previous experiments, and will build on the expertise developed scaling the technique for 50 L. It will also push to higher masses, filling in the gap where the axion wavelength shrinks to approach the detector size and the MQS approximation begins to break down.

Although novel from a design and integration perspective, both of these detectors are based on existing technologies, many of which can even be obtained commercially, such as SQUID sensors and superconducting NbTi magnets. Because of the reliability of the technology and the staged experimental program, these detectors are relatively low-risk. The most difficult part is thus integrating the different technologies into a large, working detec-

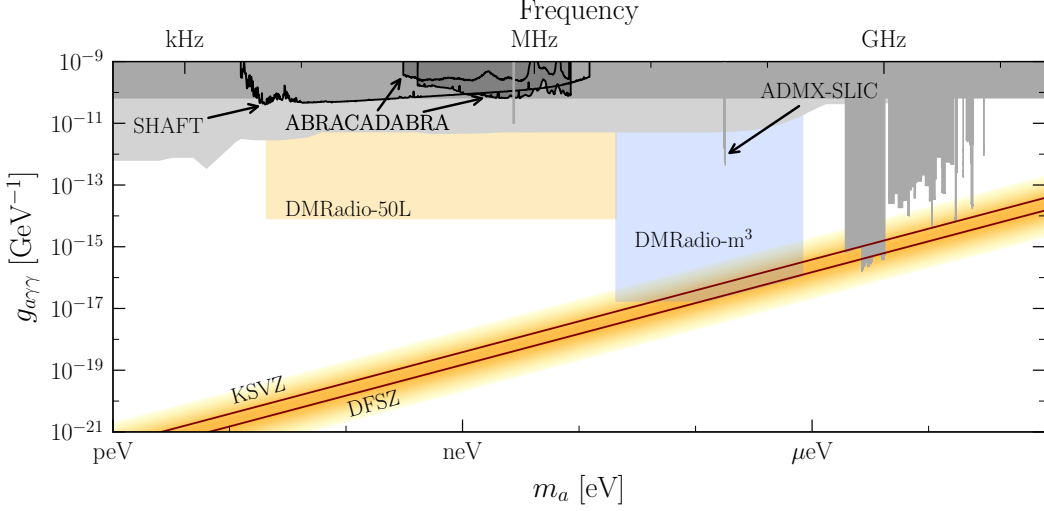


Figure 6.1: Sensitivity projections for DMRadio-50 L and DMRadio-m³ in yellow and blue respectively [162]. Existing limits are shown in grey; light grey is astrophysical limits, medium grey is terrestrial experiments, and dark grey is ABRA-CADABRA.

Parameter	DMRadio-50 L target	DMRadio-m ³ target
Geometric factor	c_{PU}	~ 0.1
Magnetic field	B_0	1 T
Pickup volume	V_{PU}	50 L
Quality factor	Q	10^6
Pickup temperature	T	100 mK
Amplifier noise	η_A	$100 \times \text{SQL}$

Table 6.1: Target detector parameters for DMRadio-50 L and DMRadio-m³.

tor design. The goal detector parameters for each experiment, summarized in Table 6.1, highlight this incremental approach. The following section lays out preliminary designs for each detector.

6.1.2 Preliminary designs

Magnet and pickup

DMRadio-50L ■ As discussed in Section 4.2.2, there are two primary configurations for a lumped-element axion detector based on the topology of the magnet: toroid and solenoid. The DMRadio-50 L magnet will be a toroid with a design similar to that of ABRACADABRA-10 cm. As in ABRA-CADABRA, the toroidal shape is advantageous in that the primary field lines are contained in the dough of the doughnut. Hence, magnet quenches are not a major concern, the superconducting electronics of the readout are automatically kept away from fields, and the sensitive pickup region sits in a field-free location. The advantages of a toroid are in fact even more distinct for DMRadio-50 L; its resonant readout requires high Q -values, which are difficult to achieve in the presence of lossy materials such as normal conductors and dielectrics. These materials are unavoidable in the magnet structure, being necessary for mechanical support and thermalization. However, a toroidal magnet can be almost entirely enclosed within a pickup sheath that serves dual functions: reading out the axion signal and shielding the rest of the readout circuit from the Q -spoiling magnet materials.

The 50 L toroid, drawings shown in Figure 6.2, will have a peak field strength of ~ 1 T and approximate dimensions 17 cm:25 cm:47 cm inner radius:outer radius:height. It will be constructed by SSI, the same company that made the ABRACADABRA-10 cm toroid, and will be of a similar design with NbTi wire wrapped and counterwound around an aluminum mandrel. The magnet will be constructed in two halves, threaded through the pickup sheath pieces, and then connected with epoxy with low-loss spacers such as alumina between the halves.

The purpose of the magnet gap and spacers is to avoid having highly lossy materials near the gap in the sheath. This reduces Q losses from modes that are able to penetrate the gaps in the sheath. A schematic of the gap region is shown in Figure 6.3. The overlapping sheath and sheath cover make a coaxial geometry that supports TEM mode propagation between the lossy magnet region and the outside region that is ‘sampled’ by the resonator. The TEM background modes die off once inside the sheath. TE and TM modes below a certain frequency threshold cannot propagate for a given set of geometric parameters. Simulation work in COMSOL was done to determine the best spacing for our needs, resulting in the values labeling Figure 6.3. The spacer material must have low losses due to interactions with the TEM modes.

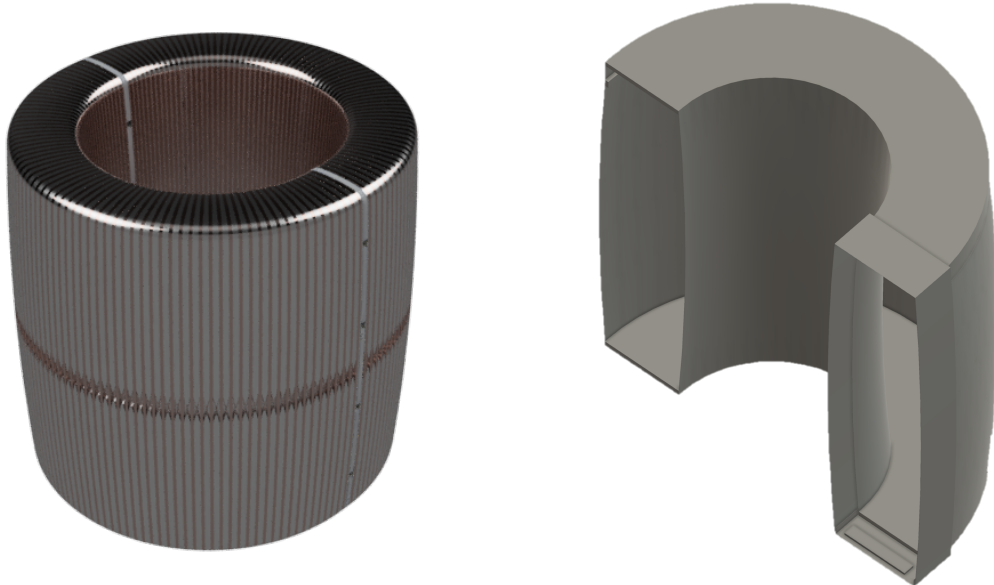


Figure 6.2: CAD drawings of the DMRadio-50 L toroidal magnet (*left*) and sheath (*right*) designs. The magnet will be wound in two sections and combined with a small gap between the halves. The sheath also has two halves, with two additional pieces to cover the gaps.

We chose the dimensions of the magnet-sheath system based on low-frequency AC COMSOL simulations of the pickup and DC Opera simulations of the magnet itself. Incorporating the magnet, sheath, shielding, and secondary ‘corset’ pickup, the COMSOL simulations scanned over a range of detector parameters to optimize the energy coupled in to the readout from the axion current. More details on those scans are presented in Appendix B. The Opera simulations determined the fringe fields for different magnet winding patterns and thus were used to set the minimum distance the superconducting sheath could be placed from the magnet wires. The goal here was to keep the niobium sheath well away from its H_{c1} ¹ critical field value of ~ 100 mT [164, 165].

¹Although Type II superconducting materials such as niobium maintain zero resistance above H_{c1} , magnetic field lines begin to penetrate. This happens via the creation of vortices, potentially spoiling the Q value or creating unpredictable effects. At H_{c2} , superconductivity is lost entirely. Note that Type I superconductors have only a single H_c value at which the Meissner effect and zero resistance ‘turn on’ at the same time.

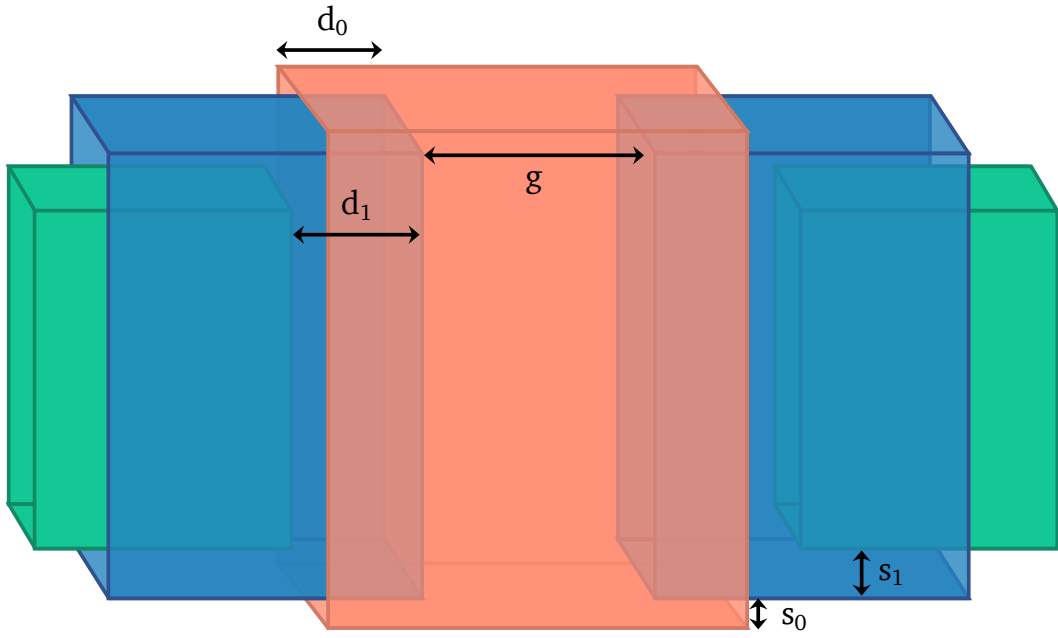


Figure 6.3: Schematic of magnet gap region, not to scale: green is the magnet halves, blue is the sheath halves, and pink is the sheath cover. The approximate dimensions (as of the time of writing) will be $s_0 = 5$ mm and $s_1 = 5$ mm on all sides, $d_1 = 0$ mm, $d_0 = 18$ mm, and $g = 10$ mm.

The existence of the sheath presents an interesting question for charging and discharging the magnet: being superconducting, reactive currents in the sheath will arise to try to cancel out any changes in magnetic flux (see Figure 6.4). As the magnet charges, an azimuthal magnetic flux will be generated. In response, poloidal currents will be induced in the sheath (up through the center hole, orthogonal to those we expect for an axion signal), cancelling the total azimuthal magnetic flux. Being superconducting, the currents will either never die off (giving us an unknown net field in the magnet) or will rise to reach the critical current of the sheath material, quenching and dumping that heat into the fridge—or tearing the sheath apart under large forces. Any quenching or mechanical disruptions would likely quench the primary magnet as well.

To avoid this situation, we need a way to dissipate poloidal currents in the sheath without dissipating the azimuthal currents that compose our signal. We plan to achieve this by adding a resistive gasket to the sheath that

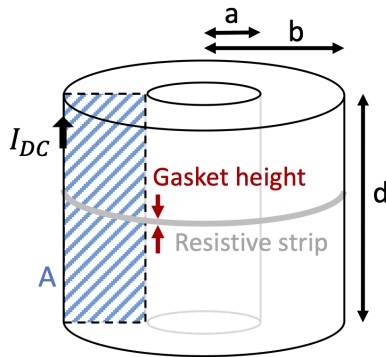


Figure 6.4: Diagram of a toy toroidal sheath gasket, credit: M. Simanovskaia. The 50 L gasket will likely be located at the upper outer corner of the sheath, where the sidewall and top cap meet.

entirely encircles it. In this way, primary field-cancelling current must travel through the resistive strip, dissipating it, but the axion-induced currents run in parallel to the strip, staying within the superconducting material. The resistive gasket will be simply a strip of normal conducting foil in one of the outer corner joints. The dimensions of the strip are chosen to be large enough to dissipate currents in the event of a magnet quench but low enough to avoid negatively impacting the resonator Q value.

DMRadio-m³ ■ The DMRadio-m³ magnet will be a solenoid instead of a toroid. Despite the advantages of the toroidal geometry, its corresponding pickup sheath necessarily has lots of overlapping areas; the gap cover must overlap with the main part of sheath to prevent Q degradation. The overlaps result in a high capacitance effectively in series with L_p . Because the resonance frequency of a series LC circuit is $\omega_0 = 1/\sqrt{LC}$, the high capacitance pushes the resonance to lower frequencies. Adding more inductance to the circuit that does not pick up axion signal degrades the sensitivity (as we discovered in the first run of ABRACADABRA!), so attempting to increase ω_0 by adding inductance in parallel, decreasing L_{tot} is not a good option. It is easy to add additional capacitance in parallel with the pickup sheath (increasing C_{tot}), but difficult to add capacitance in series² to reduce C_{tot} .

²It is interesting to think of scenarios that do add capacitance in series. One potential option that is still being explored is to have more magnet gaps with overlapping sheath sections

Adding capacitance in parallel is exactly what we do to tune the circuit. We add a variable additional C that tunes the resonance down from the natural geometric LC resonance. By having a lower ω_0 we are limited from probing high frequencies. That limitation was fine for DMRadio-50 L³ because of its lower frequency range and smaller inherent inductance, but for DMRadio-m³'s high frequency range, the parasitic resonances become important.

Even with the higher circuit resonances of the solenoidal geometry, at the highest part of the m³ frequency range, the axion wavelength will approach the pickup size, creating geometric, cavity-like modes. This signals the breakdown of the MQS approximation on which the lumped-element method is founded, but does not necessarily indicate vanishing sensitivity. Ongoing simulation work suggests that the readout will have a complex response in this range [166]. Although we plan to fully exploit our sensitivity up into the MQS breakdown region, we will avoid becoming a true cavity search by having a series of a successively smaller pickup structures for the upper end of our search range.

The preliminary design for the m³ magnet is shown in Figure 6.5. The primary field will have nominal peak strength 4 T⁴, but an additional bucking coil above the main magnet will reduce the field strength down to $|B| \lesssim 400$ mT in a region ~ 20 cm above the top of the main coil to accommodate the (further shielded) field-sensitive electronics such as the SQUIDS and superconducting, tunable capacitor. This choice of placement allows the electronics to be as close as possible to the pickup to reduce parasitic impedance without suffering performance degradation due to high fields. A similar setup is used to protect the electronics in the ADMX and HAYSTAC experiments [123, 167].

and thus more capacitors in series. The problem with this solution is that there are now more places for lossy materials to interfere with the circuit's sensitivity, although we have not yet quantified this effect.

³The limitation applies to ABRACADABRA-10 cm, too. There is always some parasitic capacitance in any system, but in the case of ABRACADABRA-10 cm, the capacitance was low enough to have a ω_0 well outside of our frequency range. In this way, ABRACADABRA is effectively a resonant search where we are searching far off-resonance. The same limitations apply that one would expect: we are amplifier noise-dominated and have no Q enhancement.

⁴4 T is the characteristic peak field on the central axis. The field reaches a peak of ~ 7 T in a small region next to the coils. The scan rate is determined by the RMS field throughout the sensitive region, which is closer to the nominal 4 T value.

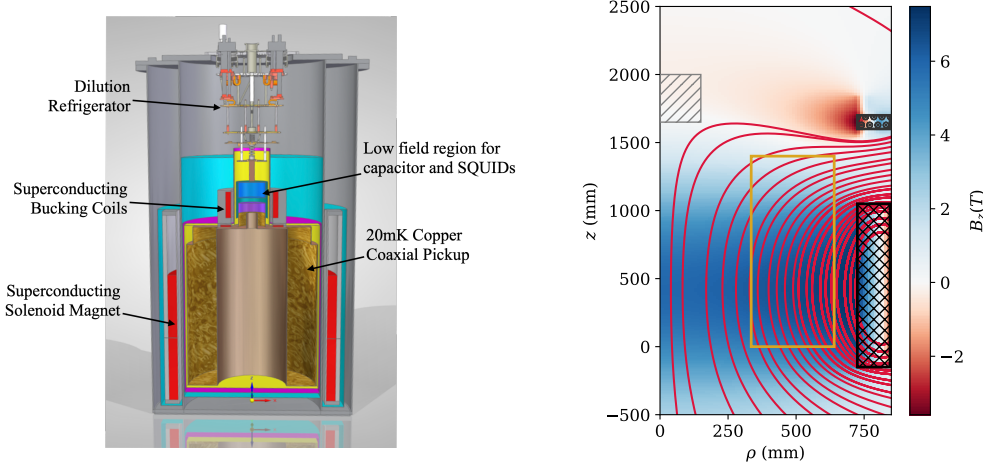


Figure 6.5: *Left*, CAD drawing of the DMRadio-m³ solenoidal magnet in the dilution refrigerator with the important features labeled. Shielding is not shown. *Right*, cross section of the corresponding magnetic field profile. The color tracks the strength of the z-component of the B-field and the streamlines delineate the field lines. The cross-hatched regions are the primary and bucking magnet coils. The slashed region on-axis is the low-field region for the superconducting electronics. They will have additional superconducting shielding. The gold rectangle marks the approximate placement of the largest coaxial pickup. Images from [162].

The pickup sheath for the solenoidal geometry does not wrap around the magnet as it can in a toroid. Instead, the pickup is a coaxial shape that sits in the high-field region, collecting the azimuthal axion B-field, as shown on the right side of Figure 4.6. Notice that this design does not require any overlaps, greatly minimizing its parasitic capacitance.

As a consequence of being in the bore of the magnet, it is difficult to make the pickup coax out of superconducting materials. ADMX SLIC, which also used a solenoidal magnet, used a superconducting NbTi wire loop hanging in the high field region as their pickup, but they encountered considerable Q degradation and resonance frequency shifting scaling with the magnet ramp [156]. This behavior has been seen before in superconducting resonators exposed to magnetic fields, and is thought to be attributed to dissipation due to vortex interaction and oscillating currents from penetrating flux [157, 158]. ADMX SLIC's readout in zero field reached Q's of >10,000, but at 4.5 T field strength, comparable to DMRadio-m³, the Q fell to ~ 4,500. DMRadio-m³ hopes to achieve $Q > 10^5$, far higher than appears possible with existing

superconducting resonator technologies.

Instead of employing a superconductor, the DMRadio-m³ pickup will use oxygen-free, high-conductivity (OFHC) copper. Copper's finite conductivity limits the achievable *Q*-value of the resonator, but it does not suffer from the non-linear effects of superconducting materials in high fields. Because of m³'s relatively low frequency range⁵, small surface-to-volume ratio, and low operating temperature, we expect a high-purity copper coax to be sufficient to reach our goal quality factor.

An additional consequence of the pickup sitting in the high-field region is that differential vibrations between the pickup and the magnet can create a fluctuating magnetic flux that can be picked up in the same manner as an axion signal. Vibrational backgrounds can, to first order, only come from the pickup moving through inhomogeneities in the magnetic field, since motion through a homogeneous field would cause no change in flux. The m³ magnetic field profile must be inhomogeneous because of the finiteness of the solenoid, and even more so because of the field cancellation effect from the upper bucking coil.

Vibrational backgrounds are alleviated by the coaxial geometry; any simple translational motion in the *xy*-plane or ‘tipping’ in the radial direction causes opposite fluxes on the two sides of the coax that cancel. Similarly, if we assume that the magnetic fields are azimuthally symmetric, relative vertical motion between the coax and magnet or relative rotations about the *z*-axis create no net flux. Despite this protection from first-order vibrations, the extremely high sensitivity of the readout means that we must also consider higher-order effects such as coax breathing modes and non-azimuthally symmetric magnet fringe fields.

To combat these backgrounds, we will install a vibration isolation system to reduce any motion of the coax-magnet system. The design of the system will likely be similar to the ABRACADABRA passive pendulum system (see hanging system in Figure 6.6), but may include higher-order filtering such as with a double pendulum or a geometric anti-spring filter [168]. Tests to determine the requirements on the isolation system are planned for the DMRadio-50 L and ABRACADABRA-10 cm fridges. We also believe that magnetic pinning effects will help stabilize the coax relative to the magnetic field.

As in DMRadio-50 L, the pickup will be inductively coupled to the rest of the readout circuit. The coupling transformer will be located at the top of the coax structure, in the low field region.

⁵The anomalous surface resistance of copper drops considerably below GHz frequencies.



Figure 6.6: Superconducting shield and its suspension system for DMRadio-50 L.

Readout circuit

Both DMRadio-50 L and DMRadio-m³ will have resonant readout circuits with resonance frequency scanned with a tunable capacitor. The design of the tunable capacitors is ongoing, but one potential design is shown in Figure 6.7. A capacitor that is readily tunable and of a size to fit in the dilution refrigerators of each experiment can reasonably tune over a factor of 10 in capacitance (or ~ 3 in resonance frequency). Therefore we plan to have a series of 5 – 10 swappable capacitors for each detector that each cover a fraction of the frequency range.

Both experiments will use SQUIDs to read out the signal. We will likely make our own custom SQUID package for each experiment. DMRadio-50 L plans to pair those with Magnicon's control electronics. The choice of control electronics has not yet been made for DMRadio-m³.

Cryomechanical

The DMRadio-50 L pickup and readout electronics will be cooled by a horizontal Blue Fors LH400 dilution refrigerator. To improve cooling power and reduce cooldown times with the large magnet, we will add an additional

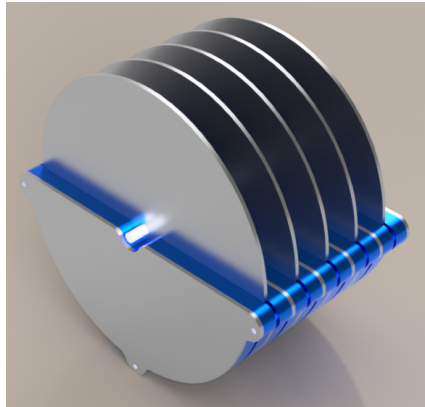


Figure 6.7: Potential tunable capacitor ‘butterfly’ design for DMRadio-50 L or DMRadio-m³, credit: A. Dones. Tuning is possible by rotating the leaves to have more or less overlap. The position shown is with minimal overlap.

pulse tube to cool and maintain the system at 4 K. Based on thermal calculations and simulations, this system will allow us to reach 4 K in a minimum of 22 hours. Blue Fors reports an empty fridge cooldown time to base of 24 hours for the LH400, so our full cooldown could take as little as 48 hours. DMRadio-m³ will have a similar dual system, but the mechanical requirements will be more stringent due to its additional weight.

6.2 DMRadio-GUT

DMRadio-50 L and DMRadio-m³ are built on existing technologies, and will be deployed over the next few years. They will probe a wide region of ALP parameter space as well as QCD axions at frequencies in the upper end of the reach of the lumped-element technique. At lower masses, $\mathcal{O}(0.1 - 10 \text{ neV})$, the photon coupling of QCD axions falls beneath the reach of current technologies. The concept of DMRadio-GUT is an experiment that can reach those minimal couplings based on reasonable R&D goals.

6.2.1 Science and technology goals

The goal reach for DMRadio-GUT, shown in pink in Figure 6.8, is DFSZ sensitivity for $m_a \in [0.4, 120] \text{ neV}$. This range is highly motivated by GUT-scale physics (see Section 3.3.3), but is difficult to reach. The scan rate for a res-

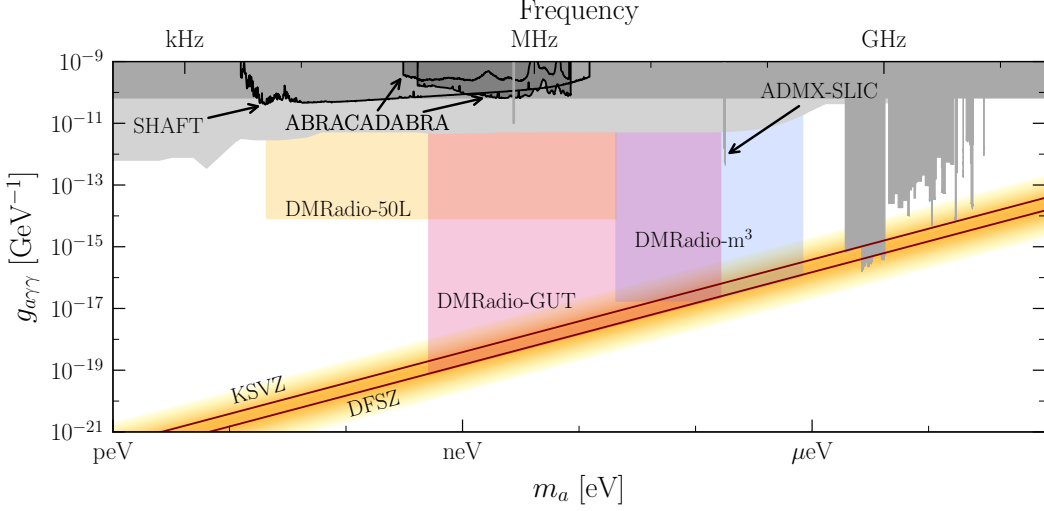


Figure 6.8: Sensitivity projection for DMRadio-GUT in pink [163]. With the baseline R&D goals listed in Table 6.3, this reach can be achieved with a scan time of ~ 6 years. As in Figure 6.1, existing limits are shown in grey; light grey is astrophysical limits, medium grey is terrestrial experiments, and dark grey is ABRACADABRA. Projections for DMRadio-50 L and DMRadio- m^3 are in yellow and blue.

onant lumped-element experiment from Equation (4.43), parametrized in terms of some reasonable values to attain the necessary sensitivity (that we are calling the ‘baseline scenario’) is

$$\begin{aligned} \frac{d\nu_r}{dt} \approx & 41 \frac{\text{kHz}}{\text{year}} \left(\frac{3}{\text{SNR}} \right)^2 \left(\frac{g_{a\gamma\gamma}}{10^{-19} \text{ GeV}^{-1}} \right)^4 \left(\frac{\rho_{\text{DM}}}{0.45 \text{ GeV/cm}^3} \right)^2 \\ & \times \left(\frac{\nu_r}{100 \text{ kHz}} \right) \left(\frac{c_{PU}}{0.1} \right)^4 \left(\frac{B_0}{16 \text{ T}} \right)^4 \left(\frac{V}{10 \text{ m}^3} \right)^{10/3} \left(\frac{Q}{2 \times 10^7} \right) \\ & \times \left(\frac{10 \text{ mK}}{T} \right) \left(\frac{0.1}{\eta_A} \right). \end{aligned} \quad (6.1)$$

Note that the rate goes as $g_{a\gamma\gamma}^4 \nu \propto \nu^5$, because $g_{a\gamma\gamma} \propto \nu_a$ for a QCD axion—low frequencies require a very high sensitivity! This extreme frequency dependence also makes it difficult to interpret the reach from the scan rate alone. The integrated scan time over our goal frequency range is perhaps a better measure; DMRadio-GUT aims to reach DFSZ sensitivities over its entire range with a baseline scan time of ~ 6 years, with varying R&D outcomes potentially extending that up to ~ 10 years or reducing it to just over 3 years.

The top line of Equation (6.1) contains the physics that we cannot change, and the second and third lines contain detector parameters. The goal c_{PU} is identical to that for DMRadio-50L (see Table 6.1). c_{PU} is fundamentally limited by energy conservation and will be optimized for the toroidal geometry with the 50L experiment. The optimization relies on the geometric coupling of the axion current to the pickup structure, and we plan to use the same aspect ratios for DMRadio-GUT if it is also a toroid (which we will see is the most likely outcome). The remaining parameters in our baseline scenario are all improved over the m³ and 50L detector designs. The following section describes how we plan to make those improvements.

6.2.2 R&D paths

There are three primary areas we plan to improve on for a GUT-scale experiment: increasing source signal strength, decreasing backgrounds, and improving the matching network that brings the signals to the amplifier. Signal strength can be increased by increasing the strength and size of the magnetic field. Backgrounds can be reduced by lowering the operating temperature (cutting thermal noise) and swapping out the quantum sensors (cutting amplifier noise). Changes to the matching network can include increasing Q with improved passive resonators or increasing the number of poles (or Q) with an active feedback system. The technologies that can achieve this are summarized in Table 6.2, and discussed in more detail below.

Technology	Parameter(s) affected	Target value
Magnets		
REBCO magnets	B_0, V	16 T, 10 m ³
Nb ₃ Sn magnets		
Backaction evasion		
RF Quantum Upconverters	η_A	-20 dB
Resonators		
Passive resonators	Q	20×10^6
Active feedback		

Table 6.2: R&D thrusts for improving the sensitivity of future lumped element experiments. The target values shown are those we assume for our baseline scenario of a 6.2 year scan.

Scenario	B_0	V_{PU}	c_{PU}	Q	η_A	T	Scan time
Baseline	16 T	10 m ³	0.1	20×10^6	-20 dB	10 mK	6.2 years
Stronger magnet, higher noise	29 T	10 m ³	0.1	20×10^6	-5 dB	10 mK	3.2 years
Lower noise, lower volume	16 T	8 m ³	0.1	20×10^6	-25 dB	10 mK	7.3 years
Higher volume, lower Q	16 T	17 m ³	0.1	2×10^6	-20 dB	10 mK	10.6 years

Table 6.3: Experimental parameters for a few different R&D scenarios. All scenarios reach DFSZ sensitivities at $\text{SNR} = 3$ for $m_a \in [0.4, 120]\text{neV}$ assuming $\rho_{DM} = 0.45\text{ GeV/cm}^3$. B_0 is peak field strength, V is volume of the pickup structure, c_{PU} is the strength of the detector-axion effective current coupling, Q is the resonator quality factor, η_A is the amplifier noise, and T is the pickup operating temperature. The alternative scenarios in rows 2-4 explore potential detector configurations for different R&D outcomes. For example, in row 2, if amplifier R&D does not reach its goal of -20 dB of backaction-noise reduction, increasing the magnetic field strength can counteract the sensitivity reduction and result in a comparable total scan time. The total scan times in the table are calculated from Equation (4.43).

Magnet and cryogenics

The predecessor experiments use one of two basic geometries: a toroidal or solenoidal magnet. The toroidal design has some major advantages. In a toroid, the magnetic field is contained within the coils, unlike a solenoidal field with field lines that return outside of the magnet bore. Magnet quenches are thus much less dangerous and also pose minimal threat to the superconducting electronics, which need to operate in a low-field region. Contained fields also allow the pickup structure to naturally sit in a field-free location. This placement avoids introducing leading-order magnet-related backgrounds into the readout, and it also allows the pickup to be easily constructed from superconducting materials, leading to higher resonator Q 's. However, the pickup geometries used in toroidal designs suffer from parasitic resonances (due to capacitance in overlapping sheath components), which can limit their sensitivity at high frequencies. Because DMRadio-GUT is designed for low frequency, the issue of parasitic resonances for a toroidal architecture is mitigated.

In the solenoidal design, the pickup is most sensitive when inside the high field region. However, this placement increases the risk of magnet-sourced noise, and large fields make the construction of a high- Q circuit difficult [157]. High-field solenoids are produced for many applications, so they benefit from existing designs and infrastructure for their construction. They are thus generally easier and cheaper to build.

Experience from the toroidal DMRadio-50L and solenoidal DMRadio-m³ experiments will be important inputs into the decision of DMRadio-GUT's geometry. For example, magnetic pinning effects in the solenoidal field could reduce vibrational noise, making that design more competitive, especially if vibrations are a dominant noise source [37]. Simulations and measurements of the DMRadio-m³ detector will guide our estimates of the importance of vibrational backgrounds in a potential solenoidal DMRadio-GUT. Likewise, we will be able to measure any stray fringe fields from the DMRadio-50L toroid that can produce interference and vibrational noise in the pickup and use that to gauge tolerances on the construction of a DMRadio-GUT toroid. Ultimately, we expect that in a solenoid, the disadvantages of the pickup being in the high-field region would be a limitation, making the toroidal design the most likely outcome.

Regardless of the geometry, the DMRadio-GUT magnet will have to be large and thus heavy. As in DMRadio-50L and DMRadio-m³, we plan to cool only the resonator to sub-K temperatures. However, even with the goal of cooling the magnet only to its superconducting transition temperature, T_c , careful consideration will have to be made in the design of the cryogenics. For the toroidal design, some of the cryogenic constraints are mitigated by surrounding the magnet with a superconducting sheath, as in DMRadio-50L, which ensures that the resonator does not couple to magnet loss or thermal noise that would otherwise degrade sensitivity. The primary decision that will determine the cryogenic requirements is the choice of magnet wire materials, which can be grouped into two categories, traditional, low- T_c superconductors and newer, high- T_c superconductors such as rare earth barium copper oxide (REBCO).

Low- T_c magnet ■ There are many low- T_c superconductors, but generally Nb-based compounds are favored for the construction of high field magnets. Here we explore two common choices that could be used in DMRadio-GUT.

The first option is to use a traditional NbTi superconducting magnet, as has been done for the other lumped-element detectors. A NbTi-based design

would require cooling the magnet below 10 K and would also limit the peak magnetic field strength to ~ 10 T [169], posing stringent practical constraints on DMRadio-GUT. In order to maintain our goal sensitivity, this restriction on field strength would require greatly increasing the magnet volume, which would further increase the load on the cryogenics and/or require large improvements in the noise and quality factor of the receiver.

A second option is to use a Nb₃Sn magnet. While more costly and difficult to use in magnet fabrication, Nb₃Sn can produce the benchmark 16 T magnetic field for a GUT-scale QCD axion search. Significant work has been done in related fields to optimize use of Nb₃Sn magnets in large-scale physics experiments. For example, the ITER fusion project will utilize solenoidal and toroidal Nb₃Sn coils operating at a temperature of ~ 5 K with peak fields of 13 T and 11.8 T, respectively [170]. The latter toroidal magnets, used for confining the plasma, will have 8500 m³ volume and 51 GJ of stored energy. This material will also be used as part of the High-Luminosity LHC, for the accelerator's dipole and quadrupole magnets, reaching 12 T peak fields and 2.5 GJ of stored energy [171, 172].

High- T_c magnet ■ Additional options beyond low- T_c magnets are on the horizon due to recent and emerging advancements in high-temperature superconductor (HTS) materials. HTS-based magnets have several advantages over traditional niobium-alloy-based magnets. First, because of the higher T_c , the cooling requirements for the large magnet mass can be relaxed; HTS magnets can operate at a few tens of kelvin instead of a few kelvin. Second, HTS materials such as REBCO are able to remain superconducting in fields exceeding 35 T [173], allowing us to increase B_0 and provide additional engineering margin for a GUT-scale search.

HTS magnets are already being used for a variety of projects, most notably in fusion, which, similar to DMRadio-GUT, requires high fields and large volumes. One such project is the SPARC tokomak [174], a toroidal magnet made of YBCO tape with an average magnetic field of 12.2 T and a major radius of 1.85 m for a total stored energy of 110 MJ. Recently, the SPARC effort demonstrated peak fields of 20 T.

By taking advantage of these developments in magnet technology, lumped-element experiments can greatly improve their reach. DMRadio-GUT plans to achieve a 12 T RMS field (equivalent to a 16 T peak field for a toroid with the same approximate aspect ratio as DMRadio-50 L) in a 10 m³ volume, for a total stored energy of 573 MJ, well within the

bounds of current and planned magnets. However, even with these magnet parameters, running the experiment with Standard Quantum Limit (SQL) amplifiers would require a runtime of ~ 50 years. A powerful magnet will consequently need to be paired with beyond-SQL amplifiers, as we explore in the next section.

Beyond-SQL amplifiers

Simultaneous with the explosion in interest in wave-like axion DM, there has been a revolution in quantum sensing, enabling measurements at unprecedented sensitivity. These new capabilities will facilitate searches for QCD axions over a much wider parameter space.

There are two primary requirements on quantum sensors for axion searches. First, they must be sensitive to tiny signals, since a receiver couples a minuscule amount of power from the axion field [175] (e.g., $\lesssim 10^{-22}$ W for traditional cavity-based DFSZ axion searches in several-tesla magnetic fields [37]). Second, because the axion mass is unknown, measurements must be able to scan over orders of magnitude in frequency. Thus, usable sensors must not only enable a high SNR, but they must also be able to do so over a wide bandwidth in frequency in order to increase step sizes and achieve a fast scan. As described in ref. [175] (see also Section VI B of [135] and [135] for an extended discussion), the figure of merit for readout sensors is thus a frequency-integrated sensitivity, increasing with both the on-resonance SNR and the bandwidth over which that SNR can be maintained.

Progress has already been made towards implementing beyond-SQL measurement in axion searches in the microwave frequency range ($\gtrsim 1$ GHz). The HAYSTAC experiment has demonstrated an axion receiver in which the cavity is injected with squeezed electromagnetic vacuum, doubling the bandwidth and consequently the experiment’s scan rate over previous work [126]. Recent work on qubit-based photon counting has demonstrated a noise reduction that could yield a factor of 1,300 increase in scan rate compared to a quantum-limited search [176].

To enable DMRadio-GUT, we must develop quantum sensing technologies at much lower frequencies, in the range of 1 kHz-100 MHz. Unlike the upper end of the microwave frequency range (the green region in Figure 6.9), at the frequencies of a GUT-scale axion, the resonator is thermally occupied, which means that quantum noise-evading techniques such as squeezing or

photon counting do not significantly improve SNR relative to a quantum-limited readout. The objective in this range (Figure 6.9’s orange region) is thus to improve the frequency-integrated sensitivity by executing quantum protocols on thermal states to increase the bandwidth rather than the SNR [177, 178].

At our low frequencies, with a quantum-limited amplifier, resonator thermal noise dominates quantum noise over a broad range of frequencies much larger than the resonator bandwidth. Over this range of thermal noise domination, the SNR is approximately constant because the resonator response to the signal and noise are identical—they both vary with frequency approximately as Lorentzian functions. This range over which the SNR is constant is what we call the ‘sensitivity bandwidth,’ because we are equally sensitive to an axion signal throughout, even in the region outside the resonator bandwidth. To enhance scan sensitivity with a quantum sensing protocol, it is then natural to increase the sensitivity bandwidth.

As illustrated in Fig. 6.10, a backaction evasion scheme both reduces the minimum added noise of the readout below the one-photon SQL and increases the sensitivity bandwidth. The bandwidth improvement relies on the fact that the amplifier noise can be divided into two components with different inherent line shapes; see Section 4.2.1, Section V of [178], and Appendix F of [135] for more information. The first component, known as imprecision noise, is a flat background that is added on the amplifier output. The second component is backaction, which is injected back into the detector resonator through the amplifier input. Because it goes through the resonator, backaction shares the resonator’s Lorentzian line shape. For an example of how this works, we can examine DC SQUIDs, which have demonstrated noise as low as 20 times the quantum limit in commercial implementations [179], and which are the baseline for DMRadio-50L and DMRadio-m³. In SQUIDs, the imprecision noise consists of intrinsic voltage fluctuations on the amplifier output, and the backaction noise consists of circulating currents in the SQUID loop, which induce a voltage and thus resonantly enhanced currents in the input coil [153, 180].

The sum of the imprecision and backaction components is the total amplifier noise plotted in Figure 6.9, and it is this sum that is subject to the SQL. By tuning the strength of the input coupling of the amplifier, one can adjust the balance of imprecision versus backaction noise. Improvement on this scheme can be accomplished with backaction evasion, shown in the bottom row of Figure 6.9, where the backaction in one quadrature of the signal

is reduced at the expense of increased backaction in the other quadrature. As in the top row, by coupling the amplifier more strongly to the readout, the imprecision noise is reduced, increasing backaction noise—but now only in the unmeasured quadrature. This process thus maintains the noise levels of the measured backaction quadrature and lowers the imprecision noise, increasing the sensitivity bandwidth.

An alternative approach to backaction evasion is variational readout. For amplifiers subject to the SQL, the imprecision and backaction noise are uncorrelated. By introducing correlations between the imprecision and backaction, one can achieve a better noise match and reduce the total noise off-resonance, thereby increasing the sensitivity bandwidth. The introduction of correlations to reduce off-resonance noise has been demonstrated in microwave measurements of mechanical resonators [181].

One possibility for implementing these quantum protocols for 1 kHz–100 MHz electromagnetic signals is the RF Quantum Upconverter (RQU); see also Chapters 6 and 7 of [182] as well as [183] and [184]. Like a DC SQUID, the RQU takes a flux signal as its input, which facilitates its integration as an upgrade to the DMRadio readout chain. However, in contrast to a DC SQUID, for which the input and output signals match in frequency, the RQU upconverts kHz-MHz flux signals to GHz voltage signals, allowing us to leverage existing microwave quantum technologies [185]. The RQU is realized by embedding an interferometer of Josephson junctions in a superconducting microwave resonator. This setup implements a measurement Hamiltonian analogous to that of cavity optomechanics, where decades of work has enabled quantum sensing on low-frequency, mechanical systems (e.g., LIGO) [186, 187]. RQUs can thus use analogous protocols for quantum noise-evasion, such as the backaction evasion scheme proposed for mechanical resonators in [188]; in an RQU, this scheme may be executed by exciting the microwave resonator with an amplitude-modulated drive.

By implementing quantum protocols, we aim to achieve readout noise levels of $\eta_A = 0.1$, corresponding to 20 dB of backaction-noise reduction and a factor of ten increase in scan rate. Quantum squeezing of 10 dB has already been achieved in the GHz regime using Josephson parametric amplifiers, and more recently, quantum squeezing of 20 dB (analogous to our goal) was demonstrated in a spin ensemble controlled by optical light [189, 190]. As part of demonstrations toward DMRadio-GUT, RQUs and quantum protocols may be integrated into the DMRadio-50 L testbed.

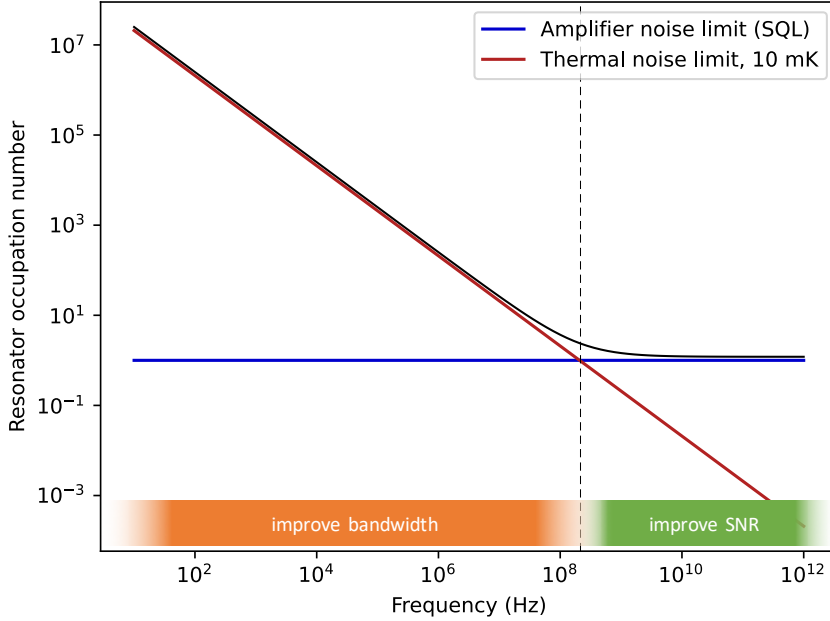


Figure 6.9: There are two distinct noise regimes in axion searches. At high frequencies, thermal noise is subdominant to readout noise, and so improvements in readout performance beyond the SQL directly improve the SNR. At low frequencies, thermal noise is dominant, and so beyond-SQL amplification does not directly improve the SNR. Instead, integrated sensitivity can be improved by increasing the sensitivity bandwidth.

Resonator R&D

To probe GUT-scale QCD axion DM, it will be necessary to improve lumped-element resonators in the frequency range 1 kHz-100 MHz. We envision a two-pronged approach: 1) increasing the quality factor of a passive resonator and 2) implementing active matching to increase bandwidth without reducing resonator gain.

Passive resonator ■ State of the art lumped-element resonators have demonstrated quality factors of $\mathcal{O}(10^6)$ using wire-wound NbTi coils and commercial capacitors when the components are kept away from magnetic fields (as would be the case for a toroidal magnet surrounded by a

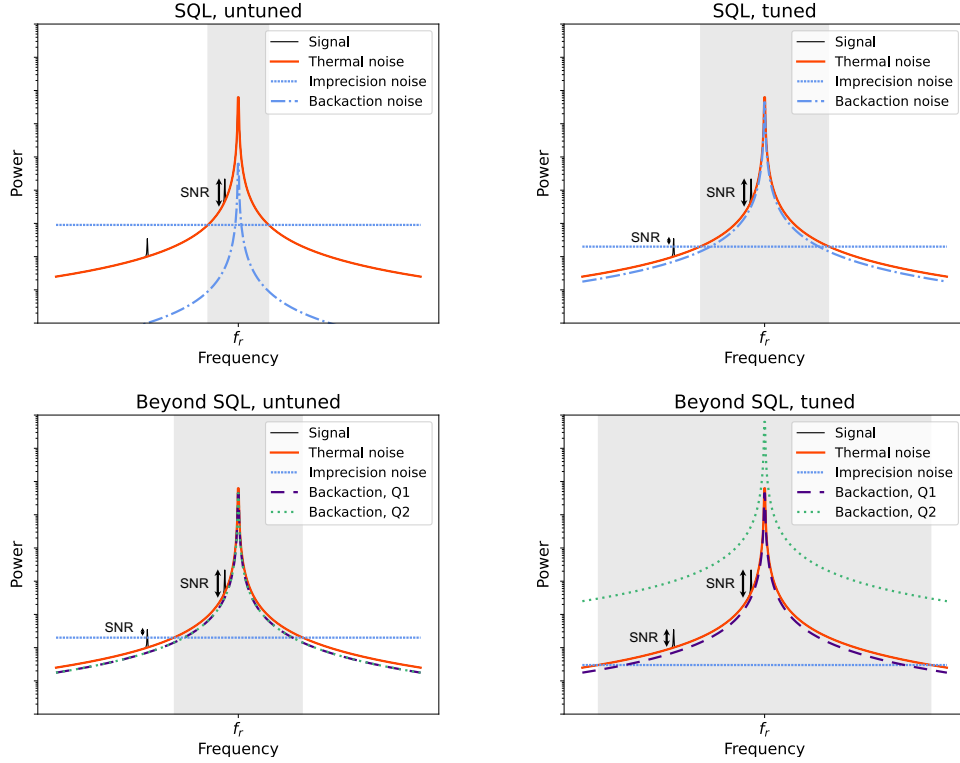


Figure 6.10: Optimizing the sensitivity bandwidth for quantum-limited amplification, *top*, and beyond-SQL amplification via backaction evasion, *bottom*. The cases with untuned amplifier input coupling are on the left, and the more optimally coupled cases are shown on the right. Note that the SNR (labeled in black) is similar for the near-resonance signal in each case while the sensitivity bandwidth (grey band) can be greatly increased by tuning the coupling. A second, off-resonance signal is shown, buried under the noise for an untuned, SQL setup. By tuning the coupling, the signal may rise above the amplifier noise, and in the final, tuned beyond-SQL case, it can reach its maximum SNR above the thermal noise background. Using beyond-SQL amplifiers allows the experimenter to shift more of the imprecision noise into backaction without affecting the SNR of signals in the sensitivity bandwidth; the noise only goes into the unmeasured quadrature, here Q2.

pickup inductor) [191, 192]. However, they possess potentially dominant loss mechanisms in the form of normal metal joints and dielectric loss in polytetrafluoroethylene (PTFE) and formvar wire coatings. Moreover, there exists only a limited understanding of what dictates quality factor in

lumped-element resonators.

These issues motivate a systematic study to understand loss mechanisms with the aim of improving Q in the 1 kHz-100 MHz frequency range. A program is underway to explore the use of a variety of superconductors for wires and electrodes—niobium, aluminum, titanium, tantalum, and their alloys—and crystalline capacitor dielectrics for frequency tuning—sapphire, silicon, rutile. Through careful experimental study and optimization of Q , superconducting radio-frequency cavities in the GHz range have demonstrated Q s on the order of 10^{12} (one million times higher than lumped-element resonators) [193]. The current goal is to improve Q in the 1 kHz-100 MHz frequency range by a factor of 20 to 20 million. Resonators with improved Q may be integrated into the DMRadio-50 L testbed as a demonstrator for DMRadio-GUT.

For resonator tuning structures, we plan to build upon the techniques developed from DMRadio-50 L and DMRadio-m³. As described previously, the physical size of the receiver is decoupled from the search frequency; therefore, we may achieve appreciable tuning with a single resonator configuration. The resonance frequency may be tuned in the LC circuit by changing the capacitance. Simulation has indicated that we may achieve a factor of 10 change in capacitance using an insertable dielectric or a tunable electrode overlap, resulting in a factor of ~ 3 in frequency change in a single cooldown. Such tuning mechanisms need not unacceptably degrade the Q ; sapphire loaded superconducting cavities have demonstrated quality factors in excess of 10^9 [194]. For coarser tuning, inductor coil sets may be changed between cooldowns to scan different frequency ranges. In this manner, DMRadio-GUT can probe the desired 0.1–30 MHz frequency range with as few as five resonator configurations.

Active feedback ■ A passive resonator is not the only option for the impedance matching network that transfers the signal to the amplifier. In a passive lumped LC circuit, the reactance of the inductor and capacitor cancel at resonance. The power absorption from axions is thus maximized at that frequency but falls off away from resonance. To circumvent the limitation, one may instead use receivers with active elements [195]. For example, if the capacitor is replaced with a negative inductor with negligible loss, one may cancel the reactance and achieve the maximum power absorption over a broad range of frequencies. Such wideband reactance-cancellation schemes would permit the evasion of the Bode-Fano criterion [175, 196],

[197], and they have been discussed for several decades in the engineering community such as in the context of white-light cavities in the optical regime [198–200]. Moreover, near-dissipationless negative inductors can be realized in the kHz and MHz regimes using Josephson Junctions [153]. Research and development toward DMRadio-GUT will aim to exploit active matching elements as a potential route to realizing a GUT-scale axion search.

Conclusion

Although the SM of particle physics has done an amazing job of categorizing the visible particles and predicting their properties and interactions, it neglects to explain some major experimental and astrophysical discoveries. Dark matter, which is not even hinted at by the SM, is about five times as prevalent as visible matter, is responsible for a host of disparate astrophysical phenomena, and is critical to our existence in the universe.

Explanations abound for the identity of these mysterious particles, from black holes born in the universe's infancy to invisible new particles carrying none of the charges with which visible matter can interact. Although we would like to carry out experiments to search for all of these possibilities, practical constraints limit us to building only a few experiments to search for the most promising candidates. One of the top candidates to be the dark matter is the axion, a light pseudoscalar boson which comes along with the solution to another hole in the SM: the strong CP problem.

If they exist, axions are so light and so prevalent that instead of interacting as individual particles, they interact collectively in the form of a classical wave. So, experiments searching for them must be configured completely differently from traditional particle detectors. For the past couple of decades, the only laboratory axion dark matter searches looked for axions with masses $\mathcal{O}(\mu\text{eV})$. At these masses, the most basic cosmological models predict that

axions can make up all of the dark matter. Also, the axion wave has a wavelength $\mathcal{O}(m)$, so experimenters can exploit boundary conditions to amplify and detect the signal.

Axions of lower masses can still be all of the dark matter and are more preferred from the standpoint of high-energy particle theory. The wavelengths associated with these axions are very long, however, too large to fit inside a detector. Instead of relying on boundary conditions, a newly proposed technique called lumped-element detection treats the axion wave as the source of an effective current that is coherent and in phase across the entire detector. The current can be inductively coupled into a physical circuit and read out to search for axion signals.

The first experiment to use this method was ABRACADABRA-10 cm, a small demonstrator we built at MIT that set world-leading limits on axion dark matter. Now that we have shown that the lumped-element technique works, we have begun designing a series of larger experiments, DMRadio-50 L, DMRadio-m³, and DMRadio-GUT, which will probe the most motivated parameter space of low-mass axions.

Within a few years the community has gone from having no probes of low-mass axion dark matter to having several experimental limits, multiple detectors in design, and a realistic R&D path towards definitively probing GUT-scale QCD axions on the horizon. And this kind of progress is not just limited to low-masses—the axion parameter space as a whole has recently seen huge advances in technology and new detection ideas. If the dark matter is an axion, it is very likely that within our lifetimes, it will go from a hypothetical construct to a well-characterized part of our model of particle physics, helping us answer questions about the universe we live in.

A

Variables and Conventions

This appendix derives or describes a number of conventions and variables used in this thesis to describe the axion-detector coupling. There are a variety of ways used in the ABRACADABRA and DMRadio literature describing how well coupled the pickup structure is to the source axion signal. In this section, I will describe each of the variables used— M_{ap} , \mathcal{G} , k , and c_{PU} —and show how they are related to each other. Note that for clarity during derivations, I often omit irrelevant variable dependences (i.e. writing \mathbf{J}_{eff} instead of $\mathbf{J}_{\text{eff}}(\mathbf{r}, t, m_a)$) and use natural units. At the end of each derivation I have rewritten the final expression with the variable dependences and in S.I. units for ease of reuse—too many hours have been wasted by graduate students tracking down \hbar 's and 2π 's.

A.1 M_{ap}

Perhaps the most intuitive but least useful way to describe the coupling is with an effective mutual inductance, M_{ap} , between the axion effective current and pickup inductor. As is readily seen in the circuit picture of Figure 4.3, the axion effective current couples into the pickup via an effective transformer. It is important to clarify that the real currents in the pickup structure do not significantly induce new axion effective currents, despite

the typical transitive nature of a mutual inductive coupling. The mutual inductance is defined by the relationship

$$M_{ap} \equiv \frac{\Phi_a}{I_{a,\text{eff}}}, \quad (\text{A.1})$$

where Φ_a is defined as the magnetic flux due to axions through the pickup structure and $I_{a,\text{eff}}$ is the integrated effective axion current density,

$$I_{a,\text{eff}} = \int_{\text{magnet}} d\mathbf{A} \cdot \mathbf{J}_{\text{eff}}(\mathbf{r}) \quad (\text{A.2})$$

Unfortunately, M_{ap} is not a very useful variable to optimize or report an experiment's sensitivity. For one, the geometry of the detector is contained in both M_{ap} and $I_{a,\text{eff}}$. It also has units of henry and thus is scale-dependent; identical detectors of different sizes would have different M_{ap} 's.

A.2 \mathcal{G}

The geometric factor, \mathcal{G} , can instead be used to combine all of the geometric information into a single, dimensionless variable. Its value can be determined from Equation (A.1) analytically using the definition of the axion current from Equation (4.4),

$$\mathbf{J}_{\text{eff}}(\mathbf{r}) = g_{a\gamma\gamma} \sqrt{2\rho_{DM}} \cos(m_a t) \mathbf{B}(\mathbf{r}), \quad (\text{A.3})$$

and the Biot-Savart law:

$$\Phi_a = g_{a\gamma\gamma} \sqrt{2\rho_{DM}} \cos(m_a t) \left(\int_{\text{pickup}} dA \int_{\text{magnet}} dV' \hat{\mathbf{n}} \cdot \frac{\mathbf{B}(\mathbf{r}') \times (\mathbf{r}' - \mathbf{r})}{|\mathbf{r}' - \mathbf{r}|^3} \right). \quad (\text{A.4})$$

Everything in parentheses describes the geometry of the detector. Note that this expression only applies within the MQS approximation. To make \mathcal{G} dimensionless and separate out the magnetic field strength and total volume scaling, we define

$$\mathcal{G} \equiv \frac{1}{B_0 V} \int_{\text{pickup}} dA \int_{\text{magnet}} dV' \hat{\mathbf{n}} \cdot \frac{\mathbf{B}(\mathbf{r}') \times (\mathbf{r}' - \mathbf{r})}{|\mathbf{r}' - \mathbf{r}|^3}, \quad (\text{A.5})$$

where B_0 is a characteristic field strength, usually pegged to the nominal maximum, and V is a characteristic volume, fixed either to the magnetic field volume (as is done in ABRACADABRA-10 cm) or to the pickup volume (as is done in DMRadio). It does not matter what choice is made for these nominal values as long as their definition is consistent within the calculation and with any comparison. This new definition of \mathcal{G} allows us to write the axion flux as

$$\Phi_a = g_{a\gamma\gamma} \sqrt{2\rho_{DM}} \cos(m_a t) B_0 V \mathcal{G} \quad (\text{A.6})$$

or written out in S.I. units:

$$\Phi_a(t) = g_{a\gamma\gamma} \sqrt{\hbar c} \sqrt{2\rho_{DM}} \cos\left(\frac{m_a c^2 t}{\hbar}\right) B_0 V \mathcal{G}. \quad (\text{A.7})$$

A.3 k

Another way to think about the efficacy of the axion-detector coupling is to consider the strength of the effective voltage source from the axion flux in an equivalent circuit. To convert to the equivalent circuit, we can use Kirchoff's voltage law: in the MQS approximation, the voltage drop around a complete loop is zero,

$$0 = \frac{\partial \Phi_a}{\partial t} + I_{\text{sig}} Z. \quad (\text{A.8})$$

Here $Z(\omega)$ is the frequency-dependent impedance of the entire readout circuit. We can see that the flux on the pickup structure can be recast as an effective voltage source in series with the circuit:

$$V_a = I_{\text{sig}} Z. \quad (\text{A.9})$$

The ‘goodness’ of the coupling can then be written down in terms of a new variable, k , defined by

$$k^2 \equiv \frac{1}{2} \frac{|V_a|^2}{|V_{a,\text{max}}|^2} \quad (\text{A.10})$$

where $|V_{a,\text{max}}|$ is the theoretical maximum voltage drive that could be induced if all of the converted axion energy was used to drive the circuit. The prefactor of 1/2 is included to account for the mismatch in the axion’s and photon’s dispersion relation.

This definition of k can immediately give us a conversion with M_{ap} . The \mathcal{EMF} from an axion drive is the change in flux with respect to time, $d\Phi_a/dt$.

Also, any mutual inductance can be written as a function of the interacting inductances,

$$M_{ap} = \kappa \sqrt{L_{a,\text{eff}} L_p}, \quad (\text{A.11})$$

where κ is a number between 0 and 1 that describes how well coupled the inductors are. We can thus rewrite Equation (A.10) in terms of the \mathcal{EMF} with M_{ap} :

$$k^2 = \frac{1}{2} \frac{\kappa^2}{\kappa_{\max}^2} \frac{L_{a,\text{eff}} L_p I_{a,\text{eff}}^2}{L_{a,\text{eff}} L_p I_{a,\text{eff}}^2} \quad (\text{A.12})$$

$$= \frac{\kappa^2}{2} \quad (\text{A.13})$$

where the second step set $\kappa = 1$, its maximum value.

Conversion between k and \mathcal{G} is less obvious and depends on the qualitative geometry of the detector (e.g. toroidal vs. solenoidal magnet or pickup loop vs. sheath). Here I will simply state the relationship,

$$k^2 = \frac{m_a^2 V}{2 L_p} \mathcal{G}^2, \quad (\text{A.14})$$

or in S.I. units,

$$k^2 = \mu_0 \left(\frac{c}{\hbar} \right)^2 \frac{m_a^2 V}{2 L_p} \mathcal{G}^2. \quad (\text{A.15})$$

A.4 c_{PU}

Although k is an intuitive measure of the effectiveness of a detector geometry at coupling to the axion effective current, it has some failings as a universal reference. In particular, k depends on m_a ; as the signal frequency goes to zero, so does the voltage across the pickup inductor. Additionally, k is dependent on the total scale of the detector. We would prefer to have a measure of the detector that is independent of the detector size and signal frequency (at least in the MQS approximation). To this end, we introduce c_{PU} , a scale- and frequency-independent rescaling of k defined by

$$k^2 = m_a^2 V^{2/3} \left(\frac{B_0^2 V}{\int_V |\mathbf{B}(\mathbf{r})|^2 dV} \right) c_{\text{PU}}^2, \quad (\text{A.16})$$

or in S.I. units,

$$k^2 = \left(\frac{c}{\hbar}\right)^2 m_a^2 V^{2/3} \left(\frac{B_0^2 V}{\int_V |\mathbf{B}(\mathbf{r})|^2 dV} \right) c_{\text{PU}}^2. \quad (\text{A.17})$$

In terms of \mathcal{G} , c_{PU} is then

$$c_{\text{PU}}^2 = \frac{V^{1/3}}{2L_p} \mathcal{G}^2 \quad (\text{A.18})$$

or in S.I. units,

$$c_{\text{PU}}^2 = \mu_0 \frac{V^{1/3}}{2L_p} \mathcal{G}^2. \quad (\text{A.19})$$

B

COMSOL Modeling

COMSOL Multiphysics [201] is a multipurpose simulation software package designed for finite element modeling of physical systems. It has many modules for different areas of physics. The work presented in this thesis includes electromagnetic COMSOL simulations, primarily for relatively low-frequency modeling using the AC/DC module; however, select analyses were also performed at higher frequencies using the RF module.

The basic idea of the finite element method (FEM) is to take a system of partial differential equations (PDEs) and discretize them to be solved numerically¹. This method is extremely useful for the modeling of many physical systems, with laws expressed in terms of PDEs. The PDEs are quite often not solvable analytically, especially for complex geometries.

This is the situation in which we find ourselves for lumped element experiments; Maxwell's equations are a system of PDEs that, although solvable analytically for simple geometries, need numerical solutions for any realistic experimental configuration. This appendix includes field diagrams and plots summarizing modeling I did for ABRACADABRA and DMRadio.

¹For an excellent introduction to FEM modeling, see COMSOL's 'Cyclopedia,' [202].

B.1 ABRACADABRA-10 cm

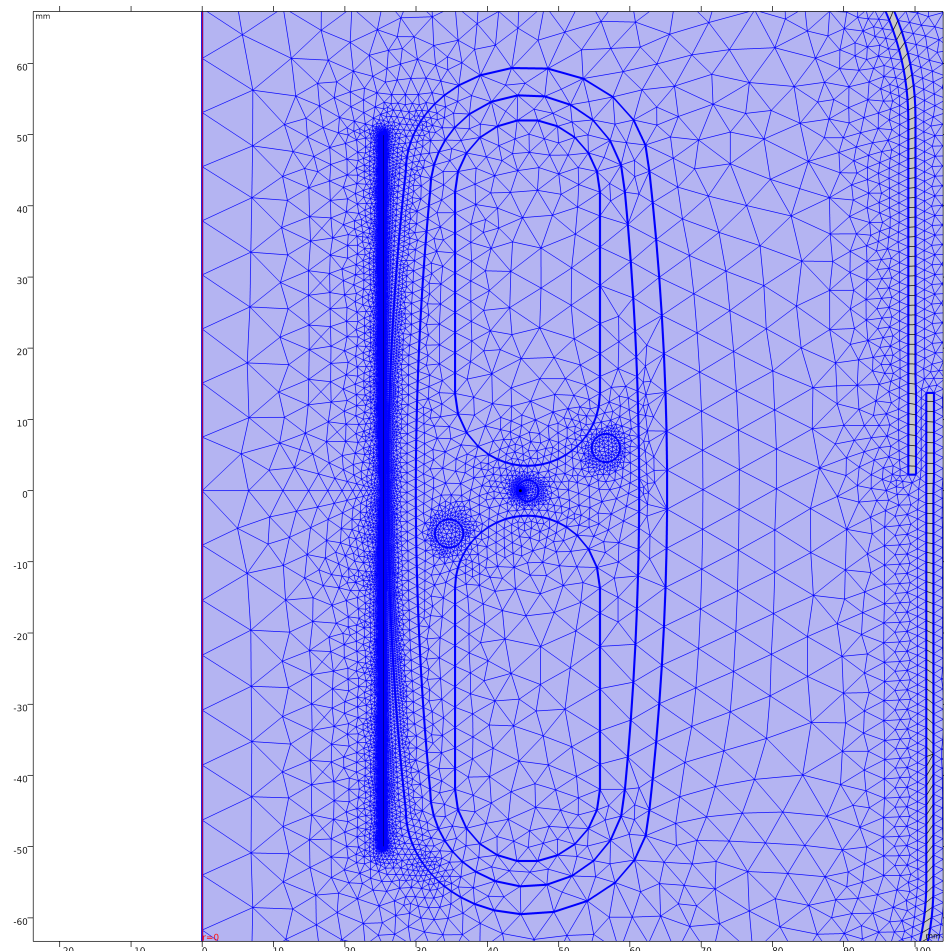


Figure B.1: A zoom of an example mesh pattern for the ABRACADABRA-10 cm run 2/3 geometry. The PDEs are calculated at the mesh nodes. The mesh is finer at the narrower regions that need more precision. The simulation is axisymmetric, and thus reduces to solving PDEs with only a ρ and z dependence. The oval structure is the cross-section of the ABRACADABRA-10 cm magnet, and the tightly meshed vertical line at $\rho \approx 24$ mm is the pickup cylinder. The wall on the outer edge is the superconducting shielding can.

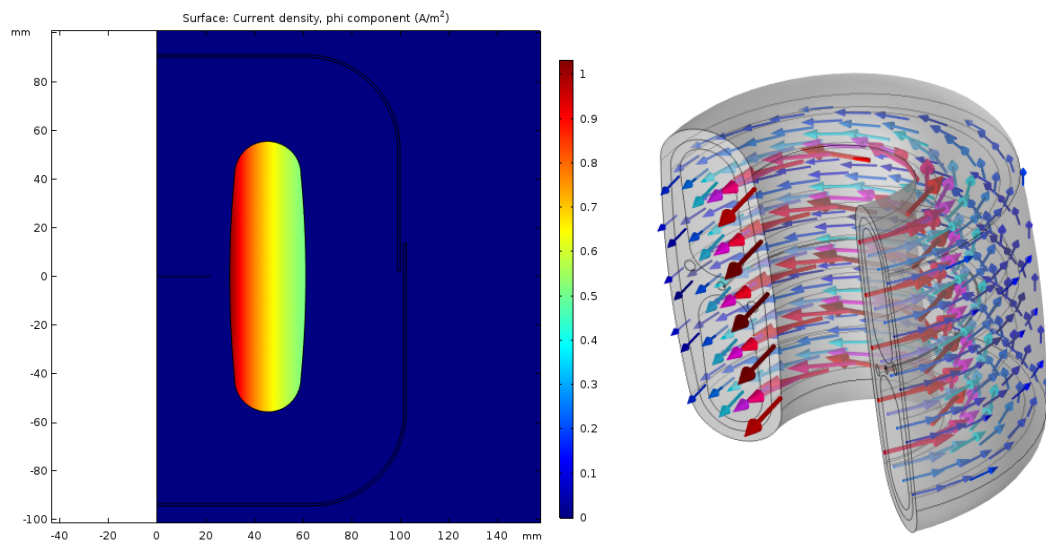


Figure B.2: The axion effective current distribution in the magnetic field region. *Left* shows a half cross section of the magnet, with the color denoting axion current density. *Right* is a 3d rendering of the current, with the color and arrow size denoting the current amplitude or, equivalently, primary magnetic field strength.

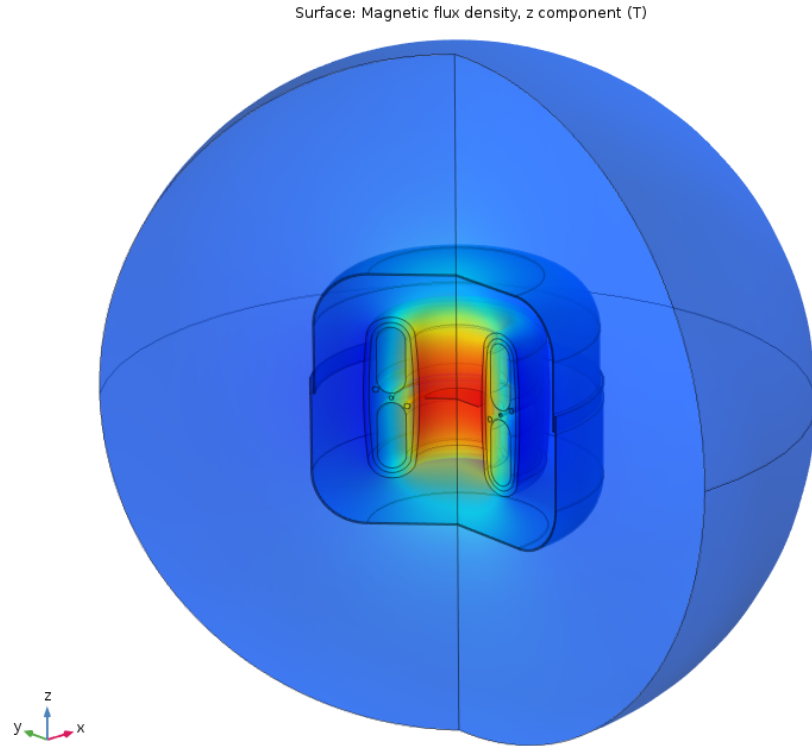


Figure B.3: The z -component of the magnetic field generated by the oscillating axion effective current. The red region in the center has the highest magnetic flux density and thus is the optimal choice for locating the pickup structure. Although not visible here, the field flux lines return on the outside of the ABRACADABRA-10 cm toroid, but inside the superconducting shielding. The large sphere outside of the shield is the edge of the simulated world. The edge is far enough from the interesting physics that the finite size of the simulation does not affect the results, which was tested by varying the sphere size and boundary conditions.

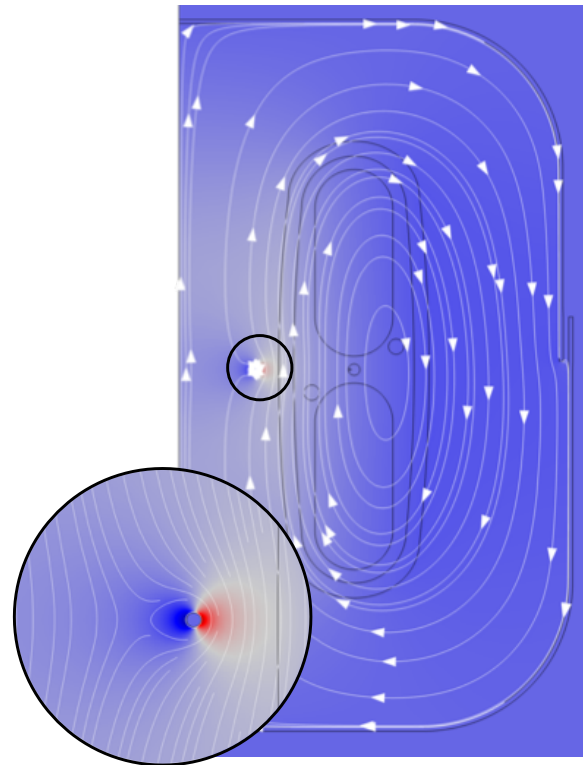


Figure B.4: The magnetic field pattern from an axion source with the inclusion of a reactive wire loop pickup. The inset shows a zoom near the wire. The color denotes the strength of the z -component of the field and the streamlines show the B-field lines. This simulation calculated the axion-pickup coupling. A similar simulation with current injected in the pickup wire, rather than from the axions, gave us the pickup inductance.

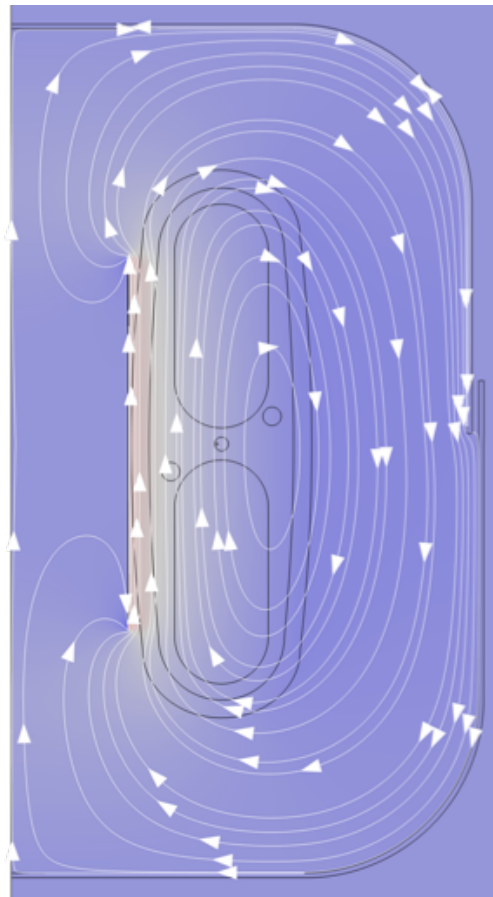


Figure B.5: The magnetic field pattern from an axion source with the inclusion of a reactive cylinder pickup. The color denotes the strength of the z -component of the field and the streamlines show the B -field lines. Similarly to the wire simulation, this model provided the axion-pickup coupling strength and pickup self inductance. One can see the better coupling of the cylinder than the wire shown in Figure B.4 by noting better ejection of flux lines from the central region.

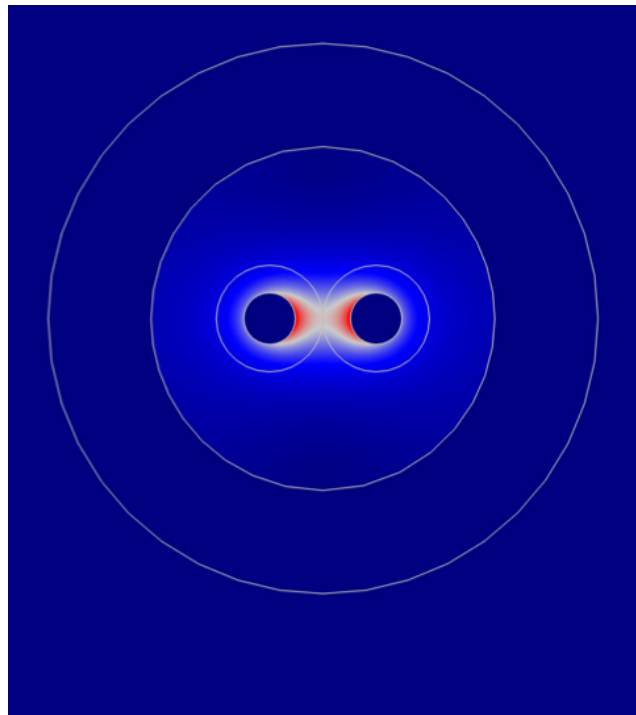


Figure B.6: A cross section of shielded twisted pair wiring. The color marks the strength of the magnetic field between the wires. The superconducting shielding contains the fields. This kind of simulation allowed us to calculate the wiring's impedance per unit length.

B.2 DMRadio-50 L

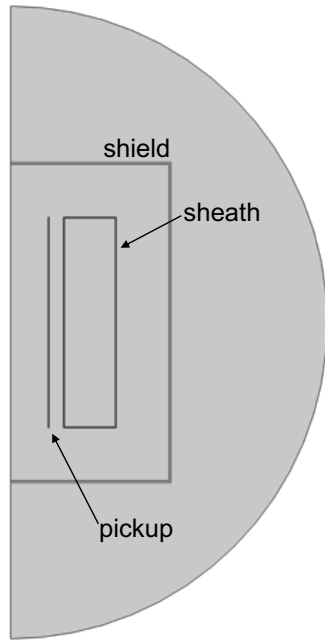


Figure B.7: 2-D axisymmetric geometry used to simulation DMRadio-50 L. All components are assumed to be superconducting (achieved in COMSOL primarily via boundary conditions, although occasionally by setting the material properties to have a very high conductivity). The region outside the superconducting shield was not simulated, as all fields are contained within it.

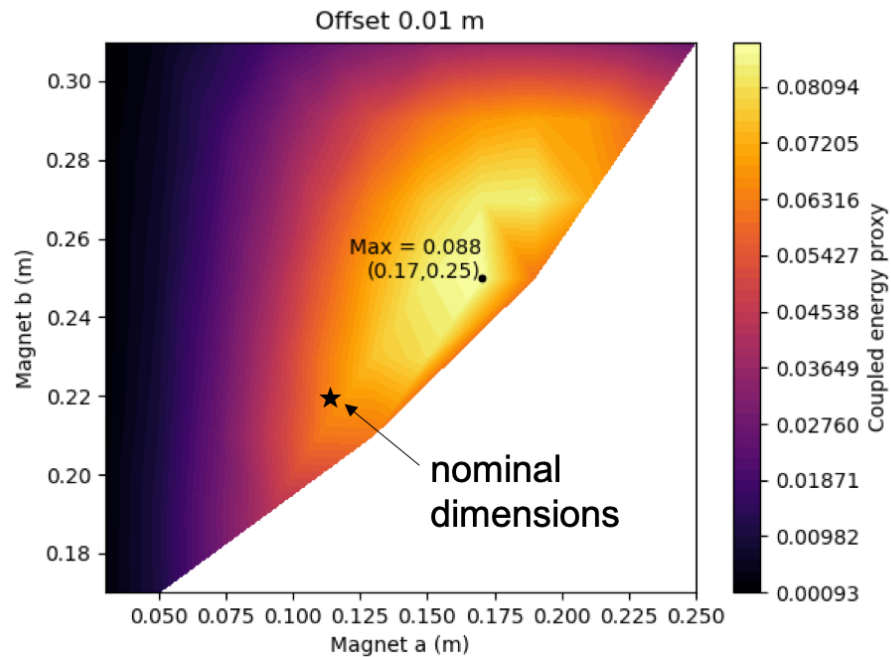


Figure B.8: Plot of the the optimization of the shielded DMRadio-50L sheath geometry with a 1 cm offset between the sheath and magnet. The x and y axes represent the magnet inner and outer radii, respectively. The color denotes a proxy for the energy coupled into the sheath from the axion source. The maximum point found from the simulations differs by several centimeters from the original choice of dimensions. The white region in the bottom right of the plot was not simulated (and includes some unphysical points where $a > b$).

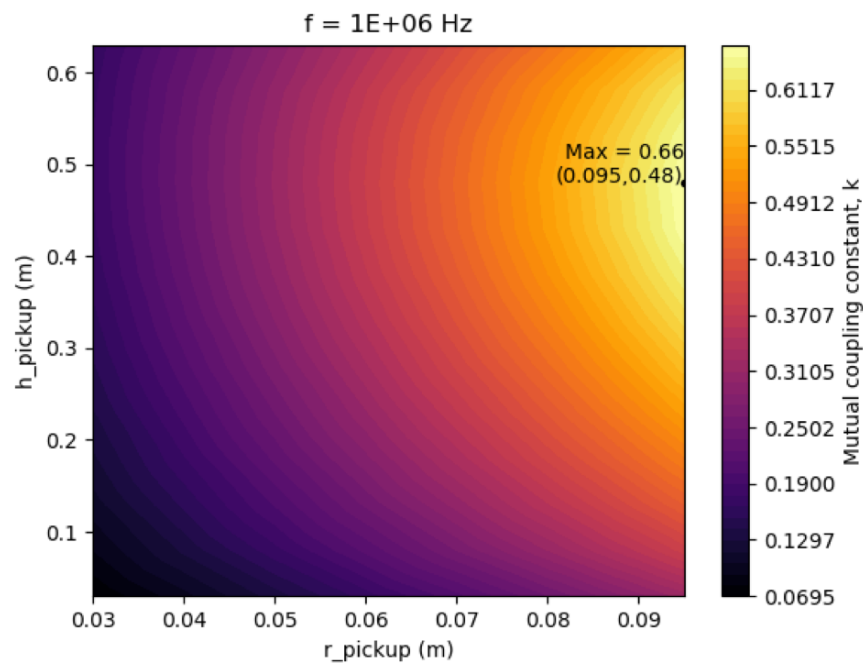


Figure B.9: Plot of the the optimization of the pickup in the central magnet/sheath bore for the optimal sheath dimensions given in Figure B.8. The x and y axes represent the pickup radius and height, respectively, for a cylindrical pickup. The color denotes the mutual inductance between the sheath and pickup.

References

- [1] F. Zwicky. “On the Masses of Nebulae and of Clusters of Nebulae”. In: *Astrophys. J.* 86 (Oct. 1937), p. 217. doi: [10.1086/143864](https://doi.org/10.1086/143864).
- [2] V. C. Rubin, W. K. Ford Jr., and N. Thonnard. “Rotational properties of 21 SC galaxies with a large range of luminosities and radii, from NGC 4605 ($R=4\text{kpc}$) to UGC 2885 ($R=122\text{kpc}$).” In: *Astrophys. J.* 238 (June 1980), pp. 471–487. doi: [10.1086/158003](https://doi.org/10.1086/158003).
- [3] Q. R. Ahmad et al. “Measurement of the Rate of $\nu_e + d \rightarrow p + p + e^-$ Interactions Produced by 8B Solar Neutrinos at the Sudbury Neutrino Observatory”. In: *Phys. Rev. Lett.* 87 (7 July 2001), p. 071301. doi: [10.1103/PhysRevLett.87.071301](https://doi.org/10.1103/PhysRevLett.87.071301).
- [4] Q. R. Ahmad et al. “Direct Evidence for Neutrino Flavor Transformation from Neutral-Current Interactions in the Sudbury Neutrino Observatory”. In: *Phys. Rev. Lett.* 89 (1 June 2002), p. 011301. doi: [10.1103/PhysRevLett.89.011301](https://doi.org/10.1103/PhysRevLett.89.011301).
- [5] K. Eguchi et al. “First Results from KamLAND: Evidence for Reactor Antineutrino Disappearance”. In: *Phys. Rev. Lett.* 90 (2 Jan. 2003), p. 021802. doi: [10.1103/PhysRevLett.90.021802](https://doi.org/10.1103/PhysRevLett.90.021802).
- [6] A. Gando et al. “Constraints on θ_{13} from a three-flavor oscillation analysis of reactor antineutrinos at KamLAND”. In: *Phys. Rev. D* 83 (5 Mar. 2011), p. 052002. doi: [10.1103/PhysRevD.83.052002](https://doi.org/10.1103/PhysRevD.83.052002).

- [7] A. Ashtekar and E. Bianchi. “A short review of loop quantum gravity”. In: *Reports on Progress in Physics* 84.4 (Mar. 2021), p. 042001. doi: [10.1088/1361-6633/abed91](https://doi.org/10.1088/1361-6633/abed91).
- [8] P. Zyla et al. “Review of Particle Physics”. In: *PTEP* 2020.8 (2020), p. 083C01. doi: [10.1093/ptep/ptaa104](https://doi.org/10.1093/ptep/ptaa104).
- [9] P. Brax. “What makes the Universe accelerate? A review on what dark energy could be and how to test it”. In: *Reports on Progress in Physics* 81.1 (Dec. 2017), p. 016902. doi: [10.1088/1361-6633/aa8e64](https://doi.org/10.1088/1361-6633/aa8e64).
- [10] R. H. Sanders. *The Dark Matter Problem: A Historical Perspective*. Cambridge University Press, 2010.
- [11] F. Zwicky. “Die Rotverschiebung von extragalaktischen Nebeln”. In: *Helvetica Physica Acta* 6 (Jan. 1933), pp. 110–127.
- [12] T. S. van Albada et al. “Distribution of dark matter in the spiral galaxy NGC 3198.” In: *ApJ* 295 (Aug. 1985), pp. 305–313. doi: [10.1086/163375](https://doi.org/10.1086/163375).
- [13] L. Necib, M. Lisanti, and V. Belokurov. “Inferred Evidence for Dark Matter Kinematic Substructure with SDSS–Gaia”. In: *The Astrophysical Journal* 874.1 (Mar. 2019), p. 3. doi: [10.3847/1538-4357/ab095b](https://doi.org/10.3847/1538-4357/ab095b).
- [14] N. Bozorgnia et al. “The dark matter component of the Gaia radially anisotropic substructure”. In: *Journal of Cosmology and Astroparticle Physics* 2020.07 (July 2020), pp. 036–036. doi: [10.1088/1475-7516/2020/07/036](https://doi.org/10.1088/1475-7516/2020/07/036).
- [15] A. Bonaca. “Reconstruction of the dark matter distribution in the Milky Way”. In: *AAS/Division of Dynamical Astronomy Meeting*. Vol. 53. AAS/Division of Dynamical Astronomy Meeting. June 2021, p. 401.06.
- [16] J. Diemand et al. “Clumps and streams in the local dark matter distribution”. In: *Nature* 454.7205 (2008), pp. 735–738. doi: [10.1038/nature07153](https://doi.org/10.1038/nature07153).
- [17] R. S. Ellis. “Gravitational lensing: a unique probe of dark matter and dark energy”. In: *Philosophical Transactions of the Royal Society A: Mathematical, Physical and Engineering Sciences* 368.1914 (Mar. 2010), pp. 967–987. doi: [10.1098/rsta.2009.0209](https://doi.org/10.1098/rsta.2009.0209).

- [18] T. H. H. Team. *NGC 4414*. June 1999. url: [https://en.wikipedia.org/wiki/File:NGC_4414_\(NASA-med\).jpg](https://en.wikipedia.org/wiki/File:NGC_4414_(NASA-med).jpg).
- [19] ESA/Hubble and NASA. *SDSS J1050+0017*. Sept. 2018. url: <https://esahubble.org/images/potw1839a/>.
- [20] D. Clowe et al. “A Direct Empirical Proof of the Existence of Dark Matter”. In: *ApJ* 648.2 (Sept. 2006), pp. L109–L113. doi: [10.1086/508162](https://doi.org/10.1086/508162).
- [21] B. Famaey and S. S. McGaugh. “Modified Newtonian Dynamics (MOND): Observational Phenomenology and Relativistic Extensions”. In: *Living Reviews in Relativity* 15.1 (2012), p. 10. doi: [10.12942/lrr-2012-10](https://doi.org/10.12942/lrr-2012-10).
- [22] S. Boran et al. “GW170817 falsifies dark matter emulators”. In: *Phys. Rev. D* 97 (4 Feb. 2018), p. 041501. doi: [10.1103/PhysRevD.97.041501](https://doi.org/10.1103/PhysRevD.97.041501).
- [23] J. Buch, S. C. (Leung, and J. Fan. “Using Gaia DR2 to constrain local dark matter density and thin dark disk”. In: *Journal of Cosmology and Astroparticle Physics* 2019.04 (Apr. 2019), pp. 026–026. doi: [10.1088/1475-7516/2019/04/026](https://doi.org/10.1088/1475-7516/2019/04/026).
- [24] S. Tremaine and J. E. Gunn. “Dynamical Role of Light Neutral Leptons in Cosmology”. In: *Phys. Rev. Lett.* 42 (6 Feb. 1979), pp. 407–410. doi: [10.1103/PhysRevLett.42.407](https://doi.org/10.1103/PhysRevLett.42.407).
- [25] C. D. Paolo, F. Nesti, and F. L. Villante. “Phase-space mass bound for fermionic dark matter from dwarf spheroidal galaxies”. In: *Monthly Notices of the Royal Astronomical Society* 475.4 (Jan. 2018), pp. 5385–5397. doi: [10.1093/mnras/sty091](https://doi.org/10.1093/mnras/sty091).
- [26] D. Savchenko and A. Rudakovskiy. “New mass bound on fermionic dark matter from a combined analysis of classical dSphs”. In: *Monthly Notices of the Royal Astronomical Society* 487.4 (June 2019), pp. 5711–5720. doi: [10.1093/mnras/stz1573](https://doi.org/10.1093/mnras/stz1573).
- [27] K. Pal, L. V. Sales, and J. Wudka. “Ultralight Thomas-Fermi dark matter”. In: *Phys. Rev. D* 100 (8 Oct. 2019), p. 083007. doi: [10.1103/PhysRevD.100.083007](https://doi.org/10.1103/PhysRevD.100.083007).
- [28] D. S. Gorbunov and V. A. Rubakov. *Introduction to the Theory of the Early Universe*. World Scientific Publishing Company, Feb. 2011. doi: [10.1142/7874](https://doi.org/10.1142/7874).

- [29] K. Freese. “Status of dark matter in the universe”. In: *The Fourteenth Marcel Grossmann Meeting*. WORLD SCIENTIFIC, Nov. 2017. doi: [10.1142/9789813226609_0018](https://doi.org/10.1142/9789813226609_0018).
- [30] J. L. Feng. “Dark Matter Candidates from Particle Physics and Methods of Detection”. In: *Annual Review of Astronomy and Astrophysics* 48.1 (2010), pp. 495–545. doi: [10.1146/annurev-astro-082708-101659](https://doi.org/10.1146/annurev-astro-082708-101659).
- [31] T. D. Brandt. “CONSTRAINTS ON MACHO DARK MATTER FROM COMPACT STELLAR SYSTEMS IN ULTRA-FAINT DWARF GALAXIES”. In: *The Astrophysical Journal* 824.2 (June 2016), p. L31. doi: [10.3847/2041-8205/824/2/131](https://doi.org/10.3847/2041-8205/824/2/131).
- [32] J. R. Primack and M. A. K. Gross. “Hot Dark Matter in Cosmology”. In: *Current Aspects of Neutrino Physics*. Springer Berlin Heidelberg, 2001, pp. 287–308. doi: [10.1007/978-3-662-04597-8_12](https://doi.org/10.1007/978-3-662-04597-8_12).
- [33] M. Fabbrichesi, E. Gabrielli, and G. Lanfranchi. *The Physics of the Dark Photon*. Springer International Publishing, 2021. doi: [10.1007/978-3-030-62519-1](https://doi.org/10.1007/978-3-030-62519-1).
- [34] D. Harvey et al. “The nongravitational interactions of dark matter in colliding galaxy clusters”. In: *Science* 347.6229 (2015), pp. 1462–1465. doi: [10.1126/science.1261381](https://doi.org/10.1126/science.1261381).
- [35] L. Roszkowski, E. M. Sessolo, and S. Trojanowski. “WIMP dark matter candidates and searches—current status and future prospects”. In: *Reports on Progress in Physics* 81.6 (May 2018), p. 066201. doi: [10.1088/1361-6633/aab913](https://doi.org/10.1088/1361-6633/aab913).
- [36] L. Hui. “Wave Dark Matter”. In: *Annual Review of Astronomy and Astrophysics* 59.1 (2021), pp. 247–289. doi: [10.1146/annurev-astro-120920-010024](https://doi.org/10.1146/annurev-astro-120920-010024).
- [37] B. M. Brubaker. “First results from the HAYSTAC axion search”. PhD thesis. 2018. doi: [10.48550/ARXIV.1801.00835](https://arxiv.org/abs/1801.00835).
- [38] R. D. Peccei. “QCD, strong CP and axions”. In: *J. Korean Phys. Soc.* 29 (1996), S199–S208. arXiv: [hep-ph/9606475](https://arxiv.org/abs/hep-ph/9606475).
- [39] M. Gell-Mann. “The interpretation of the new particles as displaced charge multiplets”. In: *Il Nuovo Cimento (1955-1965)* 4.2 (1956), pp. 848–866. doi: [10.1007/BF02748000](https://doi.org/10.1007/BF02748000).

- [40] J. F. Donoghue, E. Golowich, and B. R. Holstein. *Dynamics of the Standard Model*. Cambridge University Press, 2009. doi: [10.1017/cbo9780511803512](https://doi.org/10.1017/cbo9780511803512).
- [41] E. Witten. “Dyons of charge $e\theta/2\pi$ ”. In: *Physics Letters B* 86.3 (1979), pp. 283–287. issn: 0370-2693. doi: [https://doi.org/10.1016/0370-2693\(79\)90838-4](https://doi.org/10.1016/0370-2693(79)90838-4).
- [42] A. Belavin et al. “Pseudoparticle solutions of the Yang-Mills equations”. In: *Physics Letters B* 59.1 (1975), pp. 85–87. issn: 0370-2693. doi: [https://doi.org/10.1016/0370-2693\(75\)90163-X](https://doi.org/10.1016/0370-2693(75)90163-X).
- [43] P. J. Mohr, D. B. Newell, and B. N. Taylor. “CODATA recommended values of the fundamental physical constants: 2014”. In: *Rev. Mod. Phys.* 88 (3 Sept. 2016), p. 035009. doi: [10.1103/RevModPhys.88.035009](https://doi.org/10.1103/RevModPhys.88.035009).
- [44] H.-Y. Cheng. “The strong CP problem revisited”. In: *Physics Reports* 158.1 (1988), pp. 1–89. issn: 0370-1573. doi: [https://doi.org/10.1016/0370-1573\(88\)90135-4](https://doi.org/10.1016/0370-1573(88)90135-4).
- [45] V. Baluni. “CP-nonconserving effects in quantum chromodynamics”. In: *Phys. Rev. D* 19 (7 Apr. 1979), pp. 2227–2230. doi: [10.1103/PhysRevD.19.2227](https://doi.org/10.1103/PhysRevD.19.2227).
- [46] R. Crewther et al. “Chiral estimate of the electric dipole moment of the neutron in quantum chromodynamics”. In: *Physics Letters B* 88.1 (1979), pp. 123–127. issn: 0370-2693. doi: [https://doi.org/10.1016/0370-2693\(79\)90128-X](https://doi.org/10.1016/0370-2693(79)90128-X).
- [47] M. Kuster, G. Raffelt, and B. Beltrán, eds. *Axions*. Springer Berlin Heidelberg, 2008. doi: [10.1007/978-3-540-73518-2](https://doi.org/10.1007/978-3-540-73518-2).
- [48] C. Abel et al. “Measurement of the Permanent Electric Dipole Moment of the Neutron”. In: *Phys. Rev. Lett.* 124 (8 Feb. 2020), p. 081803. doi: [10.1103/PhysRevLett.124.081803](https://doi.org/10.1103/PhysRevLett.124.081803).
- [49] C. Vafa and E. Witten. “Parity Conservation in Quantum Chromodynamics”. In: *Phys. Rev. Lett.* 53 (6 Aug. 1984), pp. 535–536. doi: [10.1103/PhysRevLett.53.535](https://doi.org/10.1103/PhysRevLett.53.535).
- [50] C. Alexandrou et al. “Ruling Out the Massless Up-Quark Solution to the Strong CP Problem by Computing the Topological Mass Contribution with Lattice QCD”. In: *Phys. Rev. Lett.* 125 (23 Dec. 2020), p. 232001. doi: [10.1103/PhysRevLett.125.232001](https://doi.org/10.1103/PhysRevLett.125.232001).

- [51] C. S. Wu et al. “Experimental Test of Parity Conservation in Beta Decay”. In: *Phys. Rev.* 105 (4 Feb. 1957), pp. 1413–1415. doi: [10.1103/PhysRev.105.1413](https://doi.org/10.1103/PhysRev.105.1413).
- [52] J. H. Christenson et al. “Evidence for the 2π Decay of the K_2^0 Meson”. In: *Phys. Rev. Lett.* 13 (4 July 1964), pp. 138–140. doi: [10.1103/PhysRevLett.13.138](https://doi.org/10.1103/PhysRevLett.13.138).
- [53] A. Alavi-Harati et al. “Observation of Direct CP Violation in $K_{S,L} \rightarrow \pi\pi$ Decays”. In: *Phys. Rev. Lett.* 83 (1 July 1999), pp. 22–27. doi: [10.1103/PhysRevLett.83.22](https://doi.org/10.1103/PhysRevLett.83.22).
- [54] K. Abe et al. “Constraint on the matter–antimatter symmetry-violating phase in neutrino oscillations”. In: *Nature* 580.7803 (2020), pp. 339–344. doi: [10.1038/s41586-020-2177-0](https://doi.org/10.1038/s41586-020-2177-0).
- [55] A. Nelson. “Naturally weak CP violation”. In: *Physics Letters B* 136.5 (1984), pp. 387–391. issn: 0370-2693. doi: [https://doi.org/10.1016/0370-2693\(84\)92025-2](https://doi.org/10.1016/0370-2693(84)92025-2).
- [56] S. M. Barr. “Solving the Strong CP Problem without the Peccei-Quinn Symmetry”. In: *Phys. Rev. Lett.* 53 (4 July 1984), pp. 329–332. doi: [10.1103/PhysRevLett.53.329](https://doi.org/10.1103/PhysRevLett.53.329).
- [57] S. M. Barr. “Natural class of non-Peccei-Quinn models”. In: *Phys. Rev. D* 30 (8 Oct. 1984), pp. 1805–1811. doi: [10.1103/PhysRevD.30.1805](https://doi.org/10.1103/PhysRevD.30.1805).
- [58] R. D. Peccei and H. R. Quinn. “CP Conservation in the Presence of Pseudoparticles”. In: *Phys. Rev. Lett.* 38 (25 June 1977), pp. 1440–1443. doi: [10.1103/PhysRevLett.38.1440](https://doi.org/10.1103/PhysRevLett.38.1440).
- [59] R. D. Peccei and H. R. Quinn. “Constraints imposed by CP conservation in the presence of pseudoparticles”. In: *Phys. Rev. D* 16 (6 Sept. 1977), pp. 1791–1797. doi: [10.1103/PhysRevD.16.1791](https://doi.org/10.1103/PhysRevD.16.1791).
- [60] F. Wilczek. “Problem of Strong P and T Invariance in the Presence of Instantons”. In: *Phys. Rev. Lett.* 40 (5 Jan. 1978), pp. 279–282. doi: [10.1103/PhysRevLett.40.279](https://doi.org/10.1103/PhysRevLett.40.279).
- [61] S. Weinberg. “A New Light Boson?” In: *Phys. Rev. Lett.* 40 (4 Jan. 1978), pp. 223–226. doi: [10.1103/PhysRevLett.40.223](https://doi.org/10.1103/PhysRevLett.40.223).
- [62] G. G. di Cortona et al. “The QCD axion, precisely”. In: *Journal of High Energy Physics* 2016.1 (2016), p. 34. doi: [10.1007/JHEP01\(2016\)034](https://doi.org/10.1007/JHEP01(2016)034).

- [63] J. E. Kim. “Light pseudoscalars, particle physics and cosmology”. In: *Physics Reports* 150.1 (1987), pp. 1–177. issn: 0370-1573. doi: [https://doi.org/10.1016/0370-1573\(87\)90017-2](https://doi.org/10.1016/0370-1573(87)90017-2).
- [64] G. G. Raffelt. “Astrophysical methods to constrain axions and other novel particle phenomena”. In: *Physics Reports* 198.1 (1990), pp. 1–113. issn: 0370-1573. doi: [https://doi.org/10.1016/0370-1573\(90\)90054-6](https://doi.org/10.1016/0370-1573(90)90054-6).
- [65] M. S. Turner. “Windows on the axion”. In: *Physics Reports* 197.2 (1990), pp. 67–97. issn: 0370-1573. doi: [https://doi.org/10.1016/0370-1573\(90\)90172-X](https://doi.org/10.1016/0370-1573(90)90172-X).
- [66] J. E. Kim. “Weak-Interaction Singlet and Strong CP Invariance”. In: *Phys. Rev. Lett.* 43 (2 July 1979), pp. 103–107. doi: [10.1103/PhysRevLett.43.103](https://doi.org/10.1103/PhysRevLett.43.103).
- [67] M. Shifman, A. Vainshtein, and V. Zakharov. “Can confinement ensure natural CP invariance of strong interactions?” In: *Nuclear Physics B* 166.3 (1980), pp. 493–506. issn: 0550-3213. doi: [https://doi.org/10.1016/0550-3213\(80\)90209-6](https://doi.org/10.1016/0550-3213(80)90209-6).
- [68] A. R. Zhitnitsky. “On Possible Suppression of the Axion Hadron Interactions.” In: *Sov. J. Nucl. Phys.* 31 (1980), p. 260.
- [69] M. Dine, W. Fischler, and M. Srednicki. “A simple solution to the strong CP problem with a harmless axion”. In: *Physics Letters B* 104.3 (1981), pp. 199–202. issn: 0370-2693. doi: [https://doi.org/10.1016/0370-2693\(81\)90590-6](https://doi.org/10.1016/0370-2693(81)90590-6).
- [70] I. G. Irastorza and J. Redondo. “New experimental approaches in the search for axion-like particles”. In: *Progress in Particle and Nuclear Physics* 102 (2018), pp. 89–159. issn: 0146-6410. doi: <https://doi.org/10.1016/j.ppnp.2018.05.003>.
- [71] M. B. Green and J. H. Schwarz. “Anomaly Cancellation in Supersymmetric D=10 Gauge Theory and Superstring Theory”. In: *Phys. Lett. B* 149 (1984), pp. 117–122. doi: [10.1016/0370-2693\(84\)91565-X](https://doi.org/10.1016/0370-2693(84)91565-X).
- [72] P. Svrcek and E. Witten. “Axions In String Theory”. In: *JHEP* 06 (2006), p. 051. doi: [10.1088/1126-6708/2006/06/051](https://doi.org/10.1088/1126-6708/2006/06/051).
- [73] J. P. Conlon. “The QCD axion and moduli stabilisation”. In: *JHEP* 05 (2006), p. 078. doi: [10.1088/1126-6708/2006/05/078](https://doi.org/10.1088/1126-6708/2006/05/078).

- [74] B. S. Acharya, K. Bobkov, and P. Kumar. “An M Theory Solution to the Strong CP Problem and Constraints on the Axiverse”. In: *JHEP* 11 (2010), p. 105. doi: [10.1007/JHEP11\(2010\)105](https://doi.org/10.1007/JHEP11(2010)105).
- [75] A. Ringwald. “Searching for axions and ALPs from string theory”. In: *J. Phys. Conf. Ser.* 485 (2014). Ed. by M. Mondragón et al., p. 012013. doi: [10.1088/1742-6596/485/1/012013](https://doi.org/10.1088/1742-6596/485/1/012013).
- [76] M. Cicoli, M. Goodsell, and A. Ringwald. “The type IIB string axiverse and its low-energy phenomenology”. In: *JHEP* 10 (2012), p. 146. doi: [10.1007/JHEP10\(2012\)146](https://doi.org/10.1007/JHEP10(2012)146).
- [77] J. Halverson et al. “Towards string theory expectations for photon couplings to axionlike particles”. In: *Phys. Rev. D* 100.10 (2019), p. 106010. doi: [10.1103/PhysRevD.100.106010](https://doi.org/10.1103/PhysRevD.100.106010).
- [78] M. B. Wise, H. Georgi, and S. L. Glashow. “SU(5) and the Invisible Axion”. In: *Phys. Rev. Lett.* 47 (1981), p. 402. doi: [10.1103/PhysRevLett.47.402](https://doi.org/10.1103/PhysRevLett.47.402).
- [79] G. Ballesteros et al. “Standard Model—axion—seesaw—Higgs portal inflation. Five problems of particle physics and cosmology solved in one stroke”. In: *JCAP* 08 (2017), p. 001. doi: [10.1088/1475-7516/2017/08/001](https://doi.org/10.1088/1475-7516/2017/08/001).
- [80] A. Ernst, A. Ringwald, and C. Tamarit. “Axion Predictions in $SO(10) \times U(1)_{\text{PQ}}$ Models”. In: *JHEP* 02 (2018), p. 103. doi: [10.1007/JHEP02\(2018\)103](https://doi.org/10.1007/JHEP02(2018)103).
- [81] L. Di Luzio, A. Ringwald, and C. Tamarit. “Axion mass prediction from minimal grand unification”. In: *Phys. Rev. D* 98.9 (2018), p. 095011. doi: [10.1103/PhysRevD.98.095011](https://doi.org/10.1103/PhysRevD.98.095011).
- [82] P. Fileviez Pérez, C. Murgui, and A. D. Plascencia. “The QCD Axion and Unification”. In: *JHEP* 11 (2019), p. 093. doi: [10.1007/JHEP11\(2019\)093](https://doi.org/10.1007/JHEP11(2019)093).
- [83] P. Fileviez Pérez, C. Murgui, and A. D. Plascencia. “Axion Dark Matter, Proton Decay and Unification”. In: *JHEP* 01 (2020), p. 091. doi: [10.1007/JHEP01\(2020\)091](https://doi.org/10.1007/JHEP01(2020)091).
- [84] R. T. Co, F. D’Eramo, and L. J. Hall. “Supersymmetric axion grand unified theories and their predictions”. In: *Phys. Rev. D* 94.7 (2016), p. 075001. doi: [10.1103/PhysRevD.94.075001](https://doi.org/10.1103/PhysRevD.94.075001).

- [85] O. Wantz and E. P. S. Shellard. “Axion cosmology revisited”. In: *Phys. Rev. D* 82 (12 Dec. 2010), p. 123508. doi: [10.1103/PhysRevD.82.123508](https://doi.org/10.1103/PhysRevD.82.123508).
- [86] E. Armengaud et al. “Physics potential of the International Axion Observatory (IAXO)”. In: *Journal of Cosmology and Astroparticle Physics* 2019.06 (June 2019), pp. 047–047. doi: [10.1088/1475-7516/2019/06/047](https://doi.org/10.1088/1475-7516/2019/06/047).
- [87] P. Fox. *Probing a QCD String Axion with Precision Cosmological Measurements*. Tech. rep. Sept. 2004. doi: [10.2172/833013](https://doi.org/10.2172/833013).
- [88] A. Vilenkin. “Cosmic strings and domain walls”. In: *Physics Reports* 121.5 (1985), pp. 263–315. issn: 0370-1573. doi: [https://doi.org/10.1016/0370-1573\(85\)90033-X](https://doi.org/10.1016/0370-1573(85)90033-X).
- [89] T. W. B. Kibble. “Topology of cosmic domains and strings”. In: *Journal of Physics A: Mathematical and General* 9.8 (Aug. 1976), pp. 1387–1398. doi: [10.1088/0305-4470/9/8/029](https://doi.org/10.1088/0305-4470/9/8/029).
- [90] R. Davis. “Cosmic axions from cosmic strings”. In: *Physics Letters B* 180.3 (1986), pp. 225–230. issn: 0370-2693. doi: [https://doi.org/10.1016/0370-2693\(86\)90300-X](https://doi.org/10.1016/0370-2693(86)90300-X).
- [91] M. Buschmann et al. “Dark matter from axion strings with adaptive mesh refinement”. In: *Nature Communications* 13.1 (2022), p. 1049. doi: [10.1038/s41467-022-28669-y](https://doi.org/10.1038/s41467-022-28669-y).
- [92] S. Chang, C. Hagmann, and P. Sikivie. “Studies of the motion and decay of axion walls bounded by strings”. In: *Phys. Rev. D* 59 (2 Dec. 1998), p. 023505. doi: [10.1103/PhysRevD.59.023505](https://doi.org/10.1103/PhysRevD.59.023505).
- [93] Y. Akrami et al. “Planck 2018 results. X. Constraints on inflation”. In: *Astron. Astrophys.* 641 (2020), A10. doi: [10.1051/0004-6361/201833887](https://doi.org/10.1051/0004-6361/201833887).
- [94] K. J. Mack. “Axions, inflation and the anthropic principle”. In: *Journal of Cosmology and Astroparticle Physics* 2011.07 (July 2011), pp. 021–021. doi: [10.1088/1475-7516/2011/07/021](https://doi.org/10.1088/1475-7516/2011/07/021).
- [95] D. Grin, T. L. Smith, and M. Kamionkowski. “Axion constraints in nonstandard thermal histories”. In: *Phys. Rev. D* 77 (8 Apr. 2008), p. 085020. doi: [10.1103/PhysRevD.77.085020](https://doi.org/10.1103/PhysRevD.77.085020).

- [96] L. Visinelli and P. Gondolo. “Axion cold dark matter in nonstandard cosmologies”. In: *Phys. Rev. D* 81 (6 Mar. 2010), p. 063508. doi: [10.1103/PhysRevD.81.063508](https://doi.org/10.1103/PhysRevD.81.063508).
- [97] P. Agrawal, G. Marques-Tavares, and W. Xue. “Opening up the QCD axion window”. In: *Journal of High Energy Physics* 2018.3 (Mar. 2018). doi: [10.1007/jhep03\(2018\)049](https://doi.org/10.1007/jhep03(2018)049).
- [98] Y. Nomura, S. Rajendran, and F. Sanches. “Axion Isocurvature and Magnetic Monopoles”. In: *Physical Review Letters* 116.14 (Apr. 2016). doi: [10.1103/physrevlett.116.141803](https://doi.org/10.1103/physrevlett.116.141803).
- [99] M. Dine and W. Fischler. “The not-so-harmless axion”. In: *Physics Letters B* 120.1-3 (Jan. 1983), pp. 137–141. doi: [10.1016/0370-2693\(83\)90639-1](https://doi.org/10.1016/0370-2693(83)90639-1).
- [100] P. J. Steinhardt and M. S. Turner. “Saving the invisible axion”. In: *Physics Letters B* 129.1-2 (Sept. 1983), pp. 51–56. doi: [10.1016/0370-2693\(83\)90727-x](https://doi.org/10.1016/0370-2693(83)90727-x).
- [101] G. Lazarides et al. “Dilution of cosmological axions by entropy production”. In: *Nuclear Physics B* 346.1 (Dec. 1990), pp. 193–212. doi: [10.1016/0550-3213\(90\)90244-8](https://doi.org/10.1016/0550-3213(90)90244-8).
- [102] M. Kawasaki, T. Moroi, and T. Yanagida. “Can decaying particles raise the upperbound on the Peccei-Quinn scale?” In: *Physics Letters B* 383.3 (Sept. 1996), pp. 313–316. doi: [10.1016/0370-2693\(96\)00743-5](https://doi.org/10.1016/0370-2693(96)00743-5).
- [103] G. Dvali. *Removing the Cosmological Bound on the Axion Scale*. 1995. doi: [10.48550/ARXIV.HEP-PH/9505253](https://arxiv.org/abs/hep-ph/9505253).
- [104] K. Choi, H. B. Kim, and J. E. Kim. “Axion cosmology with a stronger QCD in the early universe”. In: *Nuclear Physics B* 490.1-2 (Apr. 1997), pp. 349–364. doi: [10.1016/s0550-3213\(97\)00066-7](https://doi.org/10.1016/s0550-3213(97)00066-7).
- [105] T. Banks and M. Dine. “The cosmology of string theoretic axions”. In: *Nuclear Physics B* 505.1-2 (Nov. 1997), pp. 445–460. doi: [10.1016/s0550-3213\(97\)00413-6](https://doi.org/10.1016/s0550-3213(97)00413-6).
- [106] T. Banks, M. Dine, and M. Graesser. “Supersymmetry, axions, and cosmology”. In: *Physical Review D* 68.7 (Oct. 2003). doi: [10.1103/physrevd.68.075011](https://doi.org/10.1103/physrevd.68.075011).

- [107] P. W. Graham and A. Scherlis. “Stochastic axion scenario”. In: *Phys. Rev. D* 98 (3 Aug. 2018), p. 035017. doi: [10.1103/PhysRevD.98.035017](https://doi.org/10.1103/PhysRevD.98.035017).
- [108] D. Budker et al. “Proposal for a Cosmic Axion Spin Precession Experiment (CASPER)”. In: *Phys. Rev. X* 4 (2 May 2014), p. 021030. doi: [10.1103/PhysRevX.4.021030](https://doi.org/10.1103/PhysRevX.4.021030).
- [109] D. Aybas et al. “Search for Axionlike Dark Matter Using Solid-State Nuclear Magnetic Resonance”. In: *Phys. Rev. Lett.* 126 (14 Apr. 2021), p. 141802. doi: [10.1103/PhysRevLett.126.141802](https://doi.org/10.1103/PhysRevLett.126.141802).
- [110] A. Garcon et al. “The cosmic axion spin precession experiment (CASPER): a dark-matter search with nuclear magnetic resonance”. In: *Quantum Science and Technology* 3.1 (Dec. 2017), p. 014008. doi: [10.1088/2058-9565/aa9861](https://doi.org/10.1088/2058-9565/aa9861).
- [111] M. Lawson et al. “Tunable Axion Plasma Haloscopes”. In: *Phys. Rev. Lett.* 123 (14 Oct. 2019), p. 141802. doi: [10.1103/PhysRevLett.123.141802](https://doi.org/10.1103/PhysRevLett.123.141802).
- [112] H. Primakoff. “Photo-Production of Neutral Mesons in Nuclear Electric Fields and the Mean Life of the Neutral Meson”. In: *Phys. Rev.* 81 (5 Mar. 1951), pp. 899–899. doi: [10.1103/PhysRev.81.899](https://doi.org/10.1103/PhysRev.81.899).
- [113] B. T. McAllister et al. *Broadband Axion Dark Matter Haloscopes via Electric Sensing*. 2018. doi: [10.48550/ARXIV.1803.07755](https://arxiv.org/abs/1803.07755).
- [114] M. E. Tobar, B. T. McAllister, and M. Goryachev. “Poynting vector controversy in axion modified electrodynamics”. In: *Phys. Rev. D* 105 (4 Feb. 2022), p. 045009. doi: [10.1103/PhysRevD.105.045009](https://doi.org/10.1103/PhysRevD.105.045009).
- [115] J. Ouellet and Z. Bogorad. “Solutions to axion electrodynamics in various geometries”. In: *Phys. Rev. D* 99 (5 Mar. 2019), p. 055010. doi: [10.1103/PhysRevD.99.055010](https://doi.org/10.1103/PhysRevD.99.055010).
- [116] Y. Kim et al. “Effective approximation of electromagnetism for axion haloscope searches”. In: *Physics of the Dark Universe* 26 (2019), p. 100362. issn: 2212-6864. doi: <https://doi.org/10.1016/j.dark.2019.100362>.
- [117] M. Beutter et al. “Axion-electrodynamics: a quantum field calculation”. In: *Journal of Cosmology and Astroparticle Physics* 2019.02 (Feb. 2019), pp. 026–026. doi: [10.1088/1475-7516/2019/02/026](https://doi.org/10.1088/1475-7516/2019/02/026).

- [118] K. Zhou. *Comment on "Poynting vector controversy in axion modified electrodynamics"*. 2022. doi: [10.48550/ARXIV.2203.15821](https://doi.org/10.48550/ARXIV.2203.15821).
- [119] J. W. Foster, N. L. Rodd, and B. R. Safdi. "Revealing the dark matter halo with axion direct detection". In: *Phys. Rev. D* 97 (12 June 2018), p. 123006. doi: [10.1103/PhysRevD.97.123006](https://doi.org/10.1103/PhysRevD.97.123006).
- [120] A.-C. Eilers et al. "The Circular Velocity Curve of the Milky Way from 5 to 25 kpc". In: *The Astrophysical Journal* 871.1 (Jan. 2019), p. 120. doi: [10.3847/1538-4357/aaf648](https://doi.org/10.3847/1538-4357/aaf648).
- [121] P. Sikivie. "Experimental Tests of the "Invisible" Axion". In: *Phys. Rev. Lett.* 51 (16 Oct. 1983), pp. 1415–1417. doi: [10.1103/PhysRevLett.51.1415](https://doi.org/10.1103/PhysRevLett.51.1415).
- [122] C. Hagmann et al. "Results from a search for cosmic axions". In: *Phys. Rev. D* 42 (4 Aug. 1990), pp. 1297–1300. doi: [10.1103/PhysRevD.42.1297](https://doi.org/10.1103/PhysRevD.42.1297).
- [123] S. Asztalos et al. "Design and performance of the ADMX SQUID-based microwave receiver". In: *Nuclear Instruments and Methods in Physics Research Section A: Accelerators, Spectrometers, Detectors and Associated Equipment* 656.1 (2011), pp. 39–44. issn: 0168-9002. doi: <https://doi.org/10.1016/j.nima.2011.07.019>.
- [124] N. Du et al. "Search for Invisible Axion Dark Matter with the Axion Dark Matter Experiment". In: *Phys. Rev. Lett.* 120 (15 Apr. 2018), p. 151301. doi: [10.1103/PhysRevLett.120.151301](https://doi.org/10.1103/PhysRevLett.120.151301).
- [125] L. Zhong et al. "Results from phase 1 of the HAYSTAC microwave cavity axion experiment". In: *Phys. Rev. D* 97 (9 May 2018), p. 092001. doi: [10.1103/PhysRevD.97.092001](https://doi.org/10.1103/PhysRevD.97.092001).
- [126] K. M. Backes et al. "A quantum enhanced search for dark matter axions". In: *Nature* 590.7845 (2021), pp. 238–242. doi: [10.1038/s41586-021-03226-7](https://doi.org/10.1038/s41586-021-03226-7).
- [127] A. Collaboration. *Axion Dark Matter eXperiment (ADMX) 2-4 GHz*. Snowmass2021 Letters of Interest. 2021.
- [128] A. Caldwell et al. "Dielectric Haloscopes: A New Way to Detect Axion Dark Matter". In: *Phys. Rev. Lett.* 118 (9 Mar. 2017), p. 091801. doi: [10.1103/PhysRevLett.118.091801](https://doi.org/10.1103/PhysRevLett.118.091801).

- [129] P. Brun et al. “A new experimental approach to probe QCD axion dark matter in the mass range above $\sim 40 \mu\text{eV}$ ”. In: *The European Physical Journal C* 79.3 (2019), p. 186. doi: [10.1140/epjc/s10052-019-6683-x](https://doi.org/10.1140/epjc/s10052-019-6683-x).
- [130] K. McDonald. “Voltage Drop, Potential Difference and EMF”. 2018. url: <https://www.hep.princeton.edu/~mcdonald/examples/volt.pdf>.
- [131] J. L. Ouellet et al. “Design and implementation of the ABRACADABRA-10 cm axion dark matter search”. In: *Phys. Rev. D* 99 (5 Mar. 2019), p. 052012. doi: [10.1103/PhysRevD.99.052012](https://doi.org/10.1103/PhysRevD.99.052012).
- [132] K. Wurtz et al. “Cavity Entanglement and State Swapping to Accelerate the Search for Axion Dark Matter”. In: *PRX Quantum* 2 (4 Dec. 2021), p. 040350. doi: [10.1103/PRXQuantum.2.040350](https://doi.org/10.1103/PRXQuantum.2.040350).
- [133] S. Chaudhuri et al. *Optimal Impedance Matching and Quantum Limits of Electromagnetic Axion and Hidden-Photon Dark Matter Searches*. 2018. arXiv: [1803.01627 \[hep-ph\]](https://arxiv.org/abs/1803.01627).
- [134] W. Chung. “The Coldest Axion Experiment at CAPP/IBS/KAIST in Korea”. en. In: Chung Woohyun "The Coldest Axion Experiment at CAPP/IBS/KAIST in Korea" in Proceedings (2015), 22 Jun 2015–26 Jun 2015, DESY. doi: [10.3204/DESY-PROC-2015-02/WOOHYUN_CHUNG](https://doi.org/10.3204/DESY-PROC-2015-02/WOOHYUN_CHUNG).
- [135] S. Chaudhuri et al. *Optimal Impedance Matching and Quantum Limits of Electromagnetic Axion and Hidden-Photon Dark Matter Searches*. 2021. arXiv: [1803.01627 \[hep-ph\]](https://arxiv.org/abs/1803.01627).
- [136] G. Ventura and L. Risehari. *The Art of Cryogenics*. Elsevier Science & Technology, May 2014.
- [137] A. V. Gramolin et al. “Search for axion-like dark matter with ferromagnets”. In: *Nature Physics* 17.1 (2021), pp. 79–84. doi: [10.1038/s41567-020-1006-6](https://doi.org/10.1038/s41567-020-1006-6).
- [138] J. L. Ouellet et al. “First Results from ABRACADABRA-10 cm: A Search for Sub- μeV Axion Dark Matter”. In: *Phys. Rev. Lett.* 122 (12 Mar. 2019), p. 121802. doi: [10.1103/PhysRevLett.122.121802](https://doi.org/10.1103/PhysRevLett.122.121802).
- [139] C. P. Salemi et al. “Search for Low-Mass Axion Dark Matter with ABRACADABRA-10 cm”. In: *Phys. Rev. Lett.* 127 (8 Aug. 2021), p. 081801. doi: [10.1103/PhysRevLett.127.081801](https://doi.org/10.1103/PhysRevLett.127.081801).

- [140] D. Q. Adams et al. *High sensitivity neutrinoless double-beta decay search with one tonne-year of CUORE data*. 2021. doi: [10.48550/ARXIV.2104.06906](https://doi.org/10.48550/ARXIV.2104.06906).
- [141] *Oxford Instruments*. url: <https://nanoscience.oxinst.com/>.
- [142] *Superconducting Systems, Inc.* url: <http://www.superconductingsystems.com>.
- [143] B. T. Matthias, T. H. Geballe, and V. B. Compton. “Superconductivity”. In: *Reviews of Modern Physics* 35.1 (Jan. 1963), pp. 1–22. doi: [10.1103/revmodphys.35.1](https://doi.org/10.1103/revmodphys.35.1).
- [144] M. Chang, M. M. Salleh, and D. Halin. “A short review: Properties of superconducting solder”. In: *IOP Conference Series: Materials Science and Engineering* 957.1 (Oct. 2020), p. 012059. doi: [10.1088/1757-899x/957/1/012059](https://doi.org/10.1088/1757-899x/957/1/012059).
- [145] *Bates Research and Engineering Center*. url: <https://bateslab.mit.edu/>.
- [146] *Magnicon*. url: magnicon.com.
- [147] D. Drung et al. “Highly Sensitive and Easy-to-Use SQUID Sensors”. In: *IEEE Transactions on Applied Superconductivity* 17.2 (2007), pp. 699–704. doi: [10.1109/TASC.2007.897403](https://doi.org/10.1109/TASC.2007.897403).
- [148] S. Henry et al. “Characterisation of superconducting capillaries for magnetic shielding of twisted-wire pairs in a neutron electric dipole moment experiment”. In: *Nuclear Instruments and Methods in Physics Research Section A: Accelerators, Spectrometers, Detectors and Associated Equipment* 763 (2014), pp. 155–162. issn: 0168-9002. doi: [10.1016/j.nima.2014.06.021](https://doi.org/10.1016/j.nima.2014.06.021).
- [149] W. Myers et al. “Calculated signal-to-noise ratio of MRI detected with SQUIDs and Faraday detectors in fields from $10\mu\text{T}$ to 1.5T”. In: *Journal of Magnetic Resonance* 186.2 (2007), pp. 182–192. issn: 1090-7807. doi: [10.1016/j.jmr.2007.02.007](https://doi.org/10.1016/j.jmr.2007.02.007).
- [150] *AlazarTech*. url: <https://www.alazartech.com/>.
- [151] *Stanford Research Systems*. url: www.thinksrs.com.
- [152] M. Frigo and S. Johnson. “The Design and Implementation of FFTW3”. In: *Proceedings of the IEEE* 93.2 (2005), pp. 216–231. doi: [10.1109/JPROC.2004.840301](https://doi.org/10.1109/JPROC.2004.840301).

- [153] J. Clarke and A. I. Braginski. *The SQUID handbook: Applications of SQUIDs and SQUID systems*. John Wiley & Sons, 2006.
- [154] G. Cowan et al. *Power-Constrained Limits*. 2011. doi: [10.48550/ARXIV.1105.3166](https://doi.org/10.48550/ARXIV.1105.3166).
- [155] V. Anastassopoulos et al. “New CAST Limit on the Axion-Photon Interaction”. In: *Nature Phys.* 13 (2017), pp. 584–590. doi: [10.1038/nphys4109](https://doi.org/10.1038/nphys4109).
- [156] N. Crisosto et al. “ADMX SLIC: Results from a Superconducting LC Circuit Investigating Cold Axions”. In: *Phys. Rev. Lett.* 124 (24 June 2020), p. 241101. doi: [10.1103/PhysRevLett.124.241101](https://doi.org/10.1103/PhysRevLett.124.241101).
- [157] S. Ulmer et al. “The quality factor of a superconducting rf resonator in a magnetic field”. In: *Review of Scientific Instruments* 80.12 (2009), p. 123302. doi: [10.1063/1.3271537](https://doi.org/10.1063/1.3271537).
- [158] M. S. Ebrahimi et al. “Superconducting radio-frequency resonator in magnetic fields up to 6 T”. In: *Review of Scientific Instruments* 87.7 (2016), p. 075110. doi: [10.1063/1.4958647](https://doi.org/10.1063/1.4958647).
- [159] A. Phipps et al. “Exclusion Limits on Hidden-Photon Dark Matter near 2 neV from a Fixed-Frequency Superconducting Lumped-Element Resonator”. In: *Springer Proc. Phys.* 245 (2020). Ed. by G. Carosi and G. Rybka, pp. 139–145. doi: [10.1007/978-3-030-43761-9_16](https://doi.org/10.1007/978-3-030-43761-9_16).
- [160] M. Silva-Feaver et al. “Design Overview of DM Radio Pathfinder Experiment”. In: *IEEE Transactions on Applied Superconductivity* 27.4 (2017), pp. 1–4. doi: [10.1109/TASC.2016.2631425](https://doi.org/10.1109/TASC.2016.2631425).
- [161] R. Kolb et al. *Basic Research Needs for Dark-Matter Small Projects New Initiatives: Report of the Department of Energy’s High Energy Physics Workshop on Dark Matter*. Tech. rep. US DOE Office of Science, 2018.
- [162] DMRadio Collaboration et al. *DMRadio-m³: A Search for the QCD Axion Below 1 μeV*. 2022. doi: [10.48550/ARXIV.2204.13781](https://doi.org/10.48550/ARXIV.2204.13781).
- [163] L. Brouwer et al. *Introducing DMRadio-GUT, a search for GUT-scale QCD axions*. 2022. doi: [10.48550/ARXIV.2203.11246](https://doi.org/10.48550/ARXIV.2203.11246).
- [164] K. Saito and O. Tsukuba-shi. “Critical field limitation of the niobium superconducting RF cavity”. In: 2001.

- [165] S. Posen, N. Valles, and M. Liepe. “Radio Frequency Magnetic Field Limits of Nb and Nb₃Sn”. In: *Phys. Rev. Lett.* 115 (4 July 2015), p. 047001. doi: [10.1103/PhysRevLett.115.047001](https://doi.org/10.1103/PhysRevLett.115.047001).
- [166] J. W. Foster et al. “Lumped-element searches in the breakdown of the MQS approximation, in preparation”. 2022.
- [167] S. Al Kenany et al. “Design and operational experience of a microwave cavity axion detector for the 20–100μeV range”. In: *Nuclear Instruments and Methods in Physics Research Section A: Accelerators, Spectrometers, Detectors and Associated Equipment* 854 (2017), pp. 11–24. issn: 0168-9002. doi: <https://doi.org/10.1016/j.nima.2017.02.012>.
- [168] M. Beker et al. “Seismic Attenuation Technology for the Advanced Virgo Gravitational Wave Detector”. In: *Physics Procedia* 37 (2012), pp. 1389–1397. doi: [10.1016/j.phpro.2012.03.741](https://doi.org/10.1016/j.phpro.2012.03.741).
- [169] A. Godeke et al. “Limits of NbTi and Nb₃Sn, and Development of W&R Bi–2212 High Field Accelerator Magnets”. In: *IEEE Transactions on Applied Superconductivity* 17.2 (2007), pp. 1149–1152. doi: [10.1109/TASC.2007.898447](https://doi.org/10.1109/TASC.2007.898447).
- [170] N. Mitchell et al. “The ITER Magnet System”. In: *IEEE Transactions on Applied Superconductivity* 18.2 (June 2008), pp. 435–440. doi: [10.1109/tasc.2008.921232](https://doi.org/10.1109/tasc.2008.921232).
- [171] L. Bottura et al. “Advanced Accelerator Magnets for Upgrading the LHC”. In: *IEEE Transactions on Applied Superconductivity* 22.3 (2012), pp. 4002008–4002008. doi: [10.1109/TASC.2012.2186109](https://doi.org/10.1109/TASC.2012.2186109).
- [172] E. Todesco et al. “Progress on HL-LHC Nb₃Sn Magnets”. In: *IEEE Transactions on Applied Superconductivity* 28.4 (2018), pp. 1–9. doi: [10.1109/TASC.2018.2830703](https://doi.org/10.1109/TASC.2018.2830703).
- [173] H. Maeda and Y. Yanagisawa. “Recent Developments in High-Temperature Superconducting Magnet Technology (Review)”. In: *IEEE Transactions on Applied Superconductivity* 24.3 (2014), pp. 1–12. doi: [10.1109/TASC.2013.2287707](https://doi.org/10.1109/TASC.2013.2287707).
- [174] A. J. Creely et al. “Overview of the SPARC tokamak”. In: *Journal of Plasma Physics* 86.5 (Sept. 2020). doi: [10.1017/s002377820001257](https://doi.org/10.1017/s002377820001257).

- [175] S. Chaudhuri. “Impedance matching to axion dark matter: considerations of the photon-electron interaction”. In: *Journal of Cosmology and Astroparticle Physics* 2021.12 (Dec. 2021), p. 033. doi: [10.1088/1475-7516/2021/12/033](https://doi.org/10.1088/1475-7516/2021/12/033).
- [176] A. V. Dixit et al. “Searching for Dark Matter with a Superconducting Qubit”. In: *Phys. Rev. Lett.* 126 (14 Apr. 2021), p. 141302. doi: [10.1103/PhysRevLett.126.141302](https://doi.org/10.1103/PhysRevLett.126.141302).
- [177] C. M. Caves. “Quantum limits on noise in linear amplifiers”. In: *Phys. Rev. D* 26 (8 Oct. 1982), pp. 1817–1839. doi: [10.1103/PhysRevD.26.1817](https://doi.org/10.1103/PhysRevD.26.1817).
- [178] A. A. Clerk et al. “Introduction to quantum noise, measurement, and amplification”. In: *Rev. Mod. Phys.* 82 (2 Apr. 2010), pp. 1155–1208. doi: [10.1103/RevModPhys.82.1155](https://doi.org/10.1103/RevModPhys.82.1155).
- [179] P. Falferi et al. “ $10\hbar$ superconducting quantum interference device amplifier for acoustic gravitational wave detectors”. In: *Applied Physics Letters* 93.17 (Oct. 2008), p. 172506. doi: [10.1063/1.3002321](https://doi.org/10.1063/1.3002321).
- [180] J. Clarke, C. D. Tesche, and R. P. Giffard. “Optimization of dc SQUID voltmeter and magnetometer circuits”. In: *Journal of Low Temperature Physics* 37.3-4 (Nov. 1979), pp. 405–420. doi: [10.1007/BF00119198](https://doi.org/10.1007/BF00119198).
- [181] N. S. Kampel et al. “Improving Broadband Displacement Detection with Quantum Correlations”. In: *Phys. Rev. X* 7 (2 Apr. 2017), p. 021008. doi: [10.1103/PhysRevX.7.021008](https://doi.org/10.1103/PhysRevX.7.021008).
- [182] S. Chaudhuri. “The dark matter radio: A quantum-enhanced search for QCD axion dark matter”. PhD thesis. Stanford University, 2019.
- [183] S. Kuenstner et al. “Quantum metrology of low frequency electromagnetic modes with frequency upconverters, in preparation”. 2022.
- [184] S. Kuenstner et al. “Optimizing frequency upconverters for quantum metrology of low frequency electromagnetic modes, in preparation”. 2022.
- [185] P. Krantz et al. “A quantum engineer’s guide to superconducting qubits”. In: *Applied Physics Reviews* 6.2 (June 2019), p. 021318. doi: [10.1063/1.5089550](https://doi.org/10.1063/1.5089550).

- [186] B. Abbott et al. “Observation of a kilogram-scale oscillator near its quantum ground state”. In: *New Journal of Physics* 11.7 (July 2009), p. 073032. doi: [10.1088/1367-2630/11/7/073032](https://doi.org/10.1088/1367-2630/11/7/073032).
- [187] M. Aspelmeyer, T. J. Kippenberg, and F. Marquardt. “Cavity optomechanics”. In: *Rev. Mod. Phys.* 86 (4 Dec. 2014), pp. 1391–1452. doi: [10.1103/RevModPhys.86.1391](https://doi.org/10.1103/RevModPhys.86.1391).
- [188] A. A. Clerk, F. Marquardt, and K. Jacobs. “Back-action evasion and squeezing of a mechanical resonator using a cavity detector”. In: *New Journal of Physics* 10.9 (Sept. 2008), p. 095010. doi: [10.1088/1367-2630/10/9/095010](https://doi.org/10.1088/1367-2630/10/9/095010).
- [189] M. A. Castellanos-Beltran et al. “Amplification and squeezing of quantum noise with a tunable Josephson metamaterial”. In: *Nature Physics* 4.12 (Oct. 2008), pp. 929–931. doi: [10.1038/nphys1090](https://doi.org/10.1038/nphys1090).
- [190] O. Hosten et al. “Measurement noise 100 times lower than the quantum-projection limit using entangled atoms”. In: *Nature* 529.7587 (Jan. 2016), pp. 505–508. doi: [10.1038/nature16176](https://doi.org/10.1038/nature16176).
- [191] P. Falferi et al. “A high inductance kHz resonator with a quality factor larger than 10⁶”. In: *Review of Scientific Instruments* 65.9 (Sept. 1994), pp. 2916–2919. doi: [10.1063/1.1144639](https://doi.org/10.1063/1.1144639).
- [192] H. Nagahama et al. “Highly sensitive superconducting circuits at ~700 kHz with tunable quality factors for image-current detection of single trapped antiprotons”. In: *Review of Scientific Instruments* 87.11 (Nov. 2016), p. 113305. doi: [10.1063/1.4967493](https://doi.org/10.1063/1.4967493).
- [193] A. Romanenko et al. “Three-dimensional superconducting resonators at $T < 20$ mK with the photon lifetime up to $\tau = 2$ seconds”. In: *Phys. Rev. Applied* 13 (2020), p. 034032. doi: [10.1103/PhysRevApplied.13.034032](https://doi.org/10.1103/PhysRevApplied.13.034032).
- [194] D. Blair and S. Jones. “High Q sapphire loaded superconducting cavities and application to ultrastable clocks”. In: *IEEE Transactions on Magnetics* 21.2 (1985), pp. 142–145. doi: [10.1109/TMAG.1985.1063641](https://doi.org/10.1109/TMAG.1985.1063641).
- [195] E. J. Daw. “Resonant feedback for axion and hidden sector dark matter searches”. In: *Nuclear Instruments and Methods in Physics Research Section A: Accelerators, Spectrometers, Detectors and Associated Equipment* 921 (2019), pp. 50–56. issn: 0168-9002. doi: <https://doi.org/10.1016/j.nima.2018.12.039>.

- [196] H. W. Bode. *Network analysis and feedback amplifier design*. D. van Nostrand, 1945.
- [197] R. Fano. “Theoretical limitations on the broadband matching of arbitrary impedances”. In: *Journal of the Franklin Institute* 249.1 (1950), pp. 57–83. issn: 0016-0032. doi: [https://doi.org/10.1016/0016-0032\(50\)90006-8](https://doi.org/10.1016/0016-0032(50)90006-8).
- [198] S. E. Sussman-Fort and R. M. Rudish. “Non-Foster Impedance Matching of Electrically-Small Antennas”. In: *IEEE Transactions on Antennas and Propagation* 57.8 (2009), pp. 2230–2241. doi: <10.1109/TAP.2009.2024494>.
- [199] M. Salit and M. S. Shahriar. “Enhancement of sensitivity and bandwidth of gravitational wave detectors using fast-light-based white light cavities”. In: *Journal of Optics* 12.10 (Sept. 2010), p. 104014. doi: <10.1088/2040-8978/12/10/104014>.
- [200] A. Shlivinski and Y. Hadad. “Beyond the Bode-Fano Bound: Wideband Impedance Matching for Short Pulses Using Temporal Switching of Transmission-Line Parameters”. In: *Phys. Rev. Lett.* 121 (20 Nov. 2018), p. 204301. doi: <10.1103/PhysRevLett.121.204301>.
- [201] COMSOL Multiphysics. url: www.comsol.com.
- [202] COMSOL Multiphysics Encyclopedia. url: <https://www.comsol.com/multiphysics>.